INVESTIGATIONS ON CIRCULARLY POLARIZED DIELECTRIC RESONATOR ANTENNAS AND THz ABSORBERS

Submitted in partial fulfillment of the requirements

for the award of the degree of

Doctor of Philosophy

by

Patri Upender

(Roll No. 721063)

Supervisor

Dr. Amarjit Kumar

Assistant Professor, Dept. of ECE

Department of Electronics & Communication Engineering

NATIONAL INSTITUTE OF TECHNOLOGY WARANGAL – 506004, T.S, INDIA

Febrauary-2023

APPROVAL SHEET

This thesis entitled "**Investigations on Circularly Polarized Dielectric Resonator Antennas and THz Absorbers**" by Mr. **Patri Upender** is approved for the degree of **Doctor of Philosophy**.

Examiners

_____

_____

Supervisor

_____

Dr. Amarjit Kumar

Associate Professor, Electronics and Communication Engineering Department,

NIT WARANGAL

Chairman

_____

Prof. Vakula D

Electronics and Communication Engineering Department,

NIT WARANGAL

Date:

Place:

DECLARATION

This is to certify that the work presented in the thesis entitled "**Investigations on Circularly Polarized Dielectric Resonator Antennas and THz Absorbers**" is a bonafide work done by me under the supervision of **Dr. Amarjit Kumar**, Department of Electronics and Communication Engineering, National Institute of Technology Warangal, and was not submitted elsewhere for the award of any degree.

I declare that this written submission represents my ideas in my own words and where others ideas or words have been included, I have adequately cited and referenced the original sources. I also declare that I have adhered to all principles of academic honesty and integrity and have not misrepresented or fabricated or falsified any idea/date/fact/source in my submission. I understand that any violation of the above will be cause for disciplinary action by the institute and can also evoke penal action from the sources which have thus not been properly cited or from whom proper permission has not been taken when needed.

Patri Upender
Roll No: 721063

Date:
Place: Warangal

Department of Electronics and Communication Engineering

National Institute of Technology
Warangal – 506 004, Telangana, India

CERTIFICATE

This is to certify that the dissertation work entitled **"Investigations on Circularly Polarized Dielectric Resonator Antennas and THz Absorbers"**, which is being submitted by Mr. Patri Upender (Roll No.721063), is a bonafide work submitted to National Institute of Technology Warangal in partial fulfilment of the requirement for the award of the degree of *Doctor of Philosophy in Electronics and Communication Engineering*.

To the best of our knowledge, the work incorporated in this thesis has not been submitted elsewhere for the award of any degree.

Dr. Amarjit Kumar
Supervisor
Department of ECE
National Institute of Technology
Warangal – 506004.

Dedicated to My

Family, Gurus, & Friends

Contents

ACKNOWLEDGEMENTS

I am grateful to many people who made this work possible and helped me during my Ph.D studies. I am greatly indebted to my research supervisor Dr. Amarjit Kumar for giving me excellent support during my research activity at NIT Warangal. He encouraged me in choosing my research topic, and his vision in my research area leads to successful investigations. I am very much thankful for giving research freedom and guidance, support in non-academic matters, and for the humanity shown to me. With his inimitable qualities as a good teacher, he chiseled my path toward perfection. Ever since I met him, he has been an eternal source of motivation, inspiration, encouragement, and enlightenment. He is responsible for making the period of my research work an educative and enjoyable learning experience. The thesis would not have seen the light of day without his insistent support and cooperation.

I am grateful to Prof. D. Vakula, Chairman of the Doctoral Scrutiny Committee, Head of the Department, Electronics and Communication Engineering, for the valuable suggestions and support that he shared during my research tenure.

I take this privilege to thank all my Doctoral Scrutiny Committee members, Prof. L. Anjaneyulu, for his valuable suggestions and support that he shared during my research tenure and Asst. Prof. Palash Mishra, Department of Electrical Engineering, for their detailed review, constructive suggestions, and excellent advice during the progress of this research work.

I acknowledge my gratitude to all my teachers and colleagues at various places for supporting and cooperating with me to complete this work. I would like to thank my family members for giving me mental support and inspiration. They have motivated and helped me to complete my thesis work successfully.

Finally, I thank God, for filling me every day with new hopes, strength, purpose, and faith.

Patri Upender

ABSTRACT

This thesis mainly deals with research areas related to the advancement of dielectric resonator antennas (DRAs) and THz absorbers. This research work mainly focuses on five current research issues. (i) Obtaining a tunable frequency response along with a tunable CP response using a graphene-based dielectric resonator antenna. (ii) To design MIMO DRA for terahertz applications and UAV applications. (iii) To design an ultra-wideband Circularly Polarized stacked CDRA. (iv) To design a graphene-based absorber at THz frequency for a single band, multiband and wideband response, and (v) To design narrow-band absorbers for biosensing applications.

To fulfil the first issue a 45^{o} rotated rectangular DRA is kept on top of CDRA to achieve a quad-band circularly polarized response. For the next-generation communication system, Terahertz (THz) frequency spectrum is becoming the choice of many wireless applications because of its wider bandwidth and high data rates. This antenna is coated with graphene to attain a tunable response. This antenna provides a multi-band response at different resonant frequencies. The unique feature of the proposed antenna is that it provides Circular Polarization (CP) behavior at the quad-band in the field of THz DRAs. CP tuning is achieved by varying the graphene potential of the antenna. To solve the second problem, three works are proposed. (a) 2 port MIMO DRA for THz applications, (b) 2 x 2 MIMO DRA for THz applications, and (c) 2 port MIMO antenna for UAV applications. Initially, a graphene-based MIMO DRA is designed for THz applications. In this, a two-port circularly polarized (CP) MIMO Cylindrical Dielectric Resonator Antenna (CDRA) with Quad-band response is introduced for terahertz (THz) applications. The unique feature of this antenna is that it provides resonance at the quad-band and also provides quad-sense CP response at the terahertz frequency region. Also, by varying the graphene potential of the antenna, isolation between the two antennas is increased. Next, a 2 x 2 MIMO DRA is designed for THz applications. The unique feature of this antenna is it provides a dual-band dual-sense circular polarization response in the THz frequency region. Defected Ground Structures (DGS) are made to improve the isolation between the ports. A gain of 6.7dB and RE of 73% is achieved. This antenna generates HEM11δ and HEM12δ modes. Next, a two-port MIMO DRA is designed for UAV applications. The proposed antenna provides a bandwidth of 8.4 GHz (7.5 GHz-15.9 GHz) with tri sense CP response having a 3-dB ARBW of 21.82 % (7.55-9.34 GHz), 9.36 % (11.2-12.3 GHz) and 9.72 % (13.7-15.1 GHz), respectively. The antenna exhibits a dominant RHCP wave at 8 GHz and 11.5 GHz and a

dominant LHCP wave at 14.5 GHz. Different polarizations will decrease inter-channel interference and ensure high isolation between the two frequencies because of the RHCP and LHCP response at these frequencies. To cover the third objective, ultra-wideband CP-based CDRA is designed for C-band and military satellite communication applications. In this, two identical Cylindrical Dielectric Resonator Antennas (CDRA) are stacked together to achieve Circular Polarization (CP). Three factors achieve ultra-wideband impedance bandwidth and wide axial ratio bandwidth: stacking of similar DRs, stepped conformal microstrip feed line, which will generate orthogonal modes, and new partial ground plane with circular rings. This antenna provides more than 90% radiation efficiency in the operating band. To fulfil the fourth issue, a graphene-based multiband absorber is designed using different geometric shapes for Terahertz Applications. By integrating these shapes, a unique absorber is proposed, which achieves absorption peaks at ten resonant frequencies with an average absorption rate of 97.23 percent at Terahertz frequency. The proposed structure consists of circular, triangular, square, pentagon, and hexagon-shaped absorbers to achieve multiband absorption. The proposed absorber is polarization insensitive and has a wide incidence angle tolerance. To cover the fifth issue, two dielectric-based MMA is being developed for biosensing applications for the detection of malaria, dengue, cancer, malaria, glucose content in water, and other chemicals. Two sensors are developed and analyzed for biosensing applications. First, the absorber is designed to sense cancerous cells, malaria, glucose in water, and chemicals. Results show that the absorber exhibits a high sensitivity of 1.6 THz/RIU and 1.9 THz/RIU in the LB and UB, respectively, for cancerous blood cells, 0.5516 THz/RIU and 0.5162 THz/RIU for cancerous breast cells and 0.1295 THz/RIU and 0.1316 THz/RIU for skin cancer cells detection. Second, the absorber is designed to sense dengue, malaria, and glucose content in water. For this absorber, performance is also verified by the circuit model using the transmission line method. The proposed sensor has a high S of 2.2 THz / RIU for sensing the dengue virus with a FOM of 550 RIU^{-1} and a high Q of 927.5. For malaria detection, the proposed sensor offers a high S of 1.87 THz/RIU, a high FOM of 445.24, and a high Q of 903.1. The sensor provides a high sensitivity of 1.588 with a FOM of 288.73 and Q of 712.73 during the water detection with glucose. After discussion of these research works in chapter-2, 3, 4, 5, and 6, the chapter-7 is reported with the summary, conclusions, and future scope of the current research work.

List of Figures

List of Tables

Nomenclature

2D	Two Dimensional
A	Absorption
Al_2O_3	Aluminium oxide
AR	Axial Ratio
ARBW	Axial Ratio Bandwidth
BW	Bandwidth
CCL	Channel Capacity Loss
CDRA	Cylindrical Dielectric Resonator Antenna
CP	Circular Polarization
CPDRA	Circularly polarized Dielectric resonator antenna
CST	Computer Simulation Technology
C-T-S	Circular Triangular Squae
dB	Decibels
DC	Direct Current
DG	Diversity Gain
DMMA	Dielectric Metamaterial Absorber
DMMS	Dielectric Metamaterial Sensor
DR	Dielectric Resonator
DRA	Dielectric Resonator Antenna
DWM	Dielectric Waveguide Model
E	Electric Field
ECC	Envelope Correlation Coefficient
ECD	Equivalent Circuit Design
ED	Electric Dipole
EFD	Electric Field Distribution
EFV	Electric Field Vector
EM	Electromagnetic
FBW	Fractional Bandwidth
FOM	Figure of Merit

FR	Flame Retardant
FWHM	Full-Width Half Maximum
GCR	Graphene Circular Ring
GCSR	Graphene Circular Split Ring
GHz	Gigahertz
GP	Ground Plane
H	Magnetic Field
HEM	Hybrid Electromagnetic
H-P-C	Hexagon Pentagon Circle
H-P-S	Hexagon Pentagon Square
HSRA	Hexagonal Split Ring Absorber
IBW	Impedance Bandwidth
IR	Infrared radiation
KHz	Kilohertz
LB	Lower Band
LHCP	Left Handed Circularly Polarised
LP	Linear Polarization
MD	Magnetic Dipole
MEG	Mean Effective Gain
MFD	Magnetic Field distribution
MIMO	Multiple Input Multiple Output
MLA	Matching Layer Absorber
MM	Metamaterial
MMA	Metamaterial Absorber
MPA	Microstrip Patch Antenna
Q-Factor	Quality Factor
R	Reflection
RBC	Red Blood Cells
RDR	Rectangular Dielectric Resonator
RE	Radiation Efficiency
RF	Radio Frequency
RHCP	Right Handed Circularly Polarised
RI or n	Refractive Index

RIU	Refractive Index Unit
S	Sensitivity
SC	Surface Current
SiO_2	Silicon Dioxide
SSRR	Silicon Square Ring Resonator
SSSR	Silicon Square Split Ring
STO	Strontium Titanate
T	Temperature
TARC	Total Active Reflection Coefficient
TE	Transverse Electric
TEM	Transverse Electromagnetic
THz	Terahertz
TLA	Tapered Loaded Absorber
TM	Transverse Magnetic
TU	Thickness Unit
UAV	Unmanned Aerial Vehicle
UB	Upper Band
VO_2	Vanadium Dioxide
Wi-Fi	Wireless Fidelity

Chapter 1

Introduction

The use of radio frequency (RF) technology has revolutionized modern communication, enabling wireless broadcasting and communications using antennas and trans-receivers. RF refers to a portion of the electromagnetic (EM) spectrum that ranges from 9 kilohertz (kHz) to 300 gigahertz (GHz) and 0.1 THz to 10 THz. In recent years, there has been growing interest in the development of circularly polarized dielectric resonator antennas (CPDRAs) and terahertz (THz) absorbers, which are essential components in RF systems. CPDRAs are highly efficient antennas that provide wideband operation and circular polarization, making them ideal for various applications such as satellite communication, wireless local area networks (WLAN), and mobile communication systems. They are composed of a dielectric resonator placed on a ground plane and fed by a microstrip line or a coaxial probe. The resonator's geometry and size determine the antenna's resonant frequency and polarization characteristics. On the other hand, THz absorbers are critical for attenuating EM waves in the terahertz frequency range, which is essential for applications such as terahertz communication and biosensing. THz absorbers typically consist of a structure that absorbs and converts the incident THz radiation into heat. The absorption bandwidth and efficiency depend on the materials used and the design of the absorber structure. THz spectrum has piqued the interest of researchers due to its dual characteristics of microwave and infrared frequency bands [1]. THz waves, like infrared, will radiate in a single direction and, like microwaves, travel through various non-conducting materials. Many devices are implemented in the THz regime, like antennas, for communication, absorbers, sensors, spectroscopy, and imaging for various applications [2]–[4]. Metals are a good possibility for the THz antennas and absorbers, but their poor electrical characteristics and temperature sensitivity over wide frequency range limit devices from operating at higher frequencies. Furthermore, these devices are highly susceptible to

temperature changes, and their lifetime is restricted due to oxidation and corrosion in metals. Graphene in the antenna and absorber structure has been developed recently, which allows frequency tuning [5].

This thesis explores two devices: 1. Dielectric Resonator Antenna and 2. THz Absorber.

1.1 Antenna

The antenna is an essential part of any communication system. An antenna is a transition medium between a guided wave and free space and vice versa. It's a transducer that transforms electrical energy into EM energy and vice versa [6]–[8]. In 1921, Marconi proposed that a signal may be carried in free space using a radiating device known as an antenna. A lot of advancements in the field of antennas have been recorded since then. The antenna is a critical component of a wireless communication system. Various antennas, including wire antennas, aperture antennas, reflector antennas, microstrip antennas, and dielectric resonator antennas, have been created to improve the efficiency of wireless communication systems [9]. The standards for antenna design are continuously increasing in response to market demand. Today's consumer market necessitates high-efficiency, wide-bandwidth, and compact electronic devices. Meeting these objectives in the RF and wireless domains is a significant problem since it requires the design of antennas to be incorporated into wireless devices [10]–[12]. One challenge in scaling up the frequency of millimeter bands is that most antennas nowadays operate on microwave technology, which may not be directly compatible with higher frequencies. This is because, as the frequency increases, the conduction loss in metal regions of a radiating element may become too significant for the system to function effectively. As a result, this loss may become too large for the effective functioning of a system. Microstrip patch antennas (MPAs) and dielectric resonator antennas (DRAs) have been explored for current wireless applications throughout the last few decades [12]. The MPA is made of a metallic conductor placed on a grounded substrate. It is a two-dimensional planar construction. Microstrip antennas are now widely used in various handheld devices. Microstrip patch antennas consist of metal patches of different shapes, such as rectangular, circular, and triangular, on a grounded substrate. These antennas have many advantages, such as low profile, low weight, and good mechanical stability. Fig. 1.1 shows a simple rectangular microstrip patch antenna [12]–[14]. The Dielectric Resonator Antenna (DRA) is fabricated using dielectric materials on a grounded

substrate, forming a three-dimensional structure [8], [15]. DRAs are known to offer wider bandwidth, higher gain, and improved radiation efficiency compared to MPAs. The cause for the broad impedance bandwidth is the antenna's low-quality factor, which amplifies radiations due to an abrupt change in permittivity at the dielectric air interface [16], [17].

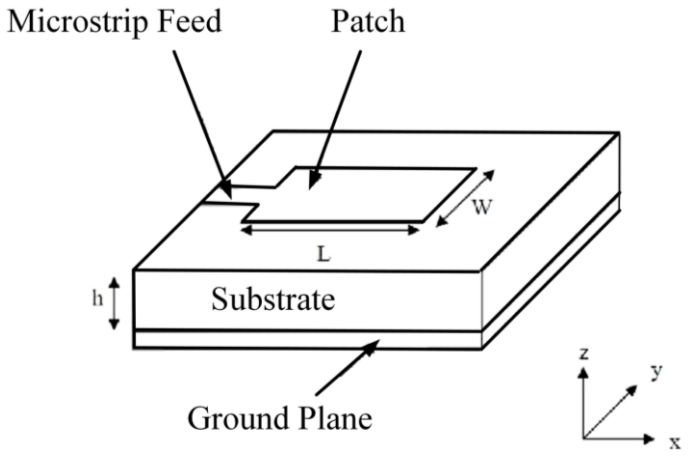

Fig. 1.1 Microstrip patch antenna.

Fig. 1.2 shows a simple aperture-coupled rectangular dielectric resonator antenna. To excite the field in DRA, the current is flowing parallel along the slot length through the aperture. The aperture consists of the slot and microstrip feed line beneath the ground plane. The most attractive feature of aperture coupling is that it offers the isolation of radiating aperture from unwanted spurious radiations as the feed network is below the ground plane [18].

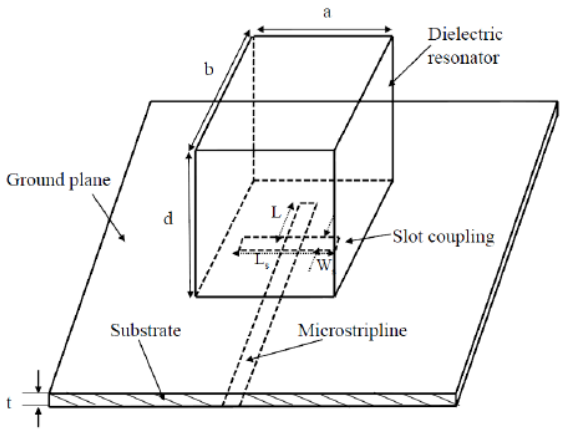

Fig. 1.2 Dielectric resonator antenna.

1.2 Dielectric resonator antennas

Dielectric Resonator Antenna (DRA) is a relatively new class of antenna whose radiator is made of a dielectric material with a relative permittivity range of 10-100 [8], [15]. DRAs are popular in the core sectors such as defense, military, radar, and especially satellite and mm-wave applications. A DRA's resonant frequency is a function of its size, shape, and dielectric constant. It has been reported that dielectric materials with specific geometries can act as resonators for higher-frequency oscillations called DRs [19]. Analysis revealed that DR must radiate in an open environment (free space). The study also reported on the concepts of resonance frequency and oscillation mode. The research investigated the potential of utilizing DR technology to create miniature antennas [20]. A comprehensive theoretical framework for estimating modal behavior in DR, as well as the characteristics of the resulting radiation field, was presented [21]. In 1983, the first experimental examination of cylindrical DR cavities was conducted [12]. Furthermore, in the same year, a rectangular DRA was analyzed and published [22], followed by the implementation of a hemispherical DRA in late 1984 [23]. Subsequently, studies of radiation properties and new applications led to the proposal of a cylindrical DRA [24]. Half-split DR is used for antenna applications placed on metal surfaces [25]. The slot-combining method is then employed with half-split DR, whereby slots are used to define leaking fields within the DR structure to define modes [25]. Until then, research into new morphologies, feeding techniques, and structures of the DRA was underway. The key information required for DRA design is the radiated field, resonant modes in the DR structure, resonant frequency, bandwidth, radiated Q-factor, and field distribution. Several research papers have been carried out to study resonant modes, and electric field distributions in the DR. These modes define field patterns for the DRA. A study of resonant modes in dielectric rod resonators has been reported [26], along with the characteristic equations of the modes present. In this work, we experimentally investigate the existence of modes. In [27] several resonant modes in open dielectric resonators is investigated, along with calculations of their properties. The generation of modes in cylindrical dielectric waveguides near and far from the cut-off frequency has been reported [28]. Transverse modes and mixed modes were studied and analysed experimentally, along with the study of modal properties [29]. The existence of modes and their radiation properties have been reported in various forms of DR [25].

This flexibility of the DRA allows it to be designed in various geometries depending on the coverage requirements of the application in the wireless communications industry. Dielectric resonators (DR) have been used for years, primarily in microwave circuits such as oscillators and filters. The unloaded quality factor (Q) generally is between 50 and 500 but can reach 10,000 [8], [15]. DRs are typically treated as energy storage devices rather than radiators. DR materials will have low-loss tangent values (10^{-4} or less). The low tangent value and high permittivity of DR make its quality factor (Q) very high ($Q \approx 1/\tan \delta$) when used in the bounded region. When a dielectric resonator (DR) is operated with open boundaries, it can radiate electromagnetic (EM) waves, which results in a decrease in the quality factor (Q) of the resonator. This effect is due to the loss of energy through radiation, and it can result in a wider bandwidth for the resonator. To explain this effect in more detail, when a DR is placed in a waveguide or other enclosed structure, the EM energy inside the resonator is trapped and oscillates back and forth at the resonant frequency, leading to a high Q value. However, when the boundaries are open, the EM energy can escape and radiate into the surrounding space, resulting in a loss of energy and a lower Q value [8], [15]. This loss of energy through radiation leads to a wider bandwidth for the resonator, which can be desirable for some applications. The amount of radiation and the resulting Q value of the DR depend on various factors, such as the resonator's geometry, dielectric constant, and the surrounding medium. By adjusting these parameters, it is possible to optimize the resonator's performance for specific applications that require a wide bandwidth. The Q of the DR is given by equation 1.1.

$$Q = \omega \frac{\text{Engery stored}}{\text{Energy lost per second}} \tag{1.1}$$

The quality factor is described as a function of frequency, including the periodic term. A periodic term represents the maximum value at each point in the DR that depends on a set of variables. For this set of variables, the current distribution within the DR is called the resonant mode [19]. In the year 1962, a microwave DR in the form of rutile DR, where the resonance frequency of the first mode ($E_{11\delta}$, $H_{11\delta}$) was calculated. Subsequently, other higher-order resonant modes ($HEM_{11\delta}$, $HEM_{12\delta}$) then calculated the resonance frequencies of these modes of the same DR [20], [30], [31]. In the year 1969 the dielectric waveguide model (DWM) was introduced [32]. The DWM model can be used to calculate the resonant frequency of the DR in higher mode calculations. Electrical and magnetic resonances within DR have been presented [26], [33], [34]. Y. Kobayashi et al., [26],

tracked and calculated the E and H field configurations where the dielectric rod is short-circuited both ends and investigated the resonant modes [26]. In the year 1983, DR-based antenna concept was proposed by S.A. Long et al.[12]. The proposed design involved a cylindrical DR with a feed attached to the bottom, which was placed on a ground plane. The DR was used to radiate EM waves through this structure [12]. Later in the same year (1983), Long et al., [22], proposed another DRA which is in the rectangular shape. An alternative type of DRA that employs a spherical-shaped DR was also investigated using the same antenna concept [23]. In sequence, several DRAs have been reported at the desired resonant frequency, like cylindrical DR with direct microstrip line feeding technique [35], broadband stacked DRA [24], an aperture coupled cylindrical DRA [36], cylindrical DRA with coplanar waveguide feeding [35], aperture coupled integrated rectangular DRA [37], half-split cylindrical DR placed above the ground plane with coaxial feeding [38]. Moreover, the radiation characteristics and parameters of the DRA have been investigated like radiation pattern [24], radiation efficiency [38], input impedance of the aperture coupled hemispherical DRA [39], hemispherical DRA with microstrip line feeding [40] with coaxial probe [39], and the resonant frequencies [24], [41]. An insight through DRs has been presented explaining the relation between the resonant frequencies, bandwidth, and quality factor of the DRs [41]. The different shapes of DR have been studied and reported, mainly consisting of cylindrical, rectangular, and hemispherical shapes. These are the typical forms of DR that are easy to create. Many structures such as triangular, spherical shaped DRs have been studied and reported as the DRA evolved [15], [42]. Fig. 1.3 shows the different geometries of DR that can be used with DRA.

Fig. 1.3 Different shapes of DR.

Different forms of DR structures create different modes that result in different field patterns. The most salient features that make DR suitable for antenna elements are its simple construction and reduced Q factor. When a dielectric resonator (DR) is operated with open boundaries, it can radiate electromagnetic (EM) waves, which results in a decrease in the quality factor (Q) of the resonator. This effect is due to the loss of energy through radiation, and it can result in a wider bandwidth for the resonator. This improves DRA bandwidth (reduces Q-factor) [8], [15]. The aspect ratio and shape of the DRA are essential parameters that determine the field patterns and modes generated within the DR structure. Each mode in DR has a different field pattern and radiation efficiency. Important antenna parameters such as operating bandwidth and gain can be improved by tuning these parameters. Due to the simple geometry of the DRA compared to other antennas, the performance and specifications of the DRA can be easily determined experimentally. The DR structure of the antenna has no conductor losses, thus improving efficiency. Changing the DR position can control the coupling between the DR structure and the transmission line. These properties make DRAs useful for microwave and millimeter wave frequency applications. DRAs can be excited using various feeding methods such as microstrip line, dielectric image waveguide feeding, aperture coupling, probes, slots, and coplanar lines. DRAs are a great alternative to microstrip antennas as they have much wider impedance bandwidth and higher power handling with many functional and attractive features. As such, these include design flexibility, low weight, compact size, versatility in geometries and feed schemes, simple construction, ease of manufacture, and wide impedance bandwidth. For the next-generation communication system, Terahertz (THz) frequency spectrum is becoming the choice of many wireless applications because of its wider bandwidth and high data rates. Many antennas are developed in the THz frequency range for different applications. Metallic radiators are not considered at this frequency because of their high losses. Hence DRA is the one of the best choice because of its low losses, high gain, and high radiation efficiency at this frequency [5], [43]–[54].

1.2.1 Advantages of DRA

DRA offers simple geometry, small size, high radiation efficiency, high gain, low loss, and relatively improved bandwidth over other antennas [41]. Dielectric resonator (DR) antennas have several advantages over microstrip patch antennas. Some of the primary benefits of using DRAs include:

1. DRA can be easily made in different shapes, such as rectangle, circle, hemisphere, and cylindrical.
2. The DR dimension is of the order $\lambda_0 / \sqrt{\varepsilon_r}$. Where λ_0 is the free-space wavelength, and ε_r is the dielectric constant of the DR material. The wavelength of an electromagnetic wave inside a material is inversely proportional to the square root of the material's relative permittivity, which is related to the dielectric constant ($\lambda = c/f\sqrt{\varepsilon_r}$). So, a higher dielectric constant material will have a smaller wavelength inside it, which means that the physical size of the DRA can be reduced while still maintaining its resonant frequency. Therefore, choosing a high dielectric constant can reduce the antenna size.
3. The DRA mode depends on the shape and aspect ratio of the DR. This provides some flexibility in the structure as different radiation patterns can be obtained by these modes depending on the requirement.
4. Since the resonator is non-metallic, DRA has no inherent conduction loss. With this advantage, DR can be used to create mm-wave antennas.
5. DRA can be easily integrated with other existing technologies such as, microstrip line, waveguide, and printed circuit board. This is to provide a simple binding scheme for all feeding techniques.
6. DR has a very high dielectric strength and provides excellent power handling capability even at higher powers. Additionally, the temperature-stable ceramic allows the antenna to operate over a wide temperature range. There is minimal frequency drift due to temperature changes in the DRA.
7. The radiation properties of the antenna can be described using different excitation modes of the DR structure. Each mode in DR has a unique field pattern depending on the external field distribution.
8. An open environment reduces the Q-factor of the resonator and increases the antenna bandwidth. Also, the bandwidth can be easily changed by changing various parameters of the DRA.

1.2.3 Applications of DRAs

Dielectric resonator antennas (DRAs) have found numerous applications in the field of wireless communication systems, owing to their unique properties and advantages. Some of the key applications of DRAs are:

1. Communication systems: DRAs can be used in wireless communication systems such as cellular networks, Wi-Fi, and satellite communication. They offer advantages such as high gain, low noise, and improved efficiency compared to traditional antennas.
2. Radar systems: DRAs can be used in radar systems for both military and civilian applications. They offer high radiation efficiency, high gain, and low side lobe levels, making them suitable for applications such as target detection and tracking.
3. Terrestrial and satellite broadcasting: DRAs are used in terrestrial and satellite broadcasting systems for transmitting and receiving signals. Their compact size and high radiation efficiency make them a good choice for applications where space is limited.
4. Medical applications: DRAs can be used in medical imaging systems, such as magnetic resonance imaging (MRI), as they offer high quality images with low interference. They can also be used in hyperthermia treatment for cancer therapy.
5. Automotive applications: DRAs can be used in automotive radar systems for collision avoidance and adaptive cruise control. They offer high gain, low profile, and low cost, making them a good choice for automotive applications.
6. Microwave and millimeter-wave systems: DRAs are used in microwave and millimeter-wave systems for applications such as point-to-point communications, radar, and sensing. They offer high radiation efficiency, low cross-polarization, and low loss at high frequencies.
7. Aerospace applications: DRAs are used in aerospace applications such as satellite communication, remote sensing, and navigation. They offer high gain and low weight, making them a good choice for space applications.
8. Military applications: DRAs are used in military applications such as electronic warfare, surveillance, and communication. They offer high gain, low side lobe levels, and low radar cross section, making them suitable for military applications.
9. IoT and wearable devices: DRAs are suitable for small form factor IoT and wearable devices due to their small size, low profile, and high efficiency.

10. RFID applications: DRAs can be used in radio-frequency identification (RFID) systems for inventory tracking and supply chain management. They offer high gain and low profile, making them suitable for RFID applications.

DRAs are also being explored for use in terahertz (THz) communication systems and other THz applications due to their non-metallic structure, which can reduce signal losses and enhance performance in this frequency range.

Some of the key applications of DRAs in THz systems include:

11. Imaging Systems: DRAs are used as imaging antennas in THz systems, where they can be used to generate high-resolution images of various materials and structures.
12. Spectroscopy Systems: DRAs are used in THz spectroscopy systems, where they can be utilized to analyze the composition and properties of materials in the THz frequency range.
13. THz Communication Systems: DRAs are being explored for use in THz communication systems, where they could provide high bandwidths and data rates, as well as reduced signal attenuation.
14. Sensing Systems: DRAs are used as sensing antennas in THz sensing systems, where they can be used to detect and analyze various types of signals, such as biological and chemical signals.

1.2.2 Circular Polarization

Circular polarization has several important applications in various fields, including communication, radar, and remote sensing. One of the most significant advantages of circular polarization is its ability to mitigate the effects of multipath interference in wireless communication. This makes it particularly useful in environments where signal reflection and scattering are prevalent, such as urban areas. Another important application of circular polarization is in satellite communication [55], [56]. Since satellites are often in motion, circularly polarized antennas can maintain a more stable link with the satellite than linearly polarized antennas. Additionally, circular polarization is less affected by atmospheric conditions such as rain and snow, which can degrade signal quality. In the field of remote sensing, circular polarization is used to study the properties of various materials and surfaces. By analysing the way that circularly polarized electromagnetic waves interact with different materials, scientists can gain insights into

their physical and chemical properties. This has important applications in areas such as geology, agriculture, and environmental monitoring.

EM waves are used in wireless communication to transport data between the transmitter and receiver. A general Transverse Electromagnetic (TEM) wave contains electric (E) and magnetic (H) field components that are perpendicular to one other and the propagation direction. TEM waves may also be distinguished by frequency, amplitude, phase, and polarisation at an observation location. Consider a z-directed planar wave having E field components in the x and y axes. The time-harmonic electric field at z = 0 is expressed as:

$$\vec{E} = E_x \cos(\omega t)\overrightarrow{a_x} + E_y \cos(\omega t + \delta)\overrightarrow{a_y} \tag{1.2}$$

Where E_x and E_y are the magnitudes of the corresponding components, δ is the phase at which the y-directed component leads the x-directed component. The antenna's polarisation can be understood from equation (1.2). For example, if $\delta = 0$, then E_x and E_y are in phase, and the net vector changes as a line. Accordingly, the wave is defined as Linearly Polarised (LP). When the two field components, $|E_x|$ and $|E_y|$, are equal, the polarisation will be linear at an angle of 45°. Furthermore, vertical polarization is obtained when the magnitude of E_x is negligible. Similarly, a horizontal polarisation is achieved when $E_y \approx 0$. If E_x and E_y have different magnitudes ($E_x \neq E_y$), the polarization can be calculated as the angle whose tangent is E_y divided by E_x:

$$\gamma = \tan^{-1}\left[\frac{E_y}{E_x}\right] \tag{1.3}$$

A diagrammatic representation of a linearly polarized wave is shown in Fig. 1.4 below.

For a wave with a phase of $\delta = \pm 90°$ and $E_x = E_y$, the field vector moves in a circular path, as seen in Fig. 1.5, and the polarisation is said to be circular. If, however, $E_x \neq E_y$, which is more common, then the field vector rotates in an elliptical path, and the polarisation is said to be elliptical as illustrated in Fig. 1.6. When the wave rotates in a clockwise direction, towards the observer, a Left Handed Circularly Polarised (LHCP) radiation is accomplished. On the other hand, if the wave rotates in an anti-clockwise direction, a Right Handed Circularly Polarised (RHCP) radiation is obtained.

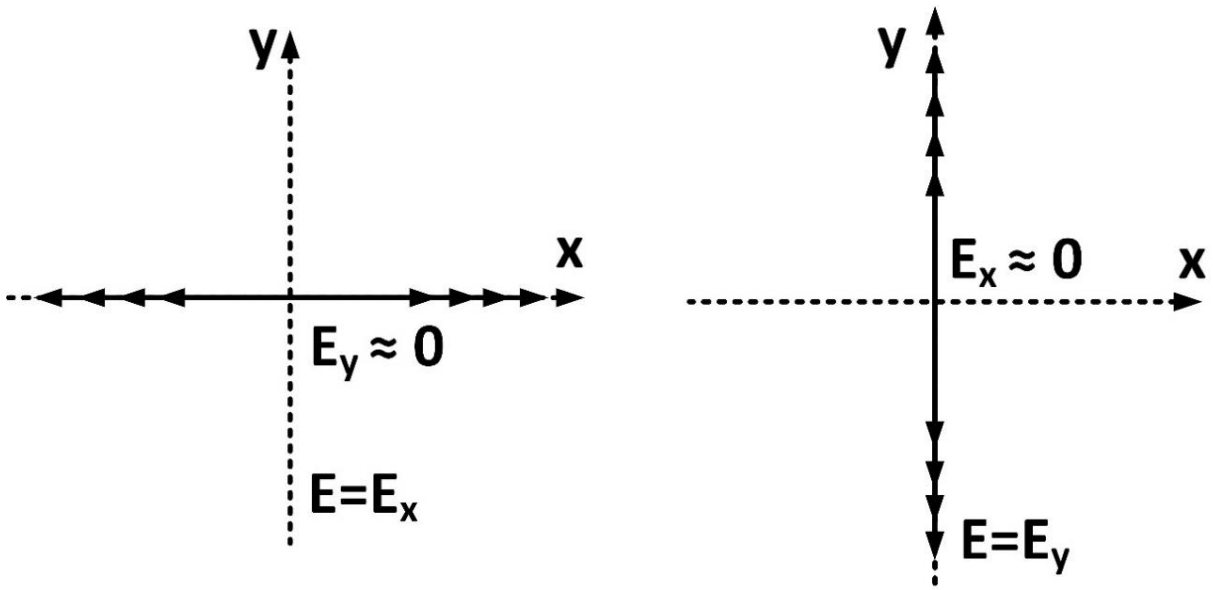

Fig. 1.4 Horizontal and vertical polarization.

Circular polarisation is defined by the Axial Ratio (AR), which is the ratio of the magnitudes of the major and minor axes of the polarization ellipse and is given in decibels by [9], [19], [41]:

$$AR = 20\log_{10}\left[\frac{|E_{max}|}{|E_{\min}|}\right] \tag{1.4}$$

It can be noticed from equation 1.4 that $1 \leq AR \leq \infty$. A pure circular polarization can be achieved when AR = 1 or 0 dB, which is difficult to achieve in practice. Therefore, a frequency range over which AR ≤ 3dB is considered and defined as [57], [58]

$$AR_{BW} = \frac{f_H - f_L}{\frac{f_H + f_L}{2}} = \frac{2(f_H - f_L)}{f_H + f_L} \tag{1.5}$$

Where f_H and f_L are the boundary frequencies for AR ≤ 3dB.

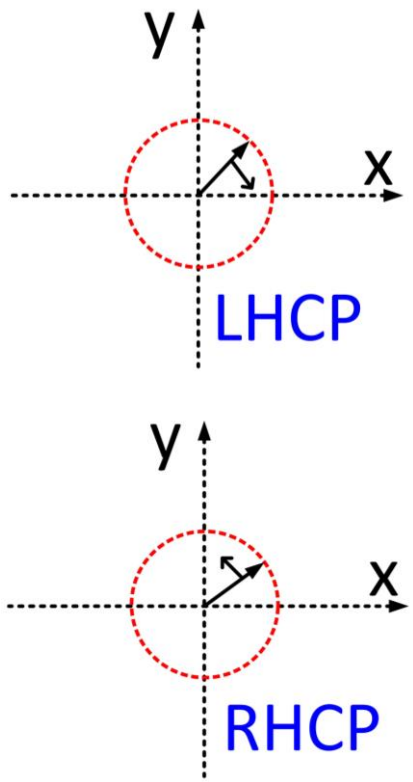

Fig. 1.5 Left-handed and Right-handed circular polarization.

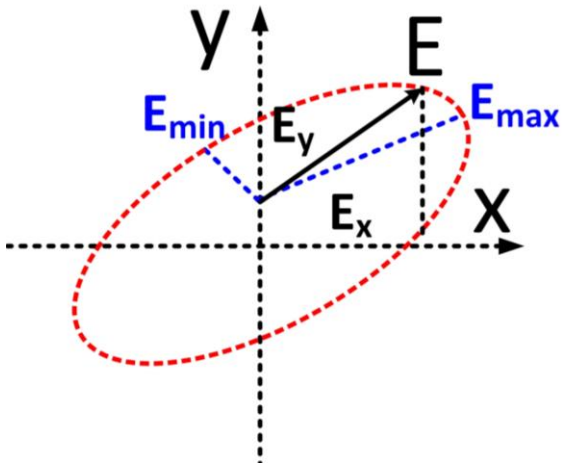

Fig. 1.6 Elliptical Polarization.

1.2.3 Techniques of CP generation in DRA

The categorization and implementation of CP-generating techniques for DRA have made significant progress. The investigations of several methods for generating CP in DRA shows that the single feeding approach is the simplest. The single feeding strategy has the problem of

providing a restricted CP bandwidth with regular DR forms [59]. The dual/multi-feeding approach was used to overcome the constraint of the single-feeding technique [60]–[62]. The multi-feeding approach may significantly increase the CP bandwidth of DRA. In comparison to the single feeding approach, the shortcoming of the multi-feeding system is that it becomes complicated and provides a large antenna structure. Another approach that comes to mind to circumvent this constraint of CPDRA with a multi-feeding technique is the use of the modified form of the DR. The changed form of DR enables the use of a single feeding procedure. The broad CP response is also provided by the change in the form of DR [63], [64]. With the wideband CP response, single feeding was used in these antenna configurations. The intricate DR forms of these antenna systems are their constraint. The intricacy of the DR forms makes manufacturing difficulty. Another option is to utilize a modified-shaped slot. The excitation slot, the most basic type of excitation, is used in the aperture-linked feeding approach. Generally, the ground plane's rectangular slot is employed for field coupling from the microstrip line to the DR. The 45° angle of inclination of DR from the slot axis excites the orthogonal modes, leading to the formation of circular polarisation [59]. Another possibility in the slot modification sequence is the cross slot [65]–[67]. The broad CP response is likewise provided by using an Archimedean spiral slot [68]. The CP response was also determined using a modified slot and the elliptical DR [69]. The CP response is provided via a logarithmic spiral slot in addition to the DR [39]. In compared to the previously described ways, using the changed form of slot appears to be relatively simple because the slot may be immediately combined with any shape of DR. Another approach for obtaining the CP response in DRA is to use a metallic strip. The use of a metallic strip on DR enables the generation of orthogonal modes [62]. Introducing a parasitic strip broadens the impedance bandwidth while generating orthogonal modes [12]. Despite the development of various techniques for circular polarization generation, there is still a need for new and innovative techniques that can be implemented in circularly polarized DRAs to achieve high-performance and reliable wireless communication, particularly in challenging environments such as military satellite communications, UAV applications and THz applications. Therefore, there is a significant gap for research and development in this area to explore new and simple techniques and optimize the performance of circularly polarized DRAs for these applications. This can involve exploring new techniques, designing novel structures, and using advanced simulation and optimization tools to improve the performance of circularly polarized DRAs.

1.2.3.1 CPDRA with single feeding technique

An Rectangular CPDRA was documented utilizing the aperture-coupled feeding technique [59]. By tilting the rectangular dielectric resonator at a 45° angle relative to the slot axis, the antenna structure exhibits orthogonal modes, as illustrated in Figure 1.7. To achieve circular polarization, the dimensions of the dielectric resonator antenna are selected to meet the prescribed criterion.

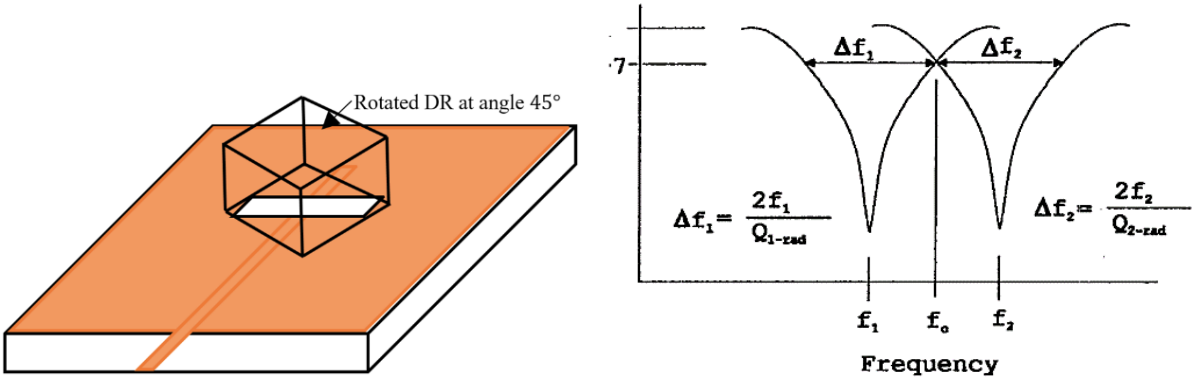

(a) (b)

Fig. 1.7. (a) Aperture coupled RDRA, (b) S-Parameter response.

A circular sector DRA was documented in [70] to achieve CP. The generation of orthogonal degenerate modes, leading to CP, was accomplished through the utilization of a single probe feeding technique and manipulation of the aspect ratio (ratio of radius to height). The modes $TM_{11\delta}$ and $TM_{21\delta}$ were excited by employing distinct probe feeding positions, as depicted in Figure 1.8. The fulfilment of the quadrature phase condition ensured the excitation of these modes, as represented by the following formula:

$$f_1 + \frac{\Delta f_1}{2} = f_2 - \frac{\Delta f_2}{2} \qquad (1.6)$$

Where, $f_1 < f_2$ and Δf is the 3-dB bandwidth of S_{11}-parameter.

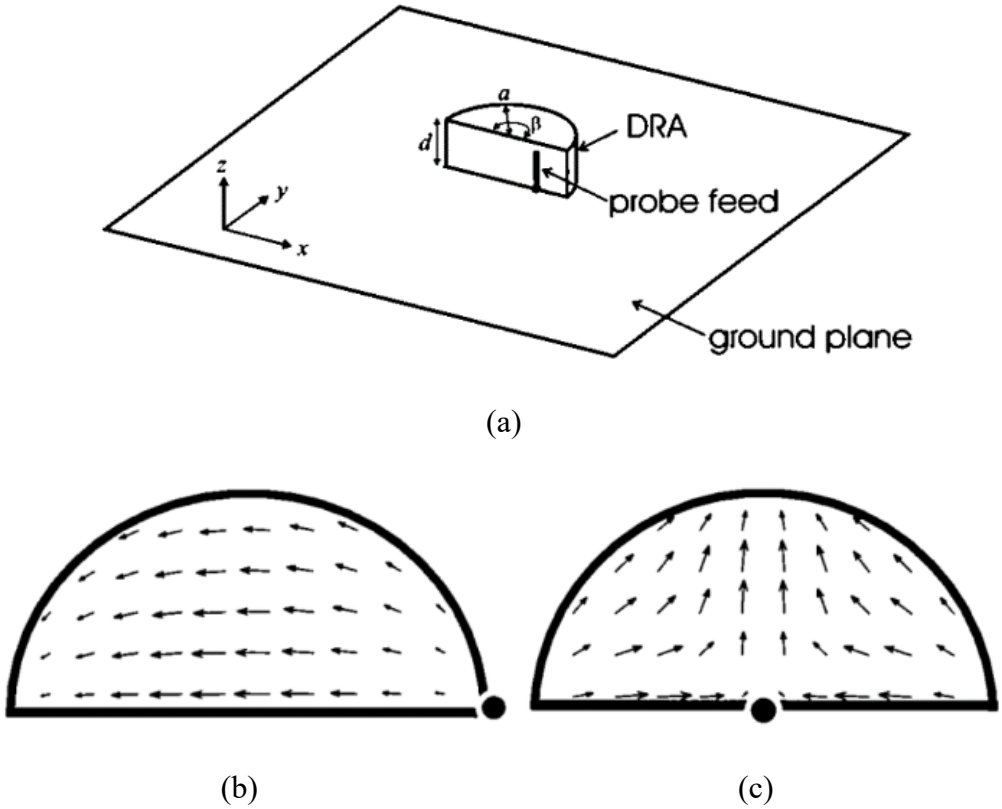

Fig. 1.8. (a) Circular sector DRA, (b) E-field distribution for $TM_{11\delta}$ mode using side feeding and (c) E-field distribution for $TM_{21\delta}$ mode using centre feeding [70].

1.2.3.2 CPDRA with multi-feeding technique

CPDRAs can be achieved using the multi-feeding technique, which offers a wideband circular polarization response. However, it should be noted that employing this technique increases the structural complexity of the antenna and enlarges its size due to the requirement of external power dividers. In this design [71], dual-slots are utilized for feeding, as illustrated in Figure 1.9. To generate orthogonal modes (HE_{111} and HE_{113}) necessary for circular polarization, an excitation strip, matching slot, and feedline are employed. The quadrature strip-fed method is primarily employed to excite the lower bands' orthogonal degenerate modes, namely HE_{111x}, HE_{111y}, HE_{113x}, and HE_{113y}, as well as the upper bands' modes. To achieve the quadrature signal, a 90° coupler is integrated into the substrate fabrication. The isolation port of the dual-band CPDRA is externally terminated at a 50Ω load. The impedance bandwidth of the antenna spans 18.9% and 7.8% for the lower and upper bands, respectively, with an axial ratio (AR) bandwidth of 12.4% and 7.4% for the lower and upper bands, respectively.

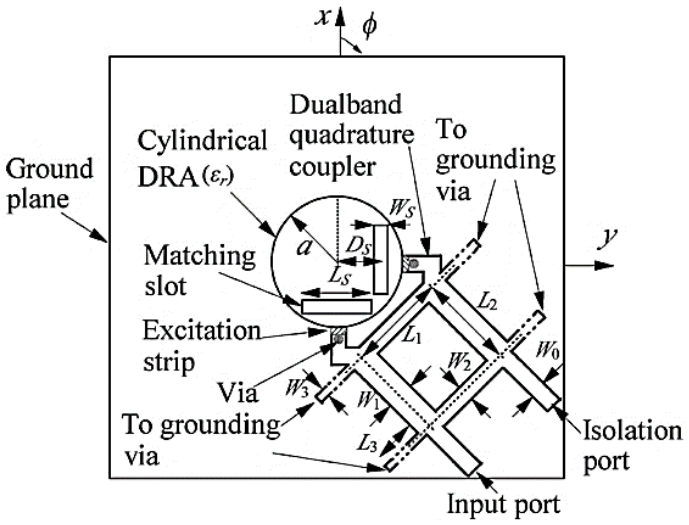

Fig. 1.9. Dual-band CPDRA with dual feeding technique [71].

1.2.3.3 CPDRA with the modified shape of DR

Various DRA geometries incorporating altered configurations of the dielectric resonator have been documented in order to attain circular polarization.

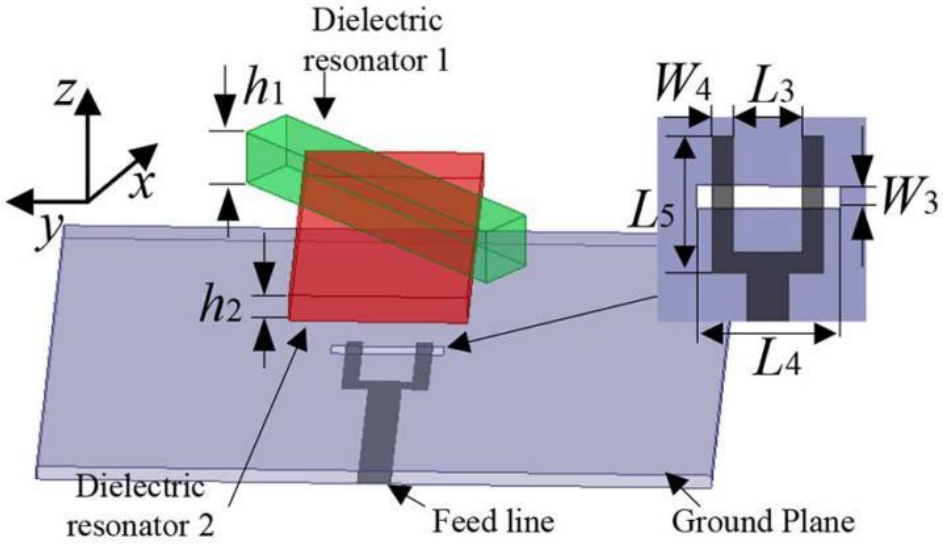

Fig. 1.10. CPDRA with rotated stair [72].

CPDRA designs have utilized modified dielectric resonator shapes. An example is the rotated-stair dielectric resonator, comprising two rectangular dielectric resonators stacked at a specific rotation angle [72] as depicted in Figure 1.22. The CPDRA achieves circular polarization through proximity

coupled feeding, employing a rectangular slot on the ground plane. The antenna exhibits an impressive impedance bandwidth of 31% and an AR bandwidth of 18.2%.

1.2.4 MIMO DRA

Multiple-Input Multiple-Output (MIMO) technology has emerged as a key enabling technology for modern wireless communication systems, including THz communication. MIMO is a wireless communication technology that uses multiple antennas at both the transmitter and receiver to increase the capacity and reliability of wireless communication. MIMO technology can be used to increase data transfer rates, which is crucial for satellite, Unmanned Aerial Vehicles (UAV), and THz communication systems [48], [73]. MIMO antennas are generally preferred because of their higher system capacity, high data speeds, high-quality network coverage, high gain, high radiation efficiency, and high data transfer, such as audio and multimedia, which are essential requirements for satellite, UAV, and THz applications for extensive data transformation [48], [73]. Furthermore, CP-based MIMO antennas are generally preferred because of the benefits of minimizing polarization mismatch. Here MIMO technology is combined with DRA to create MIMO DRAs for satellite, UAV, and THz applications. MIMO DRAs can increase the data rate and improve the reliability of wireless communication. They provide higher radiation efficiency and better impedance matching compared to other types of antennas. Circularly polarized MIMO DRAs are particularly useful in high-performance wireless communication systems. They can be used in applications such as UAVs and THz communication. Circular polarization can help to improve the signal quality and reliability of the communication system. They are particularly useful in challenging environments where reliable communication is critical. Moreover, MIMO technology based on CP is preferred because it minimizes polarization mismatch. CP-based MIMO antennas offer improved performance and reliability over other types of MIMO antennas. The use of CP-based MIMO antennas ensures that the transmitted signal is optimally received at the receiver, minimizing the impact of polarization mismatch. MIMO CPDRAs can be designed to provide a high degree of spatial diversity, which can help to increase the capacity of wireless communication. They can also be designed to reduce the overall size of the antenna system, making them suitable for compact devices. MIMO CPDRAs can operate at a range of frequencies, including microwave and millimetre-wave frequencies. They can also be designed to operate in multiple frequency bands, making them versatile for a range of applications. The use of MIMO DRAs can help to

improve the performance of 5G and beyond wireless communication systems. Several MIMO antenna systems are developed for THz frequencies for various applications [74]–[76]. In [77], a reconfigurable graphene-based THz MIMO antenna is developed, and a high spectral efficiency is reported. Although most of the research is done on the design of MIMO patch antennas at the THz region, less research is done on MIMO DRA at this frequency (THz) which provides fewer losses and is more efficient compared to patch antennas at high frequency. In this thesis MIMO CP DRA is introduced for THz applications and a two port MIMO CP DRA is designed for UAV applications.

1.3 Absorber

Recently, nearly all telecommunication systems, including television broadcasting, mobile phone (3G/4G/LTE/5G) frequencies, and Wi-Fi applications, have been operating in the lower microwave range extending from 0.3 to 30 GHz. Terahertz technology has gotten a lot of interest in recent years. Terahertz (THz) absorbers are materials or devices designed to selectively absorb electromagnetic radiation in the terahertz frequency range, typically between 0.1 and 10 THz. These absorbers are used in a variety of applications, including sensing, imaging, and communication. The THz frequency range is of particular interest because it lies between the microwave and infrared regions of the EM spectrum, where many important molecular and material properties can be probed. However, THz radiation is typically weakly absorbed by most materials, which makes it difficult to detect or manipulate. THz absorbers are designed to overcome this limitation by exploiting various physical mechanisms to enhance absorption in the THz range. These mechanisms include plasmonic resonances, phonon resonances, and polariton resonances, among others. One common approach to creating THz absorbers is to use metamaterials, which are artificial structures designed to exhibit properties not found in natural materials. Metamaterials can be engineered to have resonant properties that enhance the absorption of terahertz radiation. Other approaches include using composite materials, such as carbon nanotubes, graphene, or metal oxides, to create THz absorbers [78], [79]. THz absorbers have a wide range of potential applications. For example, they can be used for sensing and imaging applications, such as detecting chemicals, biomolecules, or explosives. They can also be used in communication systems to enhance signal-to-noise ratios and reduce interference. Additionally, THz absorbers can be used in energy harvesting devices, such as solar cells, to improve their efficiency by capturing more of the

terahertz radiation present in sunlight. Furthermore these are among the most prominent terahertz devices, with uses in terahertz imaging, sensors, heat detectors, and communication [80], [81]. It is seeing extraordinary growth not just in indoor communication but also in security monitoring systems. Active and passive components are being incorporated into numerous systems that are being developed to be more compact and resilient [82], [83]. Thin and flexible ideal absorbers are desirable and even required in these systems, in addition to outstanding absorption level, relative frequency bandwidth, insensitivity to polarisation, and angle of incidence. During World War II, both the United States and Germany designed the absorbers, marking the beginning of their use in research [81], [83]. The primary reason for researching absorbers stems from their effective utilization in possible applications. Among the applications are emitters, sensors, spatial light modulators, IR camouflage, anechoic chambers, and wireless communication. Absorbers in the applications above are classified into several classical and commercial categories, including dielectric, structural, resonant, magnetic, metamaterial, and non-metallic absorbers. Different scientific investigations have produced each type [54], [80].

1.3.1 Dielectric Absorber

This is the most basic kind of absorber. These are carbon or metal-loaded foams, polymers, or honeycomb structures. These materials are designed to have the largest dielectric loss constant, which converts the maximum of the incident wave into heat. This sort of material's impedance is not well matched to the impedance of space. As a result, they can produce a powerful reflection at their interface. These materials are often encountered in industry. Recent dielectric absorber research has centered on conductive polymer materials. They are distinguished by their low relative permittivity and high dielectric loss. The production of this sort of material is fairly complicated [84]–[86].

1.3.2 Structural Absorber

The structural absorber is a material that reduces the reflection of a wave at the interface of a material in proportion to its impedance. To enhance wave dispersion in a dielectric absorbent layer, three absorbers were developed: Pyramidal Absorber, Tapered Loaded Absorber, and Matching Layer Absorber. Achieving excellent attenuation across a wide band requires a high thickness and substantial weight of the absorber material [87].

1.3.2.1 Pyramidal Absorber

Pyramidal absorbers are typically thick materials with regularly spaced pyramidal or conical features perpendicular to the surface. These absorbers are designed to have a gradual transition from air impedance to absorber impedance at the interface. The height and periodicity of the pyramids are typically on the order of the wavelength. Pyramidal absorbers have shown excellent performance in absorbing electromagnetic waves. However, their downside is their thickness and fragility. These absorbers are commonly used in the construction of anechoic chambers [87], [88].

1.3.2.2 Tapered Loaded Absorber (TLA)

TLA is a type of absorber composed of a low-loss material plate and a high-loss material plate. These materials have the advantage of being thinner than pyramidal absorbers. The TLA design allows for a gradual transition in the impedance of the material, which enables it to attenuate a wide range of frequencies. However, TLAs are generally less efficient than pyramidal absorbers in terms of bandwidth and absorption level [89].

1.3.2.3 Matching Layer Absorber (MLA)

Matching Layer Absorber is a type of absorber that aims to reduce the thickness required for successively loaded materials. This absorber acts as a barrier between the incident wave and the absorbent materials, and the transition layer impedance is between the impedances of the two media. The goal is to create an impedance transition between different regions, which occurs when the thickness of the matching layer is a quarter of the wavelength of the incoming wave. Impedance matching only occurs at the appropriate frequency, resulting in a narrow bandwidth for this type of absorber. At low frequencies, this absorber is relatively thick [90].

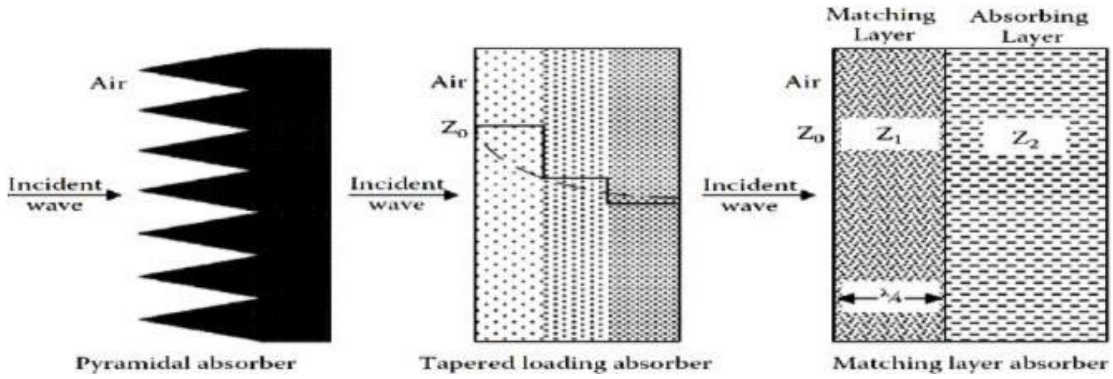

Fig. 1.11 Types of absorbers

1.3.6 Metamaterial Absorber

Metamaterials (MMs) have received a lot of attention because of their unusual features that are not seen in nature, such as tunability, polarization conversion, and absorption by providing negative refraction. Among all the features, the MM absorber (MMA) is one of the fastest-growing research fields. Landy [87] demonstrated the first MM in 2008, providing a unique idea for potentially strong absorption. Terahertz (THz) research has recently attracted great interest. THz MMAs are one of the essential devices in the THz range, with applications in THz imaging, heat sensors, and telecommunication. In recent years, absorbers have been designed with a single, dual, multi, and wideband response. Aerospace and THz communication systems require THz multiband absorber response through multiband and multi-beam systems. Multiband response is generally achieved by combining different geometric structures. Developing multiband MMAs with high absorption and high rates is challenging for researchers [91]–[93].

The equation 1.7 shows the Fresnel formula of reflection [87], which is utilized to compute the reflectivity (Γ) from the metamaterial. The reflectivity for transverse electric (TE) waves is given by equation 1.7, and for transverse magnetic (TM) waves, it is given by equation 1.8.

$$\Gamma_{TE} = \left|\frac{\mu_r cos\theta - \sqrt{n^2 - sin\theta}}{\mu_r cos\theta + \sqrt{n^2 - sin\theta}}\right|^2 \tag{1.7}$$

$$\Gamma_{TM} = \left|\frac{\varepsilon_r cos\theta - \sqrt{n^2 - sin\theta}}{\varepsilon_r cos\theta + \sqrt{n^2 - sin\theta}}\right|^2 \tag{1.8}$$

Here, θ refers to the incidence angle and $n = \sqrt{\varepsilon_r \mu_r}$ is the effective refractive index of the metamaterial. For the scenario of normal incidence, θ=0, then the above equations are written as:

$$\Gamma = \left|\frac{Z - Z_o}{Z - Z_o}\right|^2 = \left|\frac{\sqrt{\mu_r} - \sqrt{\varepsilon_r}}{\sqrt{\mu_r} + \sqrt{\varepsilon_r}}\right|^2 \tag{1.9}$$

Here $Z = \mu/\varepsilon$ is the impedance of MM and $Z_o = \sqrt{\mu_o/\varepsilon_o}$ being the impedance of free space. Since the metallic ground leads to zero transmissivity, the absorption is written as:

$$A = 1 - R = 1 - \left|\frac{Z - Z_o}{Z + Z_o}\right|^2 = 1 - \left|\frac{\sqrt{\mu_r} - \sqrt{\varepsilon_r}}{\sqrt{\mu_r} + \sqrt{\varepsilon_r}}\right|^2 \tag{1.10}$$

When the metamaterial achieves perfect impedance matching ($Z=Z_o$ or $\varepsilon_r = \mu_r$), the absorption becomes 100%. However, for a single resonance in the metamaterial (either electric or magnetic), the impedance will be strongly mismatched with that of free space, leading to the absence of a perfect absorber. To attain impedance matching in a metamaterial absorber, simultaneous electric and magnetic resonances are required.

1.3.7 Non-metallic Absorber

Current research focuses on the non-metal category. The performance of metal-based systems is limited by their poor electrical characteristics and temperature sensitivity over wide frequency ranges. Furthermore, metal-based devices are more expensive due to the use of silver or gold at higher frequencies, and their lifetime is restricted due to oxidation and corrosion in metals. Investigators have been experimenting with several methods for implementing metal-free structures. Traditional absorber materials such as metals can cause metallic losses, which can reduce the absorption efficiency of THz absorbers. Graphene, being a non-metallic material, can overcome this limitation and potentially lead to more efficient THz absorbers. Graphene is a two-dimensional material with unique properties such as high electrical conductivity, excellent mechanical strength, and high thermal conductivity. In this thesis, we will investigate the use of graphene in THz absorbers and explore its tunability characteristics. THz spectrum has piqued the interest of researchers due to its dual characteristics of microwave and infrared frequency bands. THz waves, like infrared, will radiate in a single direction and, like microwaves, travel through various non-conducting materials. Many devices are implemented in the THz regime, like antennas for communication, absorbers, sensors, spectroscopy, and imaging for various applications. Absorbers are currently being researched in various fields, including medicine, defense, and communication. Different types of absorbers are implemented, such as ultra-wide, wideband, multiband, and narrow-band absorbers [92], [94], [95].

1.3.7.1 Graphene

The ground breaking work on graphene, a two-dimensional (2D) carbon substance consisting of a monolayer of carbon atoms densely packed into a 2D honeycomb lattice, was awarded the Nobel Prize in physics in 2010 [96], [97]. However, the first graphene identified experimentally is only on the scale of a few sub-micrometres, and its consistency is poor. As a result, attempts have been made to develop manufacturing methods for creating large-area, high-quality graphene.

Meanwhile, similar graphene characterization methods that provide vivid pictures of graphene have been studied. The use of graphene material can avoid the limitations associated with metal structures [96], [97]. The discovery of graphene has accelerated not only theoretical research but also experimental validations of its material characteristics [6]. One of graphene's appealing qualities as a semi-metal material is its unique conductivity, which can be adjusted by external voltage bias or magneto static bias. Understanding graphene properties, as well as better production processes yielding high-quality graphene, pave the way for the development of graphene-based devices capable of manipulating electromagnetic (EM) waves in the THz spectrum. The main advantage of using graphene at the THz frequency region is its tunability characteristics by varying its chemical potential. In this thesis, we will investigate the use of graphene in DRAs and explore its tunability characteristics. Graphene's electrical conductivity can be modified by changing its chemical potential, which makes it an attractive material for tuning the performance of DRAs. By changing the chemical potential of graphene, we can tune the resonance frequency and radiation properties of DRAs. Additionally, we will also investigate the electric conductivity of graphene-based THz absorbers. Graphene has a high electric conductivity, which makes it an attractive material for use in absorbers. We will explore how the electric conductivity of graphene can be used to improve the absorption properties of THz absorbers. By changing the chemical potential of graphene, we can tune the absorption frequency and bandwidth of THz absorbers. Furthermore, we will investigate the non-metallic nature of graphene-based THz absorbers. Traditional absorber materials such as metals can cause metallic losses, which can reduce the absorption efficiency of THz absorbers. Graphene, being a non-metallic material, can overcome this limitation and potentially lead to more efficient THz absorbers. The advantages of using graphene in these applications:

High electrical conductivity: Graphene has an extremely high electrical conductivity, which makes it an excellent material for use in antennas. Its high conductivity allows for more efficient signal transmission and reception.

Tunability: Graphene tunability refers to the ability to modify and control the properties of graphene through various means. The tunability of graphene arises from its exceptional electronic structure, which is highly sensitive to external factors such as electric fields, chemical doping, strain, and temperature. By manipulating these factors, it is possible to modify the conductivity,

bandgap, carrier density, and other electrical properties of graphene. Furthermore, by modifying the carrier density, Fermi level, or lattice structure, graphene's resonant frequency can be precisely adjusted, enabling the design of graphene-based resonators with desired frequency characteristics for applications in sensors, communication systems, and other fields.

Low dielectric loss: Graphene has a very low dielectric loss, meaning that it can be used to create DRAs with a high Q factor. A high Q factor indicates that the antenna can store energy for longer periods, which leads to better performance.

Broadband operation: Graphene has a wide bandwidth, allowing for the creation of DRAs that can operate over a wide frequency range. This makes it particularly useful for applications that require broadband communication or sensing.

Mechanical flexibility: Graphene is mechanically flexible, which means that it can be shaped and moulded into various geometries. This property is useful for creating antennas that are conformal and can be integrated into different structures.

Strong absorption: Graphene exhibits strong absorption properties in the terahertz frequency range, making it useful for creating absorbers that can be used in applications such as sensing, imaging, and stealth technology.

The permittivity of graphene is given by, $\varepsilon_G = \varepsilon_0 - j\sigma_G / (\omega\Delta)$, where σ_G is the graphene surface conductivity and Δ is thickness [96], [97]. Graphene conductivity (σ_G) is the sum of intraband (σ_{intra}) and interband (σ_{inter}) conductivity terms [96], [97] and it is derived from Kubo-formula [96], [97] and is given by equations (1.6-1.8):

$$\sigma_G(\omega,\tau,\mu_c,T) = \sigma_{intra}(\omega,\tau,\mu_c,T) + \sigma_{inter}(\omega,\tau,\mu_c,T) \tag{1.11}$$

$$\sigma_{intra}(\omega,\tau,\mu_c,T) \approx -j\frac{e^2 k_B T}{\pi\hbar^2(\omega - j\tau^{-1})}\left[\frac{\mu_c}{k_B T} + 2\ln\left\{\exp\left(-\frac{\mu_c}{k_B T}\right)+1\right\}\right] \tag{1.12}$$

$$\sigma_{inter}(\omega,\tau,\mu_c,T) \approx -j\frac{e^2}{4\pi\hbar}\ln\left[\frac{2|\mu_c| + (\omega - j\tau^{-1})\hbar}{2|\mu_c| - (\omega - j\tau^{-1})\hbar}\right] \tag{1.13}$$

Where e is the electron's charge, k_B is the Boltzmann constant, $\hbar$ is the Planck constant, μ_c is chemical potential, T is the temperature, and τ is the graphene relaxation time [96], [97]. T is considered 300 K and τ =0.1 ps in this research work.

In this thesis, we have designed and investigated two types of antennas using graphene material for THz applications. The first one is a single-element CP DRA, and the second one is a MIMO CP DRA. The DRAs are designed to radiate EM waves in a circularly polarized manner. One of the key advantages of using graphene in the antenna design is its ability to tune the resonant frequency and axial ratio by varying the chemical potential of the graphene. This means that the resonant frequency and polarization of the antenna can be adjusted to match the frequency and polarization of the incoming signal, which improves the antenna's performance. This feature is essential for applications in THz communication, where the signal frequency is much higher than conventional communication systems. Additionally, we have investigated the isolation between the DRs in the MIMO DRA design. By varying the chemical potential of the graphene, we have increased the isolation between the DRs. This means that the interference between the DRs is reduced, which improves the performance of the MIMO DRA.

The stimulus for selecting this topic and carrying out the research work is the growing demand for advancements in dielectric resonator antennas (DRAs) and THz absorbers. Dielectric resonator antennas have gained significant interest due to their compact size, wide bandwidth, and potential applications in next-generation communication systems. The increasing need for high data rates and wider bandwidths in wireless communication systems has driven researchers to explore new techniques and designs for efficient and tunable antennas. The selection of this topic is motivated by the potential of graphene-based dielectric resonator antennas to provide tunable frequency responses and circular polarization behavior in the field of THz DRAs. Graphene's unique properties, such as its high carrier mobility and tunable conductivity, make it a promising material for achieving desired antenna characteristics. This research aims to explore the capabilities and limitations of graphene-based DRAs in achieving tunable responses and circular polarization at different resonant frequencies. Furthermore, the demand for THz applications, including wireless communication and UAV systems, has led to the investigation of MIMO (Multiple Input Multiple Output) DRA designs. The objective is to enhance the capacity and performance of these systems by utilizing multiple antennas for improved spatial multiplexing and diversity gain. Additionally,

the research addresses the need for wideband and multiband absorbers at THz frequencies for various applications, including biosensing. The development of absorbers with specific geometric shapes and materials, such as graphene, aims to achieve efficient absorption across multiple resonant frequencies while maintaining polarization insensitivity and wide incidence angle tolerance.

Different measurement techniques and methods involved in designing THz and GHz Dielectric Resonator Antennas (DRAs):

Resonant Frequency Measurement: The resonant frequency of a DRA can be determined using frequency domain measurement techniques, such as vector network analysers (VNAs). By analysing the reflection and transmission coefficients, the resonant frequency can be accurately measured.

Radiation Pattern Measurement: The radiation pattern of a DRA can be measured using an anechoic chamber or an antenna measurement system. This allows for the characterization of the antenna's directivity, gain, and polarization properties.

Impedance Measurement: Impedance measurements are crucial to ensure proper impedance matching and resonance characteristics of the DRA. Impedance analysers can be used to measure the input impedance and return loss of the antenna at different frequencies.

Near-Field Scanning Techniques: Near-field scanning techniques, such as near-field probes or near-field scanners, can be employed to analyse the near-field radiation patterns and electromagnetic coupling effects of the DRA.

Graphene Characterization: Graphene's electrical properties, such as conductivity and permittivity, can be measured using techniques like four-point probe measurements or Raman spectroscopy. These measurements help understand the impact of graphene on the antenna's performance.

Graphene Tunability Measurement: Since graphene offers tunability, its effect on the DRA's resonant frequency and radiation characteristics can be assessed by varying the graphene potential and measuring the resulting changes using frequency domain measurements or near-field scanning techniques.

Measurement techniques and methods involved in designing Graphene-Based Absorbers and Dielectric Resonator-Based Absorbers:

Absorption Measurement: The absorption characteristics of graphene-based and dielectric resonator-based absorbers can be evaluated using spectrometers or Fourier transform spectroscopy. These techniques measure the absorption spectra and identify the resonant frequencies and absorption performance of the absorbers.

Reflection and Transmission Measurements: Reflection and transmission measurements using VNAs can assess the reflection coefficient, transmission coefficient, and impedance matching of the absorbers. These measurements help optimize the absorber's performance.

Measurement techniques and methods involved in designing Biosensors:

Sensitivity Measurement: Biosensors' sensitivity, i.e., their ability to detect target analytes, can be determined by measuring the sensor response to different analyte concentrations. This can be done using calibration curves or standard solutions with known analyte concentrations. Signal-to-Noise Ratio (SNR) Measurement: SNR measurements are essential to assess the sensor's noise level and its ability to differentiate the target signal from the background noise. Techniques such as signal averaging and noise characterization can be employed to measure the SNR.

Impedance or Capacitance Measurements: Depending on the biosensor's design, impedance or capacitance measurements can be used to detect changes in electrical properties caused by the interaction between the biosensor and the target analyte. These measurements help determine the biosensor's sensitivity and selectivity.

1.4 Research Gaps

From the above explanation, the research gaps in dielectric resonator antennas and THz absorbers are listed below

- To implement new techniques for the generation of circular polarization in DRA in GHz and THz frequency regions.
- To design MIMO DRA at THz frequency regime.
- To design a non-metallic Absorber at THz frequency.

- To design a new Bio Sensor for the identification of different chemicals and diseases.

1.5 Motivation

As previously explained, the introduction of circular polarization in DRA and the implementation of graphene-based absorbers provide the following advantages -

1. Circular polarization in antennas reduces the sensitivity towards the misalignment between transmitting and receiving antennas which allow for mitigating the polarization mismatch losses.
2. The problem of the signal multipath fading is removed by using the CP antennas.
3. Metal-free absorber reduces oxidation and corrosion and increases the life time of the device.
4. Dielectric-based absorber gives an advantage over others due to their sustainability towards temperature variations and environmental effects.

Considering these advantages of the CP antennas and virtues of absorbers as motivation, this thesis is written with the following objectives-

1.6 Research Objectives

1. To design a tunable graphene-based dielectric resonator antenna for terahertz applications.
2. To design a MIMO DRA for terahertz applications and UAV applications. This objective consists of three sub-objectives:
    (a) To design a 2 port MIMO CP DRA for THz applications.
    (b) To design a 2 x 2 MIMO CP DRA for THz applications.
    (c) To design a 2-port MIMO CP DRA for UAV applications.
3. To design an ultra-wideband circularly Polarized stacked CDRA.
4. To design a graphene-based absorber at THz frequency for a single band, multiband and wideband response. This objective consists of two sub-objectives:
    (a) To design a graphene-based absorber at THz frequency for a single band, multiband response.

(b) To design a graphene-based absorber at THz frequency for a wideband response.

5. To design narrow-band absorbers for biosensing applications. This objective consists of two sub-objectives:

   (a) To design a narrow-band absorber for diagnosing malaria, cancerous cells, and other chemicals.

   (b) To design a narrow band absorber for diagnosing dengue, malaria, and glucose in water.

1.7 Thesis Organization

The thesis is organized into seven chapters. This section gives the summary of all chapters.

Chapter 1: Gives the introduction, background, and reasons for choosing the problem.

Chapter 2: The second chapter begins with the design of a quad-band Cylindrical Dielectric Resonator antenna (CDRA) along with a silicon-based Rectangular Dielectric Resonator (RDR) slab is proposed for terahertz (THz) applications. This antenna provides a multi-band response at different resonant frequencies. The unique feature of the proposed antenna is that it provides Circular Polarization (CP) behavior at the quad-band in the field of THz dielectric resonator antennas. CP tuning is achieved by varying the graphene potential of the antenna. This antenna radiates two hybrid modes, i.e., $HEM_{11\delta}$ and $HEM_{12\delta}$. These results show that the proposed Quad band CP DRA is unique and suitable for THz applications.

Chapter 3: In this chapter, a two-port and 2x2 MIMO circularly polarized (CP) MIMO Cylindrical Dielectric Resonator Antenna (CDRA) is designed for terahertz (THz) and UAV applications. This chapter consists of the design analysis of three antennas. (i) 2 Port MIMO CPDRA for THz applications, (ii) 2x2 MIMO CPDRA for THz applications, and (iii) Tri-sense Circularly Polarized wideband MIMO DRA for UAV applications.

Chapter 4: In this chapter, two identical Cylindrical Dielectric Resonator Antennas (CDRA) are stacked together to achieve Circular Polarization (CP). Three factors achieve ultra-wideband impedance bandwidth and wide axial ratio bandwidth: stacking of similar DRs, stepped conformal microstrip feed line, which will generate orthogonal modes, and new partial ground plane with

circular rings. The proposed research work heads towards providing the solution for the above objectives: ultra-wideband impedance response, wide AR response, high gain, and high efficiency.

Chapter 5: In this chapter, a multiband graphene-based absorber is designed for THz applications using different geometric shapes. By integrating these shapes, a unique absorber is proposed, which achieves absorption peaks at multi-resonant frequencies with an average absorption rate of 97.23 percent at Terahertz frequency. The proposed structure consists of circular, triangular, square, pentagon, and hexagon-shaped absorbers to achieve multiband absorption. The proposed absorber is polarization insensitive and has a wide incidence angle tolerance.

Chapter 6: In this chapter, a hexagonal split ring ultra-wideband absorber is proposed at THz frequency. The proposed structure consists of four graphene-based hexagonal split rings, a dielectric substrate, and a graphene layer at the bottom. Terahertz technology has gotten a lot of interest in recent years. Terahertz absorbers are among the most prominent terahertz devices, with uses in terahertz imaging, sensors, heat detectors, and communication. Furthermore, the existing broadband absorbers in the literature are limited by their large size, fabrication complexity, and high-temperature sensitivity. This necessitates the creation of a broadband absorber in the lower THz frequency regime with reduced size and less fabrication complexity, as well as a metal-free structure.

Chapter 7: In this chapter, a new ultrathin, ultra-narrow band Dielectric based Metamaterial Absorber (DMMA) is designed for biosensing applications. The absorber provides dual-band response with perfect absorption with ultra-narrowband absorption characteristics with resonances at 5.98 THz and 6.72 THz. For the absorber to be used for biosensor applications, narrow or ultra-narrow band absorbers with low values of full-width half maximum (FWHM), high sensitivity, high figure-of-merit (FOM) high-quality factor (Q) are required.

Chapter 2

Tunable graphene-based dielectric resonator antenna for terahertz applications

2.1 Introduction

In this chapter, a quad-band Cylindrical Dielectric Resonator antenna (CDRA) along with a silicon-based Rectangular Dielectric Resonator (RDR) slab is proposed for terahertz (THz) applications. This antenna provides a multi-band response at different resonant frequencies. The unique feature of the proposed antenna is that it provides Circular Polarization (CP) behavior at the quad-band in the field of THz dielectric resonator antennas. CP tuning is achieved by varying the graphene potential of the antenna. Robert Richtmyer first coins DRA in 1939, and the first design and testing was carried out by Long et al. [12] in 1982 by considering for dielectric surface as a leaky waveguide model. The antenna is always a powerful and supreme part of the wireless communication system [6]. Over the past few decades, the design of DRA has caught many researchers attention because of its high RE, low loss, ease to excite, and wide IBW compared with microstrip antennas. Moreover, using the dielectric constant (ε) of the DRA material, size and bandwidth can be easily controlled to achieve high gain and high radiation efficiency [15], [98]. Terahertz (THz) frequency has become a choice for the next-generation communication system because of the crowded spectrum of microwave and mm-wave [67], [99]. Furthermore, because of its high data rate and bandwidth, it enforces the research to work in the THz region. Many systems nowadays provide single-band, wide-band, or ultra-wideband response in the microwave or mm-wave region [100].

Additionally, many approaches to the design of DRA are done in the THz range with different feed mechanisms [101]. Besides this, CP behavior at different frequencies is common in any preferred antenna. In the case of LP antennas, multipath fading is quite severe. Polarization mismatch losses owing to the transmitter and receiver misalignment are also a constraint of LP antennas. The usage of CP antennas eliminates these constraints. Recently in the THz frequency region, DRA has been implemented with CP radiation behavior [102], [103].

Many current designs provide wide-band, dual-band, and single-band responses, and very little research is done on antennas that provide resonance in multiple bands while also providing circular polarization characteristics in multiple bands at THz frequencies. Another difficult task is getting high gain and radiation efficiency at THz frequency. Apart from these issues, achieving tunability for multiband antennas is also difficult at THz frequency. Graphene-based antennas could bring new capabilities to RF devices with tunability behavior at the THz frequency range. Graphene, in both single and multi-forms, has many specific characteristics, including high electrical and extreme thermal conductivity, making it ideal for RF antenna construction [48]. The antennas reported in [104], [105] focus on multiband THz frequency based on graphene. These antennas reported less gain and less radiation efficiency. To address all of these challenges, designing an antenna that can give a multiband response with high gain and high efficiency is urgently needed while tuning the resonance frequency and CP tuning.

2.2 Antenna modeling and design methodology

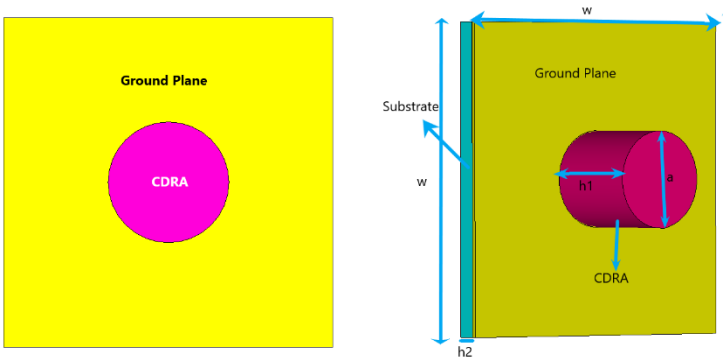

(a) (b)

Fig. 2.1 CDRA a. Top view b. Side view (with dimensions)

Fig. 2.1 depicts the configuration CDRA. It consists of silicon CDRA (ε_r = 11.9, μ_r = 1, electric conductivity (σ = 0.00025 S/m at T=300 k) with aperture slot feed on the ground plane made up of copper. Silicon dioxide (SiO_2) material with dimensions of $w \times w \times h_r$, ε_r = 3.9, μ_r =1 and loss tangent of 0.001 is used as a dielectric substrate. The feed line is etched below the substrate up to the aperture slot.

Fig. 2.1(b) shows the dimensions of CDRA, bottom substrate, and ground plane. The copper feed line etched on the bottom of the substrate has length l and width W_f, as shown in Fig. 2.2. All the optimized dimensions (μm) are given in Table 2.1. As depicted in Fig. 2.2, two patches are etched on either side of the substrate to direct the beam in a particular direction to enhance the antenna's directivity. Electromagnetic waves can be prevented from radiating under the dielectric substrate by placing two symmetrical tiny metal sheets at the substrate's rear. The dimension of the patch is given to reduce spurious radiation under a dielectric substrate [106].

The simulation procedure involved in CST is as follows:

The simulation procedure in CST for the design of the dielectric resonator antenna (DRA) involves several crucial steps. Firstly, the antenna structure is created, accurately representing the CDRA, copper ground plane with aperture slot feed, silicon dioxide (SiO2) dielectric substrate, and etched patches. Material properties are assigned to each component, including silicon for the CDRA, copper for the ground plane, and silicon dioxide for the substrate. The feed line and aperture slot are designed, ensuring proper alignment and positioning. Symmetrical metal sheets are placed at the rear of the substrate to suppress spurious radiation. The excitation source is defined, and the desired frequency range is specified. Simulation parameters, such as mesh settings and solver options, are configured for accurate results. The simulation is executed, computing characteristics such as radiation patterns, impedance bandwidth, gain, and directivity. Results are analyzed, including evaluating radiation patterns, verifying impedance bandwidth, assessing directivity enhancement, and ensuring effective suppression of spurious radiation. If necessary, the design is refined based on the analysis, and the simulation steps are iterated until satisfactory performance is achieved. This comprehensive procedure enables designers to gain insights into the DRA's behavior in the THz frequency range and optimize its performance accordingly.

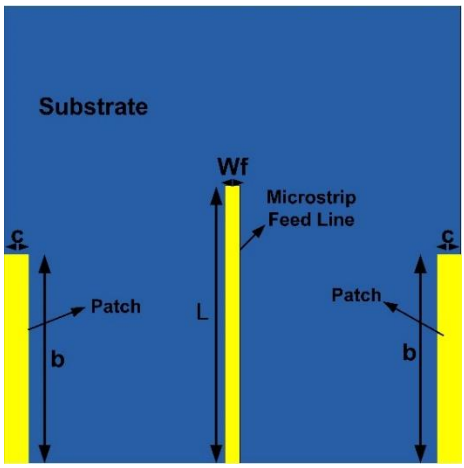

Fig. 2.2 Bottom view of the proposed antenna.

Table 2.1 Dimensions of Parameters (μm).

w	***h2***	***g***	***rout***	***rin***	***c***	***l***	***wf***	***a***	***h1***	***hr***	***wr***	***lr***
22	1.27	0.3	2	0.7	3	13.4	1	3.4	6.9	6	5	22

The thickness of the feed line is chosen so that the waves must be adequately concentrated on the surface. Coupling to the radiator must be accomplished by choosing the microstrip feed line (50Ω) dimension at the THz frequency range. To achieve the multi-band response, the dimensions are calculated for getting resonance at terahertz frequency and then optimized for obtaining the desired response. Simulation is carried out in CST Microwave Studio. The circular slot ring made on the ground plane and used for coupling efficient power to the DRA is depicted in Fig. 2.3 Proposed aperture slot.

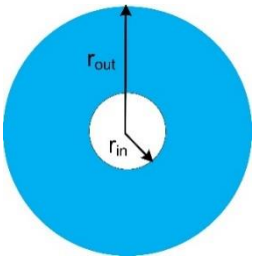

Fig. 2.3 Proposed aperture slot.

In CDRA, three modes will excite Hybrid (HE and EH or HEM) mode, TE and TM modes. Hybrid modes depend on azimuth angle (ϕ), whereas TE and TM modes will not depend on azimuth angle. CDRA excites HEM, $HEM_{npm+\delta}$, $EH_{0pm+\delta}$ and $TM_{0pm+\delta}$ where δ will range from 0 to 1. The

resonant frequency of the $HEM_{11\delta}$. The mode supported by a CDRA can be calculated using equation (2.1) [107].

$$f_{r(HEM11\delta)} = \frac{c}{2\pi r_d} \mathrm{X} \frac{6.324}{\sqrt{\varepsilon_{rd}+2}} \mathrm{X} \left[0.27 + 0.36\left(\frac{r_d}{4h_{eff}}\right) + 0.02\left(\frac{r_d}{4h_{eff}}\right)^2 \right] \quad (2.1)$$

where c is the velocity of light, r_d is the radius of CDRA, ε_{eff} is the effective permittivity, and h_{eff} is the effective height of the proposed antenna. ε_{eff} and h_{eff} can be found using equations 2 and 3 [6].

$$\varepsilon_{eff} = \frac{h_{eff}}{\frac{h_{dra}}{\varepsilon_{cdra}} + \frac{h_{sub}}{\varepsilon_{sub}}} \quad (2.2)$$

$$h_{eff} = h_{dra} + h_{sub} \quad (2.3)$$

where h_{dra} and h_{sub} are the DR height and thickness of the substrate, respectively, and ε_{cdra} and ε_{sub} are the permittivity's of DR and substrate, respectively.

Where r_d is the radius and h_d is the height of CDRA.

2.3 The operating mechanism of CDRA

In this section, the operating mechanism of the proposed CDRA is investigated. To commend the design analysis for a multi-band, CDRA without a rectangular slab is used as the allusion antenna for investigation. Different slots are used to excite DRA to demonstrate the impact of the feeding slot. The two arms on either side of the circular slot feed are of length lc=1.4μm each.

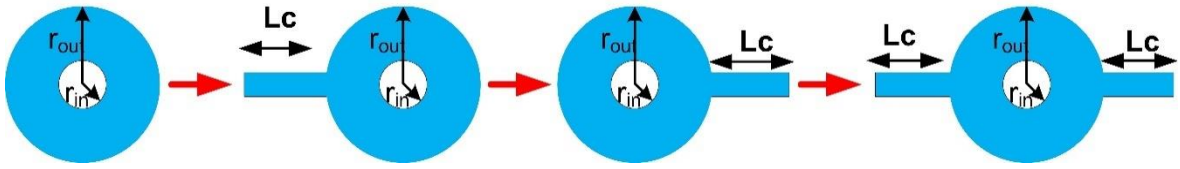

a. Ant-I b. Ant-II c. Ant-III d. Ant-IV

Fig. 2.4 Antenna configuration evolution. **a.** circular slot without any arm **b.** Circular slot with left side arm **c.** Circular slot with a right side arm. **d.** Circular slot with two arms.

As depicted in Fig. 2.4(a), antenna -I is circular slot feed without any arm and is fed with microstrip feed which is etched at the bottom of the substrate. Fig. 2.4 (b, c, and d) depicts the left side arm with circular slot feed, the right side arm with circular slot feed, and the circular slot with two arms having length ls. As depicted in Fig. 2.5, two resonant modes are excited when the antenna is fed with a circular slot (Ant-I), i.e., at 12.05 THz and 16.66 THz with an impedance bandwidth of 2.98% (11.87-12.23 THz) and 0.9% (16.56-16.71 THz) respectively. These frequencies are chosen based on the reflection coefficients (S_{11}). At these frequencies S_{11} is minimum (i.e., <-10 dB). At 12.056THz, S_{11} is approximately -19.5 dB and at 16.66 THz, S_{11} is approximately -10.74 dB. Similarly, when DRA is excited with Fig. 2.4(b), it excites at two resonant frequencies at 11.65 and 16.33 THz with S_{11} of -34.2dB at 11.65THz and -23.9 dB at 16.33 THz with impedance bandwidth of 5.86% (11.26-11.94 THz) and 8.98% (15.42-16.87 THz). When DRA is excited with Fig. 2.4(c), it excites at two resonant frequencies at 11.62 (S_{11}=-37.05dB) and 16.33 THz (S_{11}=-30.9) with impedance bandwidth of 5.87% (11.24-11.92 THz) and 9.3% (15.36-16.86 THz). Finally, the circular slot with two arms excites at three resonant frequencies as depicted in Fig. 2.5. One at 8.12 THz with S_{11} of -16.04 dB, another one at 11.38 THz with S_{11} of -23.8 dB and third one at 15.29 THz with S_{11} of -26 dB. The impedance bandwidth in percentage is given by 6.7% (7.93-8.48 THz), 7.6% (11.74-10.87 THz) and 12.65% (14.51-16.47 THz). It can be observed that a considerable increase in impedance bandwidth with the proposed feed slot design (Ant-IV of Fig. 2.4).

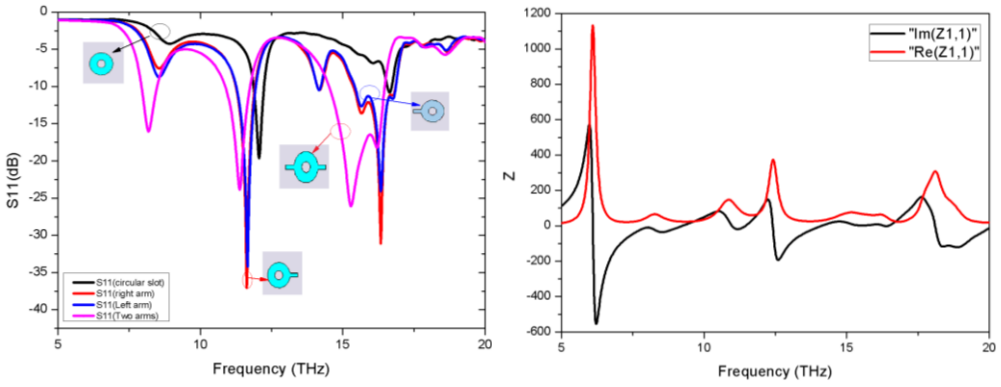

(a) (b)

Fig. 2.5 (a) Frequency response (S_{11}) of CDRA (b) Impedance response.

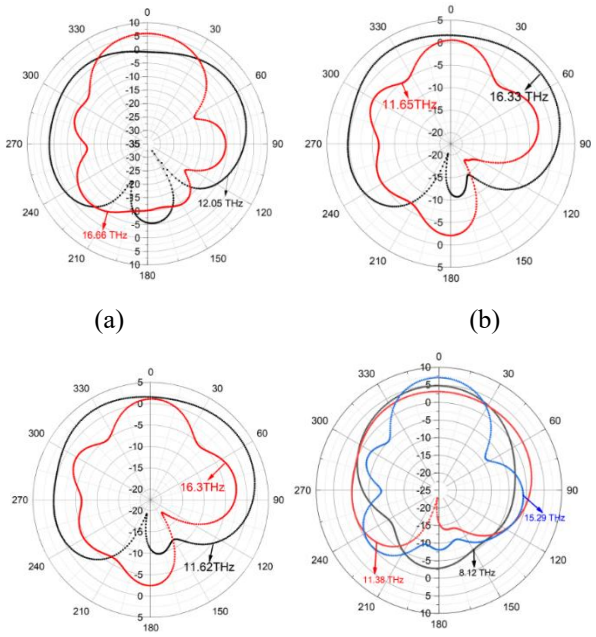

(a) (b)

(c) (d)

Fig. 2.6 2D radiation patterns for **a.** Ant-I, **b.** Ant-II, **c.** Ant-III and **d.** Ant-IV.

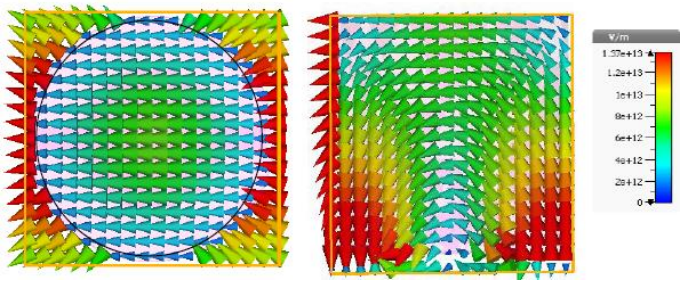

(a) (b)

Fig. 2.7 E-Field distribution on CDRA at 8.12 THz (a) Top view (XY-Plane) and (b) Side view (XZ-Plane).

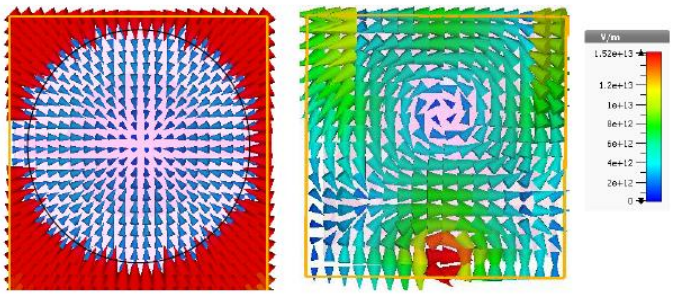

(a) (b)

Fig. 2.8 E-Field distribution on CDRA at 11.38 THz (a) Top view (XY-Plane) and (b) Side view (XZ-Plane).

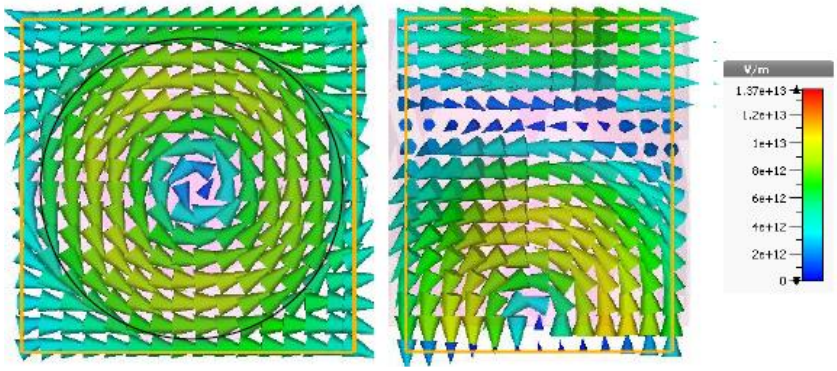

(a) (b)

Fig. 2.9 E-Field distribution on CDRA at 15.29 THz (a) Top view (XY-Plane), (b) Side view (XY-Plane).

It is found that there is a shift in the resonant frequency from model a to d of antenna configuration as depicted in Fig. 2.5(b) confirms the generation of three modes of CDRA with ant-IV configuration. Fig. 2.6 shows the radiation pattern plot for Ant-I, II, III, and IV configurations. It is observed from Fig. 2.6(a) that a gain of 3.6 and 6 dB is achieved at the main lobe direction of 59° and 0° at resonant frequencies of 12.05 and 16.66 THz. A gain of 2.9 and 0.55 dB is achieved at the main lobe direction of 55° and 1° at resonant frequencies of 11.65 and 16.33 THz as depicted in Fig. 2.6. It is observed from the Fig. 2.6(c) that a gain of 2.8 and 1.1 dB is achieved at main lobe direction of 58° and 1° at resonant frequencies of 11.62 and 16.3 THz. A gain of 4.73, 3.15, and 7.08 dB is achieved at the main lobe direction of 4°, 11°, and 0° at resonant frequencies of 8.12, 11.38, and 15.29 THz as depicted in Fig. 2.6(d). Maximum gain is achieved for the proposed slot (Ant-IV) compared to Ant-I, II, and III. Modes in CDRA can be identified based on the electric and magnetic field (E and H) distribution on CDRA. Fig. 2.7 shows E-field and H-field distribution at 8.12 THz. It can be observed that $HEM_{11\delta}$ mode is propagating inside CDRA at 8.12 THz [107]. From Fig. 2.8, the observation shows that the resonant mode is similar to $TM_{01\delta}$ is excited at 11.38 THz. Similarly, at the third resonant frequency at 15.29 THz, it is observed that $TE_{01\delta}$ mode is excited (Fig. 2.9).

2.4 Parametric analysis

To analyze the performance of the antenna, the physical parameters of the antenna are changed one at a time by keeping other parameters untouched. The height of the substrate h_2, the height of

CDRA (h1), and the radius of CDRA (a) are the key parameters of the proposed antenna. Fig. 2.10(a) depicts the frequency response of the proposed CDRA with a change in radius (a) of CDRA. It is noted that good performance and good impedance matching are obtained with a change in the radius of CDRA. However, the number of resonant frequencies remains unchanged. Fig. 2.10(b) depicts the frequency response with a change in the height of CDRA (h1). It is clear that when the height of CDRA increases, better impedance matching is observed. In Fig. 2.11, the frequency response of the antenna for change in the substrate (SiO_2) thickness (h2) is investigated. From the above analysis, it is clear that CDRA resonates at three resonant frequencies, and good impedance matching is observed even for the change of physical parameters. All these parameters are optimized and are depicted in Table 2.1.

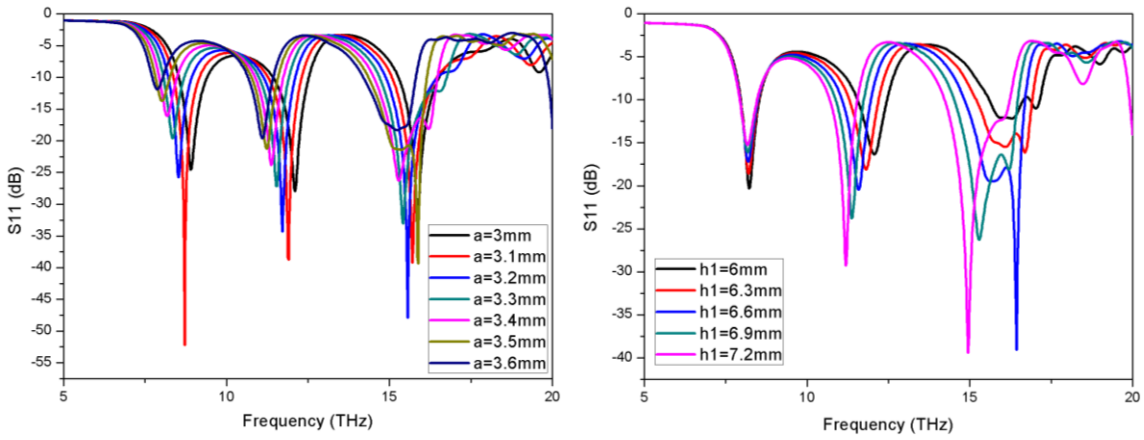

(a) (b)

Fig. 2.10 Plot of frequency response for the CDRA with change in a. radius of CDRA (a) and b. Height of CDRA (h1).

2.5 Combination of Rectangular Dielectric Resonator Slab (RS) and CDRA

To achieve circular polarization, a silicon-based Rectangular dielectric slab inclined with 45° in a clockwise direction is placed on top of CDRA as depicted in Fig. 2.12 with dimensions (μm) lr × wr × hr (22×5×6). As illustrated in the plot of frequency response (Fig. 2.13), it can be observed that this combination of CDRA and Rectangular slab known as Circularly Polarized Dielectric Resonator Antenna (CPDRA) provides resonance at four frequencies, i.e., 8.79, 11.10, 13.73, 16.21 THz with 10dB IBW of 4.66% (8.59-9THz), 2.98% (10.88-11.21THz), 4.83% (14.19-

13.52THz) and 5.86% (15.88-16.84). The resonant frequency shift between CDRA and CPDRA is due to the height of the silicon-based rectangular slab. The variation of EF and MF distribution at resonant frequencies on the top of the Rectangular slab is shown in Fig. 2.14.

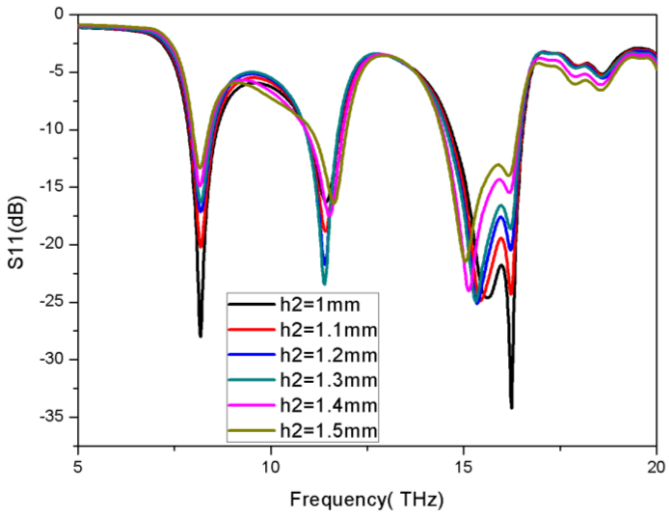

Fig. 2.11 Plot of frequency response for the CDRA with change in h2.

2.5.1 Mechanism of Circular Polarization

CP waves are generally excited by two orthogonal linearly polarized components with equal magnitude and 90^0 phases between them. To analyze the behavior of CP, consider Fig. 2.16, which shows EF vector behavior (at f=8.79, 11.1, 13.7, and 16.2 THz) at different time instants (t=0, T/4). It can be observed that two orthogonal EFs are generated with equal magnitude at the resonant frequencies. From t=0 to t=T/4 (Fig. 2.16(a) and Fig. 2.16(b)), at a frequency of 8.79 THz, electric field vectors (EFV) are rotated in a clockwise direction. This proves that Left Hand CP (LHCP) is generated. The arrangement of the rectangular slab with 45^0 orientation leads to circular polarization. The generation of the LHCP field can be observed at each time quarter with 90^0 rotations of EF vectors. This rotation occurs due to the generation of higher-order orthogonal degenerate modes. The field distribution is modified after placing a rectangular slab. From this, it is clear that adding a rectangular slab spun by 450 provides orthogonal degenerate modes that are expected and required for CP response. Similarly, at a frequency of 11.1 THz (Fig. 2.16(c) and Fig. 2.16(d)), it can be observed that EFV is rotated in an anti-clockwise direction, which means at this frequency, the proposed DRA generates Right Hand CP (RHCP) wave. Similarly, at frequencies of 13.7 and 16.2THz (Fig. 2.16(e), Fig. 2.16(f), Fig. 2.16(g), and Fig. 2.16(h)), it can be understood

from the observation that LHCP wave is generated at both the frequencies. From this, it is concluded that the proposed antenna generates a quad-band CP response at four resonant frequencies. This unique feature of the antenna makes it suitable for THz applications.

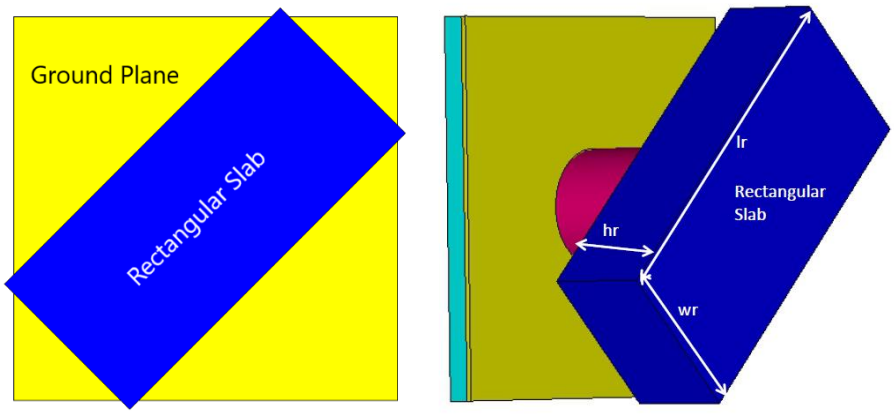

(a) (b)

Fig. 2.12 Rectangular Slab on top of CDRA (CPDRA) **(a)** Top view **(b)** Side view (with dimensions).

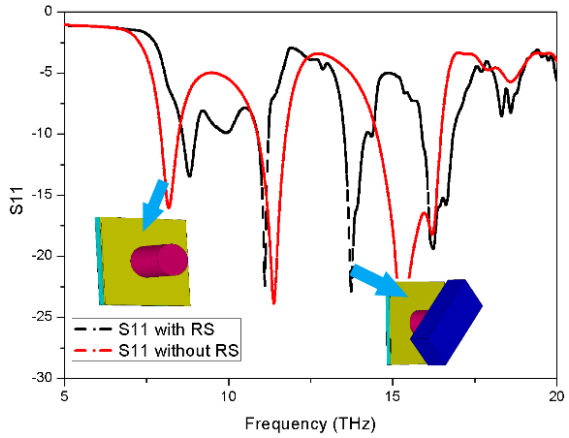

Fig. 2.13 Frequency response comparison between CDRA with rectangular slab (Black line) and without rectangular slab (Red line).

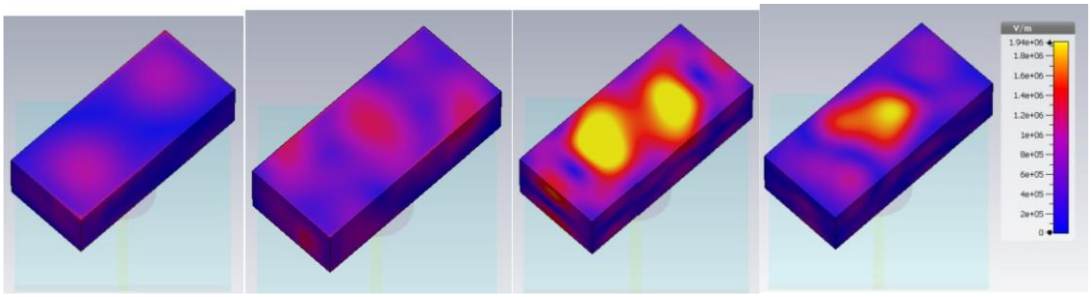

(a) (b) (c) (d)

Fig. 2.14 Electric field distribution on isolated rectangular slab ((XY-Plane) along with amplitude level bar at **a.** 8.79, **b.** 11.1 **c.** 13.7 **d.** 16.2 THz.

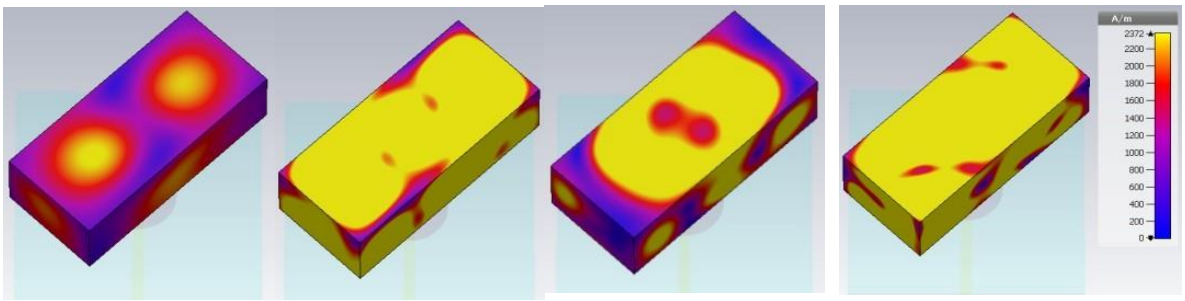

(a) (b) (c) (d)

Fig. 2.15 Magnetic field distribution on isolated rectangular slab (XY-Plane) along with amplitude level bar at (a) 8.79, (b) 11.1, (c) 13.7, and (d) 16.2 THz.

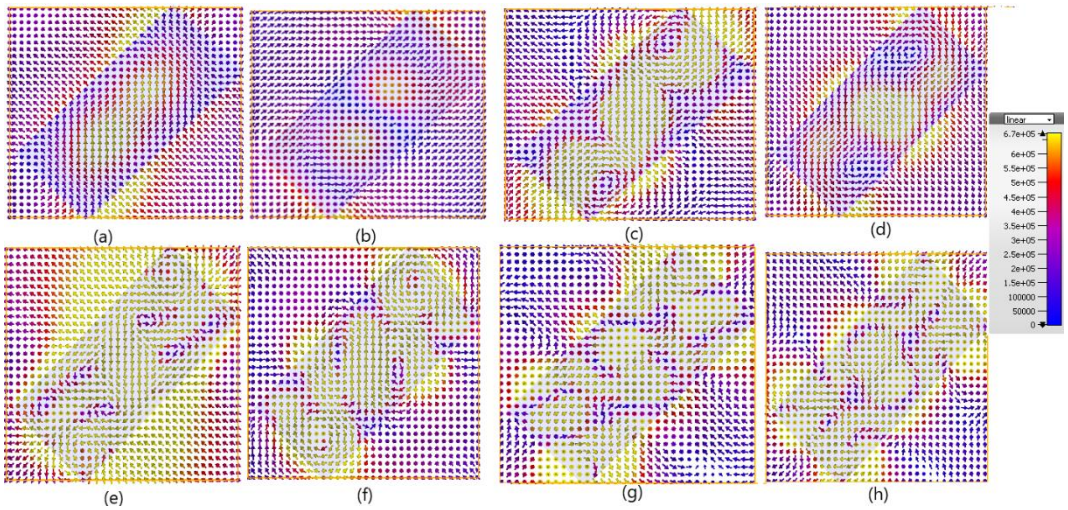

Fig. 2.16 Electric field vector distribution on rectangular slab (XY-Plane) at a frequency of 8.79 THz (a) t=0 and (b) t=T/4, at 11.1 THz (c) t=0 and (d) t=T/4, at 13.7 THz (e) t=0 and (f) t=T/4 and at 16.2 THz (g) t=0 and (h) t=T/4.

To elucidate the radiation characteristics effectively, the plot of axial ratio (AR) and Polarization (LHCP and RHCP) are shown in Fig. 2.17 and Fig. 2.18. It is observed that the proposed CPDRA produces CP characteristics as depicted in Fig. 17. A 3dB ARBW of 1.83% (8.66-8.82 THz), 6.64% (10.77-11.51), 3.84% (13.26-13.78 THz) and 4.8% (16.04-16.83 THz) is depicted in Fig. 17 which means the proposed antenna produces quad band CP response at four bands.

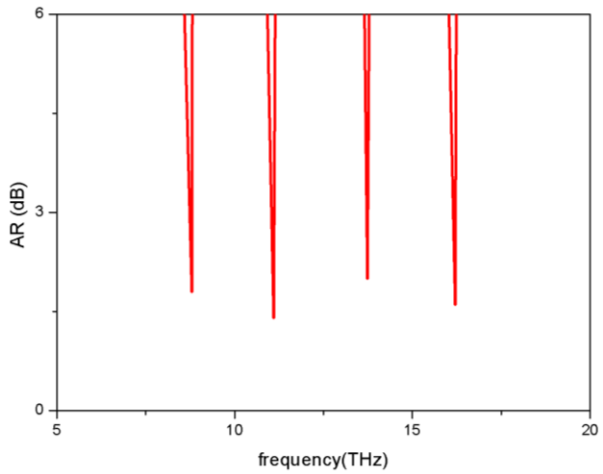

Fig. 2.17 Axial Ratio (AR) dB vs. frequency plot for Rectangular slab along with CDRA.

Fig. 2.18 shows the LHCP and RHCP far-field radiation pattern components for four resonant frequencies, i.e., at 8.79, 11.1, 13.73, and 16.2 THz. The antenna provides the dominant LHCP field at the resonant frequency of 8.79, 13.73, and 16.2 THz, whereas the RHCP wave dominates at 11.1 THz. Fig. 2.19 exhibits the plot between gain (dB) vs. frequency. This antenna provides a gain of 5dB, 4.5dB, 5.5dB, and 6.67dB at four resonant frequencies, i.e., 8.79, 11.10, 13.73, and 16.21 THz.

2.6 CPDRA response to graphene

The upper surface of CDRA is coated with graphene. The direct fabrication of graphene films on silicon/silica substrate is developed via a tri-constituent self-assembly route using the procedure given in [108]. Metal-free, ambient-pressure chemical vapor deposition was used to successfully manufacture graphene on single-crystal silicon substrates [109]. Controlling the growth

temperature allows for creation of atomically flat monolayer or bilayer graphene domains, concave bilayer graphene domains, and bulging few-layer graphene domains [109]. The main advantage of using graphene at the THz frequency region is its tunability characteristics by varying its chemical potential. According to the Kubo formula [110], the surface conductivity of graphene can be given by

$$\sigma(\omega, \mu_c, \Gamma, T) = \frac{je^2(w-j2\Gamma)}{\pi h^2}\left[\frac{1}{(\omega-j2\Gamma)^2}\int_0^\infty \in \left(\frac{\partial(f_d(\epsilon)}{\partial\epsilon} - \frac{\partial(f_d(-\epsilon)}{\partial\epsilon}\right)d\varepsilon - \int_0^\infty \left(\frac{f_d(-\epsilon)-f_d(\epsilon)}{(\omega-j2\Gamma)^2-4(\epsilon/h)^2}\right)d\varepsilon\right] \quad (2.2)$$

Equation 2.2 is the sum of intra-band (1st term) and inter-band (2nd term) conductivity contributions. Where e is the electron charge, h is Planck's constant, $f_d(\epsilon) = (e^{(\varepsilon-\mu_c)/k_BT} + 1)^{-1}$ is the Fermi-Dirac distribution, K_B is Boltzmann's constant. Γ is the chemical potential, ω is the radian frequency, and T=300 K. A relationship between voltage and μ_c is depicted in equation 2.2, depending on the external DC bias voltage applied. According to [75], the relation between DC bias, μ_c depends on the applied voltage V by using equation 2.3.

$$V = V_0 + \frac{te\mu_c^2}{\varepsilon_0\varepsilon_r\pi h^2 v_F^2} \quad (2.3)$$

Where $v_f = 9.5 \times 10^5$ m/s is the fermi level velocity, V_o is the voltage compensation dependent on the chemical doping, t and ε_r are the height and relative permittivity of the dielectric between graphene and electrode, respectively.

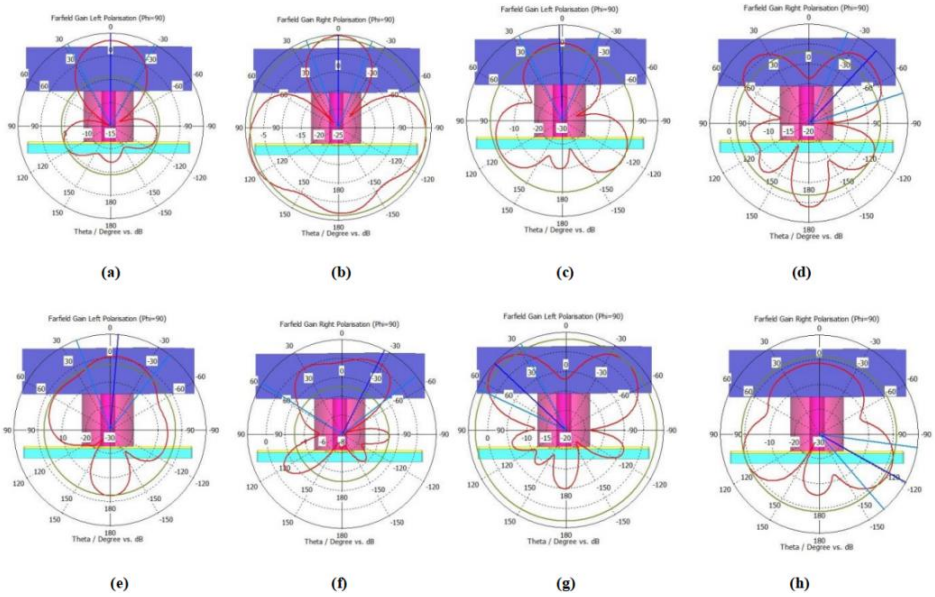

Fig. 2.18 Far-field 2D radiation pattern for θ=0° and φ=90° at 8.79 (a) LHCP, (b) RHCP, at 11.1 (c) LHCP (d) RHCP, at 13.7, (e) LHCP (f) RHCP at 16.2 THz (g) LHCP, (h) RHCP.

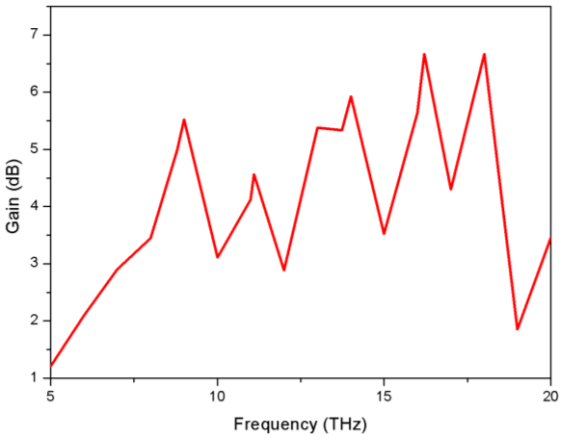

Fig. 2.19 Gain (dB) vs. frequency plot.

The conductivity of graphene can be varied by providing an electric field via DC bias. As stated in [75], the electric field changes the charge density. Equation 2.4 gives the relationship between electrostatic bias and chemical potential. Fig. 2.20 depicts the relationship between the biasing voltage with chemical potential and the relative permittivity of graphene. A metallic gate layer is placed at the top of the graphene patch to apply the DC gate voltage in the antenna configuration. When the external voltage is applied, the length and width of the metallic gate layer are kept identical to the graphene patch so that the fermi level is maintained uniformly [73].

$$\frac{2\epsilon_s E_0}{e} = \frac{2}{\pi h^2 v_f^2}\int_0^\infty E(f_d(E) - f_d(E + 2\mu_c))dE \qquad (2.4)$$

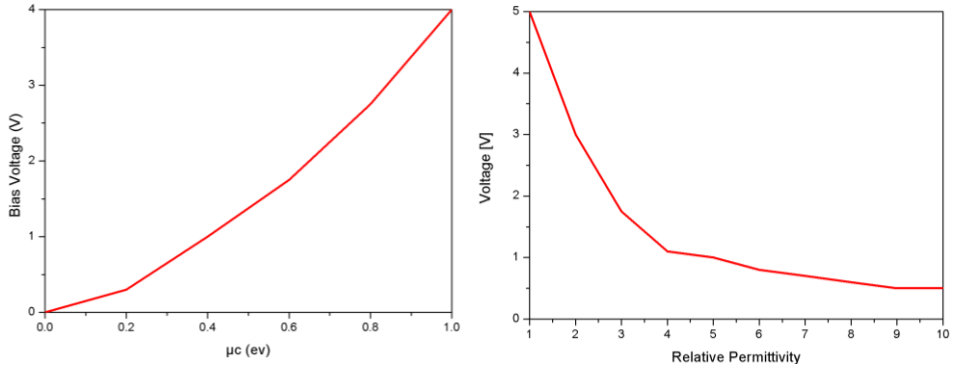

(a) (b)

Fig. 2.20 (a) μ_c vs bias voltage (b) Relative Permittivity vs voltage.

Fig. 2.21 shows the structure of CDRA with and without graphene. The radiation efficiency of the CDRA with and without graphene material is depicted in Fig. 2.22 for different values of chemical potential (μ_c) of graphene. The graphene material having thickness of 0.34 nm and T=300K is chosen. It is observed that the antenna without graphene provides a maximum gain of 85% efficiency, whereas 70% gain is shown by the antenna coated with graphene. The main disadvantage of using graphene is the antenna's radiation efficiency reduction. It is observed that there is a linear decrease in the antenna's efficiency with an increase in μ_c. Fig. 2.23 shows the frequency response (S_{11}) with and without graphene. Results shows there is forward shift in the resonant frequency of the antenna for change in μ_c from 0.2eV to 0.8eV. The tunability property of graphene material can be used to tune the antenna response after it has been manufactured. The external electrostatic DC voltage can change the chemical potential and the graphene material's conductivity. As previously stated, changes in μ_c graphene's conductivity and hence the antenna's operating frequency. The structure of the rectangular slab with CDRA layered with graphene is depicted in Fig. 2.24.

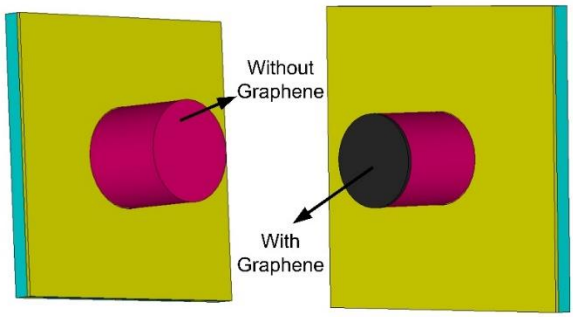

(a) (b)

Fig. 2.21 CDRA (a) without, and (b) with Graphene material.

Observations are made in terms of S_{11}, RE, AR, and gain of the antenna. Fig. 2.25 shows the frequency response (S_{11} in dB). Consequently, antenna coated with graphene has tunability characteristics. There is a forward shift in the resonant frequency of the antenna for varying graphene potential (μ_c). For graphene with μ_c=0.2eV, it resonates at f = 8.854, 11.337, 14.004, and 16.412 THz. For graphene with μ_c= 0.4eV is resonates at f = 8.91, 11.46 THz.

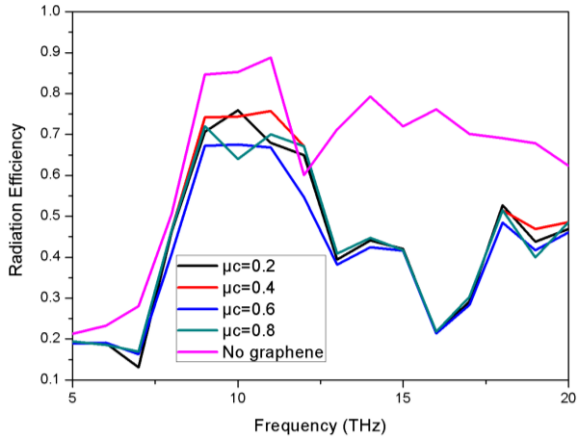

Fig. 2.22 CDRA Radiation efficiency for different values of Graphene chemical potential.

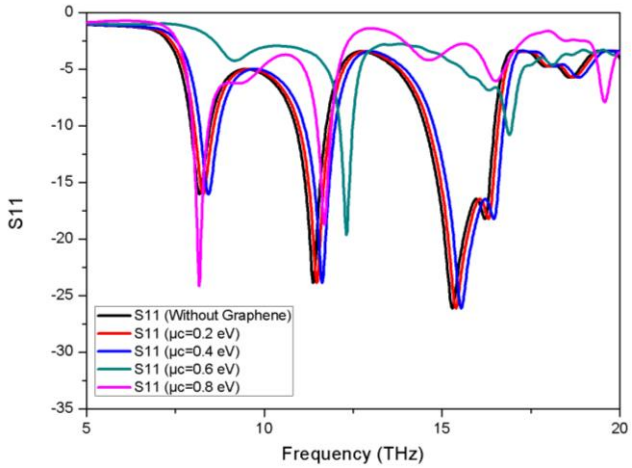

Fig. 2.23 CDRA frequency response (S_{11}) for different values of Graphene chemical potential.

For graphene with μ_c= 0.6eV, it resonates at f = 9.50, 11.92 and 16.89. Graphene with μc=0.8eV resonates at f = 9.89, 12.97, and 16.98. The findings of RE for different graphene chemical potential values are examined. Fig. 2.26 shows RE for different values of Graphene chemical potential (μ_c= 0.2, 0.4, 0.6, 0.8 eV) for the proposed antenna. Typically, RE with a graphene-coated antenna provides less efficiency than without graphene. 89% RE is achieved for antenna without graphene, whereas a maximum of 78% RE is achieved with graphene. Moreover, graphene with 0.8ev provides less RE compared to other potential values.

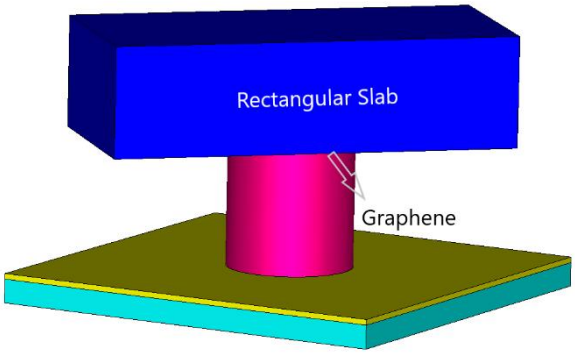

Fig. 2.24 Structure of proposed CPDRA with graphene.

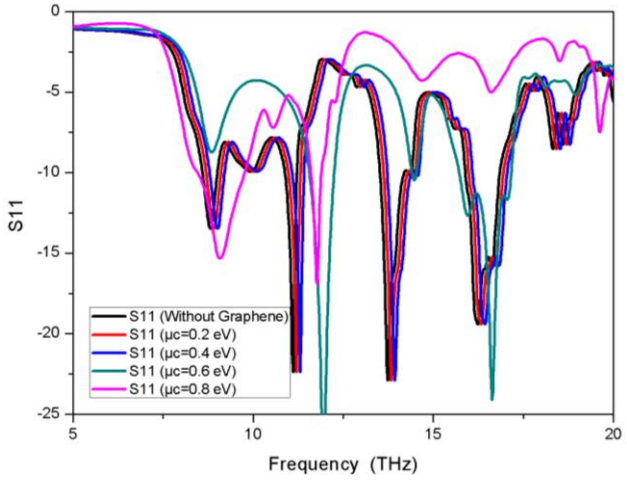

Fig. 2.25 CPDRA frequency response (S_{11}) with graphene and without graphene material.

The axial ratio for different values of graphene potential for the antenna is compared with the antenna without graphene material. Results show that AR is less than 3dB in the pass-band, as shown in Fig. 2.27. Hence it is clear that the antenna with different values of μc achieves quad band CP tuning, a unique feature at the THz frequency region.

It is essential to describe the fabrication process of the proposed CPDRA. The fabrication of structures with very small dimensions in micrometers requires advanced nanofabrication techniques. These techniques involve precise control over material deposition, patterning, and etching processes at the nanoscale level.

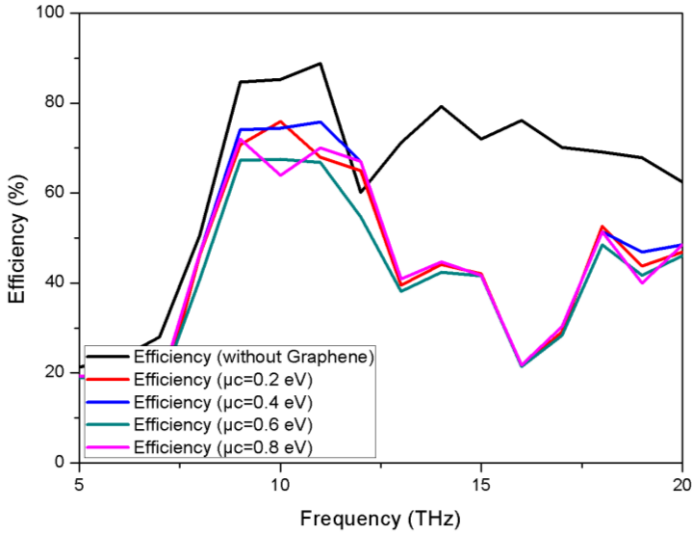

Fig. 2.26 RE for different values of Graphene chemical potential for CDRA incorporated with rectangular slab.

Firstly, high-quality graphene is grown on a suitable substrate using techniques like chemical vapor deposition or epitaxial growth. The substrate is then prepared by thoroughly cleaning it to ensure optimal graphene quality. The graphene is either transferred or directly grown on the target substrate. Patterning techniques such as photolithography or electron beam lithography are used to define the antenna's shape and dimensions. A thin layer of metal, typically gold or copper, is then deposited on the patterned graphene to provide the necessary conductivity. Excess materials are etched away, and thorough cleaning is performed to eliminate any contaminants. Finally, the fabricated graphene-based CPDRA undergoes characterization and testing using THz measurement techniques to assess its performance, including resonant frequency, radiation pattern, axial ratio, and impedance bandwidth. Through this meticulous process, the graphene-based CPDRA is realized with its desired circular polarization properties, making it suitable for THz applications. The realization of the proposed DRA requires a combination of graphene synthesis, substrate preparation, transfer or growth, patterning, metal deposition, etching, cleaning, and thorough characterization. These fabrication steps ensure the successful realization of the CPDRA structure with the desired circular polarization characteristics at THz frequencies.

Table 2.2 shows the comparison of the proposed antenna with other antennas. This proposed antenna provides CP behavior at the quad-band in the field of THz dielectric resonator antennas. CP tuning is achieved by varying the graphene potential of the antenna. Fig. 2.28 shows the plot

between the antenna gain (dBi) and frequency (THz). CDRA with graphene provides a maximum gain of 5.8 dBi. A maximum gain of 6.5dBi is achieved for the antenna without graphene. Finally, a Rectangular slab on top of CDRA with and without graphene is designed, and performance analysis is carried out. It can be concluded that the addition of graphene adds tunability to the proposed antenna and will not affect the Quad Band CP behavior of the antenna. Additionally, an antenna with graphene provides good gain and efficiency in the targeted pass bands. According to the desired frequency of operation, the antenna can be manufactured with the optimal values of its physical parameters.

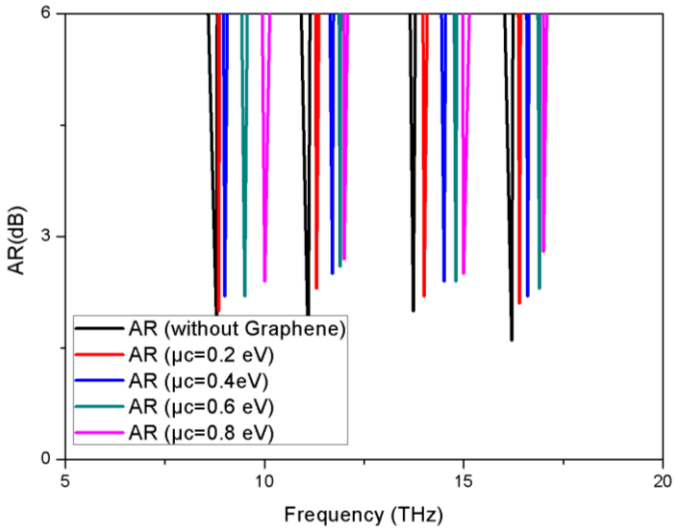

Fig. 2.27 AR (dB) for different values of Graphene chemical potential.

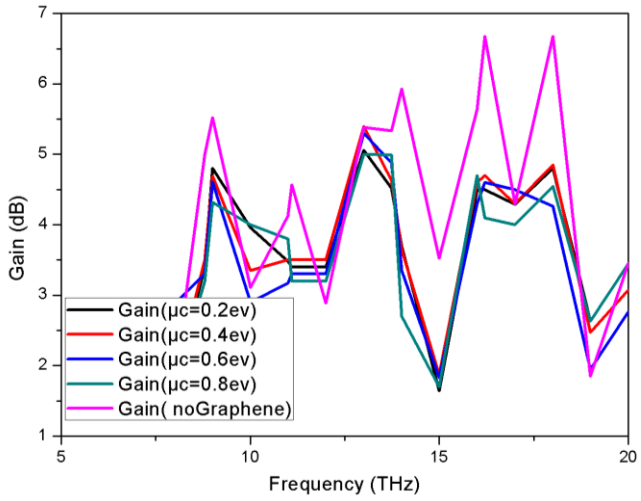

Fig. 2.28 Frequency vs. Gain for different graphene potential values.

Table 2.2 Comparison with other research articles.

Ref	Antenna	ARBW(THz)	IBW(THz)	Gain (dBi)	RE (%)	Tunability
[97]	Graphene-based microstrip antenna.	-		1.6		No
[98]	Slotted graphene patch antenna.	-	1.96 THz (Center Frequency).	4.3	95.3	No
[99]	Y-shaped graphene-based antenna.	-	0.45THz (Center Frequency).	4	25%	No
[100]	Patch Fed Higher Order Mode DRA.		7%.	7.9	-	No
[87]	CPDRA.	3.97 - 4.16.	3.95-4.1.	>6	>80%	Yes
[101]	Graphene disk loaded DR.	-	4.0629 − 4.1299.	3.8	72-75%	Yes
This antenna	Quad-band Rectangular slab incorporated CDRA based CP tunable THz antenna.	1.83% (8.66-8.82 THz), 6.64% (10.77-11.51), 3.84% (13.26-13.78 THz) and 4.8% (16.04-16.83 THz).	4.66% (8.59-9THz), 2.98% (10.88-11.21THz), 4.83% (14.19-13.52THz) and 5.86% (15.88-16.84).	>6	>85%	Yes

2.6 Conclusion

A CDRA, along with a rectangular DR slab known as CPDRA with graphene coating, is implemented for terahertz (THz) applications. This antenna provides a multi-mode response at different resonant frequencies. An IBW of 6.7% (7.93-8.48 THz), 7.6% (11.74-10.87 THz), and 12.65% (14.51-16.47 THz) is attained for CDRA. A unique feature of the proposed antenna is that it provides CP behavior at the quad-band in the field of THz dielectric resonator antennas. CP tuning is achieved by varying the graphene potential of the antenna. This antenna radiates two hybrid modes, i.e., $HEM_{11\delta}$ and $HEM_{12\delta}$. This proposed antenna shows both RHCP and LHCP behavior at different resonant frequencies. Furthermore, the designed antenna has a high gain and high radiation efficiency (RE) in the THz frequencies. Results show that a maximum gain of 6.67dB, RE of 89%, Impedance Band Width of 4.66% (8.59-9 THz), 2.98% (10.88-11.21 THz), 4.83% (14.19-13.52 THz) and 5.86%(15.88-16.84), Axial Ratio Bandwidth of 1.83% (8.66-8.82 THz), 6.64% (10.77-11.51), 3.84% (13.26-13.78 THz) and 4.8% (16.04-16.83 THz) is achieved by

the combination of CDRA and Rectangular slab. Graphene material is added to the top of CDRA to achieve tunability in CP response. These results show that the proposed Quad band CP DRA is unique and suitable for THz applications. This chapter fulfils the first objective of the thesis. In the second objective MIMO DRA is designed for THz and UAV applications to provide high data rate, high gain, and tunable response.

Chapter 3

Design of MIMO CPDRA for terahertz and UAV applications

In this chapter, MIMO circularly polarized (CP) MIMO Cylindrical Dielectric Resonator Antenna (CDRA) is designed for terahertz (THz) and UAV applications. The design analysis of three antennas is discussed to fulfill objective two: (i) A two Port MIMO CPDRA for THz applications, (ii) 2x2 MIMO CPDRA for THz applications, and (iii) A tri-sense CP wideband MIMO DRA for UAV applications.

3.1 Two port MIMO CPDRA for THz applications

For the next-generation communication system, Terahertz (THz) frequency spectrum is becoming the choice of many wireless applications because of its wider bandwidth and high data rates [10], [111]. Metallic radiators are not considered at this frequency because of their high losses [112]. DRA is the best choice because of its low losses, high gain, and high radiation efficiency at this frequency. Moreover, to have increased system capacity and high data rates without increasing the power level, Multiple Input Multiple Output (MIMO) antenna systems are generally preferred. These antennas utilize multiple antennas at the input and output sides to achieve improved channel capacity, high data rates, and excellent network coverage [113], [114]. Additionally, CP-based MIMO antennas are mainly used for their advantages compared to linear polarization (LP). These antennas are reported in [115], [116]. Several MIMO antenna systems are developed for THz frequencies for various applications [74]–[76]. In [77], a reconfigurable graphene-based THz MIMO antenna is developed, and a high spectral efficiency is reported. Although most of the

research is done on the design of MIMO patch antennas at the THz region, less research is done on MIMO DRA at this frequency (THz) which provides fewer losses and is more efficient compared to patch antennas at high frequency. The unique feature of this antenna is that it provides resonance at the quad-band and quad-sense CP response at the terahertz frequency region. Also, the varying graphene potential increases isolation between the two antennas.

3.2 Antenna geometry and design

The geometry and the dimensions of the proposed CP MIMO DRA are depicted in Fig. 3.1 and Table 3.1(all the dimensions are in μm). Two Cylindrical DRA's of height tc, made up of silicon material having $\varepsilon_r = 11.2$, are mounted on the Silicon dioxide (SiO_2) dielectric substrate ($\varepsilon_r = 3.9$, loss tangent (δ) = 0.001) having a thickness of ts. Two Rectangular 50Ω nanostrip feed lines having a length of l and width of wp are etched below the bottom of the substrate, as shown in Fig. 3.2.

3.2.1 Formation of the proposed configuration

The development of the proposed two-element MIMO DRA designed at THz frequency for circular polarization is investigated. For good isolation and for achieving CP, different antenna configurations are investigated, which are shown in Fig. 3.3.

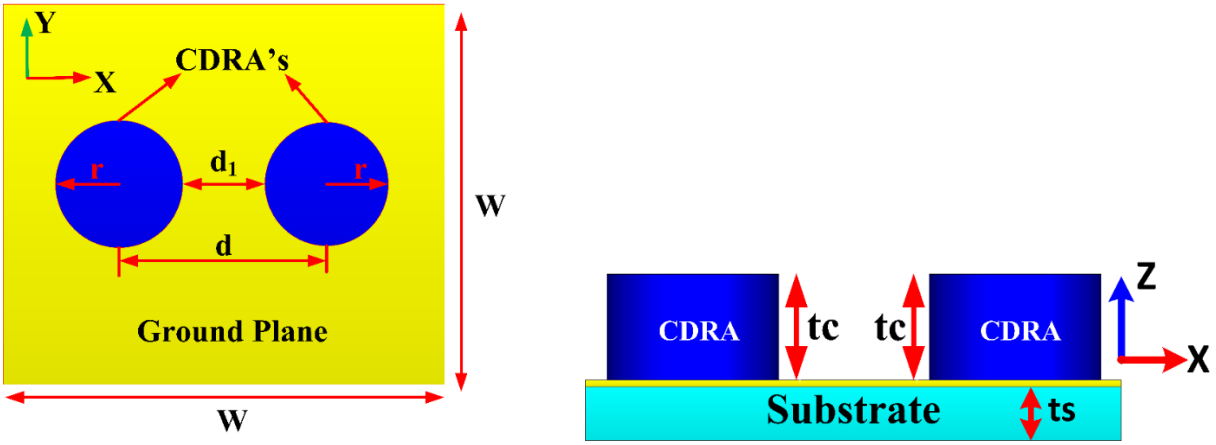

(a) (b)

Fig. 3.1 Geometry of MIMO DRA (a) Top View (XY Plane), (b) Side View (XZ Plane).

Fig. 3.3(a) shows two elements of MIMO DRA with circular aperture slot (ant-I), Fig. 3.3(b) shows circular aperture slot with left arm (ant-II), Fig. 3.3(c) shows circular aperture with right arm (ant-III), and Fig. 3.3(d) shows circular aperture with both arms (Proposed Design (ant-IV)) having an

inner and outer radius of rsloti = 2 µm and rsloto = 4 µm, respectively. The resonant frequency of CDRA for $HEM_{11\delta}$ is calculated using equation 3.1.

Table 3.1 Dimensions of proposed MIMO DRA (All the dimensions are in µm)

w	ts	d	d1	tc	r	l	wp	rsloto	rsloti
60	3.36	30	22	10	8	35	1	4	2

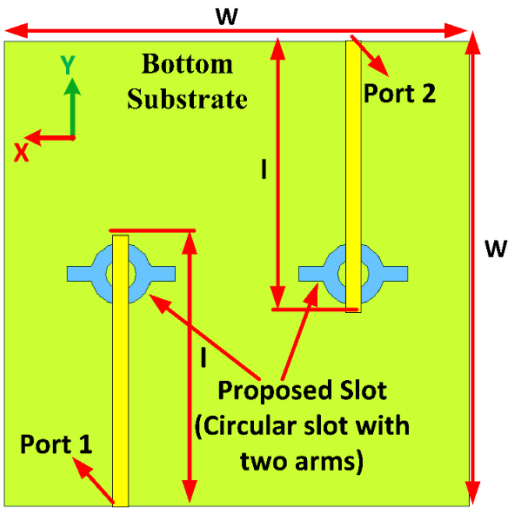

Fig. 3.2 Bottom view of MIMO DRA

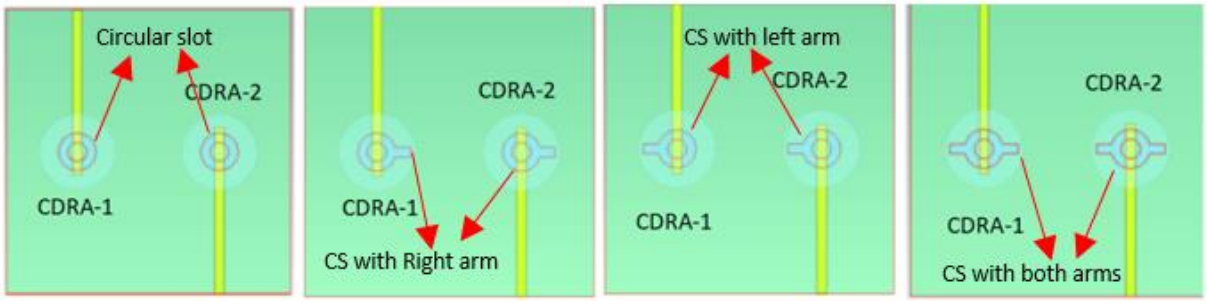

(a) (b) (c) (d)

Fig. 3.3 Antenna Configuration **a.** Circular slot (CS), **b.** CS with right arm **c.** CS with left arm, **d.** CS with both arms (Proposed)

$$f_r = \frac{6.321c}{2\pi r\sqrt{\varepsilon_{r,eff}}}\left[0.27+0.36\left(\frac{r}{2H_{eff}}\right)+0.02\left(\frac{r}{2H_{eff}}\right)^2\right] \qquad (3.1)$$

Where r is the radius of CDRA, c is the velocity of light

H_{eff} and $\varepsilon_{r,eff}$ are effective height and effective dielectric constant of MIMO DRA and are given by equations 3.2 and 3.3.

$$\varepsilon_{r,eff} = \frac{H_{eff}}{\frac{H}{\varepsilon_{silicon}} + \frac{H_s}{\varepsilon_{sub}}} \tag{3.2}$$

$$H_{eff} = H + H_s \tag{3.3}$$

Where H and Hs are the heights of CDRA and substrate, respectively.

3.3 Results and Analysis of Proposed MIMO DRA

The simulation and analysis of the proposed DRA are carried out in CST Microwave Studio. This section mainly focuses on frequency response for antenna configurations, isolation between two ports, electric field distribution, and CP mechanism. Fig. 3.4 shows the frequency response S_{11} with various modification steps for the proposed MIMO DRA configuration (Fig. 3.3(a-d)). CDRA with two arms resonates at four frequency bands, i.e., at 3.40, 5.42, 8.08 THz, and 8.85 THz, with a 10 dB impedance Bandwidth of 5.86 % (3.31-3.51 THz), 4.96% (5.3-5.57 THz), 2.64% (8.01-8.22 THz) and 5.23% (8.55-9.01THz). CDRA with a single arm resonates at only three bands, and CDRA with a circular slot resonates at two bands. Moreover, the isolation between the two ports of antenna configurations (ant-II and ant III) is approximately -14dB, as shown in Fig. 3.5. An improved isolation (-17dB) is achieved with the antenna configuration of ant-IV and is depicted in Fig. 3.5. Isolation of -25dB is achieved with the circular slot. Moreover, for the proposed MIMO DRA, the $HEM_{11\delta}$ mode is excited at the resonant frequencies.

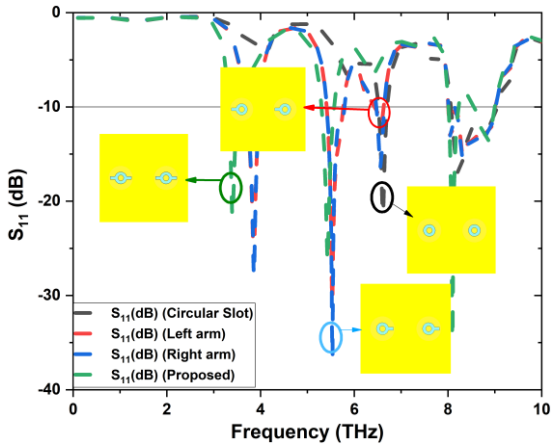

Fig. 3.4 Frequency response (S_{11}) for different antenna configurations (of Fig. 3.3).

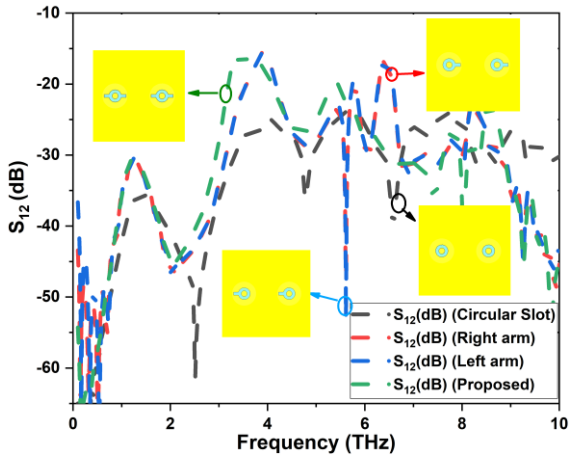

Fig. 3.5 Frequency response (S_{12}) for different antenna configurations (of Fig. 3.3)

3.3.1 Analysis of modes in CDRA

Initially, to find the operating resonant frequency, eigen mode analysis is employed. Fig. 3.6 and Fig. 3.7 shows the EF distribution on CDRA 1 and CDRA 2 in XY and XZ plane for the proposed antenna configuration (Fig. 3.3(d)). Using EF distribution, we can identify which mode is propagating in CDRA by comparing it with the theoretical behavior of CDRA. The modified aperture slot is used to excite the antenna to radiate in multiple resonant frequencies as depicted in the plot of S_{11} (Fig. 3.4). Fig. 3.6(a and b) shows the EF distribution on top and side of CDRA 1 at 3.4 THz. It can be seen that the EF distribution is similar to the $HEM_{11\delta}$. Similarly, from Fig. 3.6 (c and d), the propagation mode is $HEM_{11\delta}$ at 5.42 THz. Hence from the results of (Fig. 3.6 (a, b, c, and d)), CDRA could work in $HEM_{11\delta}$ at 3.4 and 5.42 THz frequencies. The mode $HEM_{11\delta}$

radiates as a horizontal magnetic dipole showing the maximum direction towards boresight. At 8.08 and 8.86, the EF distribution is similar to that of $HEM_{12\delta}$ as depicted in Fig. 3.6(e, f, g, and h), and behaves like an electric dipole. Similarly, the EF distribution at port 2 is depicted in Fig. 3.7. Which shows a similar response to that exhibited at port 1. Hence we can conclude that the proposed antenna radiates in two higher-order modes ($HEM_{11\delta}$ and $HEM_{12\delta}$) at ports 1 and 2. The EF distribution verifies these modes according to image theory shown in Fig. 3.6(i) [12].

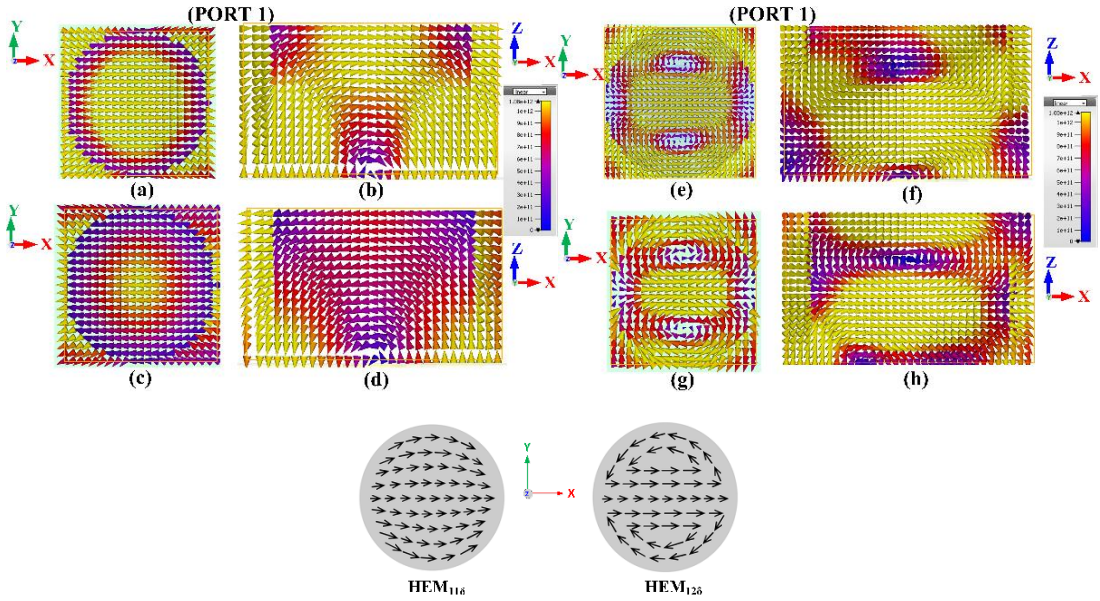

(i)

Fig. 3.6 EF distribution at port 1 of the DRA 1 at (a) 3.4 THz (XY Plane), (b) 3.4 THz (YZ Plane), (c) 5.42 THz (XY Plane), (d) 5.42 (XZ Plane), (e) 8.08 THz (XY Plane), (f) 8.08 THz (XZ Plane), (g) 8.86 THz (XY Plane), (h) 8.86 (XZ Plane), and (i) $HEM_{11\delta}$ and $HEM_{12\delta}$(Image theory).

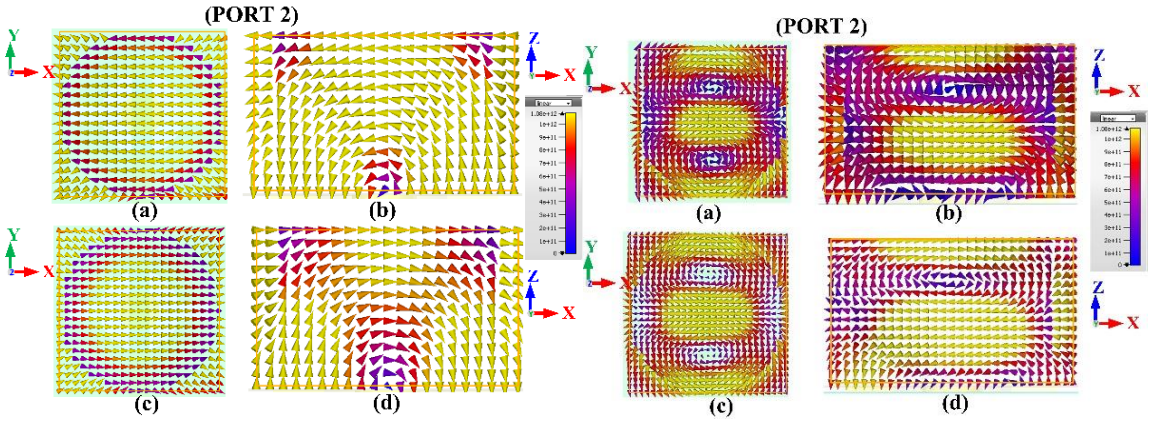

Fig. 3.7 EF distribution at port 2 of the DRA 2 at (a) 3.4 THz (XY Plane), (b) 3.4 THz (YZ Plane), (c) 5.42 THz (XY Plane), (d) 5.42 (XZ Plane), (e) 8.08 THz (XY Plane), (f) 8.08 THz (XZ Plane), (g) 8.86 THz (XY Plane), (h) 8.86 (XZ Plane).

3.3.2 Axial Ratio plot

Fig. 3.8 depicts a plot of axial ratio (AR) vs. frequency (THz) for the proposed configuration (Fig. 3.3(d)). It is confirmed that the modified circular slot (ant-IV) generates circular polarization at four frequency bands with 3dB ARBW of 8.22 % (3.38-3.67 THz), 2.48% (5.97-6.12 THz), 3.67% (6.95-7.21 THz) and 5.67% (7.88-8.34 THz). The axial ratio at the second (6 THz) and third (7 THz) bands are not part of pass bands but provide CP behavior at these bands. The nearby pass band for the 6 THz AR band is at 5.42 THz, provided by the right-side arm. The 7THz AR band is due to the left side arm, which has a resonance of 6.56 THz.

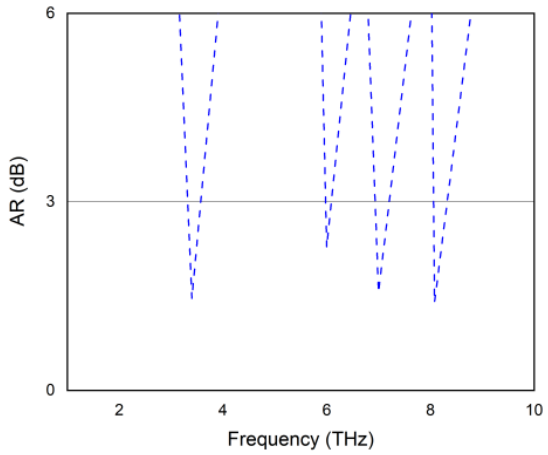

Fig. 3.8 Axial Ratio (dB) for proposed antenna configuration

3.3.3 Mechanism of CP generation using Electric Filed Vector (EFV) distribution

Fig. 3.9 shows EFV distribution on CDRA at a resonant frequency of 3.4 THz at different time instants (t= 0, t= T/4, t= T/2, and t= 3T/4) for the proposed configuration (Fig. 3.3(d)). Fig. 3.9(a) shows EF distribution with excitation at port 1 by keeping port 2 inactive, and Fig. 3.9(b) shows EF distribution with excitation at port 2 by keeping port 1 inactive. Similar observations are made at 8.08 THz (Fig. 3.10 (a and b). For the generation of CP waves, the EF components must be orthogonal to each other, and the magnitudes of EFV must be the same [12].

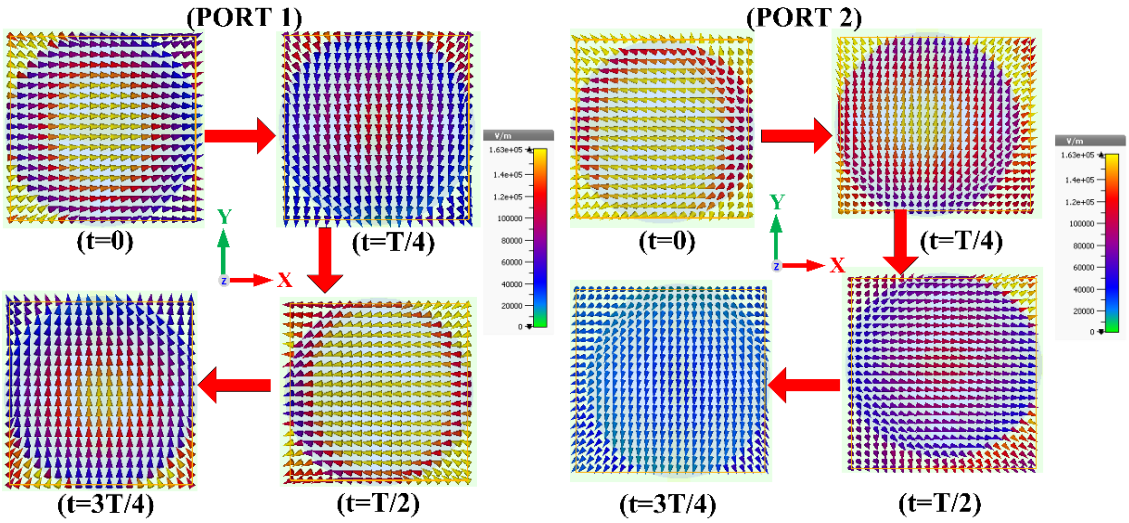

Fig. 3.9 Electric field vector (EFV) distribution on CDRA at 3.4 THz for time instants **t= 0, t= T/4, t= T/2, and t= 3T/4** at (a) Port1 and (b) Port 2.

Three observations are made from the EFV distribution of Fig. 3.9, Fig. 3.10: (i) Rotation of EF vectors is circular (t=0 to t= 3T/4). This means CP waves are generated. (ii) EF vectors are rotated in a clockwise direction with 90^0 phase shifts from t=0 to t=3T/4 (Fig. 3.9(a and b)) at 3.4 THz. This confirms left-hand circular polarization (LHCP) presence at 3.4 THz (iii) Similarly, EF vectors are rotated in a clockwise direction with 90^0 phase shifts from t=0 to t=3T/4 (Fig. 3.10(a and b)) at 8.08 THz. This confirms LHCP presence at 8.08 THz also. Hence it is clear from the above discussion that the proposed MIMO DRA exhibits LHCP wave at two bands. It is worth noting that when both the ports (Port 1 and Port 2) are excited simultaneously, the EF distribution on both the DRs will remain the same (Fig. 3.9 and Fig. 3.10) at both resonant frequencies. Fig.

3.11 shows simulated RHCP and LHCP radiation plots towards the boresight direction at 3.4 and 8.08 THz for the proposed MIMO DRA (Fig. 3.3(d)) at both ports. It is observed from figure 11 that with excitation at port 1 and port 2 at frequencies of 3.4 THz and 8.08 THz, the LHCP wave is dominated. The separation between LHCP and RHCP components (Fig. 3.11) remains 20 dB or more in the boresight direction ($\theta = 0^{o}$) in the XZ plane. The plot of gain and radiation efficiency is depicted in Fig. 3.12(a and b) for the proposed configuration (Fig. 3.3(d)). A maximum Gain of 7.86 dBi is achieved at resonant frequencies of 5.42 and 8.08 THz. Maximum efficiency of 88.8% is achieved at 5.42 THz.

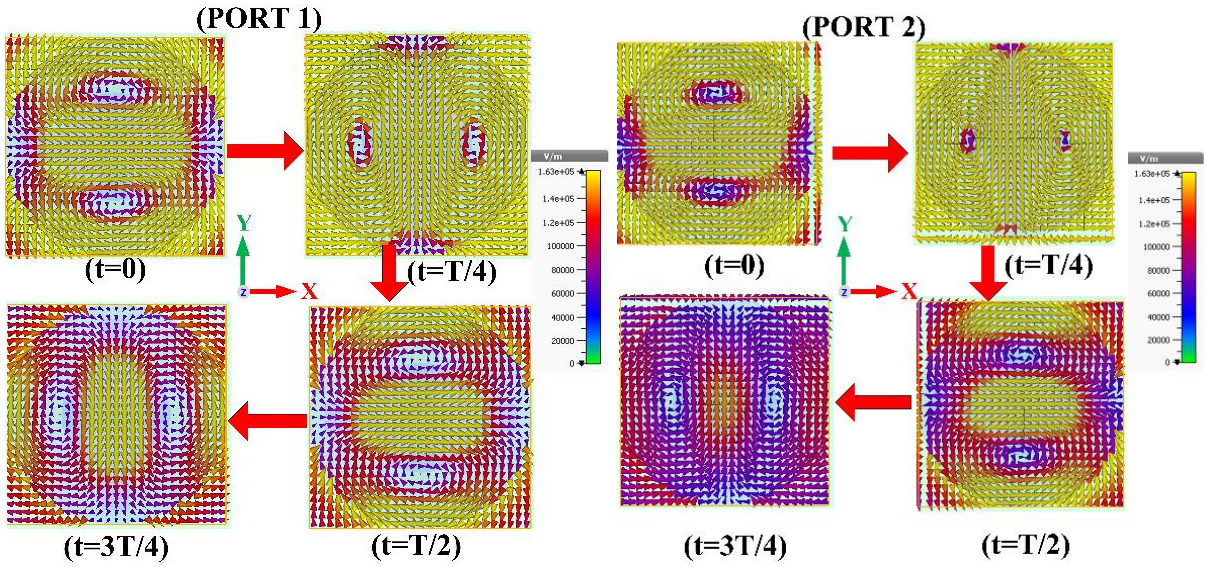

(a) (b)

Fig. 3.10 Electric field vector (EFV) distribution on CDRA at 8.08 THz for time instants t= **0, t= T/4, t= T/2, and t= 3T/4** at (a) Port1 and (b) Port 2.

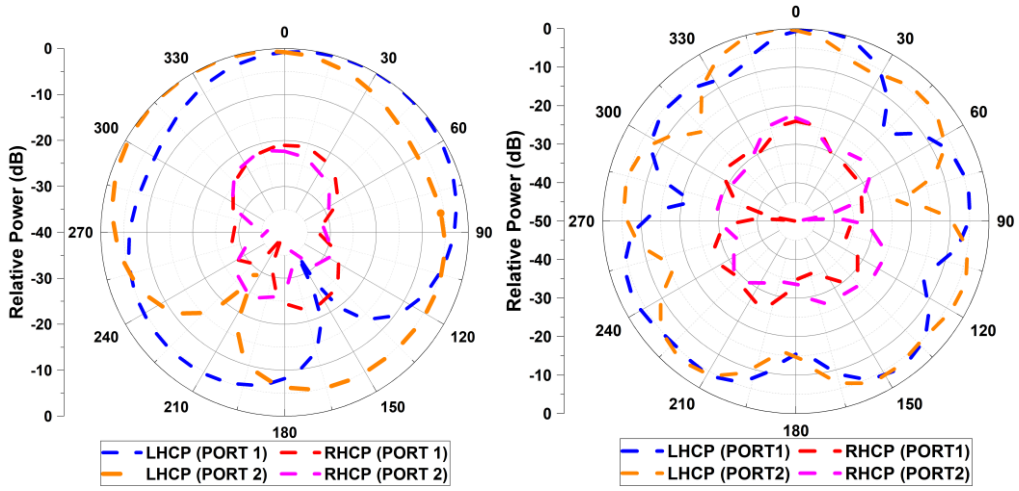

(a) (b)

Fig. 3.11 Simulated RHCP and LHCP radiation plots at ports 1 and 2 in the XZ plane for frequencies (a) 3.4 and (b) 8.08 THz.

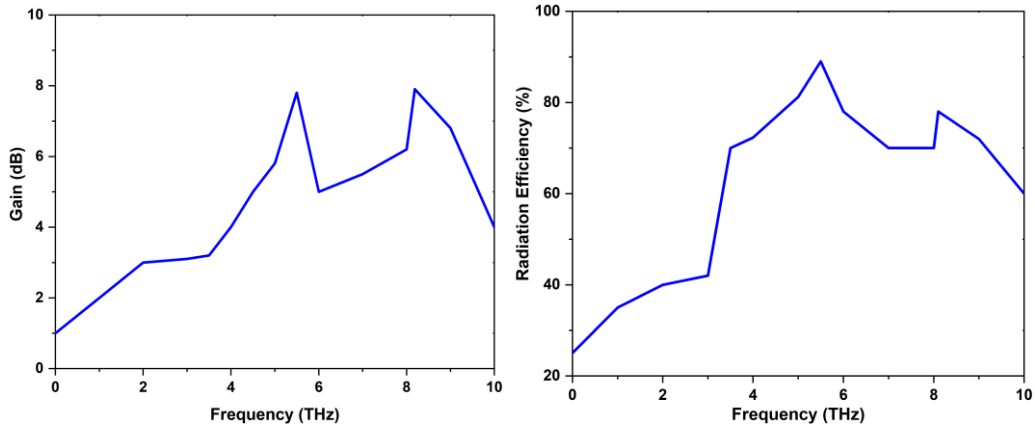

(a) (b)

Fig. 3.12 Proposed MIMO DRA plot of (a) Gain (dBi) and (b) Radiation Efficiency (RE).

3.4 Performance parameters calculation of Proposed MIMO DRA

The performance of the MIMO antenna for the proposed MIMO DRA (Fig. 3.3(d)) is verified by the calculation of different parameters ECC, DG, MEG, CCL, and TARC. The plot of ECC and DG are shown in Fig. 3.13. For better performance of the MIMO antenna, ECC must be less than 0.5, and DG must be greater than 9.5dB [7]. ECC of the antenna is calculated by equation 3.4 and is depicted in Fig. 3.13(a).

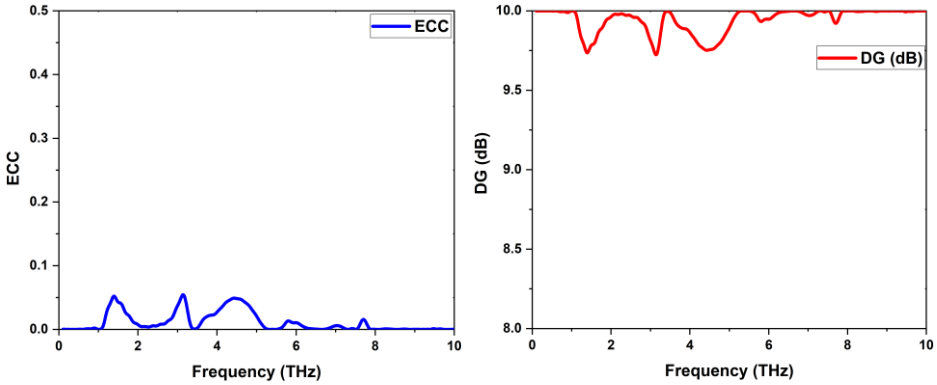

(a) (b)

Fig. 3.13 Proposed MIMO DRA plot of a. ECC, b. DG.

$$\rho_e = \frac{|S_{11}^* S_{12} + S_{21}^* S_{22}|^2}{(1-(|S_{11}|^2+|S_{21}|^2))(1-(|S_{22}|^2+|S_{21}|^2))} \quad (3.4)$$

Where S_{ii} and S_{ij} (S_{11}, S_{12}, or S_{21}) are the reflection coefficient at the input and isolation between the antenna elements respectively.

Table 3.2 DG (dB) and ECC

Frequency (THz)	DG(dB)	ECC
2.6	9.95	0.008104245
3.40	9.996	0.000709482
4.614	9.763	0.046824694
5.406	9.999	0.000101996
6.29	10	0.001725205
7.35	10	0.000435309
8.08	10	0.000000681

The DG of the antenna gives the improvement in using a multi-port antenna compared to a single-port antenna [114]. It is calculated using equation 3.5 for different frequencies. It is clear from Fig. 3.13(b) that DG is more significant than 9.5 dB, which means the designed MIMO antenna is the best choice for THz applications.

$$DG = 10\sqrt{\left(1-|0.99\rho_e|^2\right)} \quad (3.5)$$

Table 3.2 gives the simulated values of DG (dB) and ECC calculated from the far-field radiation pattern at different frequencies.

MEG finds the difference between received power by the diversity antenna and isotropic antenna in a multipath environment. MEG primarily evaluates the gain of the antenna. It is calculated using equations 3.6, 3.7, and 3.8.

$$MEG_i = 0.5\eta_{i,rad} = 0.5\left[1-\sum_{j=1}^{M}|S_{ij}|^2\right] \tag{3.6}$$

$$MEG1 = 0.5\left[1-|S_{11}|^2-|S_{22}|^2\right] \tag{3.7}$$

$$MEG2 = 0.5\left[1-|S_{12}|^2-|S_{22}|^2\right] \tag{3.8}$$

Fig. 3.14 shows the plot of MEG versus frequency. For equal power levels at both ports, the ratio of MEG1 and MEG2 should be less than 3 dB. The plot shows MEG1 and 2 are around 3 dB, the difference between MEG1 and MEG2 is 0 dB, and the ratio MEG1/MEG2 is equal to 1 dB, which indicates very good satisfactory diversity performance at the THz frequency region.

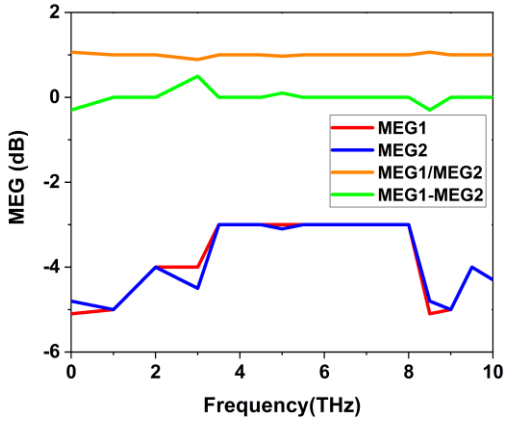

Fig. 3.14 Plot of MEG

TARC is defined as the ratio of the square root of total reflected power to the square root of total incident power and is determined using equations 3.9 and 3.10.

$$\Gamma_a^t = \frac{\sqrt{\sum_j^M |b_j|^2}}{\sqrt{\sum_j^M |a_j|^2}} \tag{3.9}$$

Where aj and bj are incident and reflected waves.

$$\Gamma_a^t = \sqrt{\frac{\left|S_{11} + S_{12}e^{j\theta}\right|^2 + \left|S_{11} + S_{12}e^{j\theta}\right|^2}{2}} \qquad (3.10)$$

Where θ is the phase angle.

Fig. 3.15 shows a plot of TARC versus frequency for seven varying phase angles (θ=0°, 30°, 60°, 90°, 120°, 150°, average) with a step size of 30°. It is clear that for different values of θ, the reflection coefficient is <- 30dB in the targeted band, which means high isolation is observed from port 1 and port 2. CCL for the proposed antenna is depicted in Fig. 3.16. CCL is the maximum allowable transmission rate for signal transmission over the MIMO antenna system. It is calculated using equations 3.11 and 3.12 [116]. For better performance of MIMO, CCL must be <0.5bps/Hz in the target pass bands. From Fig. 3.16, it is observed that CCL is < 0.5bps/Hz at the operating pass bands.

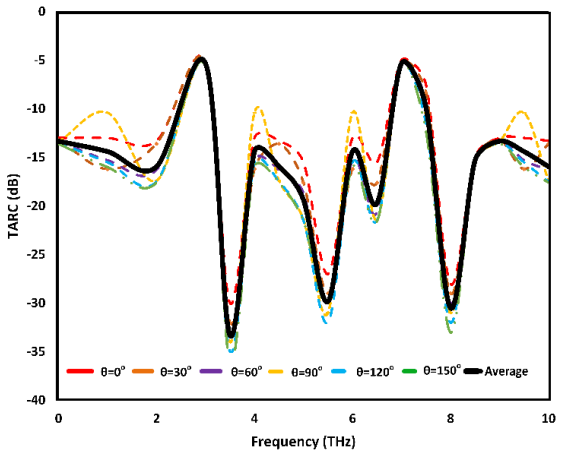

Fig. 3.15 Plot of TARC vs Frequency (THz) at different phase angles.

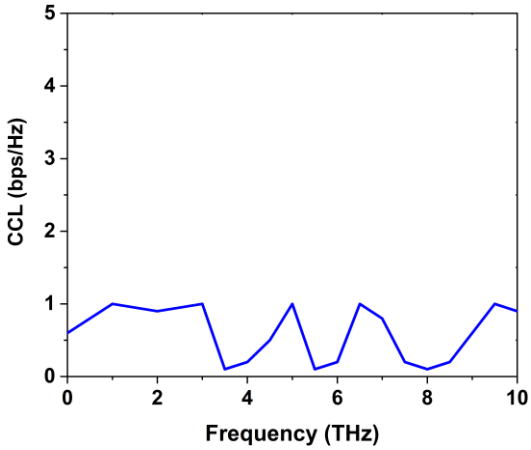

Fig. 3.16 Plot of CCL (bps/Hz) vs frequency (THz).

$$CCL = -\log_2 \det(\psi^R) \tag{3.11}$$

$$\psi^R = \begin{bmatrix} \psi_{11} & \psi_{12} \\ \psi_{21} & \psi_{22} \end{bmatrix} \tag{3.12}$$

Where $\psi_{11} = 1-\left(|S_{11}|^2 - |S_{12}|^2\right)$, $\psi_{22} = 1-\left(|S_{12}|^2 - |S_{22}|^2\right)$, $\psi_{12} = -\left(S_{11}^* S_{12} + S_{21}^* S_{22}\right)$ $\psi_{21} = -\left(S_{22}^* S_{21} + S_{12}^* S_{11}\right)$.

3.5 Improved isolation and CP tuning using Graphene

This section shows how isolation is increased with an increase in graphene chemical potential (μ_c). Fig. 3.17(a) depicts the proposed MIMO DRA with graphene material having a thickness of 0.3μm layered on the top of both CDRAs. Fig. 3.17(b) shows the isolation plot versus frequency for potential chemical values of μ_c= 0.3, 0.6, and 0.9ev. It can be easily understood from the above plot that there is an increase in isolation with an increase in μ_c. CDRA without graphene material has an isolation of -15.3 dB at 3.4 THz between the ports. Coating the upper layer of CDRA with graphene material increases isolation. At a frequency of 3.4 THz, isolation of -18.3 dB, -18.9 dB, and -20.7 dB is achieved when CDRA is coated with graphene having μ_c= 0.3, μ_c= 0.6, and μ_c= 0.9ev, respectively. It can be observed that as μ_c increases, isolation between the two ports increases.

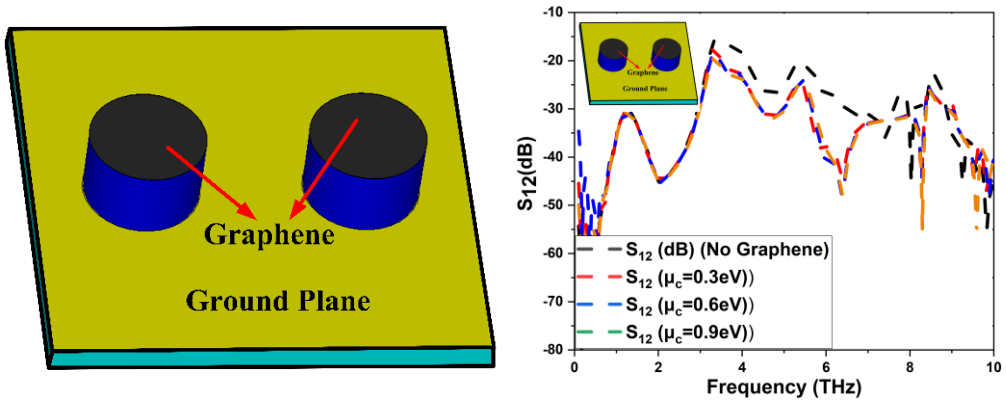

(a) (b)

Fig. 3.17 a. Graphene layered MIMO DRA, b. Isolation plot

The approach described in [76], [117] establishes a tri-constituent self-assembly route for directly synthesizing graphene films on silicon/silica substrate. Graphene was manufactured on single-

crystal silicon substrates using metal-free, ambient-pressure chemical vapor deposition. The development of atomically flat monolayer or bilayer graphene domains, concave bilayer graphene domains, and bulging few-layer graphene domains can all be achieved by controlling the growth temperature, as described in [76]. Practically, the externally provided DC electrostatic bias voltage for antennas at the nanoscale level should be kept to a minimum. As a result, the value of μ_c should be chosen within the range so that the required external voltage is kept to a minimum and antenna tuning response is possible.

The surface conductivity of graphene, according to the Kubo formula, can be given by

$$\sigma_{intraband}(\omega, \mu_c, \Gamma, T) = -j\frac{e^2 k_B T}{\pi\hbar^2(\omega - j2\Gamma)}\left[\frac{\mu_c}{k_B T} + 2\ln\left(e^{\frac{\mu_c}{k_B T}+1}\right)\right], \quad (3.13)$$

$$\sigma_{interband}(\omega, \mu_c, \Gamma, T) = -j\frac{e^2 k_B T}{4\pi\hbar}\ln\left[\frac{2|\mu_c| - (\omega - j2\Gamma\hbar)}{2|\mu_c| + (\omega - j2\Gamma\hbar)}\right], \quad (3.14)$$

Equation 3.13 is intraband, and equation 3.14 is interband conductivity contributions. Where e is the electron charge, ħ is Planck's constant, K_B is Boltzmann's constant. Γ is the chemical potential, ω is the operating frequency, and T=300 K. Depending on the external DC bias voltage applied, equation (3.15) depicts a relationship between voltage and μ_c. Equation 3.15 shows the relationship between DC bias, μ_c, which is dependent on the applied voltage V.

$$V = V_0 + \frac{te\mu_c^2}{\varepsilon_0 \varepsilon_r \pi h^2 v_F^2} \quad (3.15)$$

Where fermi velocity (v_f) is given by, $v_f = 9.5 \times 10^5$ m/s, V_0 is the voltage compensation dependent on the chemical doping, t and ε_r are the thickness and relative permittivity of the dielectric between graphene and electrode, respectively.

Applying an electric field via DC bias to the material can change the conductivity of graphene. The electric field alters the charge density, as described in [74]. The relationship between electrostatic bias (E_0) and chemical potential is obtained from equation (3.16) and Fig. 3.18 depicts the plot between V, μ_c, and ε_r of graphene. In the antenna design, a metallic gate layer is placed on the graphene patch to apply the DC gate voltage. The length and width of the metallic gate layer are kept identical to the graphene patch when the external voltage is applied, ensuring that the fermi level is maintained consistently.

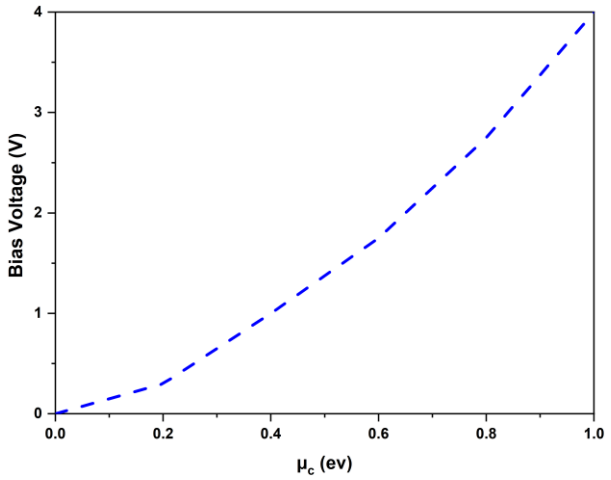

(a)

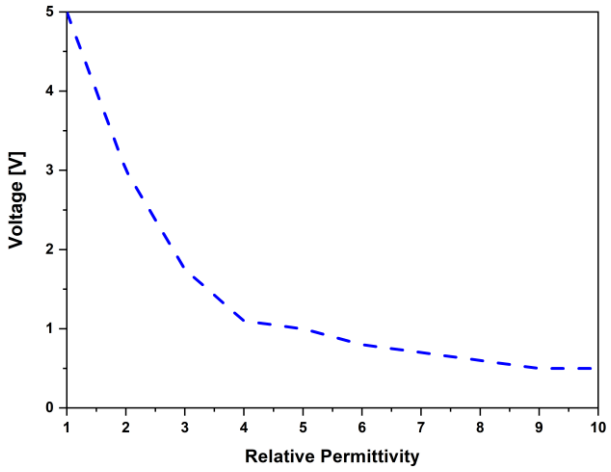

(b)

Fig. 3.18 a. Graphene potential (μ_c) vs Bias Voltage, b. ε_r *vs* V.

$$\frac{2\epsilon_s E_0}{e} = \frac{2}{\pi h^2 v_f^2}\int_0^\infty E(f_d(E) - f_d(E + 2\mu_c))dE \qquad (3.16)$$

Where $f_d(E)$ is the Fermi-Dirac distribution given by $f_d(E) = \left(e^{\frac{E-\mu_c}{k_B T}} + 1\right)^{-1}$.

This investigation is further extended to find frequency response and AR for different graphene potential values. It is observed that there is a shift in resonant frequency with graphene material, as shown in Fig. 3.19(a). Fig. 3.19(b) shows CP tuning. With an increase in graphene potential, there is a shift in AR characteristics.

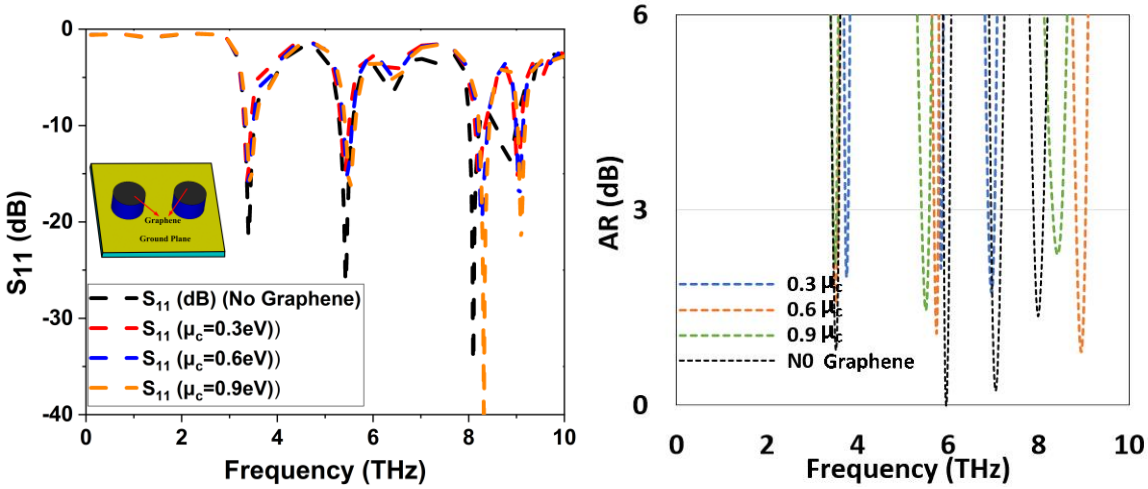

(a) (b)

Fig. 3.19 MIMO CDRA without graphene and with graphene (a) Frequency response and (b) AR (dB).

Table 3. 3 shows the comparison between previously published works and the proposed antenna. It can be observed that the proposed CP MIMO DRA offers good isolation and high gain at three bands at terahertz frequency. Furthermore, when CDRA is coated with graphene material, isolation further increases. The above results prove that the proposed multi-band CP MIMO DRA is very suitable for THz applications MIMO antenna compared with other antennas. This fulfills the first sub-objective under objective two. The next section covers the objective related to the second sub-objective under objective two.

Table 3. 3 Comparison with other MIMO antennas.

Ref	**DR type**	**Isolation (dB)**	**Gain (dB)**	**ECC**	**MEG (dB)**	**DG (dB)**	**TARC**	**CCL(bits/ sec/Hz)**
[32]	Dual port	< 17	4.4	0.0002	< 3	9.99	-	< 0.4
[33]	Dual port	17	5.8	-10	< 3	10	< 0	
[37]	Dual port	18	4	< 0.3	1	9.6	< -30	< 0.4
[39]	Dual port	27	1.99	< 0.4	-	10	-	-
This antenna	**Dual port Graphene based MIMO CDRA**	20.7	7.86	< 0.0001	< 3	10	<-30	< 0.2

3.6 2 × 2 MIMO CPDRA for THz applications

In this section, the design analysis of 2x2 MIMO CPDRA is discussed. Fig. 3. 20 shows the geometry of the proposed 2x2 MIMO CDRA. The substrate chosen here is SiO_2 which has a dielectric permittivity of 3.9 with dimensions as 44×44×2.4 µm. The 50 Ω nanostrip line is printed at the bottom of the substrate with dimensions $W_f \times l_f$. The aperture cross slot is etched on the ground plane which has dimensions of $W_s \times L_s$ as shown in fig. 1. The dimensions of the ground plane are the same as the substrate with a thickness of 0.035µm. Four CDRA's are used to make 2×2 MIMO. The dielectric material chosen for CDRA is silicon which has a dielectric permittivity of 11.9 with dimensions of radius r=7.6µm and height h=1.5µm. The distance of separation between DRs is d. The dimensions are optimized and chosen to radiate $HEM_{11\delta}$ mode. To improve the isolation between the ports various configurations of Defected Ground Structures (DGS) are made. Fig. 2(a, b, c and d) shows MIMO DRA without DGS, with vertical DGS having a length of L_v =32.5 µm and width of 0.8µm (fig. 2(b)), with horizontal DGS (fig 2(c)). To achieve more isolation between the ports the combination of horizontal and vertical DGS is utilized as shown in Fig 2(d) (proposed Configuration). Antenna shows perfect matching at all 4 ports for Ant-I to Ant-IV configuration which resonates at 5.26 THz and 6.52 THz for all the ports.

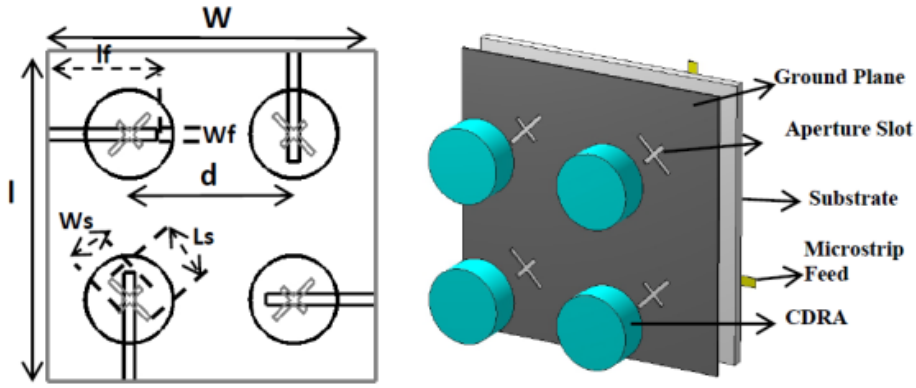

(a) (b)

Fig. 3. 20 (a) Dimensions (in µm) of reported MIMO DRA (w=44, l=44, d= 21.2, Ls=1.5, Ws=0.58, lf=13.3, Wf=0.74 µm) (b) perspective view.

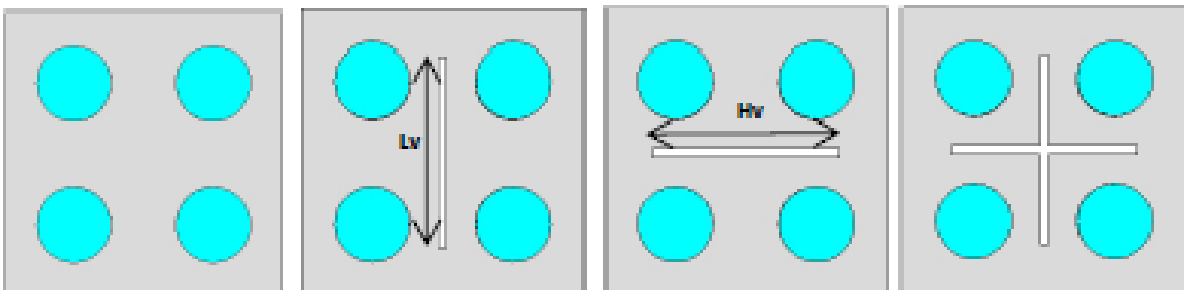

(a) (b) (c) (d)

Fig. 3. 21(a) Ant- I (b) Ant-II (c) Ant-III (d) Ant-IV (L_v=32.5 µm and H_v=32.5 µm)

The simulated 10 dB Impedance Band Width (IBW) of 8.16% (5.05-5.48 THz) with a resonant peak at 5.26 THz, 12.57% (6.11-6.93 THz) with a resonant peak at 6.52 THz respectively is achieved as depicted in Fig. 3. 22(a). Fig. 3. 22(b, c) shows an isolation plot. Impedance matching is improved for the Ant-IV configuration with an isolation of ~ -25 dB shown for the proposed MIMO configuration. The symmetricity of port 1 with the other three ports (2, 3, and 4) proves the symmetrical S parameter response of all the ports as shown in the caption of Fig. 3. 22. Fig. 3. 23 shows the plot between axial ratio vs frequency (THz) for antenna configurations. The antenna is showing dual sense CP behavior at both the pass bands (at 5.26, 6.5 THz) with 3dB Axial Ratio Band Width (ARBW) of 4.58% (5.11-5.35 THz) and 2.15% (6.43-6.57 THz) for the proposed antenna configuration (Ant-IV).

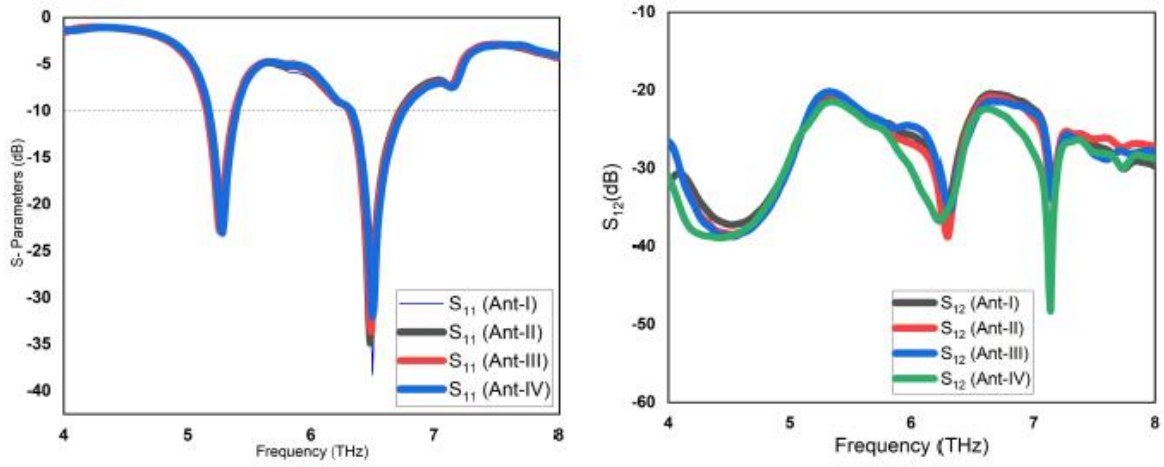

(a) (b)

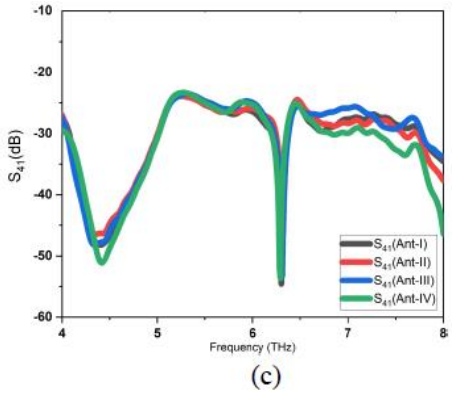

Fig. 3. 22 Frequency Response (a) S_{11} (S_{11}=S_{22}=S_{33}=S_{44}) (b) S_{12} (S_{12}=S_{31}=S_{21}=S_{42}=S_{13}=S_{43}=S_{24}=S_{34}) and (c) S_{41} (S_{41}=S_{14}=S_{32}=S_{23}).

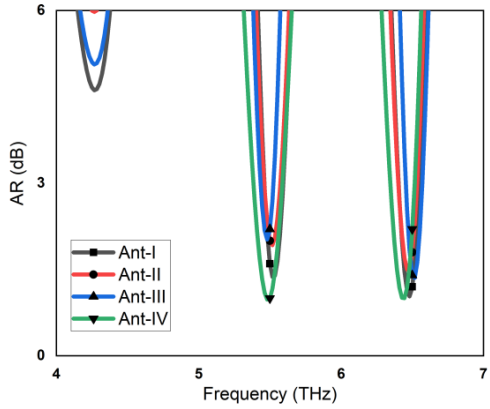

Fig. 3. 23 Plot of Axial Ratio (AR) vs Frequency (THz).

The proposed antenna will generate LHCP behavior at all the ports. Fig. 3. 24 shows simulated radiation patterns in XZ plane at resonant frequencies of 5.26 THz and 6.52 THz for proposed antenna configuration (fig. 3(d)). It can be observed that Left Hand CP (LHCP) fields are dominating Right Hand CP (RHCP) in boresight direction ($\theta=0^0$). At 5.26 and 6.52 THz, the simulated results indicate a difference of more than -25dB between the LHCP and RHCP fields. This means LHCP fields are clearly dominating RHCP fields at both resonant frequencies. Fig. 3. 25 shows the plot of gain and Radiation Efficiency (RE) vs frequency (THz) for the proposed configuration (Fig. 3. 21(d)). Maximum gain of 6.7 dBi and RE of 73% is achieved for the proposed MIMO DRA.

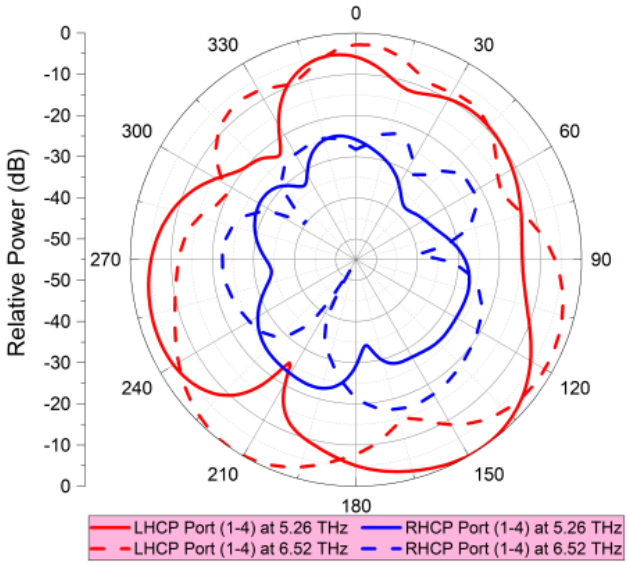

Fig. 3. 24 Radiation Pattern of the antenna at 5.26 and 6.52 THz in xz plane (Solid line indicates at 5.26 THz and Dashed line indicates at 6.52 THz).

Fig. 3. 26 shows plot of ECC vs frequency (THz). ECC is clearly very much less than 0.5 and equal to 0 in the pass band. DG of the antenna must be greater than 9.5dB. From the Fig. 3. 26 it is clear that DG of the antenna is approximately equal to 10 dB in the pass bands. Hence the proposed 2x2 MIMO antenna is very much suitable for MIMO operation. This fulfills the second sub-objective under objective two. The next section (3.7) covers the objective related to the third sub-objective under objective two.

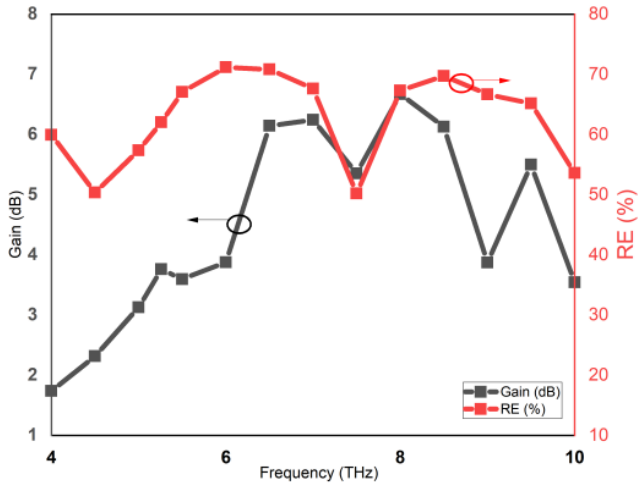

Fig. 3. 25 Plot of Gain in dB (Left) and RE in % (Right)

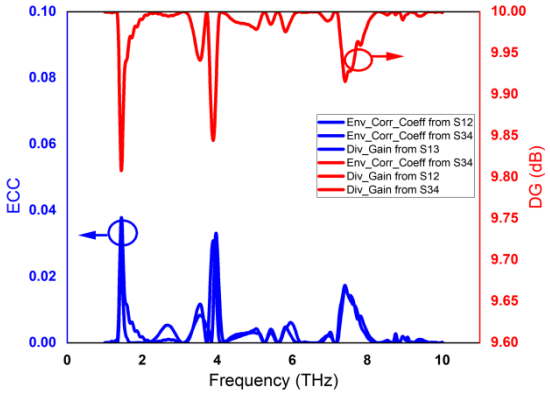

Fig. 3. 26 Plot of ECC in dB (Left) and DG (dB) vs Frequency (Right).

3.7 Tri-sense Circularly Polarized wideband MIMO DRA for UAV applications

Here, a two-port MIMO wide band tri sense CP DRA is designed for UAV satellite applications. This fulfills the third sub-objective under the second objective. Deployment of unmanned aerial vehicles (UAVs) became very popular in the fields of military, agriculture, electronics, communication, and safety and security [29], [118]–[120]. Data from UAVs is transmitted through wireless transmission. They are frequently employed to gather data and relay it to a ground station that offers real-time data on the covered region [121], [122].

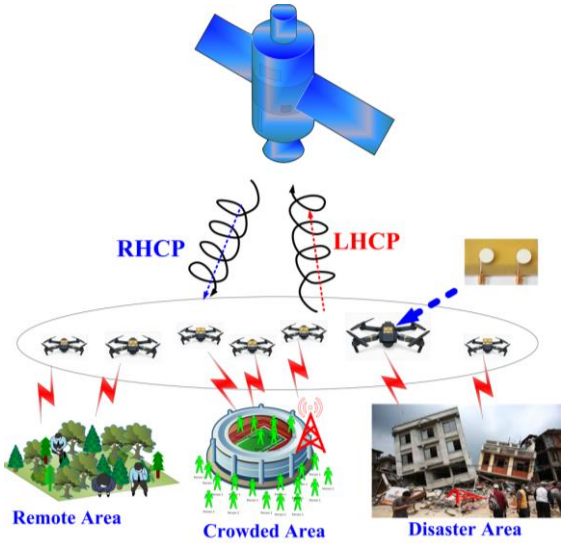

Fig. 3. 27 Demonstration of a communication link between different areas with UAVs.

Besides this, UAVs have advanced to the point where they can now be used in the wireless link as UAV access points for UAV-assisted connectivity due to their low cost and adaptable coverage [120]. In coming years, UAVs are expected to connect with satellites even more via UAV-satellite communication, creating affordable, widely reaching and satellite-sky-ground systems [123]–[125]. As depicted in Fig. 3. 27, these systems can establish a communication link between different areas with UAVs and offer enhanced paths for rural locations, emergency connections for catastrophe zones, and helper connections for access points. In these contexts, using a UAV as a bridge facilitates communication across ground stations and satellite systems. For this purpose, single antennas or antenna arrays are used for data transmission and receiving with the satellite link [126], [127].

The proposed structure consists of a substrate made of FR-4 epoxy having a permittivity of ε_s=4.4 and loss tangent of 0.002 with dimensions of Ls × Ws having a thickness of t_s=0.5 mm as shown in fig. A zigzag feed is used along with the modified ground plane to generate wide band frequency response with orthogonal modes generation for CP behavior. This new modified ground plane consists of a partial ground plane with a length of L_g and square rings with a width and height of G_w and G_L, respectively. This new defected ground plane (GP) generates a wide frequency response and helps to enhance the CP generation. Fig. 3. 28(b) and Fig. 3. 28(c) shows the top view of the proposed microstrip zigzag feed printed on the top of the FR-4 substrate and the new modified GP printed on the bottom of the FR-4 substrate, respectively. Fig. 3. 28(d) shows cylindrical dielectric resonators made up of Al_2O_3 having a permittivity of 9.9 and loss tangent of 0.025 with dimensions having a thickness of t_{dra} = 2 mm and radius of r_o = 5 mm are utilized as a radiator. Fig. 3. 28(e) and Fig. 3. 28(f) show the plot of s-parameters and axial ratio in dB. The plots of frequency response and AR response are depicted in Fig. 3. 28(e) and Fig. 3. 28(f). The proposed MIMO configuration provides a bandwidth of 8.4 GHz (7.5 GHz-15.9 GHz) and provides tri-sense AR response in the operating pass band with ARBW of 21.82 % (7.55-9.34 GHz), 9.36 % (11.2-12.3 GHz) and 9.72 % (13.7-15.1 GHz), respectively. Furthermore, good isolation values of < -25dB throughout the operating band are obtained between the two ports for the proposed antenna, as depicted in Fig. 3. 28(f).

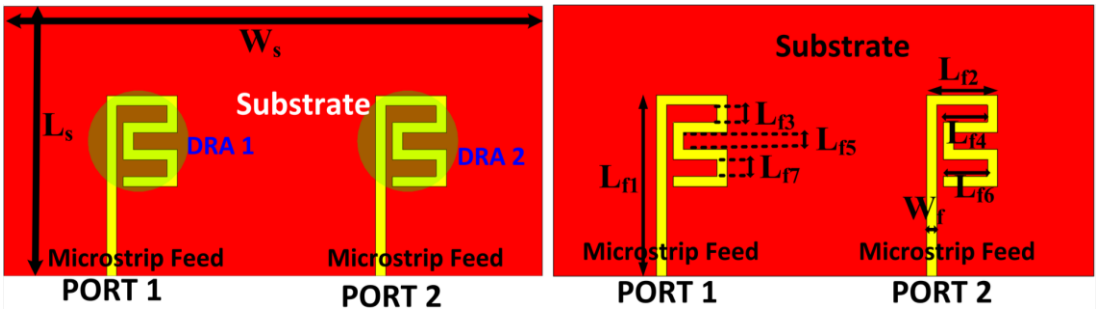
W_s
L_s
Substrate
DRA 1
DRA 2
Microstrip Feed
Microstrip Feed
PORT 1
PORT 2
Substrate
L_{f2}
L_{f3}
L_{f5}
L_{f4}
L_{f1}
L_{f7}
L_{f6}
W_f
Microstrip Feed
Microstrip Feed
PORT 1
PORT 2

(a) (b)

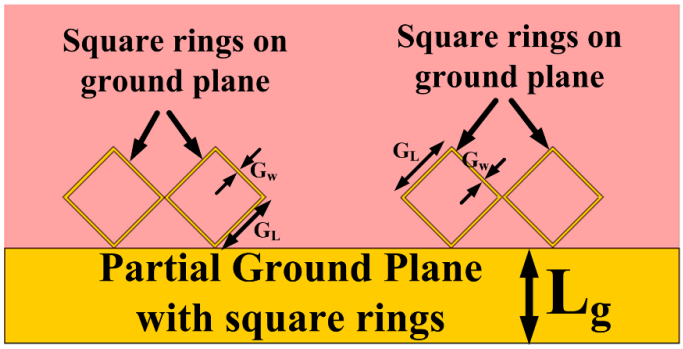
Square rings on ground plane
Square rings on ground plane
G_w
G_L
G_L
G_w
Partial Ground Plane with square rings
L_g

(c)

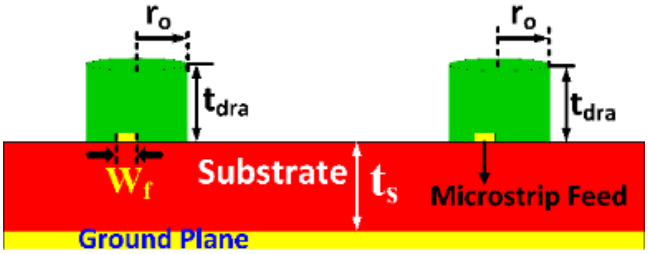
r_o
r_o
t_{dra}
t_{dra}
W_f
Substrate
t_s
Microstrip Feed
Ground Plane

(d)

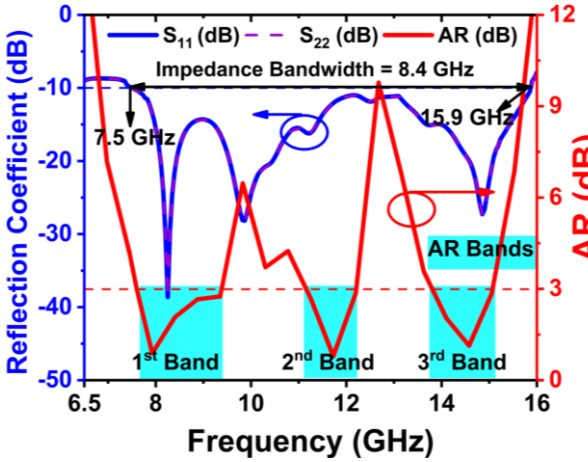
S_{11} (dB)
S_{22} (dB)
AR (dB)
Impedance Bandwidth = 8.4 GHz
7.5 GHz
15.9 GHz
AR Bands
1st Band
2nd Band
3rd Band
Reflection Coefficient (dB)
AR (dB)
Frequency (GHz)

(e)

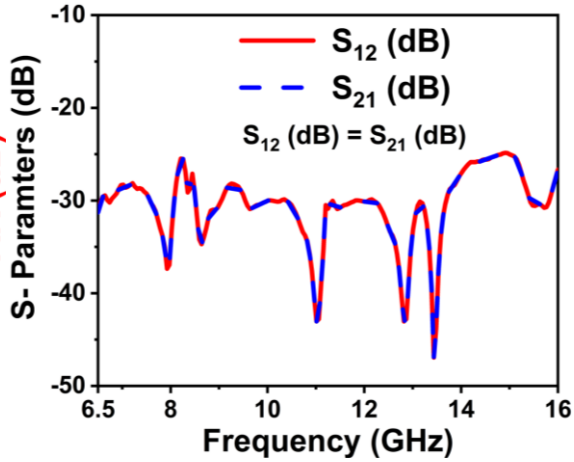
S_{12} (dB)
S_{21} (dB)
S_{12} (dB) = S_{21} (dB)
S- Paramters (dB)
Frequency (GHz)

(f)

Fig. 3. 28 Proposed MIMO antenna (a) Top view (b) Microstrip Feed configuration, (c) proposed ground plane, (d) Front view (e) S_{11} (dB), AR (dB) and (f) S_{12} (dB).

3.7.1 Tri-sense CP response

The proposed MIMO DRA produces orthogonal modes essential for CP generation at three operating bands. Fig. 3. 29 and Fig. 3. 30 depict Electric Field (EF) propagation at different time phases of t = 0, T/4, T/2, and 3T/4 at frequencies of 8 GHz, 11.5 GHz, and 14.75 GHz at port 1 and port 2, respectively. At 8 and 11.5 GHz, the EF distribution on DRA exhibits anti-clockwise rotation at both ports. Therefore, it confirms a dominant RHCP wave generation at 8 GHz and 11.5 GHz, respectively. Next, at 14.75 GHz, the EF distribution on DR at different time instants shows clockwise rotation, which confirms LHCP wave generation at this frequency at both the ports (Fig. 3. 29(c) and Fig. 3. 30(c)). Therefore, the proposed wideband tri-sense MIMO antenna can be utilized for UAV applications where 8 GHz and 11.5 GHz can be considered as transmitting/receiving frequencies, and 14.75 GHz can be considered as receiving/transmitting frequencies. This reduces the inter-channel interference and ensures high isolation between the two frequencies because of its RHCP and LHCP response at these frequencies. Furthermore, the proposed MIMO antenna provides wide frequency bandwidth that can be used for high throughput exchange of extensive data such as voice, video, and the internet. Due to the compact structure and less weight, this can be easily mounted on UAVs. Additionally, MIMO antennas are generally preferred because of their high data rates, high gain, and high radiation efficiency, which are essential requirements for UAV applications for large data transformation. Next, the EF distribution on DR at three frequencies of 8 GHz, 11.5 GHz, and 14.75 GHz is investigated. With reference to Fig. 3. 31, it is observed that the proposed antenna radiates three different higher-order modes, namely, $HEM_{11\delta}$, $HEM_{12\delta,}$ and HEM_{212} modes, respectively.

3.7.2 Simulated and measured results

A wideband tri-sense CP DRA is fabricated and tested to validate the proposed design. The prototype of the proposed MIMO design is depicted in Fig. 3. 32.

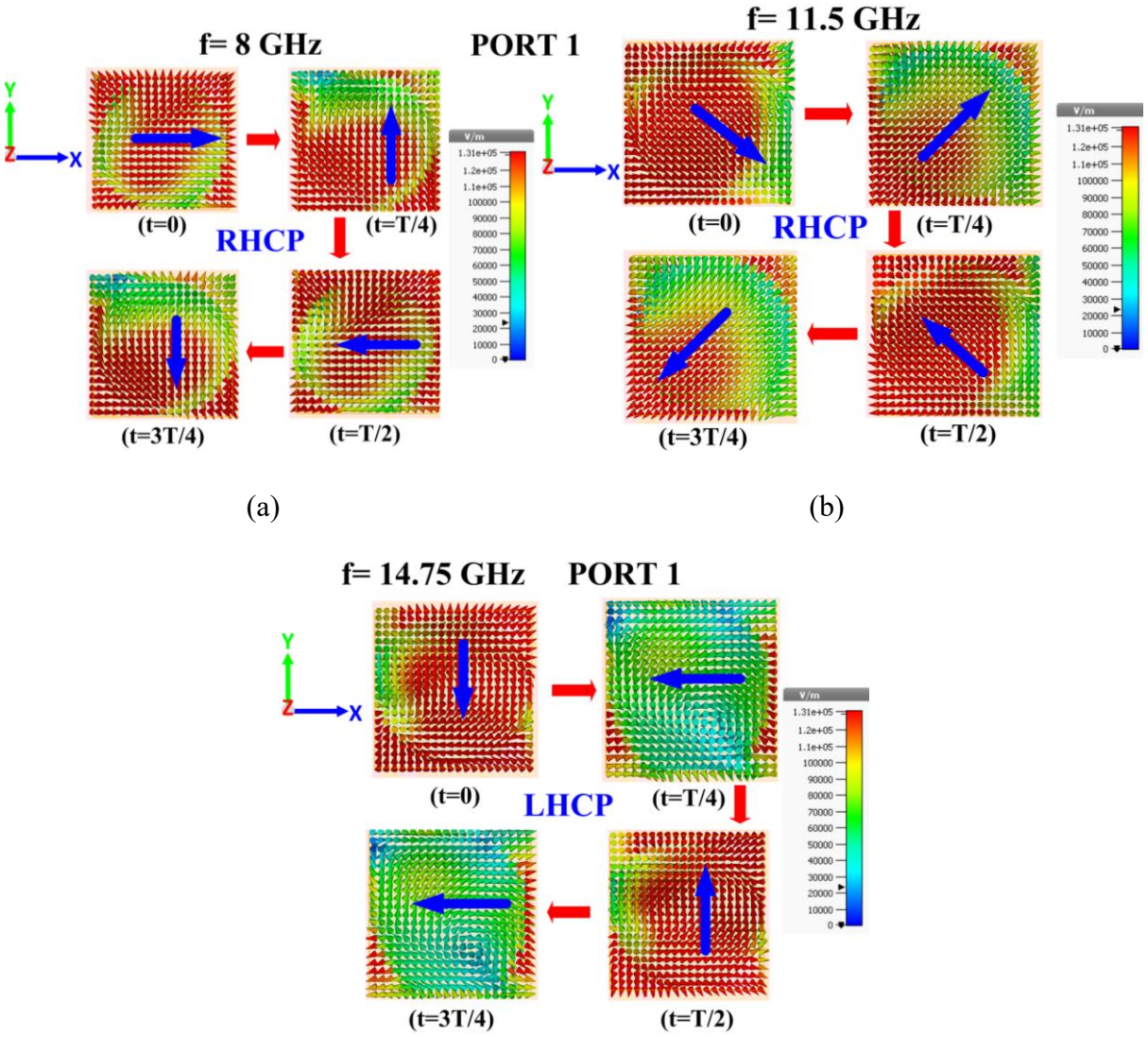

Fig. 3. 29 EF distribution at different time instants at port 1 (a) 8 GHz, (b) 11.5 GHz, and (c) 14.75 GHz.

The FR-4 substrate (ε_s=4.4), having a thickness of 0.5 mm, is used as a PCB and AL_2O_3 dielectric resonator with permittivity of 9.9, loss tangent of 0.025, with a thickness of 2 mm, and radius of 5 mm is utilized as a radiator.

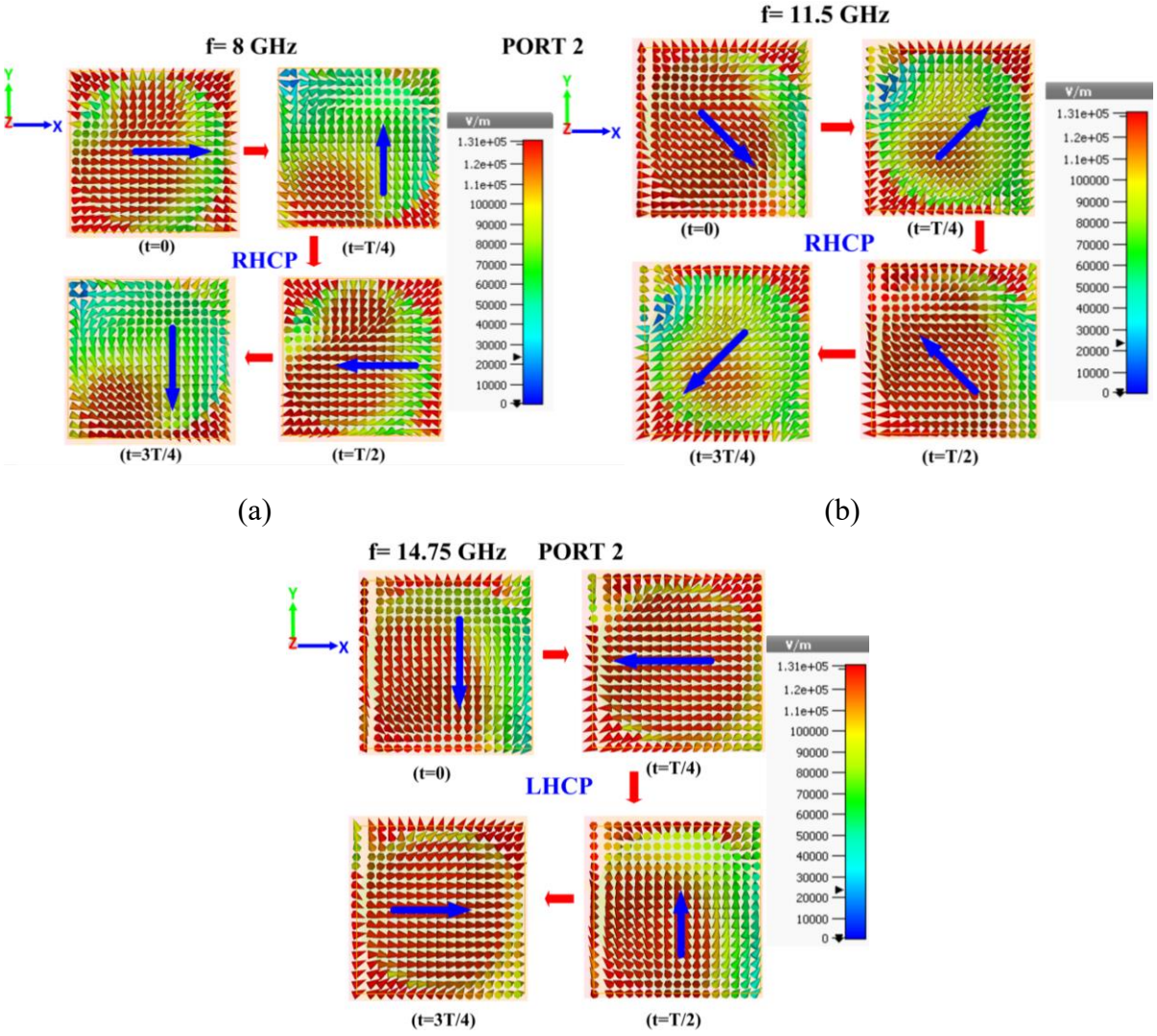

Fig. 3. 30 EF distribution at different time instants at port 2 (a) 8 GHz, (b) 11.5 GHz, and (c) 14.75 GHz.

With reference to Fig. 3. 33, there is a good agreement between fabricated and simulated results. From Fig. 3. 33(a), the proposed MIMO configuration provides measured bandwidth of 8.375 GHz (7.55 GHz-15.925 GHz) and provides tri sense AR response in the operating pass band with ARBW of 21.3 % (7.55-9.35 GHz), 10.5 % (11.09-12.32 GHz) and 10.22 % (13.68-15.16 GHz), respectively. Furthermore, as depicted in fig 10(b), good isolation values of < -25dB are observed for the measured antenna throughout the operating band. Fig. 3. 34(a)-(f) illustrates the simulated and measured normalized radiation patterns at AR bands in broadside directions at frequencies of 8 GHz, 11.5 GHz, and 14.75 GHz, respectively, in the yoz plane.

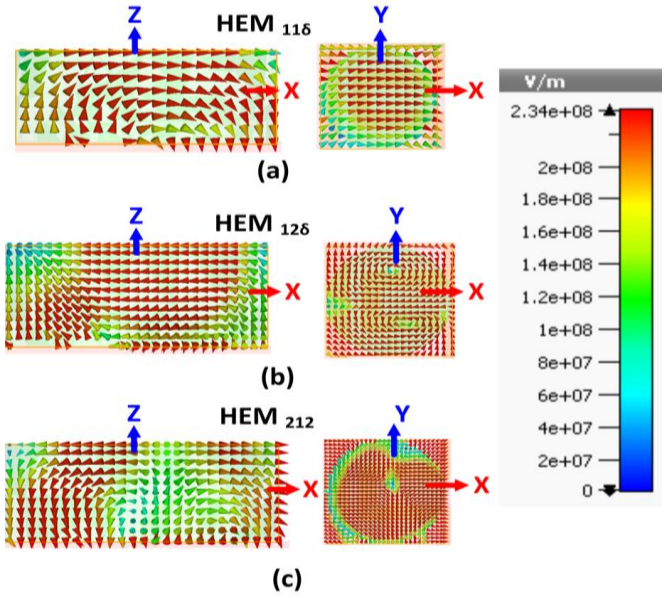

Fig. 3. 31 EF distribution on DR (a) 8 GHz, (b) 11.5 GHz, and (c) 14.75 GHz.

(a) (b) (c)

Fig. 3. 32 Fabricated Proposed MIMO antenna. (a) Top View, (b) Feed Configuration, and (c) Bottom Ground Plane.

At 8 GHz and 11.5 GHz, the simulated and fabricated antenna shows a dominant RHCP wave, and at 14.75 GHz, the antenna provides a dominant LHCP wave at both ports. Furthermore, the RHCP and LHCP waves dominate by more than -28 dB at their respective frequencies. This quantifies that the proposed MIMO DRA is a good candidate for UAV applications where we can reduce interchannel interference with very high gain. The plot of G (dB) and RE is depicted in Fig. 3. 35(a). A maximum gain of 13.85 dBi at a frequency of 13.62 GHz is observed for the proposed antenna. A high gain of more than 10 dBi is observed throughout the operating wide band. Also, the proposed antenna shows a high RE of > 94 % throughout the occupied band with a maximum RE of 99 %. The attributes such as ECC and DG (dB) are calculated and plotted to evaluate MIMO performance, as shown in Fig. 3. 35(b). These parameters are calculated based on the literature

provided in [48], [128], [129]. For better MIMO performance, ECC must be < 0.5 and close to 0, and DG must be > 9.5 dB and close to 10 dB. From the simulated and measurement plots, it is observed that ECC is < 0.025 and DG is > 9.98 dB throughout the operating band.

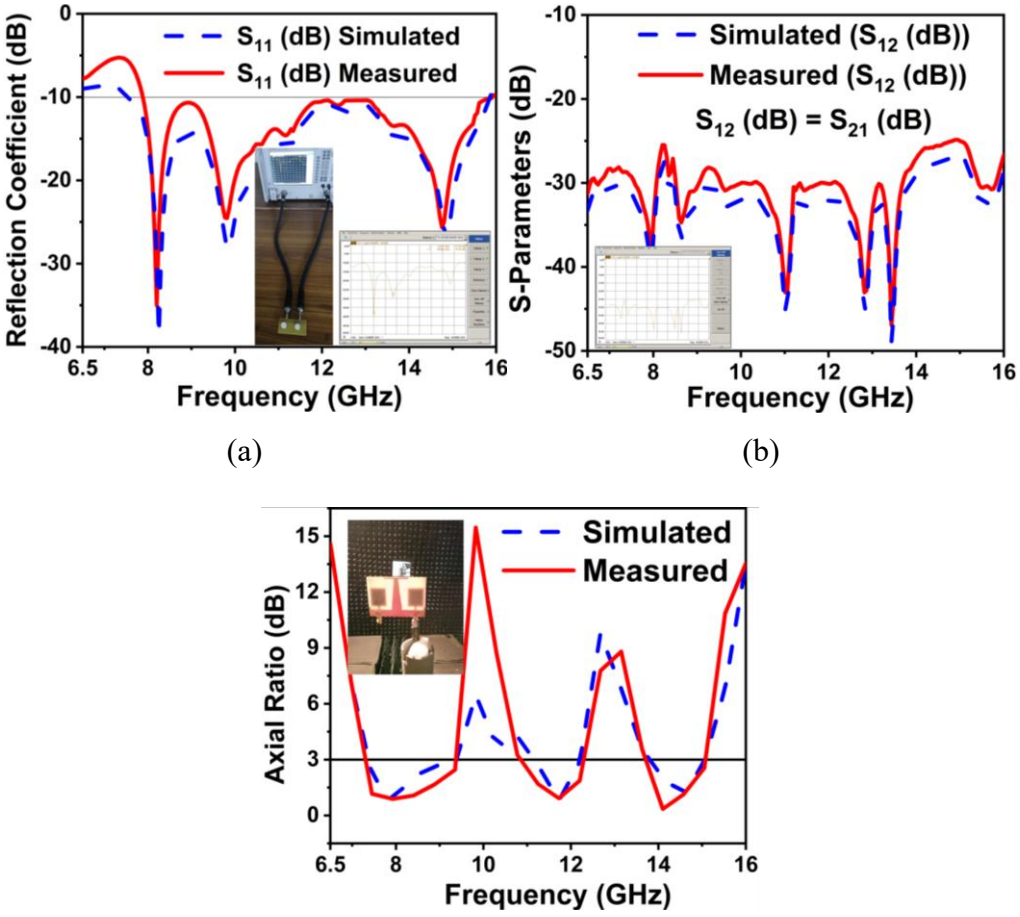

(a) (b)

(c)

Fig. 3. 33 Simulated and measured results. (a) S_{11} (dB), (b) S_{12} (dB) and (c) AR (dB).

All these features, such as wide frequency response, good isolation between the ports, tri sense CP response, very high gain, high radiation efficiency, good ECC values, good DG, low weight, compact design, easy fabrication, and broad coverage makes the proposed antenna suitable for mounting on UAVs. Finally, the comparison of the proposed work with other published articles is presented in Table 3. 4. Our work shows better results compared to the other articles in terms of IBW, ARBW, G, and RE. Additionally, CP-based MIMO DRA for UAV applications is not being implemented. Therefore, the proposed antenna is the best choice for UAV satellite communications. Therefore these three sub-objectives fulfils the second objective.

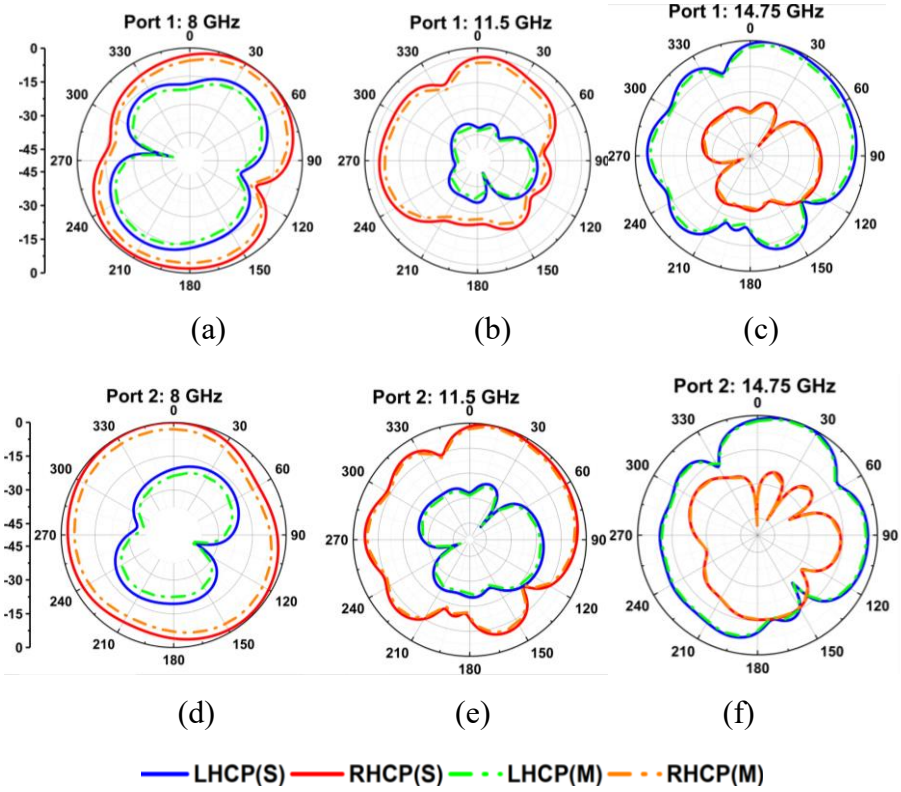

Fig. 3. 34 Simulated and measured radiation patterns at (a) 8 GHz, (b) 11.5 GHz, and (c) 14.75 GHz.

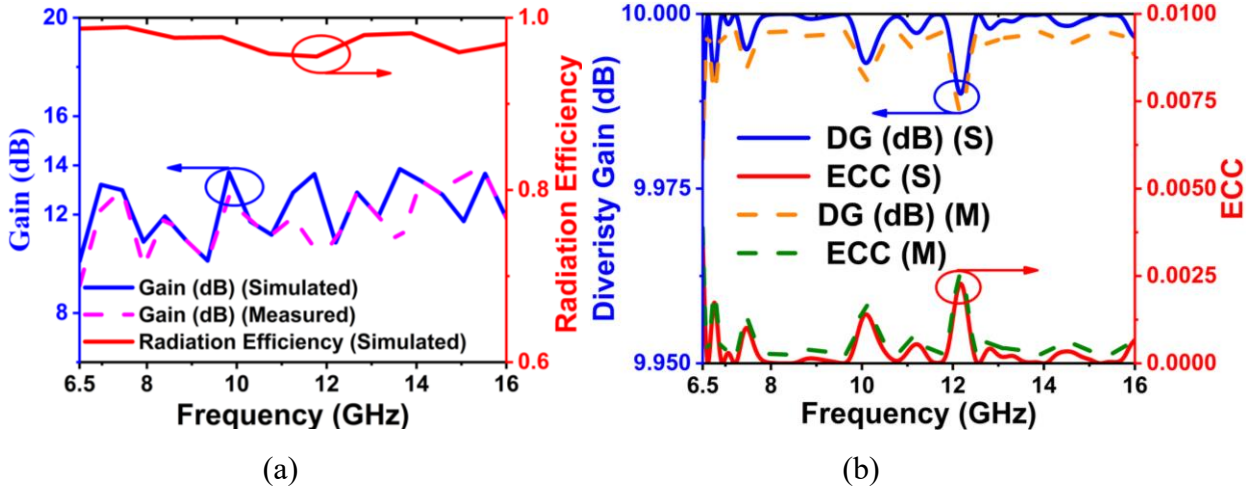

Fig. 3. 35 Simulated (S) and measured (M) results of (a) G (dB), RE, and (b) ECC, DG (dB).

Table 3. 4 Comparison with other research articles

Ref.	Frequency (GHz)	Number of frequency bands	IBW (%)	AR Bands	ARBW (%)	Gain (dBi)	Eff. (%)
[127]	11.27	1	111	1	32.29	10.77	> 90
[120]	20/30	2	6.4/12.8	2	5.2/4.1	6.6/8.2	-
[126]	1.2/1.6	2	22.69/5.68	2	7.4/3.9	9/9.58	-
[124]	1.2/1.57	2	-	2	-	2.6/3.2	-
[130]	5.05	1	37.15	1	5.94	3.45	70
[131]	3.45	1	18.6	1	9.5	7.65	97
[122]	8.2/14.5	2	16.3/29.3	2	2.4/4.1	16.1/15.2	-
Prop. Ant.	7.5-15.9 (fc=11.7)	1	71.79	3	21.82/9.36/9.7	13.85	> 94% (Max: 99%)

Ref.: Reference Number, Eff. : Efficiency, Prop. Ant. Proposed MIMO antenna.

3.8 Conclusion

Three circularly polarized MIMO designed for THz and UAV applications. **First**, a 2 port MIMO Dielectric Resonator Antenna is designed at THz frequency regime. Next, a 2x2 MIMO is designed which provides a dual band dual sense behavior for THz applications. Finally, a prototype of 2 port MIMO is designed that provides wide band tri sense response for UAV applications is designed. The unique feature of 2 port MIMO antenna for THz applications is that it provides resonance at four bands (Quad Band) and dual sense CP response at the THz frequency region, and by the varying graphene potential of the antenna, isolation between the two antennas is increased. CP tuning can be achieved, which another unique feature of this is proposed antenna at the THz region. The proposed DRA generates two higher-order modes ($HEM_{11\delta}$ and $HEM_{12\delta}$). Isolation between the two ports is more than 17dB for the proposed antenna configuration. Various MIMO performance parameters are evaluated. A Peak Gain of 7.86 dBi is achieved at 8.08 THz resonant frequency. These features allow the proposed MIMO DRA to be utilized for THz applications. **Second**, 2x2 MIMO DRA for the first time is designed in the THz frequency range. The unique feature of this antenna is it provides dual band dual sense circular polarization response in the THz frequency region. Defected Ground Structures (DGS) are made to improve the isolation between

the ports. Gain of 6.7 dBi and RE of 73% is achieved. This antenna generates $HEM_{11\delta}$ and $HEM_{12\delta}$ modes. Results shows the proposed antenna is very good candidate for THz applications. **Finally**, a CP-based wideband MIMO DRA for UAV satellite communications is introduced. A new defected ground structure (DGS) technique is used to enhance impedance bandwidth (IBW) and ARBW. For UAV applications, the designed antenna must generate a high G, high beamwidth, high RE, CP behavior, and high data exchange. The proposed antenna provides a bandwidth of 8.4 GHz (7.5 GHz-15.9 GHz) with tri sense CP response having a 3-dB ARBW of 21.82 % (7.55-9.34 GHz), 9.36 % (11.2-12.3 GHz) and 9.72 % (13.7-15.1 GHz), respectively. The antenna exhibits a dominant RHCP wave at 8 GHz and 11.5 GHz and a dominant LHCP wave at 14.5 GHz. Different polarizations will decrease inter-channel interference and ensure high isolation between the two frequencies because of the RHCP and LHCP response at these frequencies. Furthermore, the proposed MIMO DRA provides a high radiation efficiency of 99.02 % and a maximum gain of 13.85 dBi. Additionally, the antenna offers suitable MIMO diversity performance parameters such as ECC and DG.

Chapter 4

Design of Ultra wideband Circularly Polarized stacked CDRA

4.1 Introduction

In this chapter, two identical Cylindrical Dielectric Resonator Antennas (CDRA) are stacked together to achieve Circular Polarization (CP). Three factors achieve ultra-wideband impedance bandwidth and wide axial ratio bandwidth: stacking of similar DRs, stepped conformal microstrip feed line, which will generate orthogonal modes, and new partial ground plane with circular rings. The proposed research work heads towards providing the solution for the following objectives: ultra-wideband impedance response, wide AR response, high gain, and high efficiency. A simple DR structure is designed to generate CP waves with reduced DR height to achieve the above objectives. CP waves are generally produced by providing the required path difference between linearly polarized components, generating orthogonal modes required for CP generation. As described in [58], [132], the easiest way to enhance ARBW is to provide the necessary path difference to generate orthogonal modes for circular polarization. The microstrip feed length or DR structure must produce a 90^{o} phase difference between the orthogonal modes. To achieve ultra-wideband impedance response, wide axial ratio response, and high gain, two similar Cylindrical Dielectric Resonators (CDRA's) are stacked such that the antenna must provide orthogonal fields over a wide frequency range. The proposed ground plane, which contains partial ground with two circular rings, enhances IBW. The advantages and novel points of the proposed research work are

as follows: (i) The novel configuration of stacking CDRA's enhances ARBW and gain, (ii) a new partial ground plane with two circular rings provides an enhancement in IBW, (iii) Simple design, and small height of DRs produces enhanced IBW, ARBW, Gain and Efficiency. Moreover, by changing the position of circular rings on the ground plane, the proposed antenna provides dominant LHCP to RHCP conversion and achieves polarization reconfigurability. The proposed antenna covers the frequency range of C-band and military satellite communication applications.

4.2 DRA configuration

Fig. 4.1 shows the geometry of the proposed Circularly Polarized (CP) Dielectric Resonator Antenna (DRA) (CPDRA). Fig. 4.1(a) shows the top view of stacked CPDRA, which consists of a substrate of the length of $L_s \times L_s$ mm made up of FR-4 epoxy material having permittivity (ε_r) of 4.4 and loss tangent (tan δ) of 0.025 with a thickness of W_s is used. Fig. 4.1(b) shows a front view of the proposed stacked two Cylindrical Dielectric Resonators (CDRA's) having a height of h and a radius of r mm. The top CDRA is placed at a distance of d from the bottom CDRA, as shown. The stacked CDRA's are made up of the same alumina material (Al_2O_3) with permittivity (εr) = 9.8 and a loss tangent of 0.002. Alumina-based DR is chosen because of its lower price and low fabrication cost, and it can be used for both microwave and mm-wave applications. The stepped microstrip feed is used for the generation of Circular Polarization (CP) and is shown in Fig. 4.1(c), having a width of W_f. RF excitation is applied using a 50Ω microstrip line. The microstrip feed is etched at the bottom of the top CDRA, as depicted in Fig. 4.1(d).

The stepped microstrip feed is shown in Fig. 4.1(e), which consists of a feed length of l_{f1}, stub-I length of l_{f2}, stub-II length of l_{f3}, and stub-I length of l_f. Fig. 4.1(f) shows the novel partial ground plane, which consists of two circular rings etched at the bottom of the substrate, which enhances 10dB impedance bandwidth. This new configuration of stacked CDRAs, along with a new modified ground plane and stepped microstrip feed, enhances impedance bandwidth and CP bandwidth.

The following empirical formulas of equations (1-3) have been used in the literature to compute the dimensions of a dielectric resonator for a particular fundamental mode resonant frequency [3].

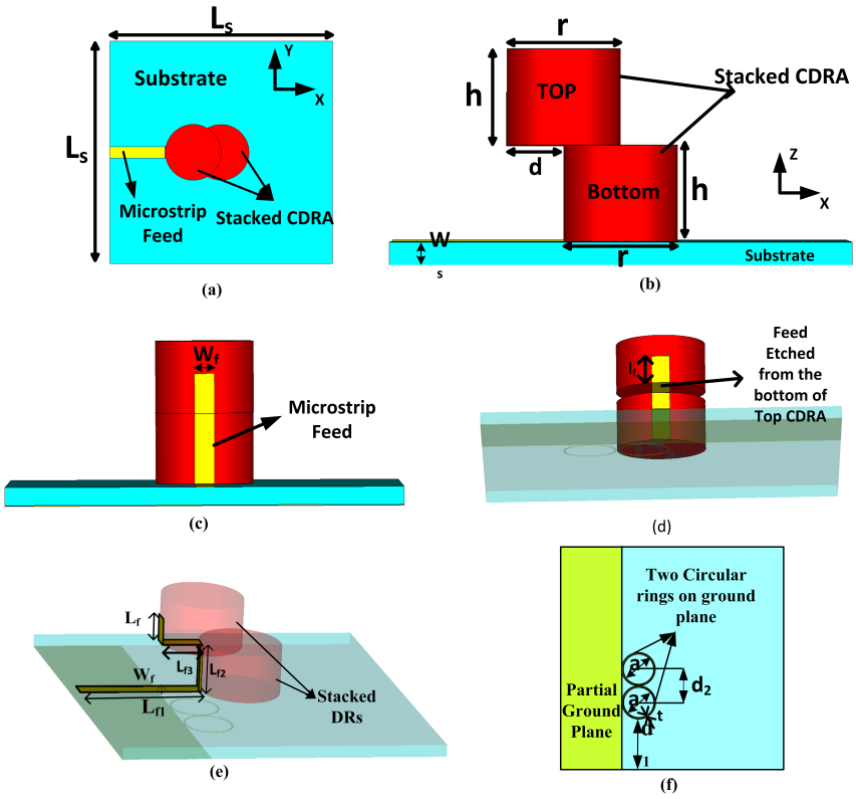

Fig. 4.1 Proposed antenna Configuration (a) Top view of proposed stacked DRA (b) Front view of stacked DRA (c) Proposed conformal Stepped Microstrip feed (d) Stepped Microstrip Feed etched on DRA's (e) Stepped Microstrip feed view (f) Proposed Ground Plane (L_s=40, W_s=1, d= 6.5, h=4, r =10, W_f=2, l_{f1}=15, l_{f2}=4, l_{f2}=6.5, and l_{f2}=2.5 mm).

$$f_{r(HEM11\delta)} = \frac{c}{2\pi r_d} \times \frac{6.324}{\sqrt{\varepsilon_{eff}+2}} \times \left[0.27 + 0.36\left(\frac{r_d}{4h_{eff}}\right) + 0.02\left(\frac{r_d}{4h_{eff}}\right)^2\right] \quad (4.1)$$

Where c is the velocity of light, r_d is the radius of CDRA, ε_{eff} is the effective permittivity of the proposed antenna, h_{eff} is the effective of the proposed antenna. ε_{eff} and h_{eff} can be found by using equations 2 and 3.

$$\varepsilon_{eff} = \frac{h_{eff}}{\frac{h_{dra}}{\varepsilon_{cdra}} + \frac{h_{sub}}{\varepsilon_{sub}}} \quad (4.2)$$

$$h_{eff} = h_{dra} + h_{sub} \quad (4.3)$$

4.3 Proposed antenna evolution

Fig. 4.2 shows four different DRA configurations and their Electric Field (EF) vector distribution on the antenna, with the proposed partial ground plane having two circular rings. Fig. 4.2 depicts

their respective simulated frequency response, Axial Ratio (AR) bandwidth, and gain (dB). This evolution exhibits ultra-wideband impedance bandwidth, wide AR bandwidth, and enhanced gain.

4.3.1 DRA configuration –I

Fig. 4.2(a) shows DRA configuration-I. It consists of a single CDRA with a microstrip feed line length L_{f1}. The concentration of EF for this configuration is depicted in Fig. 4.2(e). It can be observed that the concentration of EF is very low. Hence, its frequency response shows less excitation as shown in Fig. 4.3(a), fails to show the -10dB IBW, and suffers an impedance mismatch. This is due to the microstrip feed line being weak for coupling the CDRA. This antenna arrangement does not exhibit 3 dB AR bandwidth, as depicted in Fig. 4.3(b), because the AR bandwidth is determined by the DRA's generation of orthogonal fields. From the gain plot, as shown in Fig. 4.3(c), a maximum gain of 5.15 dBi is observed for this configuration.

4.3.2 DRA configuration – II

The second configuration of the DRA is obtained by adding a conformal strip, stub-I of length $l_{f2,}$ to the microstrip feed of DRA configuration - I to achieve better impedance matching, as depicted in Fig. 4.2(b). The concentration of EF for this configuration is depicted in Fig. 4.2(f). It can be observed that the concentration of EF is low. This configuration also does not show -10 dB impedance bandwidth and suffers impedance mismatch. This happens because of the low permittivity of CDRA material which will not support perfect matching but shows better matching than DRA configuration-I.

It is found that this configuration also does not generate orthogonal modes because the conformal microstrip feed does not provide the required path difference to generate CP waves and hence fails to achieve CP generation, as depicted in the AR plot of Fig. 4.3(b). From the gain plot, as shown in Fig. 4.3(c), a maximum gain of 5.9 dBi is observed for this configuration.

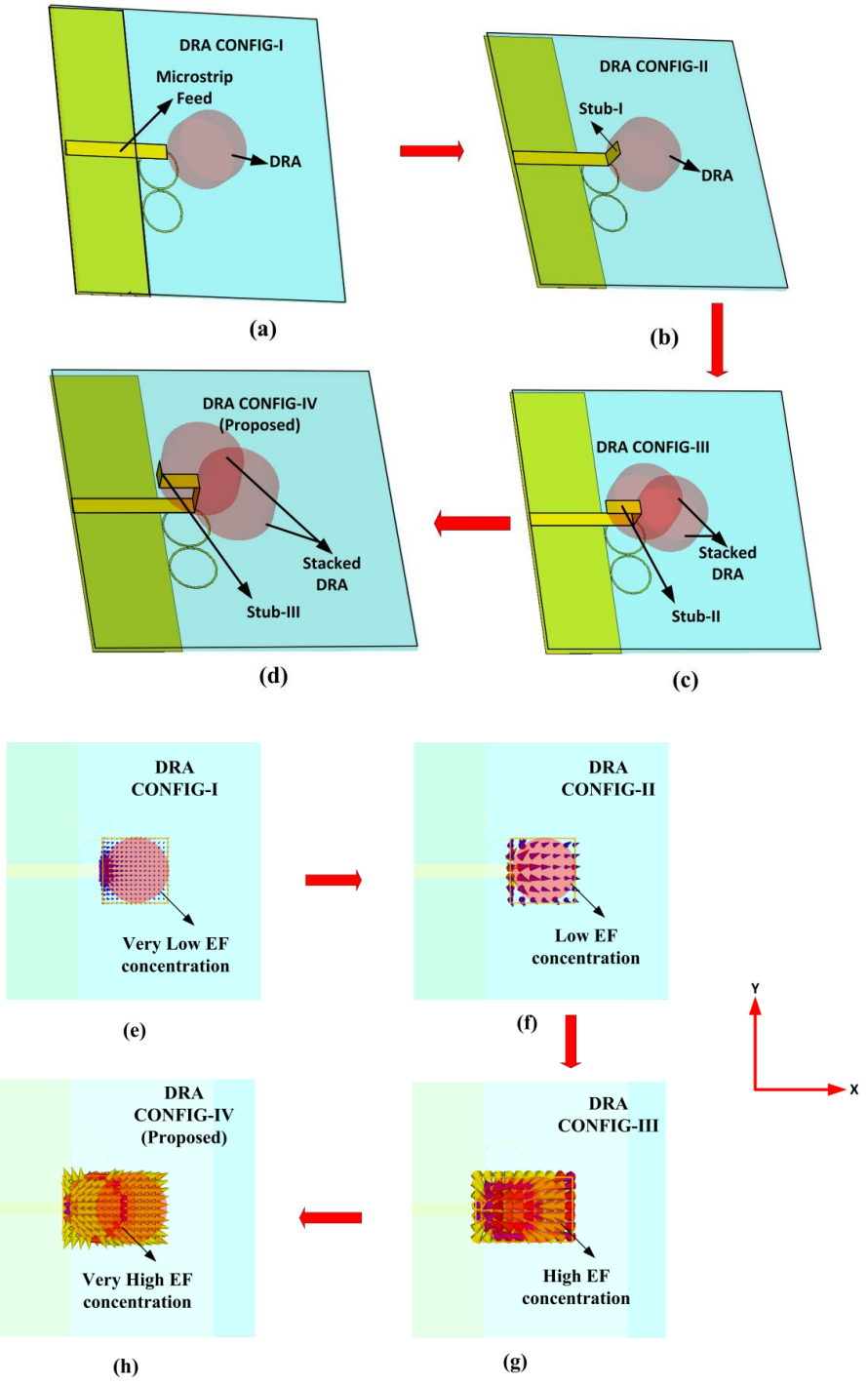

Fig. 4.2 Evolution of proposed antenna Configuration(a) Configuration-I, (b) Configuration-II, (c) Configuration-III and (d) Configuration-IV (Proposed); its Electric Field (EF) distribution on DRA (e) Configuration-I (f) Configuration-II(g) Configuration-III and (h) Configuration-IV (Proposed).

4.3.3 DRA configuration – III

To enhance the impedance bandwidth and to obtain the matching, another CDRA is stacked on top of the first DR, as depicted in Fig. 4.2(c). To get better impedance matching, stub-II is added to the existing microstrip feed, as depicted in Fig. 4.2(c). This configuration is named DRA configuration-III. The concentration of EF for this configuration is depicted in Fig. 4.2(g). It can be observed that the concentration of EF is high with the addition of stub-II. Hence, from the plot of frequency response as depicted in Fig. 4.3(a) that the addition of another DR along with the stub-II enhances the -10 dB IBW and resonates at 4.3 GHz and 7.1 GHz with impedance bandwidth (S_{11}< -10 dB) of 28.57% (3.75-5 GHz) and 22.8 % (6.2-7.8 GHz). Furthermore, the addition of stub-II to the microstrip feed and the stacking of DRs provide orthogonal modes required for CP generation. From the plot of the axial ratio, as depicted in Fig. 4.3(b), it is clear that this configuration provides CP response at two bands. The Axial Ratio Bandwidth (ARBW) for AR < 3dB at two bands are 9.67 % (4.23-4.67 GHz) and 3.54 % (6.96 - 7.18 GHz), respectively. From the gain plot, as shown in Fig. 4.3(c), a maximum gain of 5.96 dBi is observed for this configuration.

4.3.4 DRA configuration – IV (Proposed antenna)

To further enhance the IBW and ARBW, stub-III is added to the existing microstrip feed of DRA configuration-III, as shown in Fig. 4.2(d). This proposed configuration is named DRA configuration - IV. The concentration of EF for this configuration is depicted in Fig. 4.2(h). It can be observed that the concentration of EF is very high with the addition of stub-II.

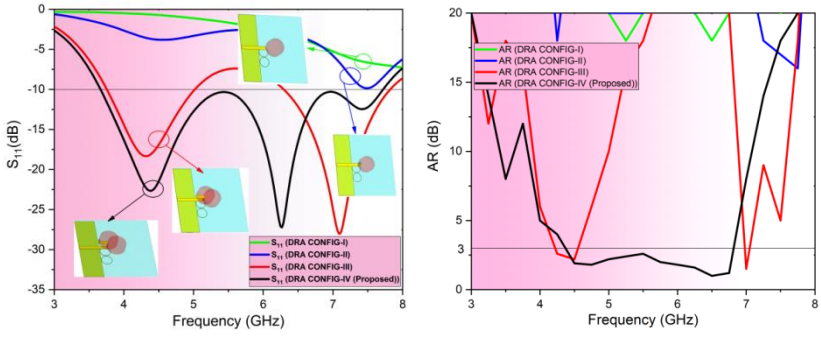

(a) (b)

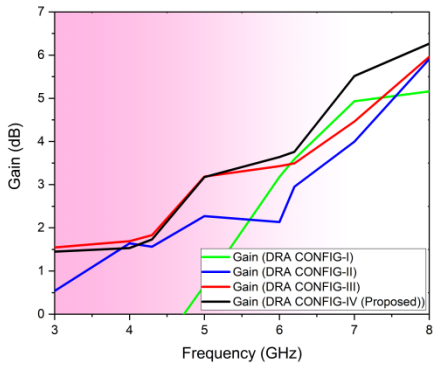

(c)

Fig. 4.3 Plot of (a) Frequency response, (b) AR response, and (c) Gain for different DRA configurations.

This addition of stub-III conformal strip makes the microstrip feed a stepped conformal strip and provides adequate path difference to generate CP waves. This proposed microstrip feed configuration enhances impedance bandwidth and AR bandwidth, as depicted in Fig. 4.3(b). This is because it gives a suitable path difference to obtain the 90^0 phase difference between the two linearly polarized signals, according to equation 4.4. Therefore, the proposed antenna produces ultra-wideband response with IBW (S_{11}< -10 dB) of 72.48 % (3.65 - 7.8 GHz) and ARBW (AR < 3 dB) of 44.12 % (4.38 - 6.86 GHz), respectively. From the gain plot, as shown in Fig. 4.3(c), a maximum gain of 6.27 dBi is observed for this configuration. From this, it is clear that the proposed antenna configuration exhibits enhanced gain compared to the other configurations. This DRA configuration stepped microstrip feed structure and modified partial ground make the antenna novel and suitable for C- band and military satellite communication applications.

$$\text{Phase difference} = \frac{2\pi}{\lambda} \times \text{Path difference} \quad (4.4)$$

4.4 Effect of Ground plane

Fig. 4.4 shows the evolution of the proposed ground plane configuration by keeping DRs stacked together and with the proposed microstrip feed (Fig. 4.2(d)). Fig. 4.5 depicts their respective frequency response, axial ratio response, and gain plots. This evolution of the ground plane shows the impact of the ground plane on the enhancement of IBW and ARBW.

4.4.1 Full Ground plane

Fig. 4.4(a) shows a full ground plane with dimensions of Lg × Wg with the proposed stacked DR configuration and the proposed microstrip feed. Its frequency response and axial ratio response plots are depicted in Fig. 4.5. As depicted in Fig. 4.5(a), this configuration suffers an impedance mismatch and does not show -10 dB impedance bandwidth. This may be because the fields are tightly bounded between the stacked DRs, feed, and the ground plane. Because of this full ground plane configuration, the antenna will not generate orthogonal modes and does not show 3dB AR bandwidth. From the gain plot as shown in Fig. 4.5(c), a maximum gain of 2.4 dBi is observed for this configuration.

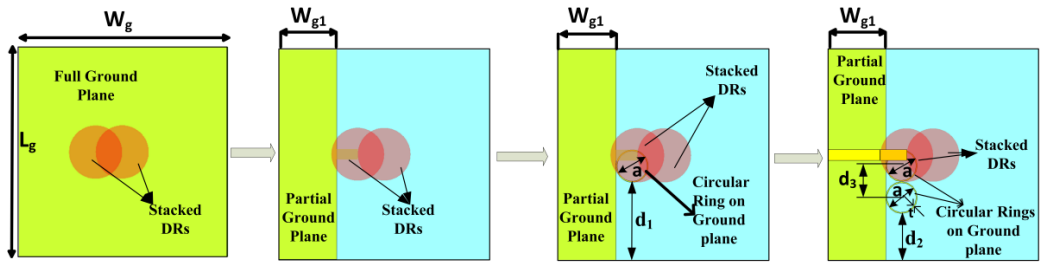

(a) (b) (c) (d)

Fig. 4.4 Ground plane configuration (a) Full Ground Plane (b) Partial Ground Plane (c) Partial Ground Plane with one circular ring and (d) Partial Ground Plane with two circular rings (Proposed) (L_g = 40, W_g = 40, W_{g1} = 11, d_1 = 22, d_3= 5.6, d_2 = 9.2, t = 0.2 and a = 5.6 mm).

4.4.2 Partial Ground Plane

In this configuration, the ground plane is modeled as a partial ground plane having a width of W_{g1} to get improved impedance bandwidth and axial ratio bandwidth. It can be seen from the plot of frequency response depicted in Fig. 4.5(a) a good impedance match is observed, and the antenna radiates in two bands centered at frequencies of 5.5 and 7.3 GHz. Furthermore, this configuration supports the formation of orthogonal fields required for CP generation. The axial ratio plot (Fig. 4.5(b)) shows that this configuration exhibits CP behavior at 5.56 GHz. This is because the partial ground plane is optimum enough to couple to the proposed DR configuration and also suitable for CP generation. From the gain plot, as shown in Fig. 4.5(c), a maximum gain of 6.1 dBi is observed for this configuration.

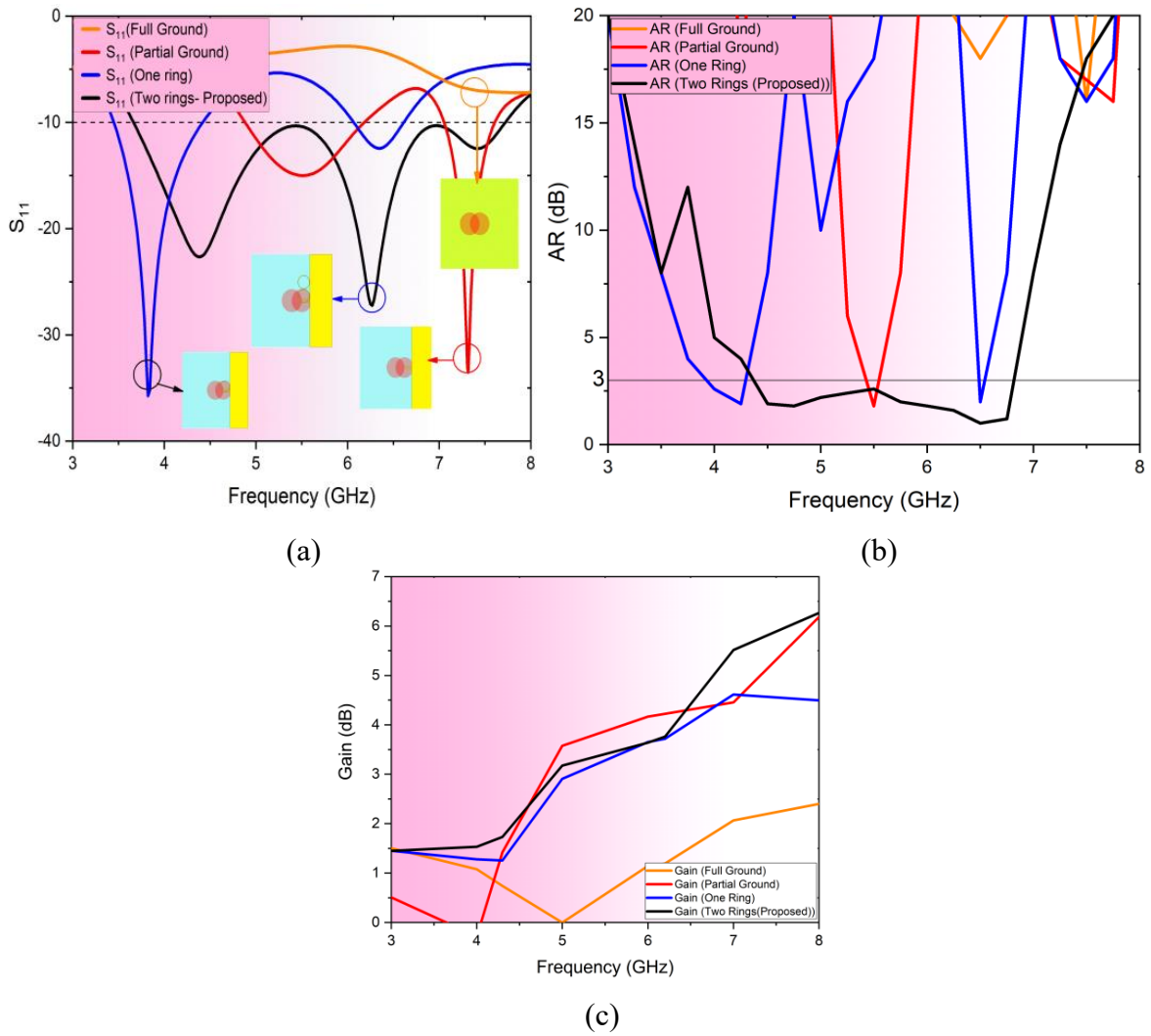

Fig. 4.5 Plot of (a) Frequency response, (b) AR response, and (c) Gain for different ground plane configurations.

4.4.3 Partial Ground Plane with one circular ring

In this configuration, the ground plane is modeled as a partial ground plane along with one circular ring to enhance IBW and ARBW, as depicted in Fig. 4.4(c). Adding one circular ring with a thickness of t and diameter of a mm enhances the impedance bandwidth and ARBW. This configuration shows the good coupling between feed and DRA. This antenna shows resonance at two bands centered at frequencies of 3.8 GHz and 6.3 GHz and AR response centered at 4GHz and 6.47 GHz, as depicted in Fig. 4.5(a and b). From the plot of the AR response, it is clear that the

addition of a circular ring enhances IBW and ARBW. From the gain plot, as shown in Fig. 4.5(c), a maximum gain of 4.5 dBi is observed for this configuration.

4.4.4 Partial Ground Plane with two circular rings (Proposed Configuration)

In this configuration, two circular rings are etched along with the partial ground plane to get enhanced bandwidth, as depicted in Fig. 4.4(d). By adding another circular ring to the existing configuration, it can be observed that strong coupling is achieved, which results in enhancement in IBW and ARBW. From the frequency response plot and AR response plot of Fig. 4.5(a and b), it is clear that this proposed configuration having a partial ground plane with two circular rings, exhibits ultra-wideband response with IBW (S_{11}< -10 dB) of 72.48 % (3.65 - 7.8 GHz) and ARBW (AR < 3 dB) of 44.12 % (4.38 - 6.86 GHz) respectively. This is because the addition of circular rings generates orthogonal fields, which are required for CP generation and enhance IBW. From the gain plot, as shown in Fig. 4.5(c), a maximum gain of 6.27 dBi is observed for this configuration. This new configuration of the ground plane to enhance IBW, ARBW, and gain make the proposed antenna unique, novel, and suitable for C- band and military satellite communication applications.

4.5 Arrangement of DRs

In this section, the behavior of the antenna in terms of frequency response and axial ratio response is investigated by changing the position of the top CDRA. Five different configurations, namely Ant-I to Ant-V, are investigated as depicted in Fig. 4.6, and their respective frequency response, axial ratio response, and gain are depicted in Fig. 4.7.

4.5.1 Ant- I configuration

As depicted in Fig. 4.6(a), the top DR is placed precisely on top of the bottom DR. This antenna resonates at 4.18 GHz and exhibits CP response at 4 GHz. The generation of orthogonal modes at 4 GHz is due to the length of the conformal microstrip feed of length $l_{f2,}$ which provides the critical path difference required for CP generation. From the gain plot, as shown in Fig. 4.7(c), a maximum gain of 5.56 dBi is observed for this configuration.

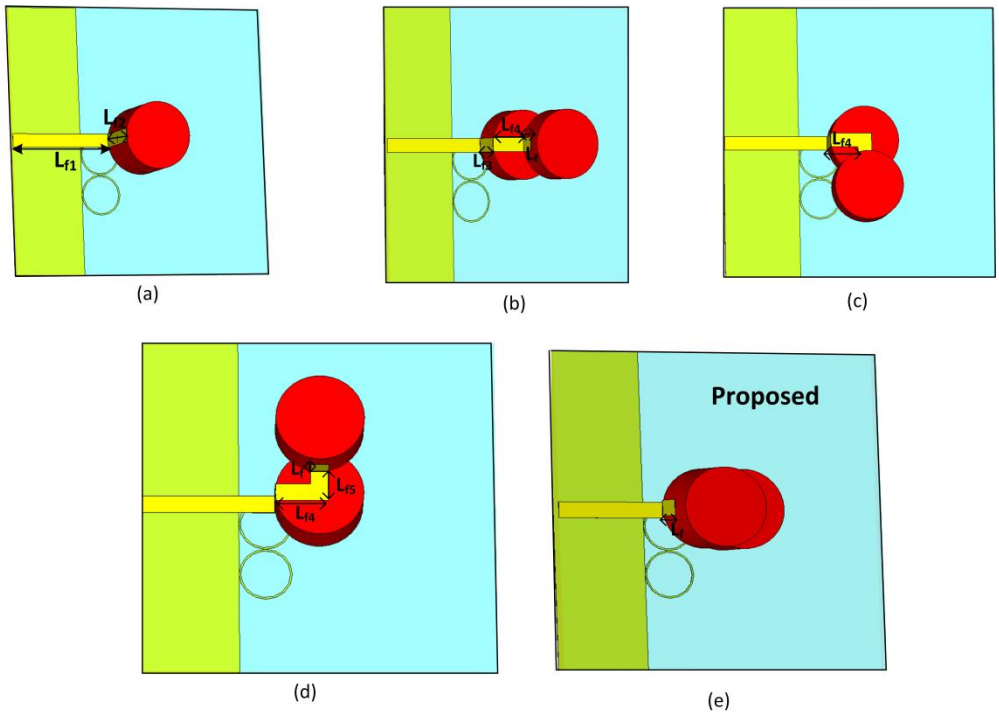

Fig. 4.6 Arrangement of top DR (a) Ant-I (b) Ant-II (c) Ant-III (d) Ant-IV and (d) Ant-V (Proposed) (L_{f1}=15, L_{f2}=8, L_{f3}=4, L_{f4}=6, L_{f5}=2.5, and L_f=2.5mm).

4.5.2 Ant- II configuration

When the position top CDRA is placed towards the front direction with respect to the feed, the configuration is similar to step-shaped DR, as shown in Fig. 4.6(b). This configuration provides wide band response with IBW of 53.65 % (3-5.2 GHz) and ARBW of 13 % (3.6-4.1 GHz). Hence, this configuration confirms strong coupling between the antenna and the stepped microstrip feed. Furthermore, due to the stepped microstrip feed, the path difference provided by this configuration will generate circular polarization, as depicted in Fig. 4.6(b) from the plot of the axial ratio. From the gain plot, as shown in Fig. 4.7(c), a maximum gain of 5 dBi is observed for this configuration.

4.5.3 Ant- III configuration

When the top DR is placed towards the right side with respect to the feed, as shown in Fig. 4.6(c), it exhibits a similar response to the Ant-II configuration. The IBW of 53.25 % (3.1-5.35 GHz) and ARBW of 9.47% (3.92-4.31 GHz) are observed for this configuration. It is observed that when the top DR position is changed from Ant-II to Ant-III configuration, there is a shift in frequency

response and IBW towards the right side, as exhibited in Fig. 4.7(a) and Fig. 4.7(b). It also confirms that this configuration provides the required path difference to generate orthogonal modes to achieve CP. From the gain plot, as shown in Fig. 4.7(c), a maximum gain of 6.2 dBi is observed for this configuration.

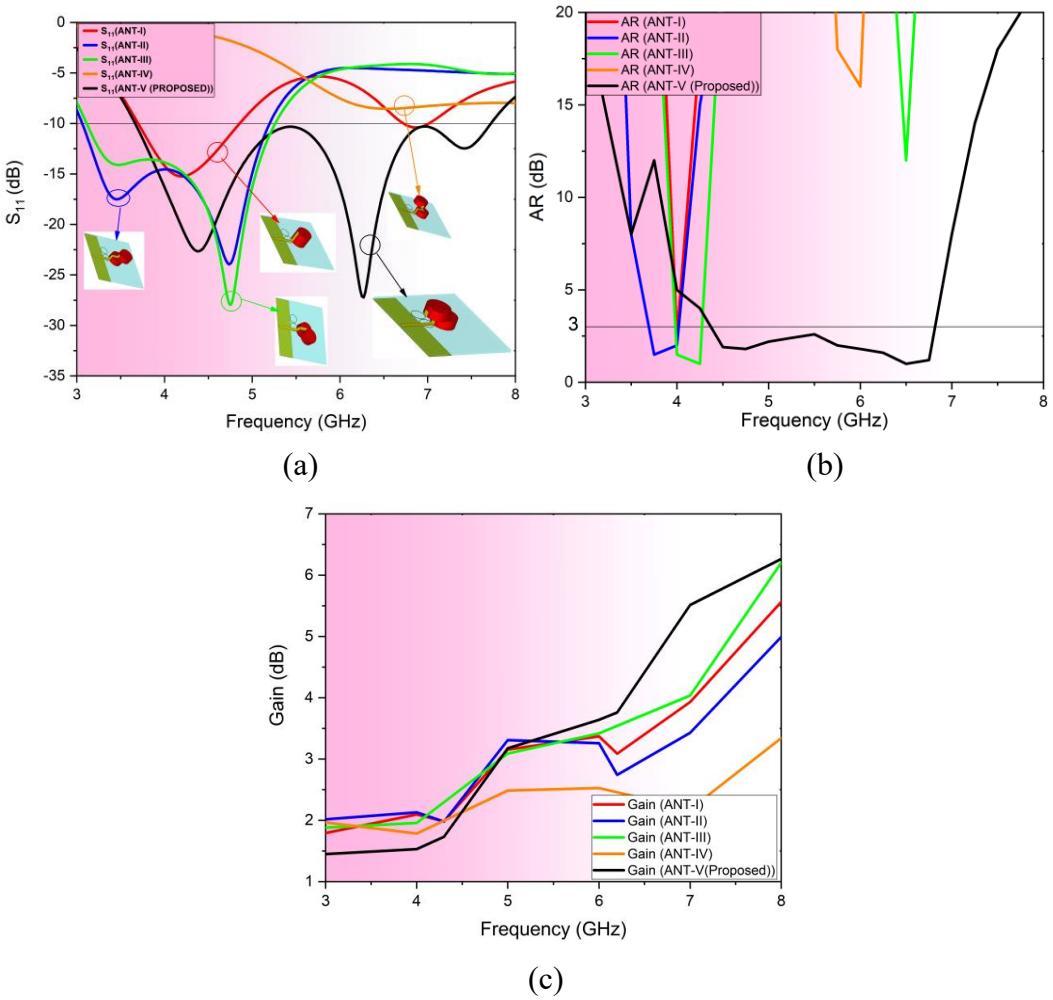

Fig. 4.7 Plot of (a) Frequency Response, (b) AR response, and (c) Gain for different DR configurations.

4.5.4 Ant- IV configuration

When the top DR is placed towards the left side with respect to the feed, as shown in Fig. 4.6(d), it suffers an impedance mismatch and does not show -10 dB impedance bandwidth. It may be because the microstrip feed is not perfectly coupled to the antenna, hence not providing any pass band in the required frequency band. It is observed that this antenna provides resonance greater

than 8 GHz but not in the operating band. This antenna does not generate orthogonal modes required for CP generation and hence does not show a 3 dB axial ratio. Frequency response and axial ratio response plots are depicted in Fig. 4.7(a) and Fig. 4.7(b). From the gain plot, as shown in Fig. 4.7(c), a maximum gain of 3.34 dBi is observed for this configuration.

4.5.5 Ant- V configuration (Proposed)

When the top DR is placed as depicted in Fig. 4.6(e), this configuration provides an ultra-wideband impedance response as well as a wide axial ratio response. This proposed antenna configuration provides a strong coupling between DRs, feed, and the ground plane. The stepped feed configuration also provides the orthogonal modes required for the generation of CP. This configuration exhibits ultra-wideband response with IBW (S_{11}< -10 dB) of 72.48 % (3.65 - 7.8 GHz) and ARBW (AR < 3 dB) of 44.12 % (4.38 - 6.86 GHz), respectively, as depicted in Fig. 4.7(a) and Fig. 4.7(b). From the gain plot, as shown in Fig. 4.7(c), a maximum gain of 6.27 dBi is observed for this configuration. This novel DRs Arrangement, stepped microstrip feed, and new ground plane configuration make the proposed antenna unique and suitable for C- band and military satellite communication applications.

4.6 Effect of DR Heights

In this section, the behavior of the antenna in terms of frequency response and axial ratio response is investigated by changing the height of CDRA by keeping the proposed ground plane and feed heights unchanged.

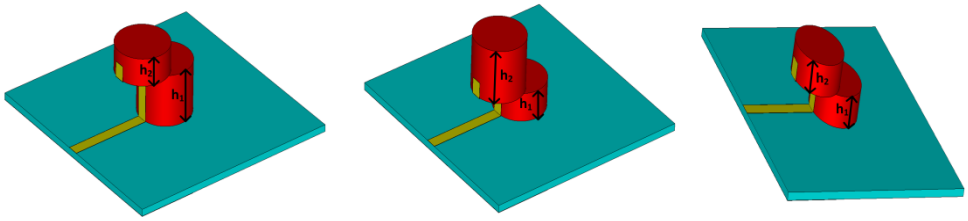

(a) (b) (c)

Fig. 4.8 Configuration of Heights of DRs: (a) h_1>h_2, (b) h_2>h_1, and (c) h_1=h_2.

Three configurations are investigated by considering the heights of DRs as h_1 (Height of bottom DR) and h_2 (Height of Top DR). These configurations are named: (i) h_1>h_2, (ii) h_2>h_1, and (iii)

h_1=h_2 as depicted in Fig. 4.8. Their respective frequency response, axial ratio response, and gain is depicted in Fig. 4.9.

4.6.1 h_1>h_2

In this case, the bottom DR height (h_1) is considered greater than the top DR height (h_2), as depicted in Fig. 4.8(a). The heights of DR considered in this case are h_1=7.5mm and h_2=4 mm. The antenna shows good impedance and axial ratio response, as shown in Fig. 4.9. This configuration resonates at three bands at frequencies of 3.2, 5, and 7.16 GHz, as depicted in Fig. 4.9(a) and provides a 3 dB AR response at 7.23 GHz as depicted in Fig. 4.9(b). CP waves are formed due to the generation of orthogonal modes provided by the microstrip feed. From the gain plot, as shown in Fig. 4.9(c), a maximum gain of 5 dBi is observed for this configuration.

4.6.2 h_2>h_1

In this case, the top DR height (h_2) is considered greater than the bottom DR height (h_1), as depicted in Fig. 4.8(b). The heights of DR considered in this case are h_1=4mm and h_2=7.5 mm. The antenna shows the strong coupling between feed and antenna and provides wide impedance bandwidth and good axial ratio response as shown in Fig. 4.9. This configuration provides -10 dB IBW of 58.3 % (3.44-6.27 GHz) and ARBW of 14.28% (3.9-4.5 GHz) as depicted in Fig. 4.9(a) and Fig. 4.9(b) respectively. From this, when the top DR height exceeds the bottom DR height, the antenna provides good impedance matching and generates orthogonal modes required for CP generation. From the gain plot, as shown in Fig. 4.9(c), a maximum gain of 5.73 dBi is observed for this configuration.

4.6.3 h_1=h_2 (Proposed)

In this case, the top and bottom DR heights (h_1 and h_2) are made equal (h_1=h_2) as depicted in Fig. 4.8(c). The heights of DR considered in this case are h_1=4mm and h_2=4 mm. This proposed antenna configuration shows the very strong coupling between feed and antenna and provides ultra-wide impedance bandwidth and wide axial ratio response as shown in Fig. 4.9. This configuration exhibits ultra-wideband response with IBW (S_{11}< -10 dB) of 72.48 % (3.65 - 7.8 GHz) and ARBW (AR < 3 dB) of 44.12 % (4.38 - 6.86 GHz) respectively as depicted in Fig. 4.9(a) and Fig. 4.9(b).

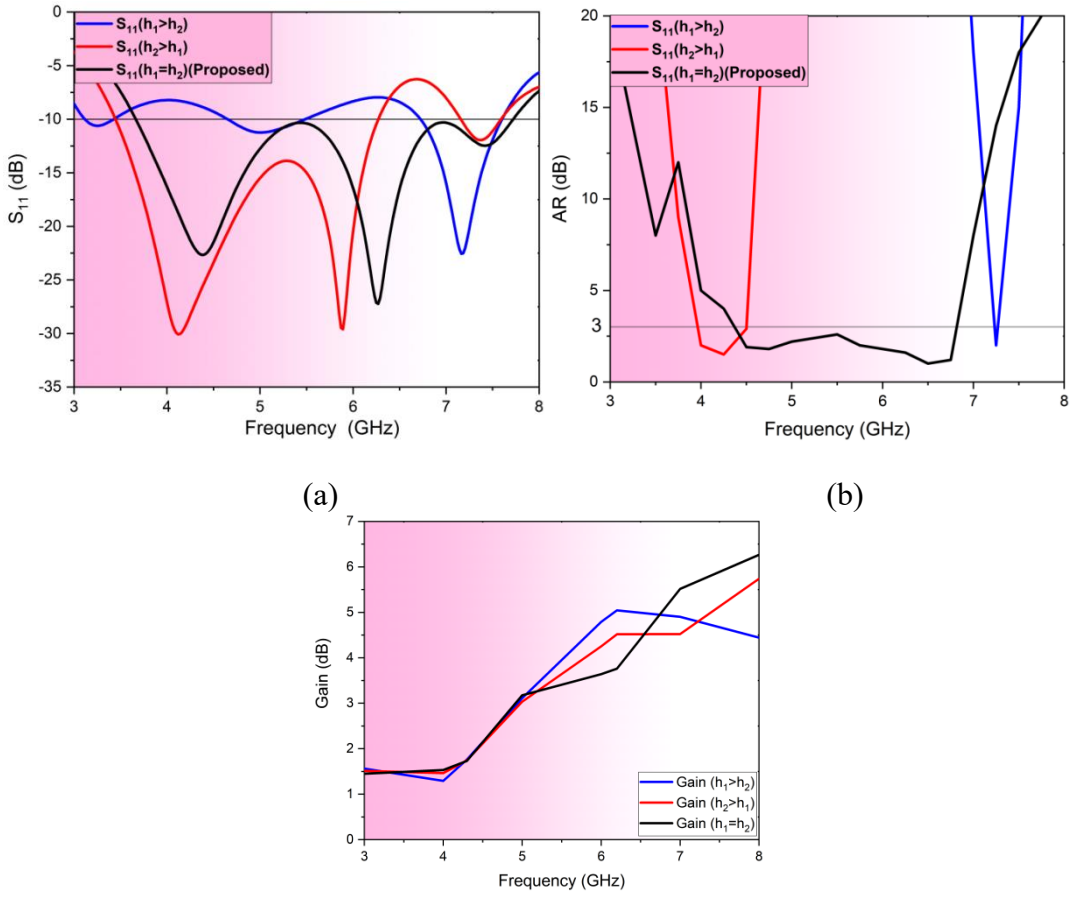

Fig. 4.9 Plot of (a) Frequency Response, (b) AR response, and (c) Gain for different heights of DR.

From the gain plot, as shown in Fig. 4.9(c), a maximum gain of 6.27 dBi is observed for this configuration. From the above, it is evident that when both DR heights are the same, then the antenna provides perfect impedance matching, generates orthogonal modes required for CP generation, and enhances gain, which is accomplished using unique DR arrangement, stepped feed configuration, and unique ground plane configuration.

4.7 Effect of Feed length

Fig. 4.10 depicts the proposed CPDRA configuration with feed length (l_f) and its frequency response and axial ratio response in Fig. 4.11 with a change in the feed length (l_f).

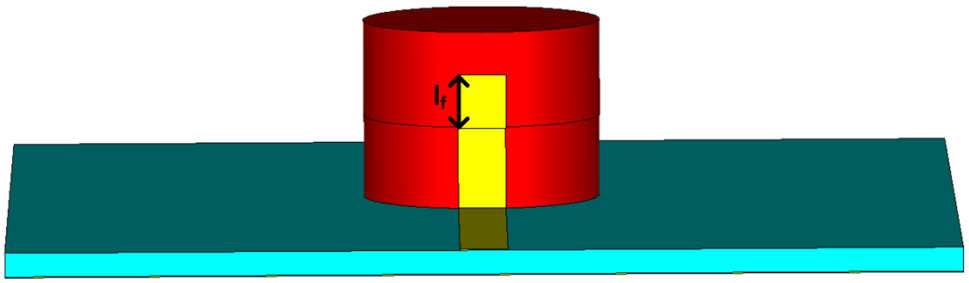

Fig. 4.10 Proposed DRA configuration.

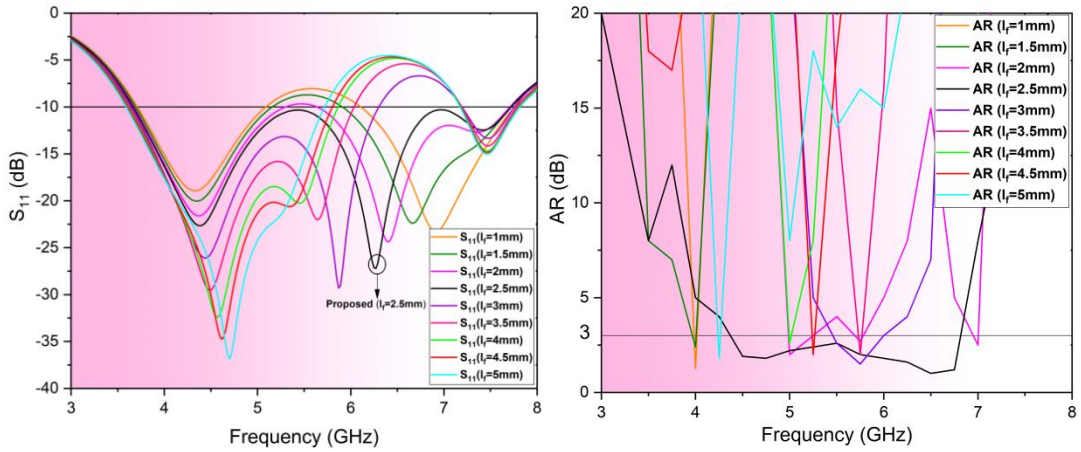

(a) (b)

Fig. 4.11 Plot of (a) Frequency Response and (b) AR response for different feed lengths (l_f).

As the l_f increases from 1mm to 2.5 mm, the IBW and ARBW increase. When the feed length is equal to 2.5mm, it provides perfect impedance matching and provides the required path difference to generate orthogonal modes required for CP generation, as depicted in Fig. 4.11(a) and Fig. 4.11(b). When the feed length is further increased (>2.5mm), the antenna shows good impedance matching but does not provide ultra-wideband response and exhibits narrow ARBW. Hence the optimum length of the feed for the generation of CP waves and to provide an ultra-wide response for the proposed configuration is 2.5mm.

4.8 Simulation and Measurement Results

4.8.1 Mechanism of CP generation

CP waves are generally excited by two orthogonal linearly polarized components with equal magnitude and with 90^0 phase difference between them [7]. To analyze CP generation inside the

proposed CPDRA, EF vector distribution at time instants of t= 0, T/4, T/2, and 3T/4 at the center frequency of 5.72 GHz is depicted as shown in Fig. 4.12. A 90^0 phase difference is observed between EF vectors in the proposed DR, as depicted in Fig. 4.12(a-d). Furthermore, the rotation of EF vectors is clockwise direction. It can be concluded that the antenna generates Left Hand CP (LHCP).

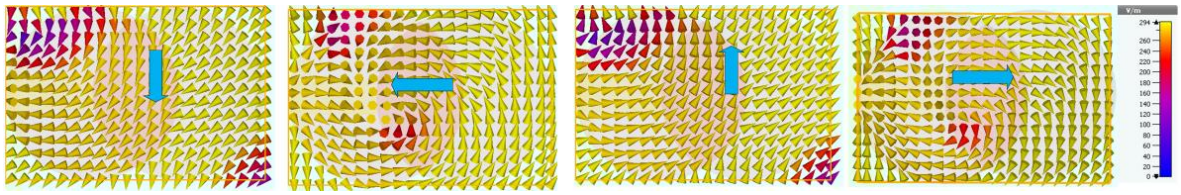

(a) (b) (c) (d)

Fig. 4.12 EF vector distribution at a center frequency of 5.72 GHz at different time instants of (a) t=0, (b) t=T/4, (c) t=T/2, and (d) t=3T/4 (T is time period).

4.8.2 EF distribution analysis

Modes in DRA are generally analyzed by EF distribution inside DR. Fig. 4.13 shows EF vector distribution at frequencies of 4.3 GHz and 6.2 GHz. It is observed that the EF distribution at 4.3 GHz is similar to that of $HEM_{11\delta}$ mode, and $TE_{01\delta}$ mode is excited at a frequency of 6.2 GHz. The fabricated antenna prototype is shown in Fig. 4.14. Two alumina dielectrics with permittivity (Ɛr) = 9.8 and a loss tangent of 0.002 of height h are stacked together to make CPDRA. The CDRA's are placed upon each other and then glued. The stacked DR is placed on the FR-4 substrate and fixed using glue. Fig. 4.14(a) shows the top view of the proposed stacked CPDRA, Fig. 4.14(b) shows a 3D view, Fig. 4.14(c) shows conformal strip feed, and Fig. 4.14(d) shows the proposed ground plane with two circular rings. The frequency response (Input Reflection coefficient) was measured using a Vector Network Analyzer, while far-field radiation measurements were conducted in an anechoic chamber.

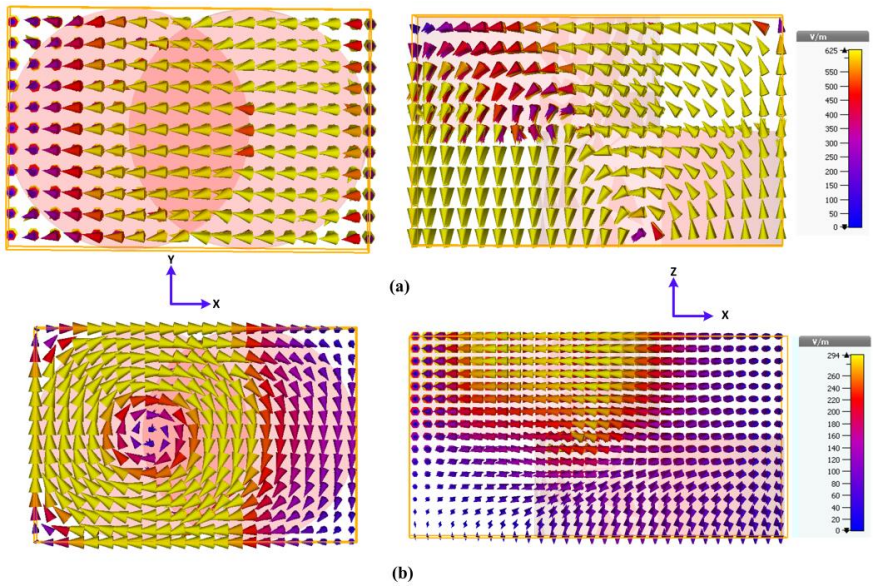

Fig. 4.13 EF vector distribution at resonant frequencies of (a) 4.3 GHz and (b) 6.2 GHz (Left side images: XY Plane; Right side images: XZ plane).

The simulated and measured frequency response (Input Reflection coefficient) and its Axial Ratio response of the proposed stacked CPDRA are depicted in Fig. 4.15. The proposed stacked CPDRA exhibits simulated ultra-wideband response with IBW (S_{11}< -10 dB) of 72.48 % (3.65 - 7.8 GHz) and ARBW (AR < 3 dB) of 44.12 % (4.38 - 6.86 GHz) respectively as depicted in Fig. 4.15(a) and Fig. 4.15(b). Whereas, the measured result shows the IBW (S_{11}< -10 dB) of 75.74 % (3.65-8.1 GHz) and ARBW of 46.24% (4.3-6.9 GHz). The proposed antenna resonates at 4.3 GHz and 6.2 GHz. Both measured and simulated are in good agreement which is suitable for C- band, and military satellite communication applications. Small differences between simulated and measured results may be due to the position of DRs and fixing them with glue and also the length of the microstrip feed.

Fig. 4.16 shows simulated and measured radiation patterns in XZ, YZ, and XY planes at resonant frequencies of 4.3 GHz and 6.3 GHz. In the boresight direction ($\theta=0^0$), it can be observed that Left Hand CP (LHCP) fields are dominating Right Hand CP (RHCP). From Fig. 4.16(a) in the XZ plane, the simulated and measured results show a difference of more than -25dB for both LHCP and RHCP fields respectively at 4.3 GHz.

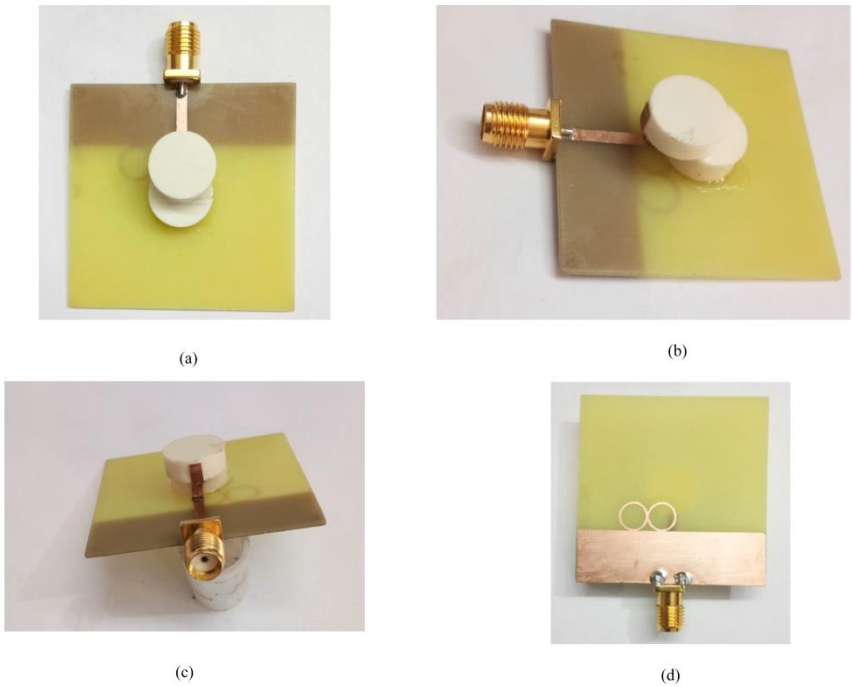

Fig. 4.14 Fabricated antenna prototype (a) Proposed stacked CPDRA, (b) 3D view of proposed CPDRA, (c) Stepped Conformal Feed view, and (d) Partial Ground plane with two circular rings.

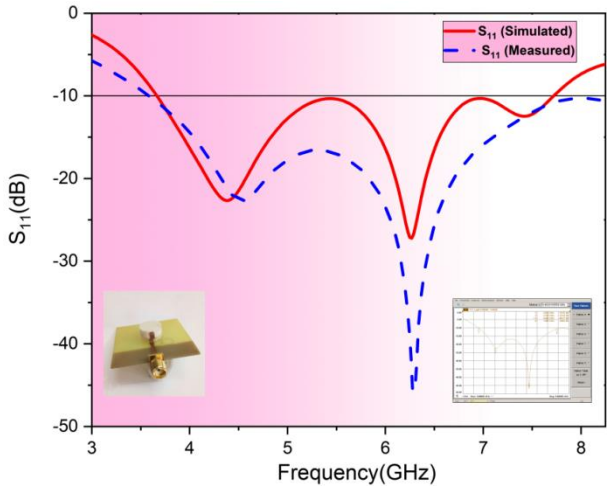

(a)

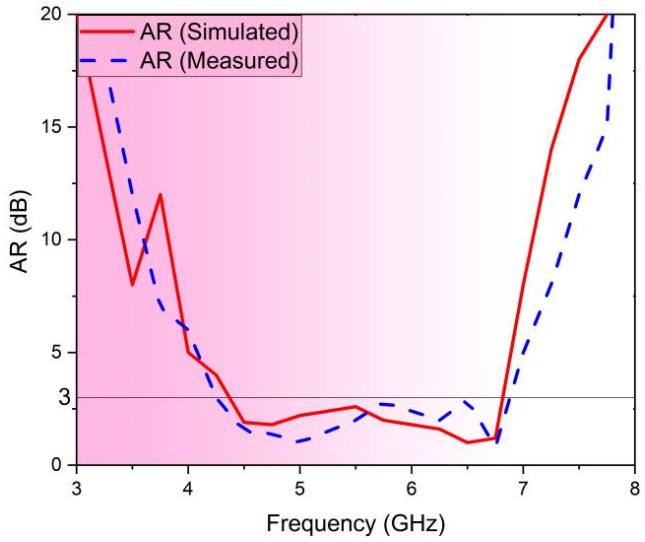

(b)

Fig. 4.15 Plot of simulated and measurement results of proposed stacked CPDRA: (a) Frequency Response and (b) AR response.

This means LHCP fields are dominating RHCP fields. Fig. 4.16(b) shows LHCP and RHCP radiation patterns at 4.3 GHz in the YZ plane. From the figure, it is clear that LHCP fields are dominating RHCP fields by more than -25dB at 4.3 GHz in the YZ plane. Similarly, Fig. 4.16(c) shows LHCP and RHCP radiation patterns at 4.3 GHz in the XY plane. From Fig. 4.16, it is clear that LHCP fields are dominating RHCP fields by more than -25dB at 4.3 GHz in the XY plane. Similarly, in Fig. 4.16(d), Fig. 4.16(e), and Fig. 4.16(f) it can be observed that at a frequency of 6.2GHz, LHCP fields are dominating RHCP fields by more than -25dB in XZ, YZ, and XY planes respectively. The proposed antenna generates dominant LHCP waves in a boresight direction at both resonant frequencies. Fig. 4.17 shows 3-dimensional radiation patterns in the XZ plane at resonant frequencies of 4.3 GHz, 6.2 GHz, and 7.4 GHz respectively. From the radiation plot, we can observe that a partial omnidirectional pattern is exhibited by the proposed antenna.

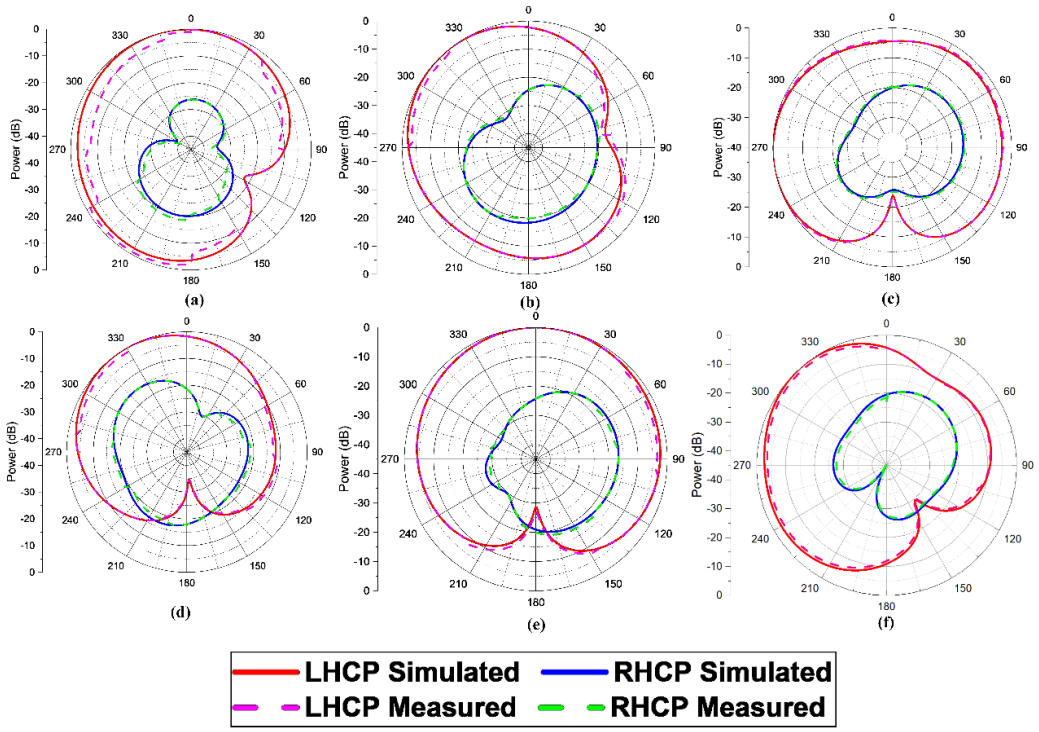

Fig. 4.16 Simulated and measured radiation plots (Normalized) at a frequency of (a) 4.3 GHz (XZ - Plane), (b) 4.3 GHz (YZ - Plane), (c) 4.3 GHz (XY – plane) (d) 6.2 GHz (XZ - Plane) and (e) 6.2 GHz (YZ - Plane), (f) 6.2 GHz (XY - Plane).

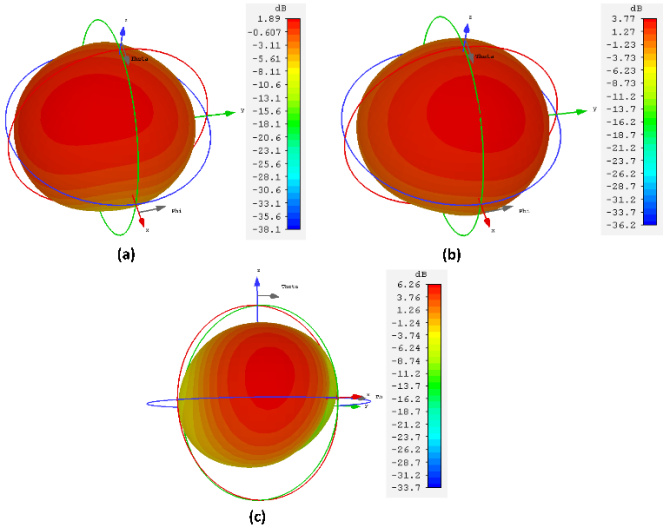

Fig. 4.17 3-dimensional radiation pattern for the proposed antenna at (a) 4.3GHz, (b) 6.2 GHz, and 7.4 GHz.

It is observed from the simulation results that if the circular rings on the ground plane are placed towards the left side of the microstrip feed as depicted in Fig. 4.18(a) and Fig. 4.18(b), then the antenna provides dominant RHCP radiation at both the resonant frequencies in the boresight direction. Hence, polarization reconfigurability is achievable by using this simple technique which is useful for wireless systems. The simulated and measured CP gain and radiation efficiency for a proposed antenna in the boresight direction are depicted in Fig. 4.18. From Fig. 4.19 the simulated CP gain varies from 1.5 to 6.27 dBic, whereas the measured gain varies from 1.4 to 6.5 dBic in the boresight direction respectively in the entire pass band. The radiation efficiency plot is also incorporated in Fig. 4.19. It can be observed that a maximum efficiency of 93.3% and average radiation efficiency of 90.82% is achieved for the proposed stacked CPDRA in the boresight direction in the operating pass band. Table 4.1 shows a comparison of the proposed stacked CPDRA with other published works. It is observed that the proposed antenna shows better performance in terms of IBW, ARBW, efficiency, and gain.

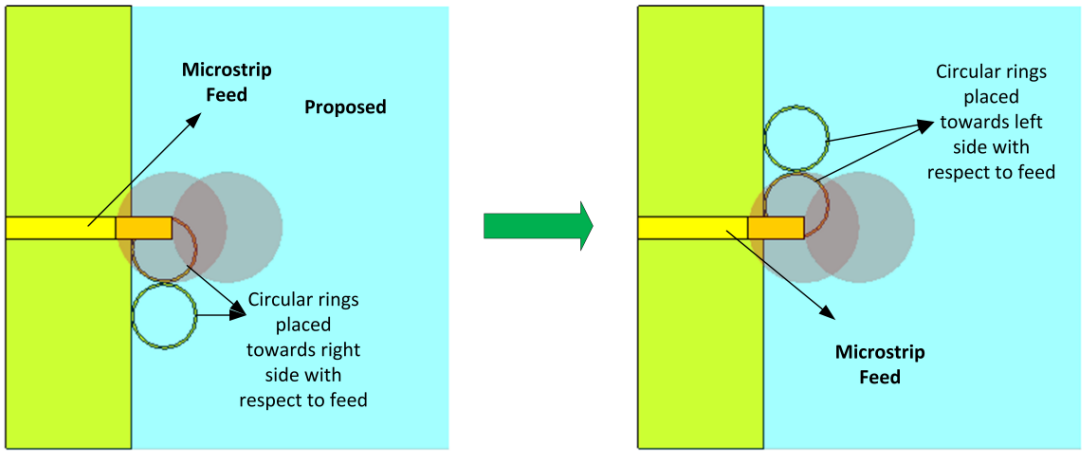

(a) (b)

Fig. 4.18 With respect to microstrip feed Circular rings in the ground plane are placed towards (a) the Right side (Proposed) and (b) the Left side.

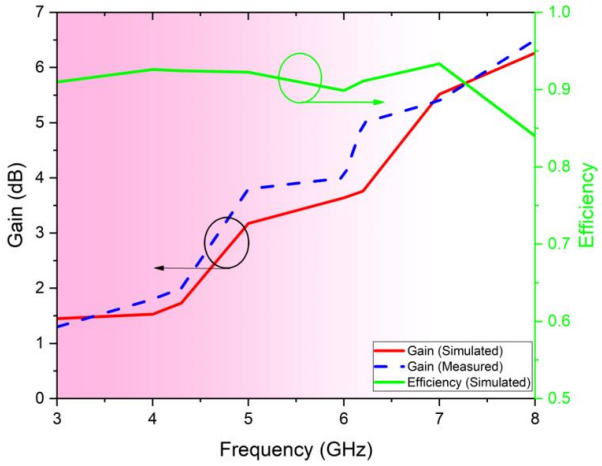

Fig. 4.19 The plot of Gain (dBi) and Efficiency (Green) of proposed Stacked CPDRA.

Table 4.1 Comparison of proposed work with other CPDRAs

Ref	**DR shape**	**Feed method**	**Center Frequency (GHz) (f_o)**	**ε_r**	**% of IBW**	**% of ARBW**	**Gain (dBic)**	**Efficiency (%)**
[133]	Notched Cylindrical DRA	Arc shaped slots (MSP)	5.3	9.8	26.25	15.28	4.3	-
[134]	Cubic shaped DR	Question mark shaped MSP	3.25	9.8	35.35	20.62	1.51	90.65
[135]	Glass DR	Spiral Slot (MSP)	2.4	6.85	8.6	6.2	0.4	80
[136]	Stacked Rectangular DRA	Conformal MSP	2.34	9.8	54.84	11.53	5.9	89.48
[137]	Stacked DRA	Aperture coupled (MSP)	2.7	12.8	25.52	26.97	6-7.37	92.87
This work	Stacked Cylindrical DR	Conformal step shaped MSP	5.725	9.8	75.74	46.24	6.25	93.3

MSP: Microstrip Feed

4.9 Conclusion

An ultra-wideband stacked CPDRA is proposed in this chapter. A new technique is proposed with the partial ground along with two circular rings for enhancing IBW. The stepped conformal strip along with the placing of stacked DRs, produces orthogonal modes for generation CP fields and also enhances ARBW. Measurement results show that the proposed stacked Cylindrical CPDRA achieves an Impedance Bandwidth (IBW) (S_{11} < -10 dB) of 72.48% (3.65 - 7.8 GHz) and Axial Ratio Bandwidth (ARBW) (AR < 3 dB) of 44.12% (4.38 - 6.86 GHz) respectively. In addition, the proposed antenna shows dominant Left Hand CP with gain ranges from 1.4 to 6.5 dBic with a maximum radiation efficiency of 93.3%. Furthermore, by changing the position of circular rings on the ground plane, the proposed antenna provides dominant LHCP to RHCP conversion and achieves polarization reconfigurability. The proposed antenna configuration covers the frequency range of applications of C- band and military satellite communication. This fulfils the requirement of objective three.

Chapter 5

Graphene-based Multiband Absorber for Terahertz Applications

5.1 Introduction

In this chapter, a multiband graphene-based absorber is designed for THz applications using different geometric shapes. Multiband response is generally achieved by combining different geometric structures [138]. Developing multiband MMAs with high absorption and with high rates is a challenge for researchers.

In [139], using U shaped slot, six band THz absorber is designed with peak average absorption of 97.3% using a multipolar plasmon structure. In [140], dual band tunable graphene based THz absorber is designed owing to polarization insensitive property and also tolerance of wide angle of incidence. In [141], a multi-band absorber designed with metal ring resonators is developed ranging from 0.1 to 1 THz. This design will provide absorption at five bands with an incidence angle tolerance of up to 60^0. In [142], triple-band and five-band MMA is designed at THz frequency using a sandwich structure with the concept of resonance behavior of metallic resonator. In [143], a graphite-based absorber for multiband absorption is developed. This structure will provide a metal-free absorber structure and is polarization insensitive and operates with a wide incident angle.

5.2 Modelling of proposed absorber

In this section, the design modelling of the proposed graphene Absorber is discussed. Here two absorber structures, namely Model I and Model II are developed and designed. Fig. 5.1(a) and Fig. 5.1(b) shows the geometry of a multiband graphene-based absorber. The polyimide substrate is sandwiched between two graphene layers. This whole structure is placed on a graphene sheet. The thickness of the graphene layer is chosen such that it remains more than skin depth for complete reflection of the incident wave. A frequency domain solver with a mesh cell size of 100 cells per wavelength and a total number of tetrahedrons of 1, 62,253 is utilized for simulation. Each form has its coupling effect based on its shape and electromagnetic qualities, such as edge coupling in a circular shape, broadside coupling in a rectangular shape or square shape, and so on. The dimensions of Model I are shown in Fig. 5.1(a) and values are shown in Table 5.1. The second absorber, Model II (Fig. 5.1(b)) consisting of a circular ring, triangular, square, pentagon, and Hexagon shapes with no contact with each absorber is modeled. The dimensions are shown in Fig. 5.1(b) and values are given in Table 5.1.

Table 5.1 Optimized parameters (all dimensions are in μm)

rin	**rout**	**R1**	**R2**	**R3**	**R4**	**Ln1**	**L**	**W**
21	23	25	30	35	40	40	80	80
Wn	**Ln**	**Ro**	**Ln2**	**Ln3**	**Ln4**	**Ln5**	**Ln6**	**Ln7**
80	80	20	39	38	37	30	35	40
L1	**L2**	**L3**	**L4**	**Ro1**	**Ro2**	**t**	**t1**	**t_s**
43	42	41	40	22	24	2	2	18

Various configurations of absorbers are considered by combining different absorber shapes to verify which configuration will provide better absorption results. To evaluate the performance of the absorber two of the above-mentioned absorbers, model I and model II (Fig. 5.1(a), Fig. 5.1(b)) are studied individually to check the better absorber performance.

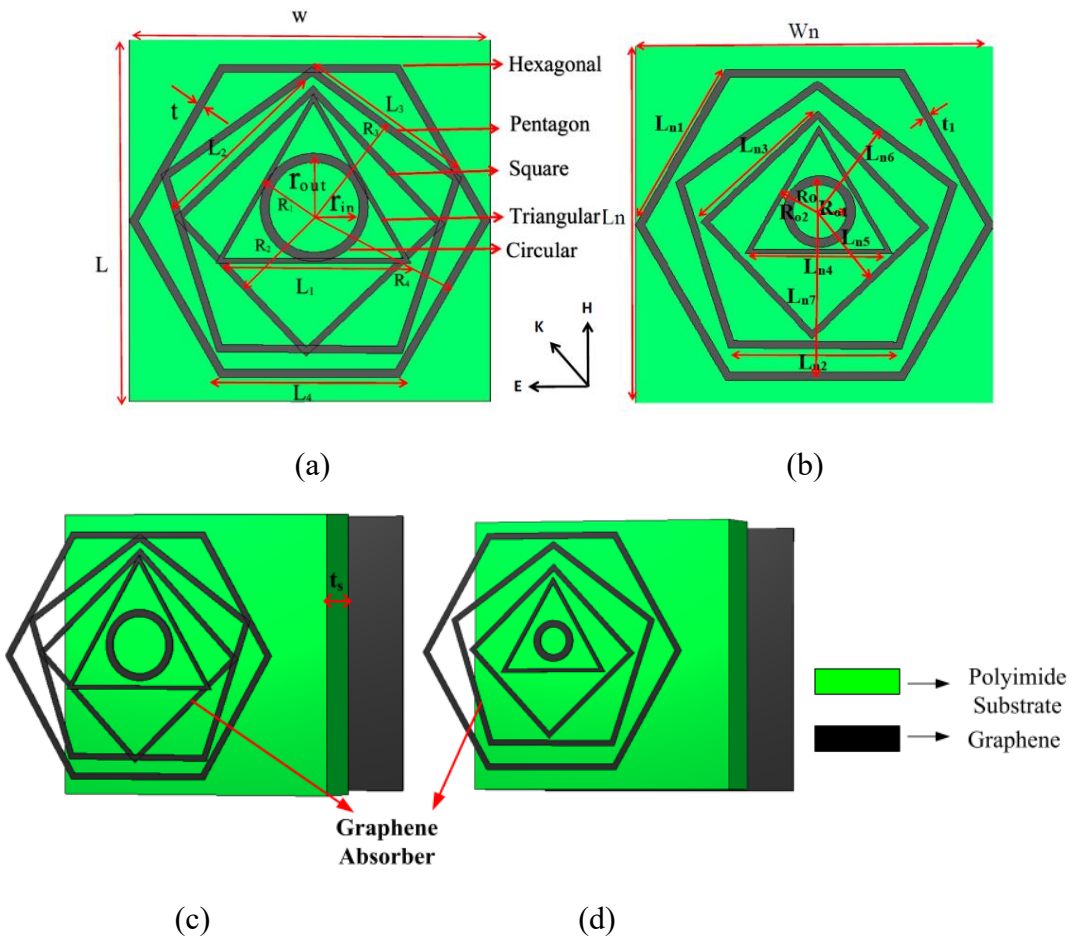

Fig. 5.1 Front view of unit cell Metamaterial Absorber (a) In contact with each other (Model I) (b) Without contact (Model II) (all the dimensions are in μm).

5.3 Design and simulation of the model I absorber

Fig. 5.1(a) shows the model I absorber along with dimensions and Fig. 5.1(c) shows exploded view of Model I, with absorbers in contact with each other. It consists of a polyimide substrate with dimensions of $W \times L \times t_s$ μm having a relative permittivity of 3.5 is placed above the graphene sheet having dimensions of $W \times L \times t_g$μm. On the top of the polyimide substrate, different shapes of absorbers are placed. A circular ring having radius r_{in} with a thickness of 2 μm is placed above the substrate. Similarly triangular ring having a radius of R_1 and length of L_1 with a thickness of 2 μm, a square ring with a radius of R_2 and length of L_2 with a thickness of 2 μm, the pentagon-shaped ring having a radius of R_3 and length of L_3 with a thickness of 2 μm and hexagonal ring

having a radius of R_4 and length of L_5 with a thickness of 2 μm respectively are placed above the polyimide substrate.

The dimensions of graphene-based absorbers are initially selected to resonate at a center frequency of 5 THz. The final dimensions were acquired by optimizing the structure using CST microwave studio after computing the initial values. The shape of the absorbers is selected based on the absorber performance of the individual absorbers.

The periodic pattern with directions of Electric (E), Magnetic (H), and Incident wave (K) of Model I and model II is shown in Fig. 5.1. In the simulation, unit cell boundary conditions were used along the x and y directions. An Electromagnetic Wave (EMW) with Electric Field (EF) polarized along the y-direction was an incident on the absorber along the z-direction.

The graphene material's electrical characteristics are chosen based on the literature [144]. Initially, the chemical potential of graphene is chosen as $\mu_c = 0.2\text{eV}$ with a relaxation time of 1 ps with thickness t=0.34 nm at temperature 300K. According to the Kubo formula [144], the surface conductivity of graphene is given by

$$\sigma(\omega, \mu_c, \Gamma, T) = \frac{je^2(w-j2\Gamma)}{\pi h^2}\left[\frac{1}{(\omega-j2\Gamma)^2}\int_0^\infty \in \left(\frac{\partial(f_d(\epsilon)}{\partial\epsilon} - \frac{\partial(f_d(-\epsilon)}{\partial\epsilon}\right)d\varepsilon - \int_0^\infty \left(\frac{f_d(-\epsilon)-f_d(\epsilon)}{(\omega-j2\Gamma)^2-4(\epsilon/h)^2}\right)d\varepsilon\right] \quad (5.1)$$

Equation 1 is the sum of intra-band and inter-band conductivity. Where e is the electron charge, h is Planck's constant, $f_d(\varepsilon) = \left(e^{(\varepsilon-\mu_c)/k_BT}+1\right)^{-1}$ is the Fermi-Dirac distribution, k_B is Boltzmann's constant. Γ is the chemical potential, ω is the radian frequency, and T=300 K.

CST Microwave studio is used to perform numerical simulations for the proposed absorber. The simulation is carried out for the TE mode case. The Absorption A for graphene-based absorber is obtained by using A=1-T-R. Where T is Transmission and R is Reflection. The transmission T is zero because the graphene metal thickness is much greater than its skin depth and the equation of absorption will be reduced to A=1-R. When Reflection R=0, the absorber is perfect (the impedance (z=1) matches with the free space impedance) and absorption is equal to 1 which means 100% absorption [six bands]. In terms of scattering parameters Reflection is given by $R=|S_{11}^2|$ and transmission T is given by $T=|S_{21}^2|$ respectively.

To achieve a multiband absorber response, initially, individual absorbers are investigated. Each form has its coupling effect based on its shape and electromagnetic qualities, such as edge coupling in a circular shape, broadside coupling in a rectangular shape, and so on. Fig. 5.2(a, b, c, d, and e) shows the absorbance spectra of individual absorbers for TE incidence along with Surface Current (SC) distributions, and Table 5.2 depicts its respective absorption performance. The individual absorbers will only provide absorption at a single frequency or dual frequency. This is because of the small dimension/perimeter of the absorber and also from surface current distribution it is clear that very weak coupling is associated with circular and triangular rings (Fig. 5.2(a) and Fig. 5.2(b) which results in weak electric and magnetic resonances. Hence does not show absorption greater than 90%. For square, pentagon, and hexagonal rings we can observe a strong coupling of surface current which results in absorption at two bands. Circular, triangular rings have smaller dimensions than square, pentagon, and hexagonal rings, and the corners generated in the square, pentagon, and hexagonal rings result in strong electric and magnetic resonances, which is why dual band performance was obtained. To achieve multi-band absorption, the combination of individual absorbers is investigated in the next section. Fig. 5.3(a, b, c, and d) shows absorption spectra for the combination of Hexagonal-pentagon (H-P), Circular-Triangle-square (C-T-S), Hexagonal-Pentagon-Circular (H-P-C) and Hexagonal-pentagon-Square shaped absorbers respectively of Model I (Absorbers in contact with each other). Table 5.3 depicts the respective number of absorption peaks above 90% and the percentage of absorption peaks.

The above configurations provide multi-band response which is mainly because of strong surface current vectors localized around the rings which in turn create strong electric and magnetic resonances and hence provide resonance at multi bands. Since it is a multiple rings structure, the resonant frequencies also depend on capacitive coupling between adjacent rings along with the dimensions of the rings. From Table 5.3 it is evident that configuration H-P-C provides resonance at five bands this is because when graphene rings in this configuration are placed apart from each other resulting in a decrease in capacitance which will increase in resonant frequencies [15]. This investigation is further extended to check the multiband behavior of graphene absorbers with various configurations of absorbers of Model I (Absorbers in contact with each other). Fig. 5.4(a) shows a plot of absorption vs frequency for Hexa-Penta-Square-Triangular (named as without circular ring-shaped absorber) absorber along with its surface current distribution and its respective absorption peaks in percentage with resonant frequency is depicted in Table 5. 4.

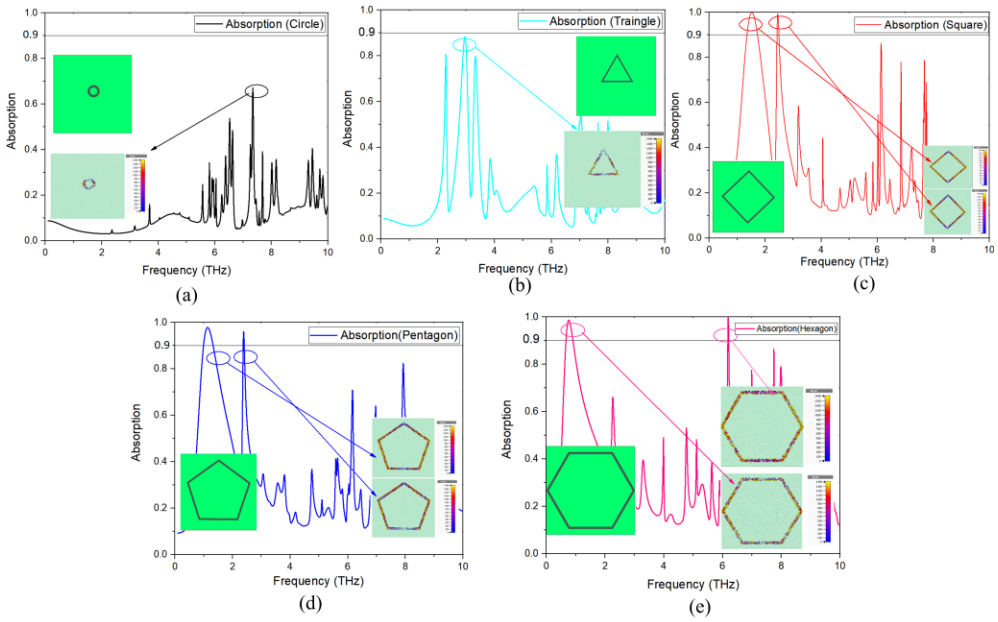

Fig. 5.2 The Plot of Absorption vs frequency for individual absorbers (a) Circular, (b) Triangular (c) Square (d) Pentagon, and (e) Hexagon along with vectored surface current distribution

Table 5.2 Absorption peaks of individual absorbers

Shape of Absorber	**Percentage of Absorption and its resonant frequency (THz)**	**Number of peaks > 90% absorption**
Circular ring	67.2 at 7.34 THz	0
Triangular ring	88.2 at 2.95 THz	0
Square ring	99.8 and 98.5 at 1.81 and 2.505 THz	2
Pentagon ring	97.8 and 98.4 at 1.24 and 2.4 THz	2
Hexagonal ring	98.5 and 99.7 at 0.75 and 6.18 THz.	2

This configuration provides resonance at five bands. This is because when graphene rings are closely placed to each other the capacitance between the rings increases which will reduce the number of resonant frequencies. From the surface current distribution, it is clear that as the percentage of absorption increases most of the energy is strongly localized on the rings which in turn creates strong electric and magnetic resonances.

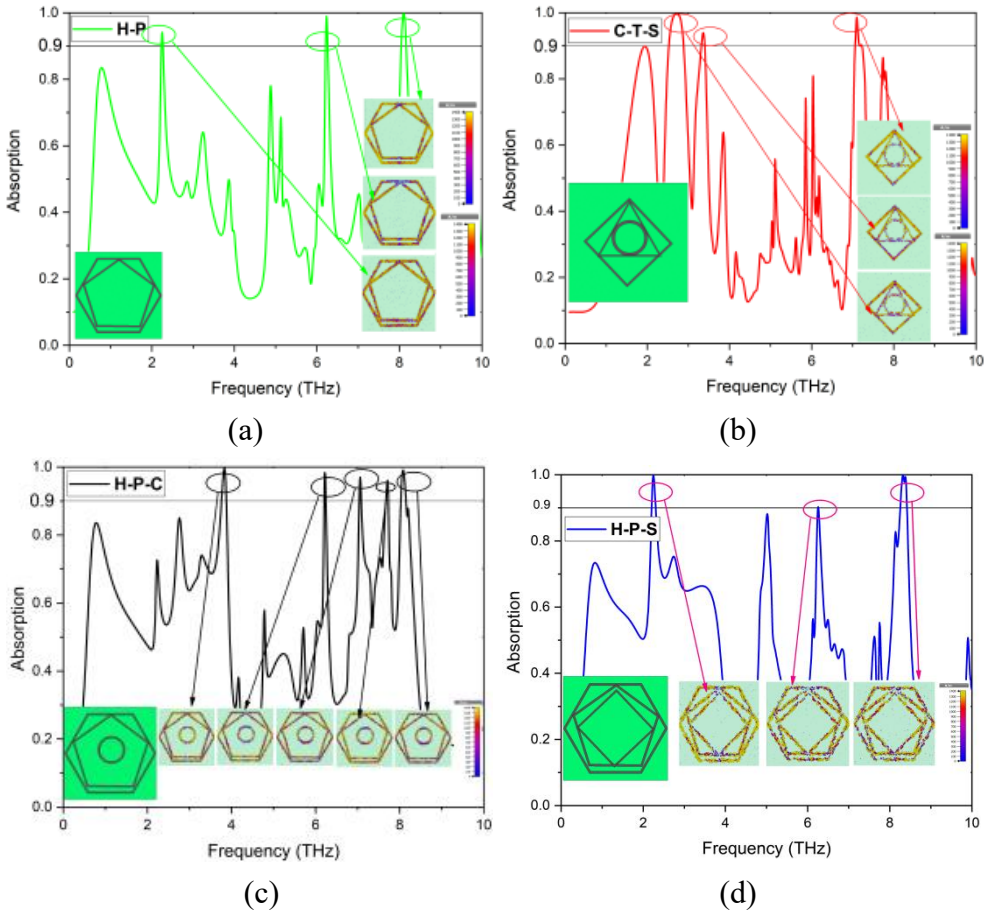

Fig. 5.3 The plot of Absorption vs Frequency for different combinations of (a) Hexa-pentagon (H-P), (b) Circle-Triangle-Square (C-T-S), (c)Hexa-Penta-Circle (H-P-C), and (d) Hexa-Penta-Square (H-P-S) along with vectored surface current distribution.

Fig. 5.4(b) shows an absorber configuration consisting of Hexa-Penta-Square-Circular (without triangular absorber). Similarly, Fig. 5.4(b, c, d, and e) shows absorber configuration without a triangular absorber (Fig. 5.4(b)), without a square-shaped absorber (Fig. 5.4(c), without pentagon-shaped absorber (Fig. 5.4(d)), without hexagonal-shaped absorber (Fig. 5.4(e)) and Fig. 5.4(f) shows absorber configuration with all shapes of absorbers connected to each (Hexa-Penta-Square-Triangular-Circular) respectively. Its respective absorption peaks in percentage along with resonant frequency are depicted in Table 5. 4. It is clear from Table 5. 4 that when graphene rings are closely placed (Ex: Fig. 5.4(e, f)), due to an increase in capacitance between the rings there is a decrease in the number of resonant frequencies. Seven peaks are observed without triangular, square, and pentagon-shaped configurations.

Table 5.3 Absorption peaks of individual absorbers

Shape of Absorber	**Percentage of Absorption and its resonant frequency (THz)**	**Number of peaks > 90% absorption**
H-P	94.2, 99.07, and 99.9 at 2.24, 6.23, and 8.09 THz	3
C-T-S	99.6, 93.9, and 98.5 at 2.71, 3.35, and 7.09 THz	3
H-P-C	99.5, 98.2, 96.5, 95.8, and 99 at 3.82, 6.21, 7.05, 7.71, and 8.07 THz.	5
H-P-S	99.8 and 90.55 and 100 at 2.24, 6.25, and 8.36 THz	3

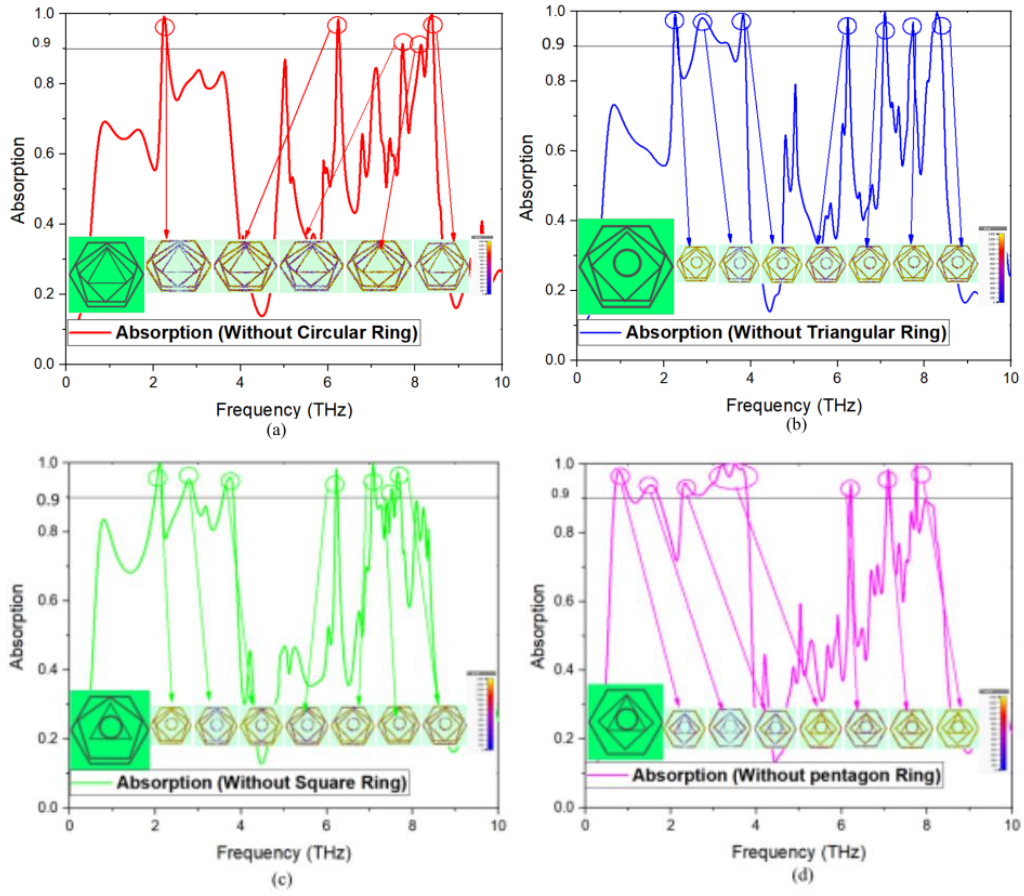

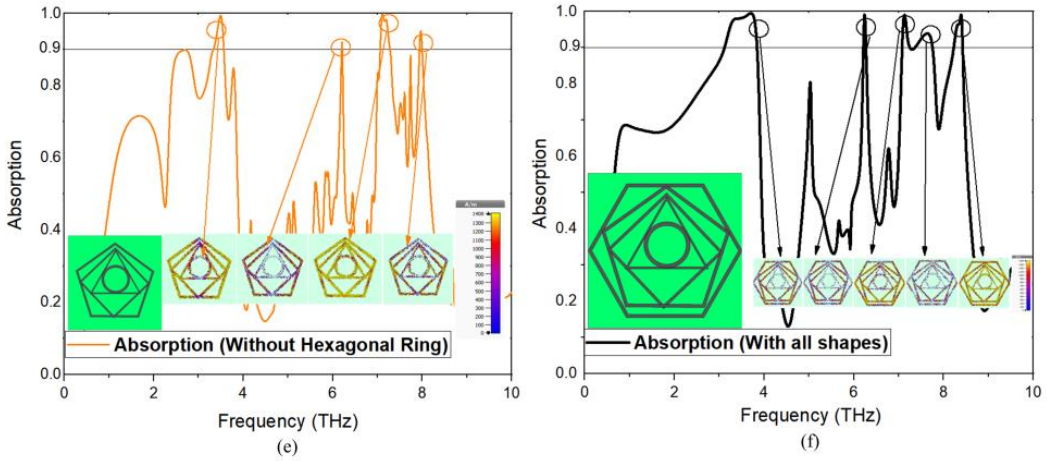

Fig. 5.4 Plot of frequency vs Absorption (A), Reflectance (R), and Transmittance (T) for absorber (a) without circular ring-shaped absorber (b) without triangular absorber, (c) without square absorber, (d) without pentagon absorber, (e) without hexagonal shaped absorber and (f) with all shapes of absorbers.

This is due to a decrease in capacitance between the rings as the rings in these configurations are separated apart.

Table 5. 4 Absorption peaks of individual absorbers

Shape of Absorber	**Percentage of Absorption and its resonant frequency (THz)**	**Number of peaks > 90% absorption**
Without Circular ring	99.3, 98.1, 91.5, 91.46, and 99.79 % at 2.23, 6.23, 7.71, 8.12, and 8.37 THz.	5
Without Triangular ring	98.4, 97.8, 99.15, 98, 99.8, 96.5, and 99.5 % at 2.25, 2.83, 3.82, 6.23, 7.09, 7.73, and 8.29 THz.	7
Without Square ring	99.7, 95.3, 95.8, 97.9, 99.8, 97, and 92.4% at 2.09, 2.78, 3.75, 6.22, 7.07, 7.5, and 7.65 THz	7
Without pentagon ring	98.1, 94.01, 94.3, 100, 93.7, 97.7, and 99.9% at 0.78, 1.53 2.32, 3.19, 6.21, 7.1, and 7.75 THz	7
Without Hexagonal ring	99.4, 91.5, 99.8, and 95%. At 3.49, 6.2, 7.1, and 7.96 THz	4
with all shapes of absorbers	99.5, 98.8, 98.9, 94, and 99% at 3.71, 6.2, 7.1, 7.65, and 8.4 THz	5

Hence there is an increase in resonant frequencies. Moreover, as the absorption increases there is a strong surface current distribution on the graphene rings is observed. Similar investigations are carried out on Model II configuration. The results of model I and model II are compared in section III from which the better performance absorber configuration will be proposed.

5.4 Design and Simulation of Model II absorber

In this section design analysis on Model II configuration is exhibited for TE mode. The dimensions of the absorber are already depicted in Fig. 5.1and Table 5.1. The results of the model I investigations and model II investigations are then compared to bring out a better performance proposed absorber configuration. Fig. 5.1(d) shows exploded view of the model II absorber with absorber shapes not in contact with each other. The modelling of the absorber is the same as model I which consists of a polyimide substrate having a relative permittivity of 3.5 and dimensions of W × L × ts μm placed above a graphene sheet having dimensions of W × L × tg μm. The investigations that are carried out on model I will be done on model II to check the absorbance performance to bring the proposed absorber that will provide high absorption with multiband behavior.

The combinations of different shapes are considered similar to model I. Fig. 5.5 shows a plot of absorption vs frequency along with surface current distributions for Hexagon-Pentagon (H-P), Circular-Triangular-Square (C-T-S), Hexagon-Pentagon-Circular (H-P-C) and Hexagon-Pentagon-Square (H-P-S) shaped absorber configuration similar to Fig. 5.3 of the model I except that the rings are not in contact with each other. Table 5.5 depicts the respective absorption percentage with its resonant frequencies. When absorber rings are close together (Fig. 5.5(a, b) they produce peaks at fewer resonant frequencies than when they are separated by a distance (Fig. 5.5(c, d)). Hence the configurations H-P and C-T-S provide resonance at three and four bands. Whereas the configurations H-P-C and H-P-S provide resonance at six bands each.

Furthermore, H-P configuration provides bandwidth percentage of 50% in the first band. Another important parameter to analyze the wide band performance is Full Width at Half Maximum (FWHM) and Fractional bandwidth (FBW). FBW is calculated by using equation (5.2).

$$\text{FBW} = \frac{FWHM}{f_c} \tag{5.2}$$

Where f_c is the center frequency corresponding to FWHM.

P configuration provides absorption in first band from 0.69-1.15 THz which means 50% bandwidth. Also the H-P-S configuration provides bandwidth percentage of 84.29% (0.7-1.73 THz) as depicted in Fig. 5.5(d).

From the above investigations it is evident that model II configurations providing better absorption peaks and more bands compared to model I. This behavior is because of individual absorber shapes without in contact with each other (Model-I) generates less capacitance effect providing better absorber performance compared to that of absorbers that are in contact with each other (Model-I). This investigation is further extended to check the multiband behavior of absorbers with various configurations of absorbers similar to what is discussed for Model I (Fig. 5.4). Fig. 5.6(a) shows the absorber configuration with Hexa-Penta-Square-Triangular shaped absorbers. This configuration is named as without circular ring-shaped absorber. Similarly, Fig. 5.6(b, c , d, e, f), shows absorber configuration without triangular shaped absorber, without square shaped absorber, pentagon-shaped absorber, hexagonal shaped absorber, with all shapes of absorbers (Hexa-Penta-Square-Triangular-Circular (Proposed)).

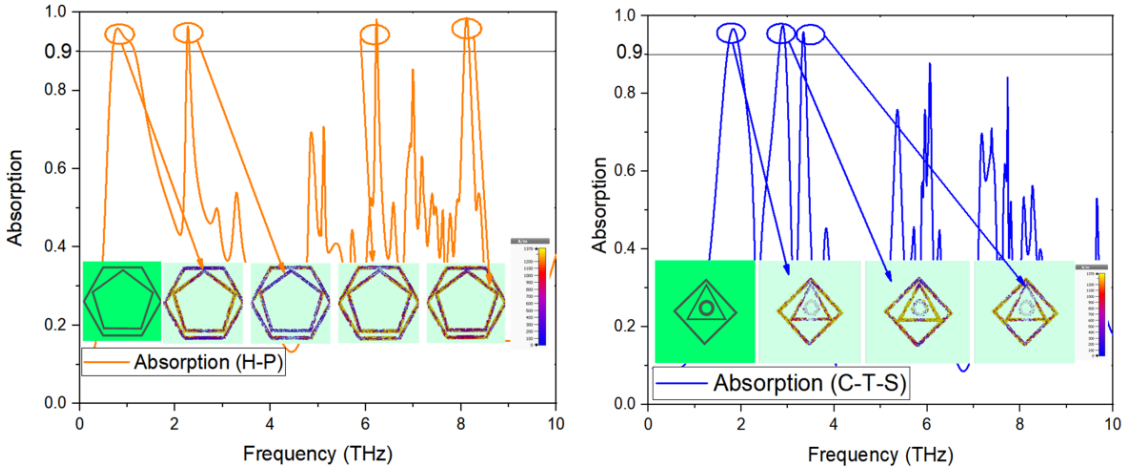

(a) (b)

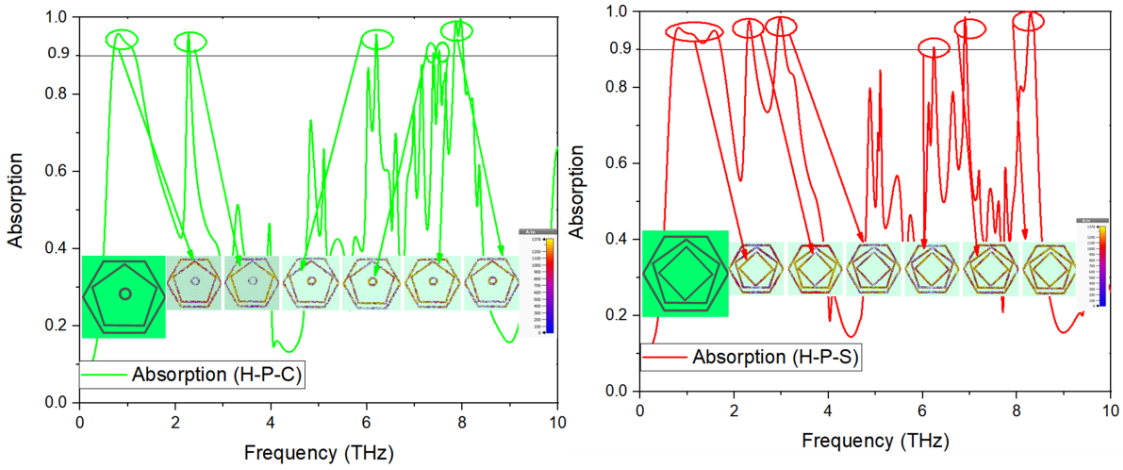

(c) (d)

Fig. 5.5 The plot of Absorption vs Frequency (Model-II) for combinations of (a) Hexa-pentagon (H-P) (b) Circle-Triangle- Square (C-T-S), (c) Hexa-Penta-Circle (H-P-C), (d) Hexa-Penta-Square (H-P-S).

Table 5.5 Absorption peaks of individual absorbers

Shape of Absorber	**Percentage of Absorption and its resonant frequency (THz)**	**Number of peaks > 90% absorption**
H-P	95.8%, 96%, 97.6%, and 98.6% at 0.78, 2.26, 6.22, and 8.11 THz	4
C-T-S	96.6, 97.2, and 95.03% at 1.82, 2.87, and 3.34 THz	3
H-P-C	95.6, 95.5, 95.2, 90.7, 91.4, and 99.3% at 0.81, 2.26, 6.19, 7.4, 7.52, and 7.8 THz	6
H-P-S	95.6, 97.7, 98.34, 92.1, 98.4, and 99.7% with 0.79, 2.31, 2.96, 6.2, 6.9, and 8.3 THz with	6

The number of resonant frequencies along with absorption percentage is depicted in comparison Table 5.6. The number of resonant frequencies for model II is greater than that of model I. This is because when the absorber rings are placed close to each other, the capacitance increases. This will reduce the resonant frequencies. The reverse effect will take place when absorber rings are placed a distance apart. In this case the capacitance between the rings decreases which increases resonant frequencies. Fig. 5.6(f) shows the proposed absorber configuration (with all ring-shaped absorbers). Surface current distribution for the proposed absorber is separately shown in Fig. 5.8.

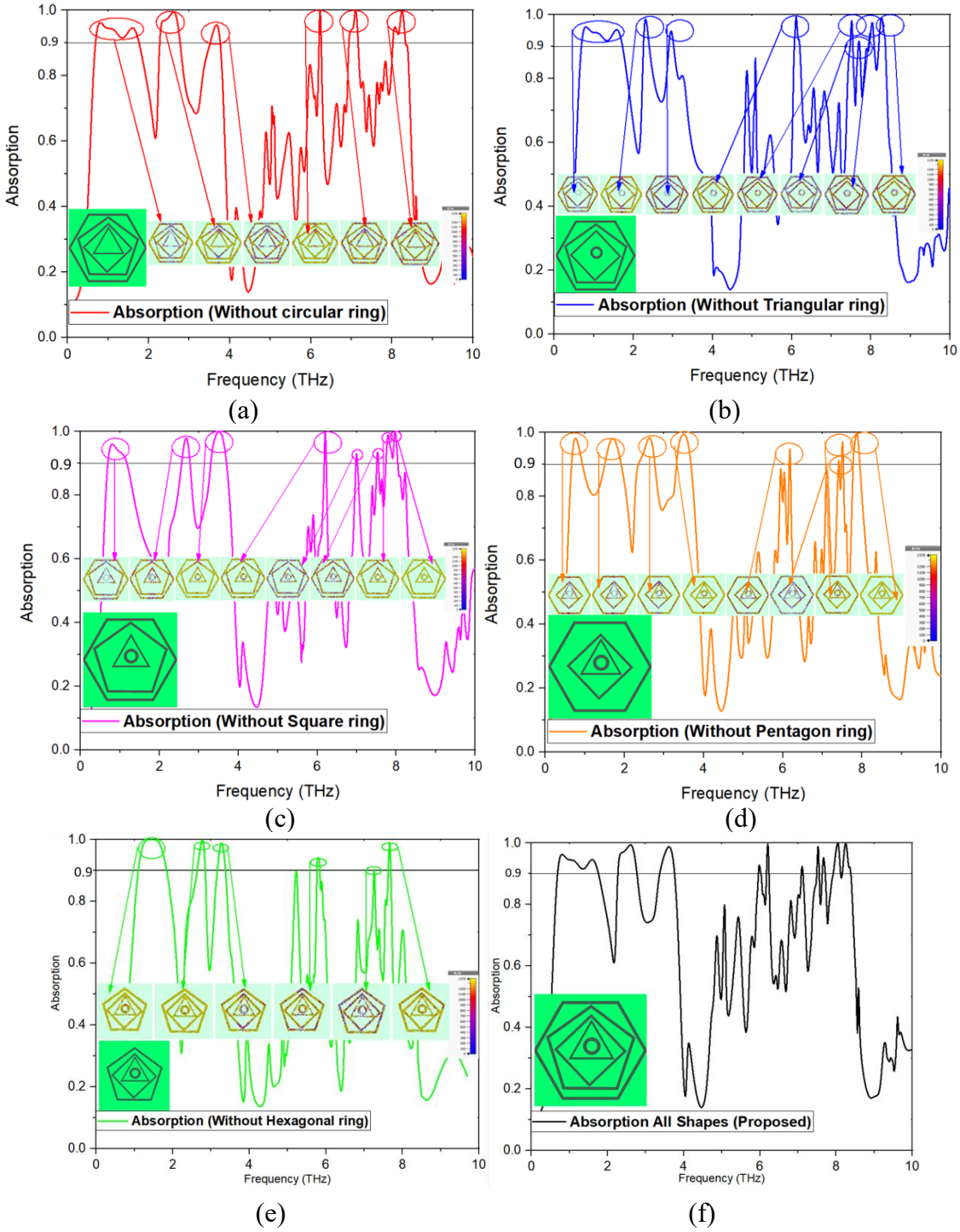

Fig. 5.6 Absorption vs frequency plot with combination of (a) Hexa-Penta-Square -Triangular (without Circle) (b) Hexa-Penta-Square-Circular (without Triangle) (c) Hexa-Penta-Triangular-Circular (without Square) (d) Hexa-Square -Triangular ((without Pentagon) (e) Penta-Square-Circular shape absorbers (without Hexagon) (f) Hexa-Penta-Square-Triangular-Circular (All shapes-Proposed absorber).

This configuration provides absorption peaks at ten resonant frequencies of 0.79, 2.6, 3.6, 5.97, 6.2, 7.1, 7.52, 7.68, 8.03 and 8.24 THz with absorption rates of 96.2%, 99.4%, 98.7%, 92.6%, 100%, 92.2%, 98.7%, 94.6%, 100% and 100% respectively. Furthermore this configuration provides a bandwidth percentage of 88.52% (0.68-1.76 THz), 20.71% (2.25-2.77 THz) and 7.12% (3.36-3.76 THz). Therefore, compared to all the configurations of model I and model II, this configuration (Fig. 5.6(f)), containing Hexagon, Pentagon, Square, triangular, circular and shaped absorbers provides absorption peaks at ten resonant frequencies and better absorber absorption rate response. This proposed configuration provides ultra ultra-widesponse at first band with absorption bandwidth percentage of 88.52. The comparison table between Model 1 and Model II is shown in Table 5.2.

Table 5.6 Comparison between Model I and Model II

Configuration	**Number of absorption peaks using Model I Configurations**	**Number of absorption peaks using Model II Configurations**
Without a Circular Ring absorber	**Five** absorption peaks at 2.23, 6.23, 7.71, 8.12, and 8.37 THz with absorption rates of 99.3%, 98.1%, 91.5%, 91.46%, and 99.79%	**Seven** absorption peaks at 0.77, 2.63, 3.66, 6.22, 7.11, 8.08, and 8.24 THz with absorption rates of 96%, 99.4%, 95.5%, 99.5%, 99.7%, 94.7%, and 99.7%
Without a Triangular Ring absorber	**Seven** absorption peaks at 2.25, 2.83, 3.82, 6.23, 7.09, 7.73, and 8.29 THz with absorption rates of 98.4%, 97.8%, 99.15, 98%, 99.8 %, 96.5 %, and 99.5 %	**Eight** absorption peaks at 0.79, 2.29, 2.95, 6.11, 7.51, 7.7, 8.04, and 8.28 THz with absorption rates of 86.17%, 98.38%, 94.8%, 99.12%, 98.11%, 91.3%, 96.9%, and 98.8%
Without a Square Ring absorber	**Seven** absorption peaks at 2.09, 2.78, 3.75, 6.22, 7.07, 7.5, and 7.65 THz with absorption rates of 99.7%, 95.3%, 95.8%, 97.9%, 99.8, 97% and 92.4%	**Eight** absorption peaks at 0.79, 2.66, 3.5, 6.19, 7, 7.53, 7.8, and 7.97 THz with absorption rates of 96%, 97.82%, 100%, 99.46%, 92.6%, 93%, 98.8%, and 100%
Without a Pentagon Ring absorber	**Seven** absorption peaks at 0.78, 1.53 2.32, 3.19, 6.21, 7.1, and 7.75 THz with absorption rates of 98.1%, 94.01%,	**Eight** absorption peaks at 0.75, 1.7, 2.63, 3.48, 6.17, 7.41, 7.5, and 7.86 with absorption rates of 98.16%, 98.12%,

	94.3%, 100%, 93.7%, 97.7%, and 99.9%	98.33%, 99.42%, 94.8%, 91.22%, 97.09%, and 99.95%
Without a Hexagon Ring absorber	**Four** absorption peaks at 3.49, 6.2, 7.1, and 7.96 THz with absorption rates of 99.4%, 91.5%, 99.8%, and 95%	**Six** absorption peaks at 1.48, 2.9, 3.42, 6, 7.48, 7.9 THz with absorption rates of 100%, 99.5%, 98.78%, 94.1%, 90.2%, and 98.7%
With all the absorbers	**Four** absorption peaks at 3.72, 6.23, 7.12, and 8.39 THz with absorption rates of 99.4%, 99.1%, 99.1%, and 99.09%.	**Ten absorption peaks at 0.79, 2.6, 3.6, 5.97, 6.2, 7.1, 7.52, 7.68, 8.03, and 8.24 THz with absorption rates of 96.2%, 99.4%, 98.7%, 92.6%, 100%, 92.2%, 98.7%, 94.6%, 100%, and 100%**

Fig. 5.7(a) shows the plot of Absorption (A), Reflection (R), and Transmission (T) for the proposed graphene-based absorber configuration (fig. 6(f)). Absorption is given by A=1-R-T, where Reflection (R) is calculated by R=$|S_{11}^2|$ and transmission T is calculated by T=$|S_{21}^2|$ respectively. Transmittance is approximately equal to zero for the configuration. Hence Absorption is calculated by A= 1-R. When absorption is high, reflection is low and when reflection is high, absorption must be low and transmittance is equal to zero throughout the band.

It is evident that impedance plays a major role in absorber performance and the parameters, transmission, and reflection are dependent on impedance. Impedance is given by z(f) = $\sqrt{\mu(f)/\varepsilon(f)}$ =z_1+iz_2, μ(f) and ε(f) are tuned to achieve perfect impedance matching with free space z(f) = $\sqrt{\mu(f)/\varepsilon(f)}$ =1. The E and H fields which are incidents of EM wave will be absorbed completely providing 100% absorbance.

The impedance is calculated by equation (5.3)

$$z(f) = \frac{\sqrt{(1+S_{11})^2+S_{21}^2}}{\sqrt{(1-S_{11})^2 S_{21}^2}} = \frac{1+S_{11}}{1-S_{11}} = \frac{1+R}{1-R} \quad (5.3)$$

Where R is a reflection and is equal to S_{11}. From the above equation (5.3) the effective impedance is calculated and is shown in Fig. 5.7(b). At the resonant frequencies (0.79, 2.6, 3.6, 5.97, 7.1, 7.52, 7.68, 8.03, and 8.24 THz) of the entire band, the real part (Re (z)≈1) of impedance z for proposed absorber configuration is near to unity and imaginary part (Im(z)≈0) of impedance z for proposed absorber configuration is near to zero, this corresponds to perfect absorption at these frequencies.

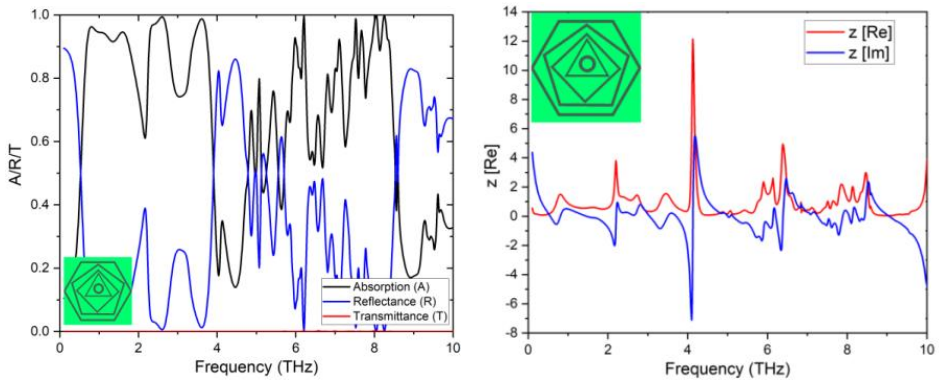

(a) (b)

Fig. 5.7 (a) Plot of frequency vs Absorption (A), Reflectance (R), and Transmittance (T) for the proposed absorber and (b) Extracted Real and imaginary impedance plot for the proposed absorber (proposed).

We explore the Surface Current (SC) and EF distributions of the absorber at 10 different resonant frequencies to understand more about the process of the absorber multi-band terahertz absorption from 0.7 THz to 8.24 THz under the normal incidence of TE polarization. Fig. 5.8 shows the top views of SC and EF distribution on graphene MMA on the x-y plane. Fig. 5.8 Surface current distribution and EF on proposed absorber at frequencies of (a, b) 0.79 THz, (c, d) 2.6 THz, (e, f) 3.6 THz, (g, h) 5.97 THz, (i, j) 6.2 THz, (k, l) 7.1 THz, (m, n) 7.52 THz, (o, p) 7.68 THz (q, r) 8.08 THz and (s, t) 8.24 THz.(a, b) shows the surface current distribution and EF distribution at the resonant frequency of 0.79 THz. Smaller EF and SC distribution is observed at this frequency and the absorption at this frequency is mainly contributed by a pentagon-shaped absorber as most of the surface current is localized on it. Fig. 5.8(c, d) shows the surface current distribution and EF distribution at the resonant frequency of 2.6 THz. At this frequency, absorption is higher compared to that at 0.79 THz and is mainly contributed by triangular and hexagonal-shaped absorbers. Fig.

5.8(e, f) shows the surface current distribution and EF distribution at a frequency of 3.6 THz. At this frequency incident, EM waves are mostly absorbed by circular, triangular, square, and pentagon-shaped absorbers. Fig. 5.8(g, h) shows the surface current distribution and EF distribution at a frequency of 5.97 THz. At this frequency incident, EM waves are mostly absorbed by circular, triangular, square, and hexagon-shaped absorbers. Fig. 5.8(i, j) shows the surface current distribution and EF distribution at a frequency of 6.2 THz. At this frequency incident, EM waves are absorbed by all the absorbers since the surface current is localized on all the absorbers and provides ≈100% absorption. Fig. 5.8(k, l) shows the surface current distribution and EF distribution at a frequency of 7.1 THz. At this frequency incident, EM waves are absorbed by all the absorbers. Fig. 5.8(m, n) shows the surface current distribution and EF distribution at a frequency of 7.52 THz. At this frequency, absorption is mainly contributed by the square, pentagon, and hexagon-shaped absorbers as most of the current distribution is centered on these absorbers. Fig. 5.8(o, p) shows the surface current distribution and EF distribution at a frequency of 7.68 THz. At this frequency absorption is contributed by all the absorbers as most of the current distribution is centered on all the absorbers. Fig. 5.8(q, r, s, t) shows the surface current distribution and EF distribution at a frequency of 8.03 and 8.24 THz. At these frequencies, absorption is contributed by all the absorbers as most of the current distribution is centered on all the absorbers and provides ≈100% absorption. From the surface current and EF distributions it is clear that when only one or two rings are present, weak electric and magnetic resonances are observed hence contribution from these rings will be only single or dual band. As the number of rings increases the peak resonances indicate strong electric and surface current resonances in the absorber structure and mainly occur at the top layer.

To elucidate the absorber performance further, the behavior of the proposed absorber for various incidence (θ) and polarization angles (ϕ) for both TE and TM modes is examined. Fig. 5.9(a) shows the plot of absorption with frequency for various incidence angles (θ). It is observed that the average absorbance maintains over 90% at all the resonant frequencies under a wide range of incidence angles ranging from 0° to 60° for TE polarization. When the incident angle is greater than 75°, the absorbance drops significantly to less than 60%. Fig. 5.9(b) shows that the absorbance spectra for TM polarization are also resistant to the angle of incidence up to 60° at the resonant frequencies, but begin to drop substantially when the incident angle approaches above 60°. As a result, even at higher angles of 60°, the proposed absorber attains greater angular stability for TE

and TM polarization, which is a very attractive behavior for numerous terahertz application scenarios. In addition to the incidence angle, the behavior of the proposed absorber is examined for various polarization angles (ϕ). Fig. 5.9(c) shows the plot of absorption with frequency for various polarization angles (ϕ). It is observed that the average absorbance maintains over 90% at all the resonant frequencies under a wide range of polarization angles ranging from 0° to 90° for TE polarization. Fig. 5.9(d) shows that the absorbance spectra for TM polarization are also resistant to polarization angle up to 60° at the resonant frequencies, but there is no drop in absorption rate when the polarization angle approaches 90°. As a result, even at higher angles of 90°, the proposed absorber attains a greater polarization-independent angular stability for TE and TM polarization, which is a very attractive behavior for numerous terahertz application scenarios. Furthermore, the performance of the proposed absorber is examined for different values of graphene chemical potential values ranging from 0.1eV to 0.9eV. By applying a DC bias voltage to the graphene layer, the chemical potential of graphene can be changed. Over the graphene layer, an ion-gel layer of thickness 0.1 μm with a permittivity of 1.852 is coated, allowing all of the periodically organized unit cells to be biased together [145], [146]. It is found that with the increase in graphene potential value absorption increases and the absorption peaks shift towards the right side as shown in Fig. 5.10. Hence as the graphene potential value increases there is an increase in absorption as well as resonant frequency will be tuned. Therefore graphene plays an important role in enhancing the absorber performance and also achieves tunability characteristics. It is necessary to report the fabrication steps for the proposed absorber structure. Two graphene layers can be prepared using the chemical vapor deposition method and one of the layers is transferred to the other side of the polyimide substrate. This graphene layer can be patterned into different geometric shapes on the top of the substrate. The fabrication of proposed graphene-based structures is possible with the methods reported in [147], [148].

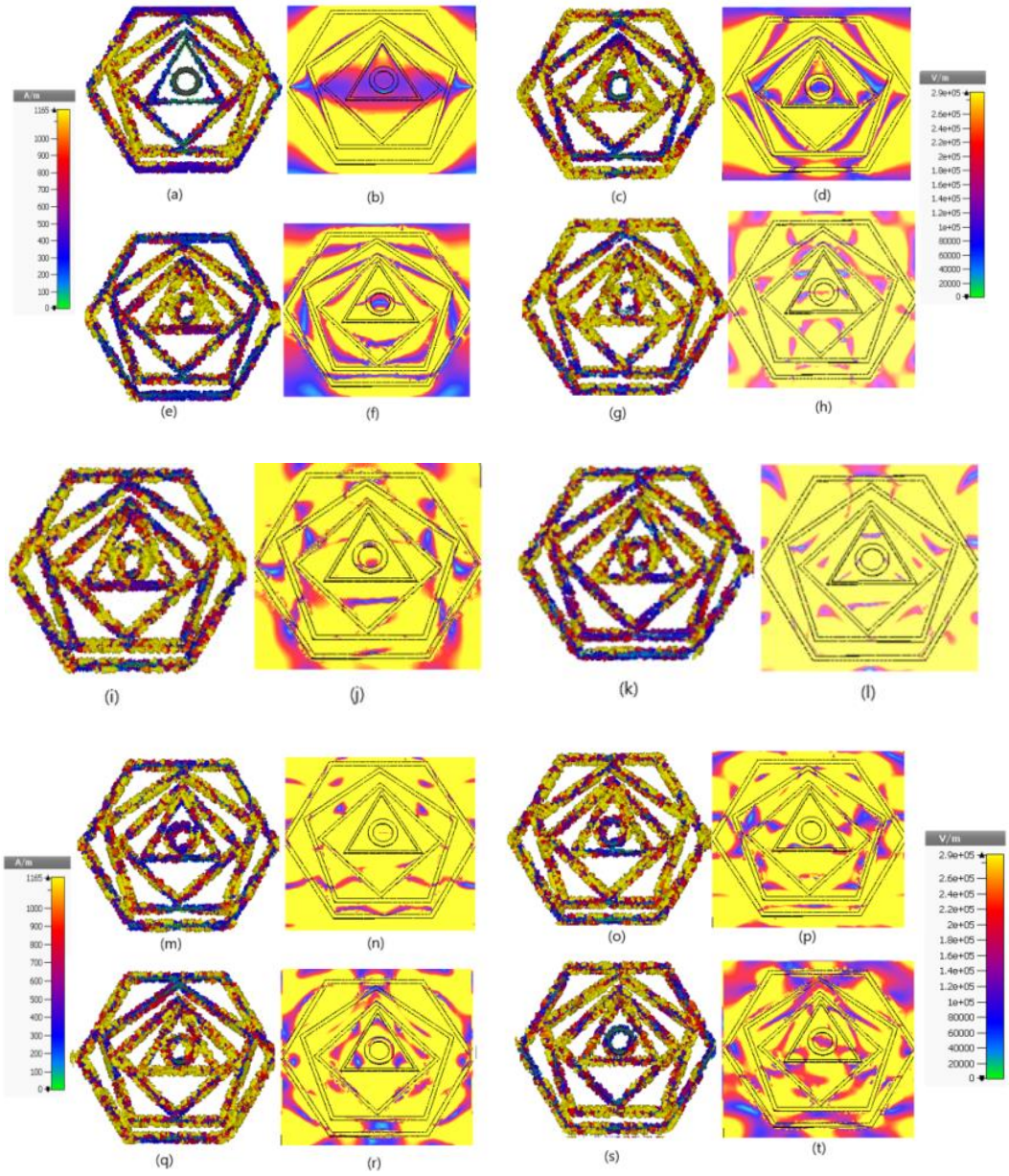

Fig. 5.8 Surface current distribution and EF on proposed absorber at frequencies of (a, b) 0.79 THz, (c, d) 2.6 THz, (e, f) 3.6 THz, (g, h) 5.97 THz, (i, j) 6.2 THz, (k, l) 7.1 THz, (m, n) 7.52 THz, (o, p) 7.68 THz (q, r) 8.08 THz and (s, t) 8.24 THz.

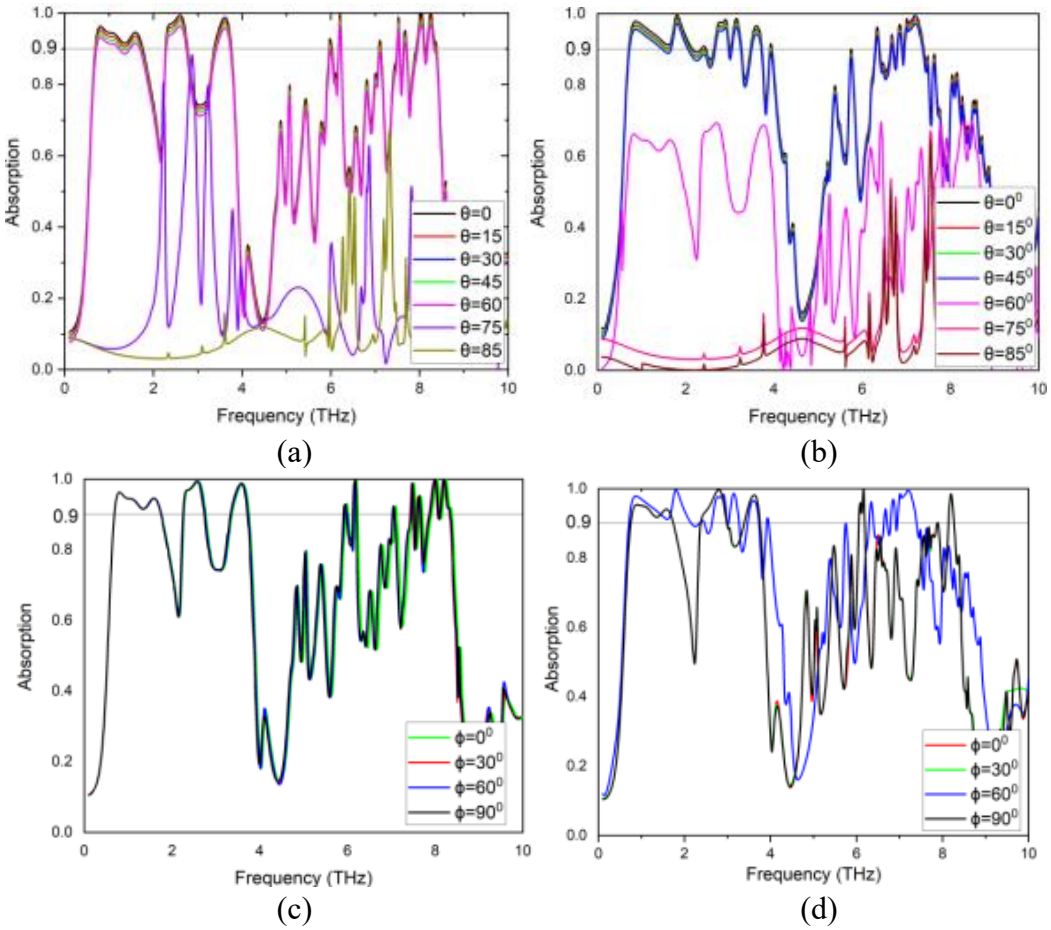

Fig. 5.9 The plot of absorption spectra for the proposed absorber for various incidence angles (θ) (a) TE mode (b) TM mode and for various polarization angles (ϕ) (a) TE mode (b) TM mode.

A comparison table of proposed absorbers with already published research articles is presented in Table 5.6. Most of the previously published articles have absorption peaks at a maximum of five or six bands. Whereas this proposed absorber produces ten resonant peaks with a simple design. Finally, the proposed design (Fig. 5.6(f)) incorporating Hexagon, Pentagon, Square, triangular, and circular-shaped absorbers gives absorption peaks at ten resonant frequencies and improved absorber absorption rate response when compared to all other models I and model II configurations. With an absorption bandwidth percentage of 88.52, this proposed configuration provides an ultra-wide-band response. In addition, this unique configuration design has superior stability in terms of incidence angle, polarization angle, and graphene chemical potential variations.

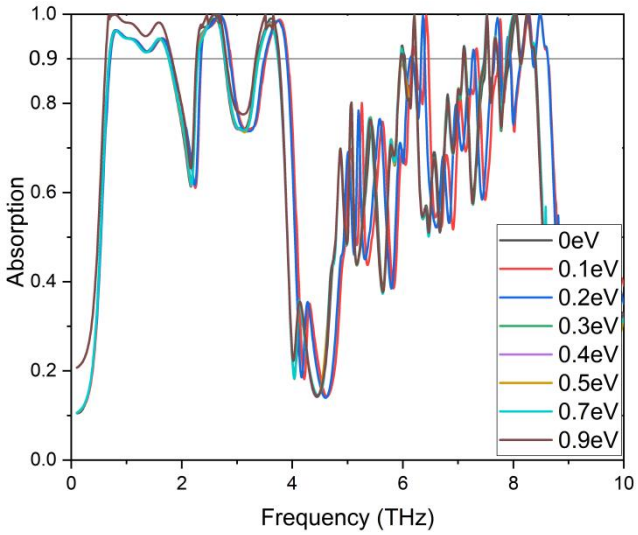

Fig. 5.10 The plot of absorption spectra for the proposed absorber for various fermi level values of graphene (0.1 eV to 0.9eV).

Table 5.7 Comparison of the proposed multiband absorber with published research articles.

Ref No.	**Method**	**No. of Absorption peaks**	**Frequency (THz)**	**Absorption rate (%)**	**Incidence angle (θ)**	**Polarization Insensitive**
[140]	Metamaterial	Six	0.72, 1.62, 2.28, 2.98, 3.41, and 4.27 THz	Average absorbtion-97%	-	No
[142]	Metamaterial	Five	0.2809, 0.415, 0.5437, 0.6373, 0.9217 THz	98.20%, 98.45%, 99.38%, 99.43%, and 79.26%	Up to 60º	No
[143]	Metamaterial	Three	0.88, 1.94, and 2.63 THz	99%, 98% and 99%	No	No
[149]	Graphite	Three	2.06, 2.8 and 3.47 THz	95.2, 93 and 84%	60º	Yes
[150]	Metamaterial	Two	0.45 and 0.92 THz	99.9% and 99.9%	No	No
[151]	Metamaterial	Five	148.9 THz, 179.8 THz, 213.1 THz, 269.8 THz, and 287.2 THz	98.90%, 99.39%, 86.46%, 92.80% and 97.96%	60º	Yes
This absorber	**Graphene**	**Ten**	**0.79, 2.6, 3.6, 5.97, 6.2, 7.1, 7.52, 7.68, 8.03 and 8.24 THz**	**96.2%, 99.4%, 98.7%, 92.6%, 100%, 92.2%, 98.7%, 94.6%, 100% and 100%**	**60º**	**Yes**

5.5 Conclusion

A novel graphene absorber is proposed by integrating multiple geometric-shaped absorbers to achieve multiband resonance at the THz frequency regime. This proposed configuration provides absorption peaks at ten resonant frequencies of 0.79, 2.6, 3.6, 5.97, 6.2, 7.1, 7.52, 7.68, 8.03, and 8.24 THz with absorption rates of 96.2%, 99.4%, 98.7%, 92.6%, 100%, 92.2%, 98.7%, 94.6%, 100%, and 100% respectively. Additionally, this novel configuration design exhibits better stability with respect to incidence angle, polarization angle, and also the changes in graphene chemical potential. Additionally, increasing the graphene chemical potential value increases absorption while also tuning the resonance frequency. Two graphene-based absorbers are designed. One with geometric shapes that are in contact with one another, and the other with geometric shapes that are not in contact with one another. Several investigations are exhibited on these two models to find the perfect combination of absorber configuration. All of these characteristics and findings distinguish the proposed multiband graphene-based absorber, which is well-suited for THz applications.

Chapter 6

Graphene-based Ultra-wideband Absorber for Terahertz Applications

6.1 Introduction

In this chapter, a hexagonal split ring ultra-wideband absorber is proposed at THz frequency. The proposed structure consists of four graphene-based hexagonal split rings, a dielectric substrate, and a graphene layer at the bottom.

Most of the ultra-wideband absorbers are developed using metal, dielectric, multi-layered, and graphene-metal based [94], [152]–[155]. For example, in [153], the authors presented a multi-layered structure with an absorption bandwidth of 2.7 THz with a center frequency of 3 THz. In [154], a graphene-based multi-layered geometry is designed with a bandwidth of 6.9 THz. In [92], a metal-based absorber shows absorption bandwidth from 1.3-2.7 THz and is sensitive to polarization changes. In [156], a graphene-based absorber shows an absorption bandwidth from 1.1-1.86 THz with incidence angle up to 50^{o} and 60^{o} for TE and TM incidence respectively. In [157], a metallic array at the bottom and a graphene patch array with a dielectric spacer is used for the generation of dual-band absorption behavior which occurs from 4.56-9.02 THz and 16.95-60.23 THz with an absorption bandwidth of 67 % and 112 %, respectively [157]. A five-layer graphene structure is proposed in [158] and shows absorption bandwidth from 1.51–8.25 THz. In [152], a dual-band ultra-broadband THz absorber is designed based on graphene and strontium titanate (STO) that shows an absorption bandwidth from 3.04–6.4 THz. A broadband tunable vanadium dioxide (VO_2) based THz MMA is proposed in [159], which shows absorption bandwidth from

1.2-3.2 THz with incidence angle up to 45º for TE and TM incidence. These geometries have several disadvantages, including higher fabrication complexity, a multi-graphene gating difficulty, and a complex unit cell structure. In a variety of interesting terahertz applications, a high-performance terahertz absorber with Ultra-wideband absorption for wide incidence angle for both TE and TM incident waves along with tunability characteristics, polarization insensitiveness, and a compact configuration at the same time is required. Moreover, achieving ultra-wideband characteristics towards lower THz frequency regions is a challenging task.

To address the above issues a Hexagonal Split Ring graphene-based mono-layered absorber is proposed with ultra-wideband absorption and bandwidth of 2.1 THz towards the lower THz frequency region. Tunability is achieved by varying the graphene chemical potential of the absorber. The proposed absorber is polarization insensitive because of symmetry geometry for both TE and TM modes and also exhibits absorption greater than 90% for incidence angle up to 75º for both TE and TM waves making it useful for solar and photovoltaic cells. These features make the proposed metal-free absorber useful for terahertz applications and future nanoscale systems. The proposed absorber shows narrow absorption characteristics for higher graphene chemical potential values which can also be utilized for sensor applications.

6.2 Structure of Proposed absorber

Fig. 6.1 shows, the schematic of the proposed Ultra-wideband absorber along with its absorption characteristics. The incident THz wave on the proposed absorber is depicted in Fig. 6.1(a). It consists of a polyimide substrate with a dielectric constant of ε=3.5 and having dimensions of $L \times W \times t_s$. At the bottom of the substrate, a graphene sheet is placed having dimensions of $L \times W \times t_g$. At the top of the substrate, a graphene-based hexagonal split ring (HSR) absorber (HSRA) structure is designed as depicted in Fig. 6.1(b). It consists of four rings, namely, the center ring, 2nd ring, 3rd ring, and 4th ring. The proposed structure has a dimension of W_1, W_2, W_3, and W_4 as the width of hexagonal split rings, g as the split gap, d as the distance of separation between the HSRs, and t_1 as the thickness of HSRA. All the dimensions are depicted in Table 6.1. HSRA is among the most widely used artificial magnetic materials, and it is designed using non-metallic rings printed in a dielectric medium in circular, rectangular, spiral, omega, and other geometries [160], [161].

Table 6.1 Proposed absorber parameters (in µm)

L	W	t_s	W_1	W_2	W_3	W_4	g	d	t_1	h_g	t_{s1}
80	80	20	40	30	20	10	4	8	2	0.1	18.7

Each geometry has its coupling effect based on its structure and electromagnetic characteristics, such as edge coupling in a circular form, broadside coupling in a rectangular shape, and so on. A single split ring resonator also has bianisotropic responses and cross-polarization implications when the magnetic dipole moment is excited by an electric field. If the rings have a broadside composition, the bianisotropic behaviour and cross-polarization effects are removed [160]–[162]. As a result, the HSRA has been developed. It can minimize bianisotropic responses and cross-polarization problems in the dielectric medium because of its broad side structure. Another benefit of using a hexagonal geometry is that it creates more capacitive loading in the geometry, resulting in enhanced resonance behavior.

Fig. 6.1(c) shows the periodic array pattern of the proposed absorber and Fig. 6.1(d) depicts the absorption spectra of the proposed absorber. The proposed absorber shows ultra-wideband characteristics with an absorption bandwidth percentage of 102.8 %. The proposed ultra-wideband metal free absorber is simulated and optimized using CST microwave studio 2021, where we have set unit cell boundary conditions along x and y directions and open add space boundary condition along z direction while the electric field polarized along the x-direction was an incident on HSRA along the z-direction. A frequency-domain solver in CST 2021 with a mesh cell size in tetrahedrons of 37,923 is utilized for simulation.

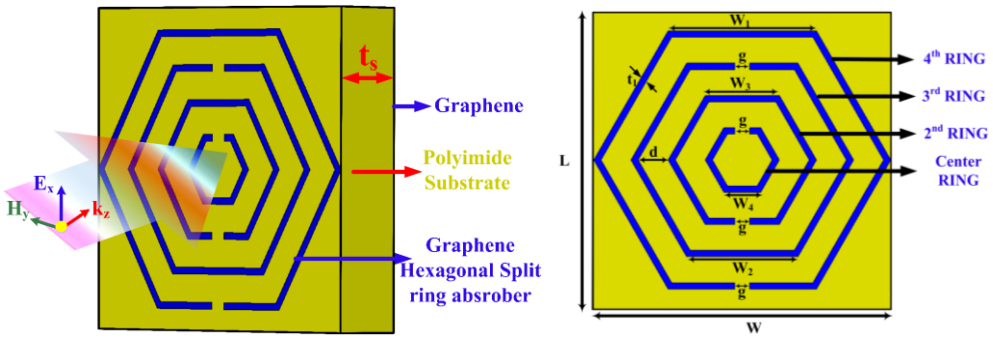

(a) (b)

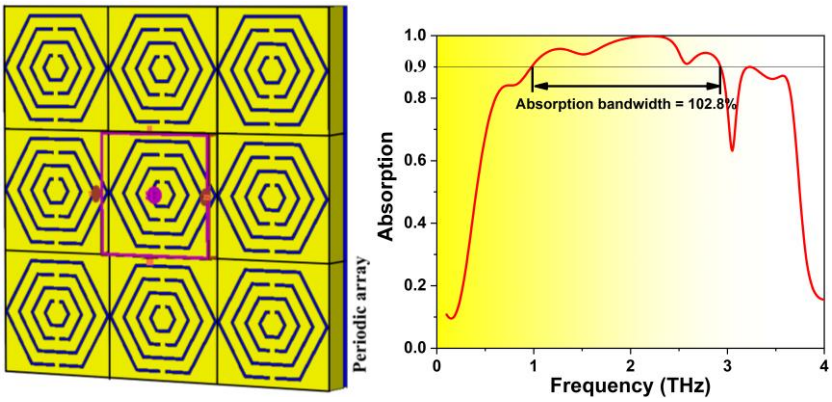

(c) (d)

(e)

Fig. 6.1 (a) Proposed absorber with incident THz waves, (b) Unit cell of the proposed absorber, (c) Periodic pattern and (d) Absorption plot (e) absorber structure with biasing (Dimensions: L= 80, W=80, d=8, g=4, t_1=2, W_1 = 40, W_2 = 30, W_3 = 20 and W_4 =10 (all dimensions are in µm)).

Because the graphene layer thickness is thin, the adaptive mesh parameters keep the mesh cell size small. Initially, the chemical potential of graphene is chosen as μ_c = 0 eV. In addition, the efficiency of the suggested absorber is investigated for various μ_c values varying from 0.1eV to 0.9eV. The μ_c can be altered by providing a DC bias voltage to the graphene layer as shown in Fig. 6.1(e). An ion-gel layer with a permittivity of 1.852 and a height of h_g is placed over the graphene layer, allowing all of the periodically structured unit cells to be biased together [146], [152], [163], [164]. In the fabrication process, the Chemical vapor deposition (CVD) method can be used to grow two graphene layers, one of which is then transferred to the other side of the polyimide substrate. On top of the substrate, this graphene layer can be shaped into hexagonal split ring patterns and unwanted material portions can be removed by the standard electron beam lithography (EBL) method. The methods described in [152], [148], [165] can be used to fabricate the proposed graphene-based structure. In this research, graphene is modeled as an ultrathin sheet

having a thickness of 1nm. The permittivity of graphene is given by $\varepsilon_G = \varepsilon_0 - j\sigma_G / (\omega\Delta)$, where σ_G is the graphene surface conductivity and Δ is thickness. Graphene conductivity (σ_G) is the sum of intraband (σ_{intra}) and interband (σ_{inter}) conductivity terms [96], [97] and it is derived from Kubo-formula [96], [97] and is given by equations (6.1-6.3):

$$\sigma_G(\omega,\tau,\mu_c,T) = \sigma_{intra}(\omega,\tau,\mu_c,T) + \sigma_{inter}(\omega,\tau,\mu_c,T) \tag{6.1}$$

$$\sigma_{intra}(\omega,\tau,\mu_c,T) \approx -j\frac{e^2 k_B T}{\pi\hbar^2(\omega - j\tau^{-1})}\left[\frac{\mu_c}{k_B T} + 2\ln\left\{\exp\left(-\frac{\mu_c}{k_B T}\right)+1\right\}\right] \tag{6.2}$$

$$\sigma_{inter}(\omega,\tau,\mu_c,T) \approx -j\frac{e^2}{4\pi\hbar}\ln\left[\frac{2|\mu_c| + (\omega - j\tau^{-1})\hbar}{2|\mu_c| - (\omega - j\tau^{-1})\hbar}\right] \tag{6.3}$$

Where e is the charge of the electron, k_B is the Boltzmann constant, $\hbar$ is the Planck constant, μ_c is chemical potential, T is the temperature, and τ is the graphene relaxation time [96], [97]. In this research work, T is considered as 300 K and τ =0.1 ps.

6.3 Proposed absorber modeling, design, and results

The proposed graphene-based HSRA is modeled in three steps. In step one, a single isolated absorber structure performance will be analyzed. In step two, all combinations of split ring absorbers by considering two split rings at a time will be investigated. In step three, three split-ring absorber combinations will be analyzed. Eventually, all the possible configurations with four hexagonal split rings will be analyzed to exhibit the ultra-wide performance of the proposed absorber.

6.3.1 Single ring

Fig. 6.2 shows a schematic view of individual four hexagonal absorbers. Fig. 6.2(a, b, c, and d) shows central HSRA, 2nd HSRA, 3rd HSRA, and 4th HSRA respectively. Its respective surface current (SC) distribution on rings and absorption plots are depicted in Fig. 6.3, and Fig. 6.4 respectively.

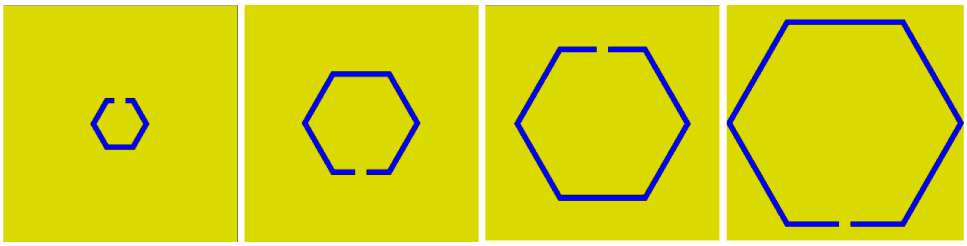

(a) (b) (c) (d)

Fig. 6.2 Schematic view of individual absorbers (a) central Hexagonal ring (b) 2nd Hexagonal ring (c) 3rd Hexagonal ring (d) 4th Hexagonal ring.

Individual absorber performance is analyzed and the results show that absorption contribution from the central ring is very less compared to the other absorbers. This is due to the dimensions of the central ring.

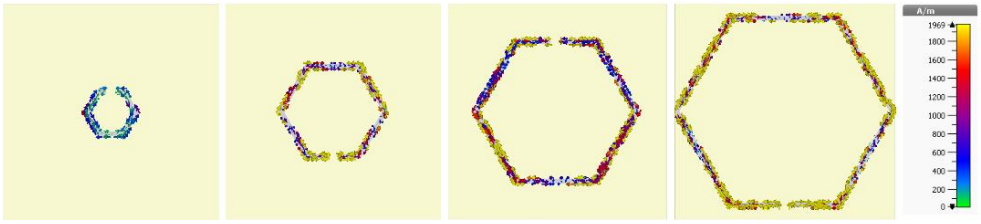

(a) (b) (c) (d)

Fig. 6.3 Surface current distribution on (a) central Hexagonal ring (b) 2nd Hexagonal ring (c) 3rd Hexagonal ring (d) 4th Hexagonal ring.

As a result, the surface current distribution on the ring is very low as depicted in Fig. 6.3(a). As the dimension of the rings increases, better absorption is exhibited. The absorption from the 2nd hexagonal ring shows a maximum absorption of 80% and 73 % at a frequency of 2.96 and 3.42 THz respectively as depicted in Fig. 6.4 and also confirmed from the SC distribution (Fig. 6.3(b)) on the ring. The absorption from the 3rd hexagonal ring shows a maximum absorption of 99.4%, 99.3%, and 87.8 % at a frequency of 2.06, 2.31, and 3.12 THz respectively. Similarly, the absorption from the 4th hexagonal ring exhibits a maximum absorption of 99.8% and 76.4 % at a frequency of 1.42 and 2.17 THz respectively. Hence from the above, it is clear that the 3rd and 4th rings provide more absorption compared to the center and 2nd hexagonal rings and its SC distribution also shows high charge accumulation on the rings as depicted in Fig. 6.3(c) and Fig. 6.3(d).

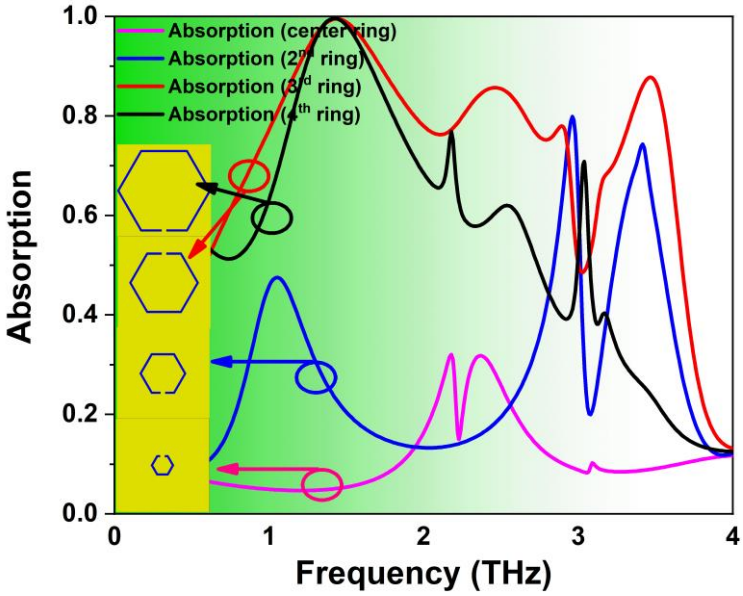

Fig. 6.4 Absorption vs frequency spectra of individual absorbers

6.3.2 Combination of two rings

In the second step, the absorber performance is examined by merging two hexagonal rings, as shown in Fig. 6.5. Subsequently, six configurations are developed by combining two hexagonal rings.

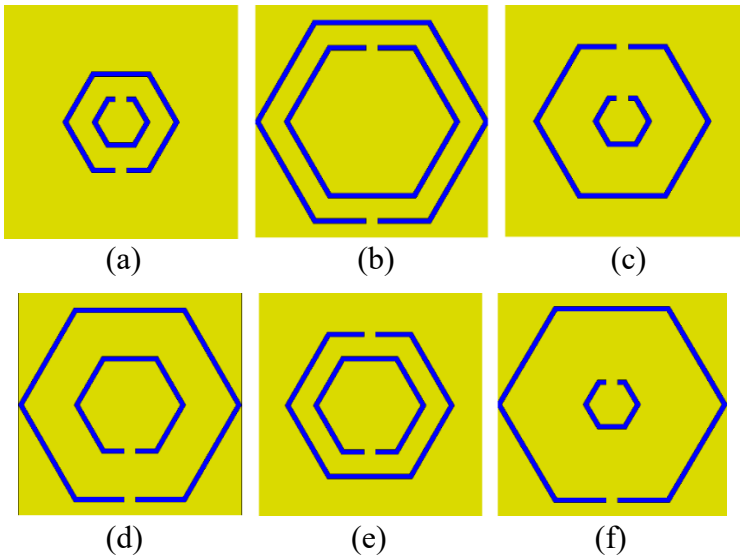

Fig. 6.5 Schematic view of absorbers with a combination of (a) central and 2nd Hexagonal rings (b) 3rd and 4th Hexagonal rings (c) central and 3rd Hexagonal rings (d) 2nd and 4th Hexagonal rings (e) 2nd and 3rd Hexagonal rings (f) Central and 4th Hexagonal rings.

Fig. 6.5(a) shows the absorber configuration with a combination of central and 2nd hexagonal rings, Fig. 6.5(b) shows the absorber configuration with a combination of 3rd and 4th hexagonal rings, Fig. 6.5(c) shows the absorber configuration with a combination of central and 3rd hexagonal rings, Fig. 6.5(d) shows absorber configuration with a combination of 2nd and 4th hexagonal rings, Fig. 6.5(e) shows absorber configuration with a combination of 2nd and 3rd hexagonal rings and Fig. 6.5(f) shows absorber configuration with a combination of Central and 4th hexagonal rings respectively. Fig. 6.6 and g. 6.7 exhibit SC distribution and absorption spectra for the absorber configurations shown in Fig. 6.5. Fig. 6.6(a) and g. 6.7(a) illustrate the SC distribution and absorption spectra for the structure in Fig. 6.5(a), which has a maximum absorption of 80% at 2.96 THz. This configuration provided less absorption because of less charge accumulation on both rings.

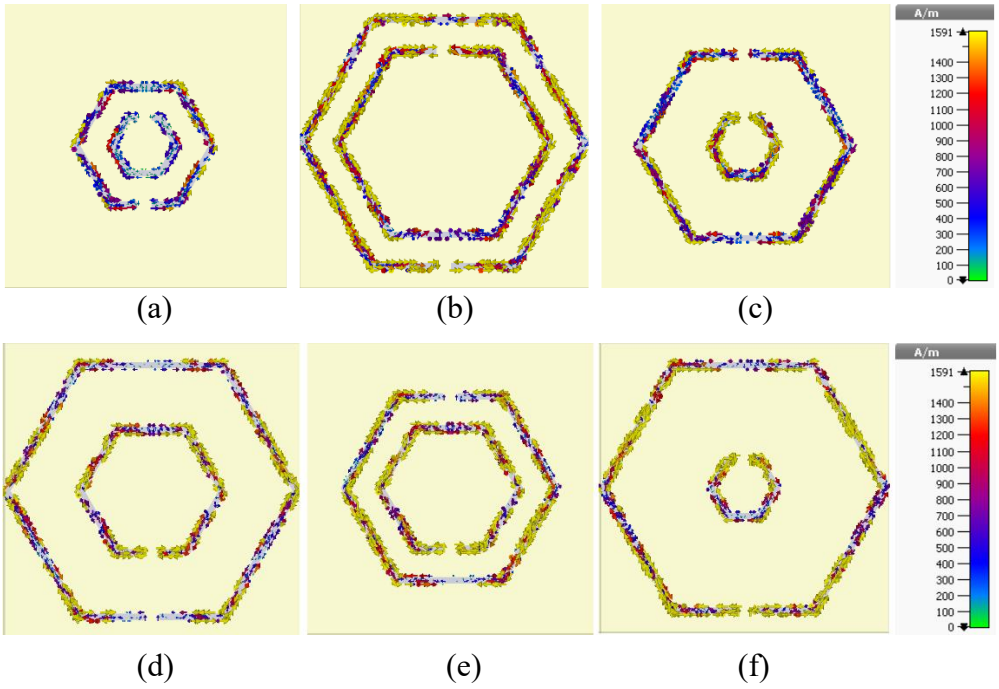

Fig. 6.6 Surface current distribution on absorber configuration of (a) central and 2nd Hexagonal rings (b) 3rd and 4th Hexagonal rings (c) central and 3rd Hexagonal rings (d) 2nd and 4th Hexagonal rings (e) 2nd and 3rd Hexagonal rings (f) Central and 4th Hexagonal rings.

Fig. 6.6(b) and g. 6.7(b) shows SC distribution and absorption spectra for Fig. 6.5(b) configuration which exhibits an absorption bandwidth of 70% (1.14-2.35THz). This is because EM radiation is primarily concentrated on the third and fourth rings, resulting in a large absorption bandwidth as

shown in Fig. 6.6(b). Fig. 6.6(c) and g. 6.7(c) illustrate the SC distribution and absorption spectra for the structure shown in Fig. 6.5(c), which has a maximum absorption of 99.6%, 98.1%, and 86.7% at 2.08, 2.36, and 86.7 THz. The 3rd ring is primarily responsible for the resonance at three peaks in this configuration. Fig. 6.6(d) and g. 6.7(d) depict the SC distribution and absorption spectra for the structure in Fig. 6.5(d), which has a maximum absorption of 99.5% and 87% at 1.41 and 2.96 THz. Additionally, this configuration provides an absorption bandwidth of 35.5% (1.18-1.69 THz). The 4th ring is the dominant contributor to absorption in this design. The SC distribution and absorption spectra for the structure in Fig. 6.5(e) is shown in Fig. 6.6(e) and g. 6.7(e), respectively, which shows absorption at four peaks of 99.5 %, 97.2 %, 96.8%, and 82.1% at 2.06, 2.31, 2.91, and 3.11 THz. Both 2nd and 3rd rings contribute to the four-peak resonance. The SC distribution and absorption spectra for the structure in Fig. 6.5(f) are shown in Fig. 6.6(f) and g. 6.7(f), which shows an absorption bandwidth of 35.5% (1.18-1.69 THz) with a peak absorption of 99.8% at 1.44 THz.

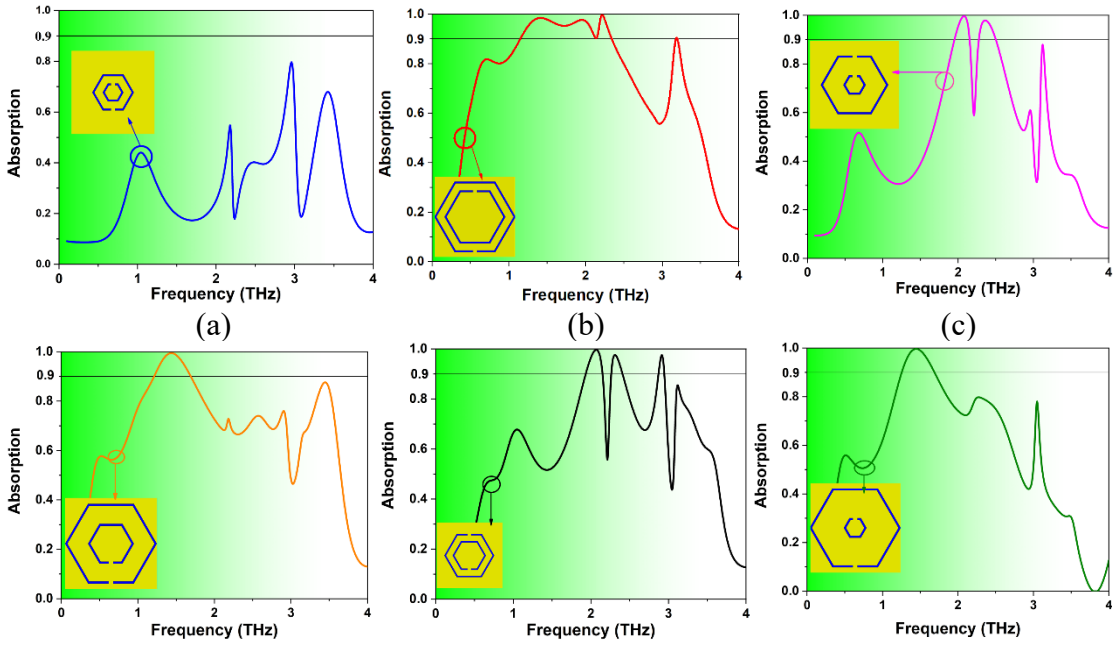

g. 6.7 Absorption spectra for the combination of (a) central and 2nd Hexagonal rings (b) 3rd and 4th Hexagonal rings (c) central and 3rd Hexagonal rings (d) 2nd and 4th Hexagonal rings (e) 2nd and 3rd Hexagonal rings (f) Central and 4th Hexagonal rings.

From the above, it is clear that the configuration of Fig. 6.5(b) provides a wide-band response (absorption bandwidth of 70%) compared to the other configurations. Whereas configurations of Fig. 6.5(d) and Fig. 6.5(f) provide an absorption bandwidth of 35.5 %.

6.3.3 Combination of three rings

In the next step, three hexagonal rings are merged to evaluate the ultra-wideband absorption behavior as shown in Fig. 6.8. Fig. 6.8(a) shows the absorber configuration with a combination of 2^{nd}, 3^{rd} and 4^{th} hexagonal rings (without a center ring). Fig. 6.8(b) shows the absorber configuration with a combination of central, $3^{rd,}$ and 4^{th} hexagonal rings (without the 2^{nd} ring). Fig. 6.8(c) shows the absorber configuration with a combination of central, $2^{nd,}$ and 4^{th} hexagonal rings (without the 3^{rd} ring). Fig. 6.8(d) shows the absorber configuration with a combination of central, 2^{nd}, and 3^{rd} Hexagonal rings (without the 4^{th} ring) respectively. The SC distribution and the absorption spectra for the absorber structure shown in Fig. 6.8 are depicted in Fig. 6.9 and Fig. 6.10 respectively. Fig. 6.9(a) shows the absorption spectra for the structure in Fig. 6.8(a), which exhibits an absorption bandwidth of 88.56 percent (0.95-2.46 THz).

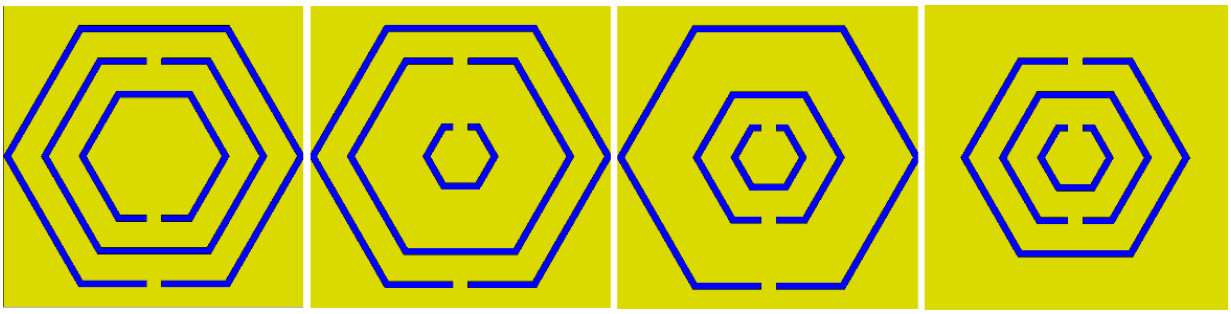

(a) (b) (c) (d)

Fig. 6.8 Schematic view of absorbers with a combination of (a) 2^{nd}, 3^{rd}, and 4^{th} Hexagonal rings (b) Central, 3^{rd} and 4^{th} Hexagonal rings (c) central, 2^{nd} and 4^{th} Hexagonal rings (d) Central, 2^{nd} and 3^{rd} Hexagonal rings.

Surface current distribution plots are also included to exhibit the contribution of the absorber rings. The incident EM energy as depicted in Fig. 6.9(a) is mostly centered on the second, third, and fourth hexagonal rings, resulting in a wide absorption band.

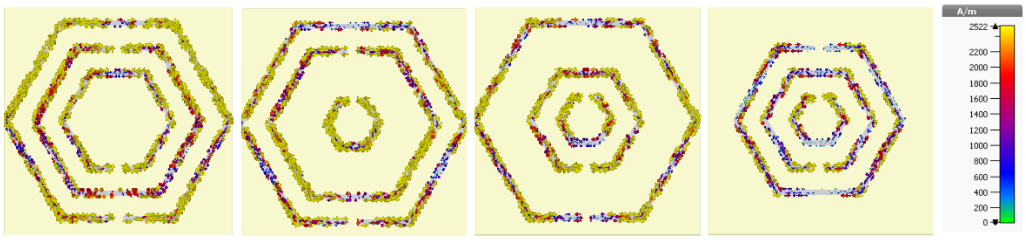

(a) (b) (c) (d)

Fig. 6.9 Surface current distribution on absorber configuration of (a) 2nd, 3rd, and 4th Hexagonal rings (b) Central, 3rd and 4th Hexagonal rings (c) central, 2nd and 4th Hexagonal rings (d) Central, 2nd and 3rd Hexagonal rings.

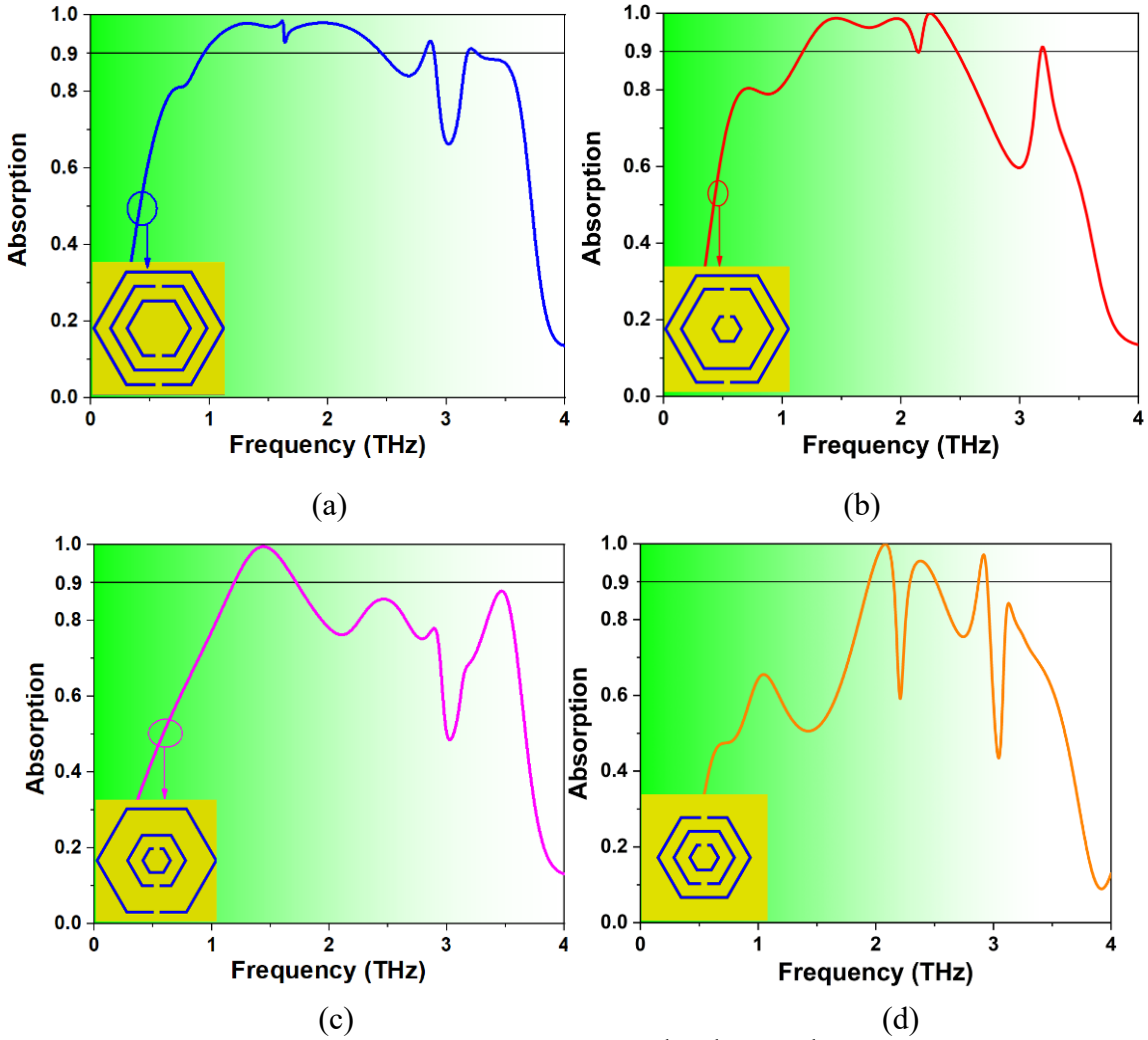

(a) (b)

(c) (d)

Fig. 6.10 Absorption spectra for a combination of (a) 2nd, 3rd, and 4th Hexagonal rings (b) Central, 3rd and 4th Hexagonal rings (c) central, 2nd and 4th Hexagonal rings (d) Central, 2nd and 3rd Hexagonal rings.

Fig. 6.9(b) and Fig. 6.10(b) illustrate the SC distribution and absorption spectra for the structure in Fig. 6.8(b), which shows an absorption bandwidth of 71.4% (1.17-2.47 THz). The difference between the absorption spectra of Fig. 6.10(a) and Fig. 6.10(b) is that in Fig. 6.10(a), the central ring is removed, resulting in better absorption than in Fig. 6.10(b), where the central ring is present and the 2nd Hexa ring is removed. This emphasizes the importance of the 2nd ring's absorption contribution in comparison to the central ring. Furthermore, the structure without the central ring (Fig. 6.10(a)) covers the absorption band from 1.17 THz, whereas the configuration with the central ring (Fig. 6.10(b)) covers the absorption band from 0.95 THz. Fig. 6.9(c) and Fig. 6.10(c) show the SC distribution and absorption spectra for the structure in Fig. 6.8(c), which exhibits an absorption peak at 1.44 THz with an absorption rate of 99.5%. Fig. 6.9(d) and Fig. 6.10(d) show the SC distribution and absorption spectra for the structure in Fig. 6.8(d), which exhibits absorption peaks at 2.08, 2.38, and 2.92 THz with an absorption rate of 99.8%, 95.3%, and 96.2%, respectively. From the above analysis, configurations of Fig. 6.8(a) and Fig. 6.8(b) exhibit better wide-band performance compared to Fig. 6.8(c) and Fig. 6.8(d) configurations.

6.4 Proposed absorber

In the final design step, all four hexagonal rings, namely, the center, 2nd, 3rd, and 4th absorber rings are merged to provide Ultra-wideband performance. Fig. 6.11 depicts the schematic unit cell configuration of the proposed HSRA.

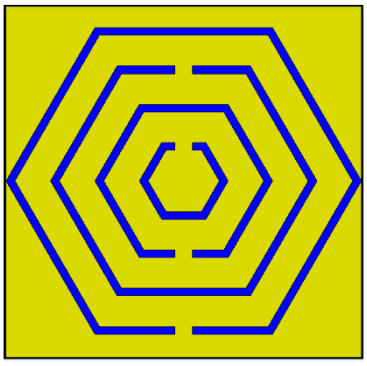

Fig. 6.11 Schematic view of the proposed absorber.

As depicted in Fig. 6.12, the proposed configuration provides ultra-wideband performance with a bandwidth of 2.01 THz and absorption bandwidth in a percentage of 102.8% (0.95-2.96 THz) for

absorption greater than 90%. The center frequency f_c can be obtained by $f_c = \frac{f_l + f_h}{2} = 1.95\ THz$, where f_l and f_h represent low and high frequencies.

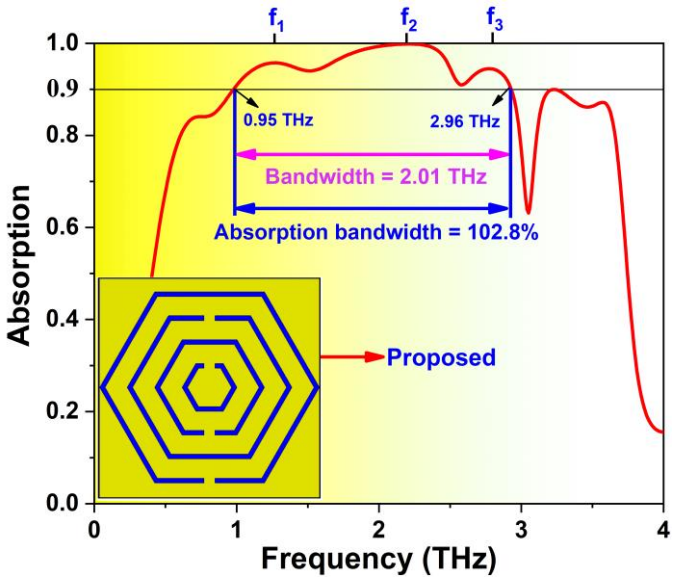

Fig. 6.12 Absorption spectra of proposed absorber

The proposed absorber provides absorption peaks at 1.24 (f_1), 2.21 (f_2), and 2.77 (f_3) THz with absorption rates of 96.1%, 100%, and 95.2 % respectively. Furthermore, 100% absorption is achieved from 2.07 to 2.33 THz making this a unique feature for THz applications. This peak absorption is mainly due to strong magnetic resonance. Fig. 6.13 illustrates the absorption spectra of the proposed absorber for TE and TM incidence. The proposed absorber achieved the same absorption spectra curve due to the symmetry of the absorber configuration.

6.5 Influence of physical parameters

In this section, the influence of physical parameters on the proposed absorber configuration is investigated by varying one parameter at a time and by keeping all other parameters unchanged. At first, the effect of variation of substrate thickness (t_s) is investigated and is depicted in Fig. 6.14(a). As the thickness of the substrate increases (from t_s=16μm to t_s=20 μm), there is a decrease in the absorptivity in the higher frequency region and gradually increases for t_s > 20 μm. At t_s=20 μm, the absorber provides an ultra-wideband response with perfect absorption.

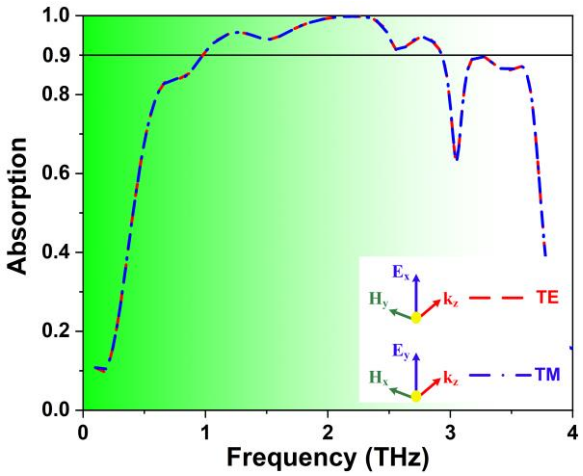

Fig. 6.13 Simulated absorption spectra for TE and TM incidence for the proposed absorber.

Fig. 6.15(a) shows absorber performance for change in graphene split gap (g). For lower values of the split gap, there is a decrease in the absorptivity in the lower frequency region and for higher values, there is a decrease in absorptivity in the higher frequency region. The absorber shows better absorption performance for a graphene split gap of 4 μm. Next, the effect of variation in the width of hexagonal rings (t_1) is investigated. As the width of the rings increases, the absorption decreases. From 1.5 THz to 1.76 THz and from t_1=2 μm to t_1=2.5 μm, the absorption is maintained close to 100 %. As t_1 is further increased (from t_1=2.5 μm to 3.5 μm) the absorption gradually deteriorates in the higher frequency region as depicted in Fig. 6.15(b), nevertheless, the absorption is still maintained above 85% in the absorption bandwidth. The excellent ultra-wideband absorption characteristics are shown for t_1 = 2 μm.

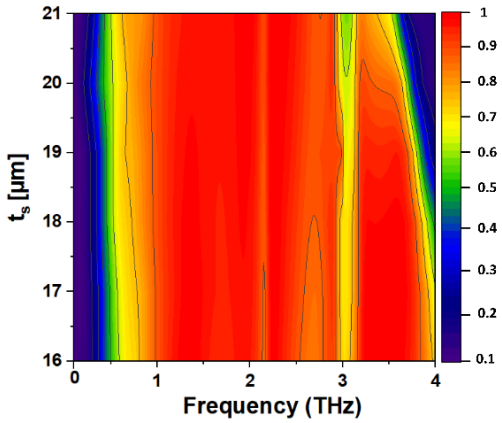

Fig. 6.14 Absorption performance for variation in substrate thickness (t_s).

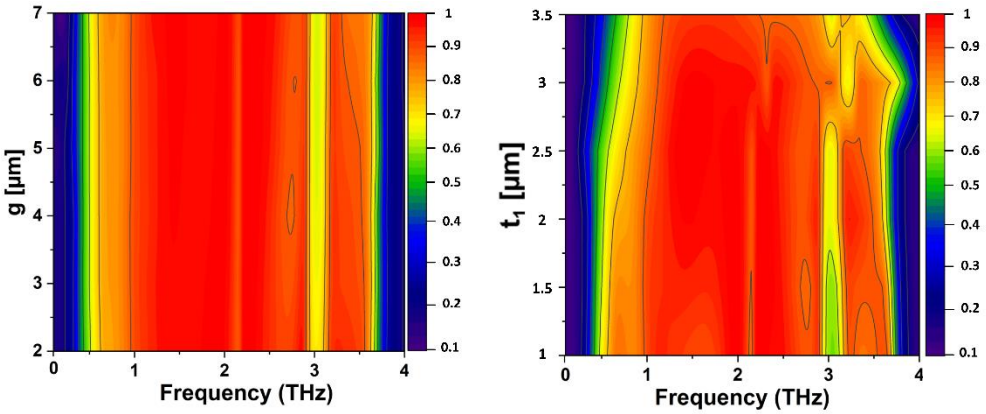

(a) (b)

Fig. 6.15 Absorption performance for variation in (a) graphene split gap (g) and (b) graphene ring width (t_1).

Fig. 6.16 shows absorption spectra for variation in graphene parameters. Fig. 6.16(a) depicts the absorber response for variation in graphene relaxation time (τ). The absorber shows the same absorption response for all the values of τ as illustrated in Fig. 6.16(a). Fig. 6.16(b) shows the absorber response for variation in graphene chemical potential (μ_c). As μ_c increases, there is a decrease in absorption as shown. But the absorber shows ultra-wideband absorber performance up to μ_c = 0.6 eV. For higher values of μ_c (0.8 eV and 1 eV), the absorber shows a decrease in absorption and exhibits 60 % absorption with a narrow band. Also, as μ_c increases, there is a shift in the absorption spectra towards the higher frequency region (right side). Hence, the proposed absorber is tunable with an increase in μ_c.

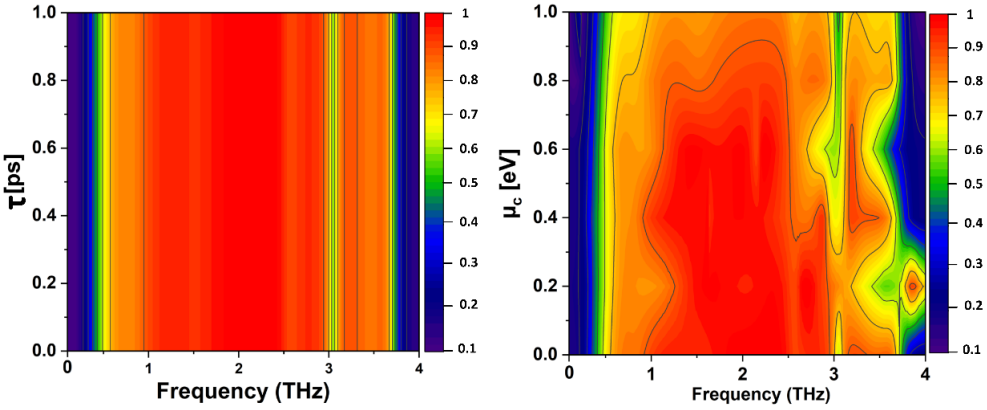

(a) (b)

Fig. 6.16 Absorption performance for variation in graphene (a) relaxation time (τ) and (b) chemical potential (μ_c).

Finally, the behavior of the absorber for variation in incidence angle (θ) and polarization angle (ϕ) is investigated. Fig. 6.17(a) shows absorption characteristics for different polarization angles from 0º to 89º with a step width of 10º. The absorber shows the same absorption characteristics for variation in ϕ because of the symmetry of the structure. The proposed absorber shows ultra-wide absorber characteristics for both TE and TM incidence as depicted in Fig. 6.17(b) and Fig. 6.17(c) with absorption > 90% up to an incidence angle of θ = 75º. The primary reason is that when the incidence angle increases up t0 75º, the magnetic flux remains constant, allowing magnetic resonance to be effectively induced in the absorber. For higher values of θ, the absorption reduces to 70 %. The reason is, when the incidence angle increases beyond 75º, the magnetic component of the incident wave decreases and hence it can no longer induce effective magnetic resonance. This signifies that the absorber is a very good candidate for THz applications with a wide angle of absorption.

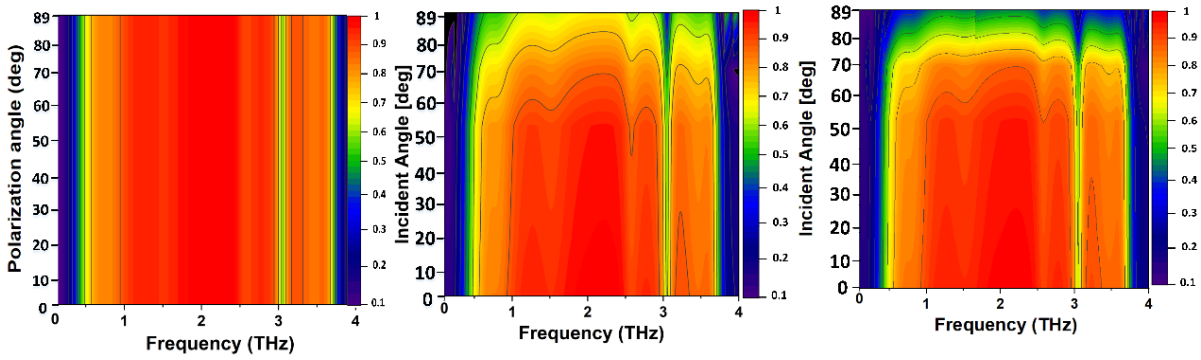

(a) (b) (c)

Fig. 6.17 Absorption performance for variation in graphene (a) polarization angle, (b) TE incident, (c) TM incident.

6.6 Resonant mode analysis

To know the resonant modal analysis of the proposed ultra-wideband absorber, Electric Field (EF) distribution (EFD), magnetic field (MF) distribution (MFD), and Surface current distribution at the absorption peaks with a normal incidence of EM wave at 1.24, 2.21 and 2.77 THz are depicted in Fig. 6.18, Fig. 6.19 and Fig. 6.20, respectively. Each hexagonal ring in the proposed structure is responsible for a unique concentration of surface current at a certain frequency.

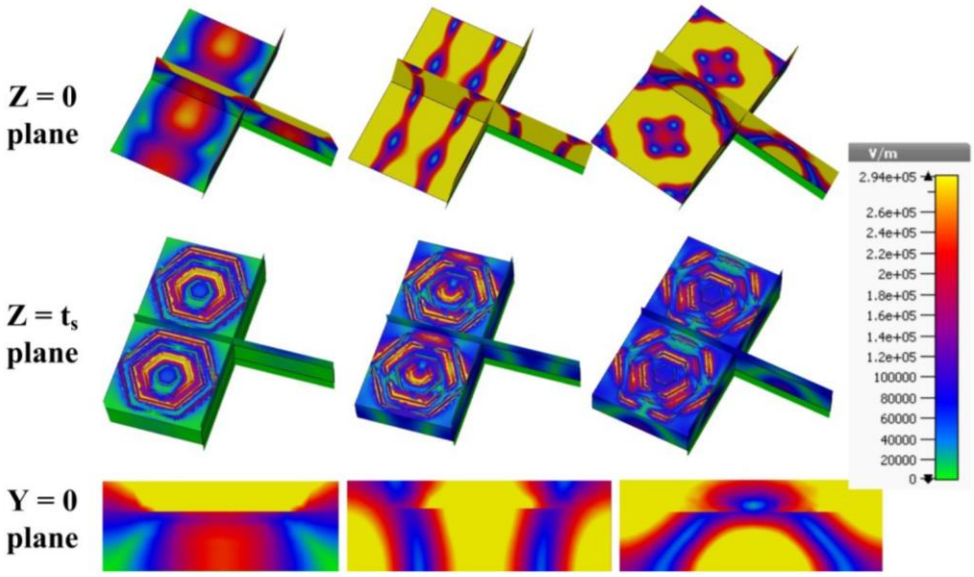

(a) (b) (c)

Fig. 6.18 EF distribution on proposed absorber at frequencies of (a) 1.24 THz, (b) 2.21 THz, and (c) 2.77 THz.

From the EF distribution plot (Fig. 6.18), the E-fields are vertically oriented in the absorber cells while the magnetic field (Fig. 6.19) is oriented horizontally form. This results in the formation of electric dipoles at the three resonant frequencies. It is also noted that with an increase in frequency there is an increase in the formation of electric dipoles inside the absorber. This increase in electric dipole formation is observed at resonant frequencies of 2.21 and 2.77 THz. The formation of electric dipoles leads to higher absorption for the incident EM wave normal to the surface. SC distribution for the proposed absorber is shown in Fig. 6.20. At 1.24 THz (Fig. 6.20(a)), from SC distribution, accumulation of charge is mostly on the 2nd, 3^{rd,} and 4th hexagonal rings. At 2.21 THz (Fig. 6.20(b)), the center also contributed to the resonance, and SC distribution is mostly centered on the center, 3^{rd,} and 4th ring respectively. At 2.77 THz (Fig. 6.20(c), SC distribution is mostly concentrated on the 2nd, 3rd, and 4th rings. Hence, from this analysis, it is clear that all the hexagonal rings are contributors to ultra-wideband absorption characteristics. The proposed absorber performance is compared with other recently published ultra-wideband research articles as shown in

Table 6.2. The proposed absorber shows ultra-wideband absorption with an absorption bandwidth of 108.2% with its simple structure. The proposed absorber is insensitive to polarization and it also shows high absorption for higher incidence angles up to θ=75^{o}.

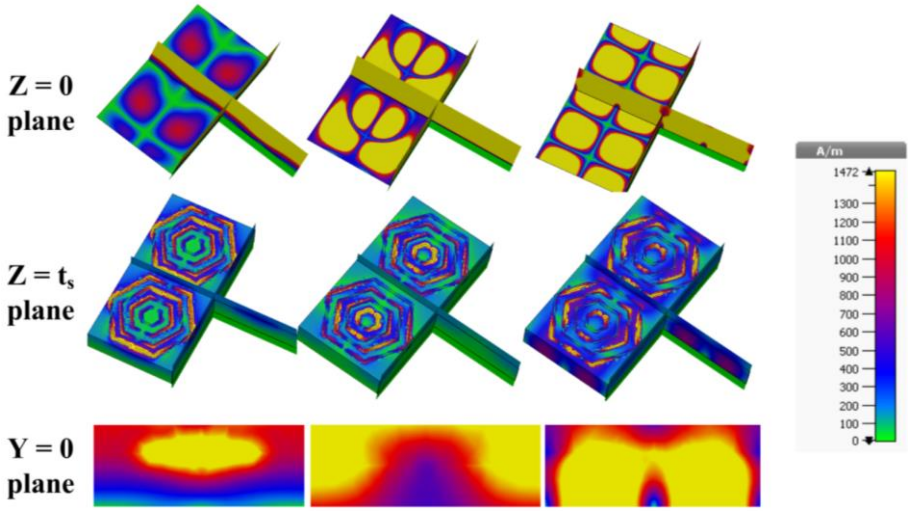

(a) (b) (c)

Fig. 6.19 MF distribution on proposed absorber at frequencies of (a) 1.24 THz, (b) 2.21 THz, and (c) 2.77 THz.

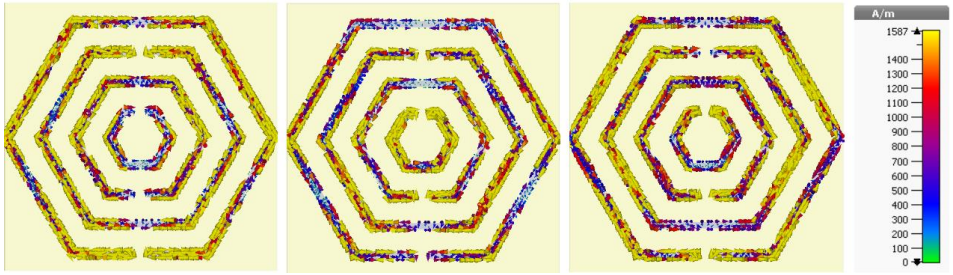

(a) (b) (c)

Fig. 6.20 SC distribution on proposed absorber at frequencies of (a) 1.24 THz, (b) 2.21 THz, and (c) 2.77 THz.

Moreover, 100% absorption is achieved from 2.07 to 2.33 THz making this a unique feature for THz applications. Furthermore, the proposed absorber does not use metallic ground for obtaining the ultra-wideband characteristics. The use of metals may cause backscattering which deteriorates the ultra-wideband characteristics of the proposed absorber. This problem can be avoided using the proposed metal-free graphene-based absorber. The proposed ultra-wideband absorber could be employed for THz applications including solar energy harvesting, photodetectors, Photoacoustic - based sensing, and high-resolution printing.

Table 6.2 Comparison table

Ref	Material	Bandwidth	Center frequency (f_c)	Absorption Bandwidth in %	Polarization insensitivity	Incident angle (θ) for Absorptivity > 90 %	
						TE	TM
[92]	Metal	1.3-2.7 THz	2 THz	70%	No	-	-
[166]	Graphene	1.38-3.12 THz	2.25 THz	77.3 %	No	45°	40°
[167]	Graphene	1.27-2.08 THz	1.675 THz	48 %	No	70°	-
[156]	Graphene	1.1-1.86 THz	1.48 THz	51%	No	50°	60°
[157]	graphene/metallic	4.56–9.02 THz	6.79 THz	65.68%	Yes	-	-
[158]	Graphene	1.51–8.25 THz	4.88 THz	138.1%	-	-	-
[152]	Graphene and STO	3.04 - 5.77 THz	4.405 THz	61.9 %	Yes	55°	50°
[168]	VO_2	1.43-3.44 THz	2.442 THz	82%	Yes	45°	45°
[169]	Graphene	1.15-2.73 THz	1.94 THz	81%	Yes	60°	60°
[170]	Dielectric	0.6-1.7 THz	1.15 THz	95.65%	No	45°	40°
[159]	VO_2	1.2-3.2 THz	2.2 THz	90.9%	No	50°	50°
[171]	Graphene	1.6-3.2 THz	2.4 THz	66.66%	No	50°	-
This absorber	Graphene (Metal Free)	0.95-2.96 THz	2.01 THz	102.8%	Yes	75°	75°

6.7 Conclusion

An ultra-wideband THz absorber is designed using graphene-based hexagonal split rings. Four graphene HSRs are used for the generation of ultra-wideband characteristics with absorption greater than 90 %. The proposed absorber achieves ultra-wideband absorption characteristics from 0.95 THz to 2.96 THz with a percentage bandwidth of 102.8% and bandwidth of 2.1THz with absorptivity beyond 90%. Also, 100% absorption is achieved from 2.07 to 2.33 THz making this a unique feature for THz applications. The modes generated within the graphene split rings are merged for achieving an ultra-wideband response. Moreover, the absorber exhibits polarization

insensitivity along with wide incidence angle variation for both TE and TM modes making it useful for solar and photovoltaic cells. The absorber provides tunability characteristics with variation in graphene chemical potential and exhibits a narrow absorption response for $\mu_c > 0.8$ eV which can also be utilized for sensor applications.

Chapter 7

Dielectric Metamaterial Absorber for biosensing applications

7.1 Introduction

In this chapter, Dielectric based Metamaterial Absorber is designed for biosensing applications. THz spectrum has piqued the interest of researchers due to its dual characteristics of microwave and infrared frequency bands [171]. THz waves, like infrared, will radiate in a single direction and, like microwaves, travel through various non-conducting materials [172]. Many devices are implemented in the THz regime, like antennas, for communication, absorbers, sensors, spectroscopy, and imaging for various applications [117], [128], [173], [174]. Absorbers are currently being researched for use in a variety of fields, including medicine, defense, and communication [79]. Different types of absorbers are implemented, such as ultra-wide [175], wideband [176], multiband [177], and narrow-band absorbers [178]. For the absorber to be used for biosensor applications [179], [180], narrow or ultra-narrow band absorbers with low values of full-width half maximum (FWHM), high sensitivity, high figure-of-merit (FOM) high-quality factor (Q) are required [148]. In the past few years, metamaterial (MM), an artificial material with exceptional characteristics made up of periodic arrays of unit cells with a size smaller than $\lambda_g/4$ (λ_g: Guided Wavelength), has been a major focus of THz structures [1], [181]. Metals are an excellent possibility for the THz absorber, but their poor electrical characteristics and temperature sensitivity over wide frequency range limit devices from operating at higher frequencies [182]. Furthermore, these devices are highly susceptible to temperature changes, and their lifetime is restricted due to

oxidation and corrosion in metals [183]. Graphene in the absorber structure has been developed recently, which allows frequency tuning, but it complicates fabrication [140], [184]. Few metal-free absorbers are also implemented using graphene, which provides tunability capability [163], [174], [185], [186]. Recently, dielectric-based absorbers have been implemented at THz frequency [146], [176], [187], [188]. Compared to graphene-based absorbers, the fabrication of dielectric MM-based absorbers (DMMA) is feasible in the present era [146]. Obtaining narrow or ultra-narrow absorption frequency response with low thickness structure and simple design is highly recommended. Furthermore, obtaining high sensitivity, high FOM, and high Q is still a challenging task in dielectric-based absorbers. Also, the absorber must be capable of sensing different diseases such as cancerous blood cells [189], malaria, dengue and other chemicals [1], [146]. Previously, individual absorbers are designed to identify these diseases. However, a single sensor capable of sensing these diseases must be designed. In fact, in the case of a dielectric-based absorber, attaining the ideal absorption required for biosensing applications is still challenging [190].

In summary, the research highlighting the advancement of DMMA is as follows: (i) Decreasing the thickness of the absorber to make it compatible with nanotechnology systems, (ii) attaining suitable performance parameters with requisite ideal ultra-narrow absorption which can adequately be used in biosensing applications, (iii) Simple structure must be designed which reduces the difficulty in fabrication, (iv) capable of sensing different diseases and chemicals with a single design.

Here, two absorbers are designed for biosensing applications:

1. For detecting cancerous cells.
2. For detecting dengue.

Apart from detecting these diseases, the proposed sensors are capable of sensing malaria in blood and glucose content in the water.

7.2 DMMA for detecting cancerous and other diseases

The proposed structure is ultrathin and provides ultra-narrow full-width half maximum (FWHM) dual response, with high sensitivity, high FOM, and a very high-quality factor (Q). Also, the proposed absorber is polarization insensitive and is capable of sensing cancerous blood cells along with malaria and other chemicals, as reported in later sections. The absorber provides dual-band

response with perfect absorption with ultra-narrowband absorption characteristics with resonances at 5.98 THz and 6.72 THz.

A simple dielectric-based metamaterial absorber structure is implemented to address the above issues. The proposed structure consists of a silicon square split ring (SSSR) with ultrathin thickness compared to the structures reported in [1], [93], [191]. A graphene circular split ring (GCSR) is placed in the center of the structure, which changes electric and magnetic dipoles, allowing for perfect absorption. The easy design and availability of silicon material may significantly reduce fabrication difficulty, which is currently a significant challenge in THz development [146]. Furthermore, the proposed biosensor shows the highest sensitivity of 0.5 (THz/TU) (TU: Thickness Unit) and 0.4625 (THz/TU) with a high FOM of 33.33 (TU^{-1}) and 43.24 (TU^{-1}) and with high Q of 394.2 and 624.4 during analyte thickness sensing in the lower band (LB) and upper band (UB) respectively. For refractive index sensing, the sensor shows a sensitivity of 1.9 (THz/TU) and 1.45 (THz/TU) with a high FOM of 126.6 (TU^{-1}) and 100 (TU^{-1}) and with a very high Q of 470.8 and 560 is exhibited in the LB and UB respectively. Also, the proposed sensor shows excellent performance characteristics for sensing cancerous cells, malaria, and other chemicals. These features make the proposed biosensor new in the dielectric-based sensors field that can sense different diseases and chemicals using a single sensor.

7.2.1 Design Considerations

Fig. 7.1(a) shows the schematic unit cell structure of the proposed DMMA in perspective view. It comprises a bottom gold layer with $p_x = p_y = 80$ μm periodicity along the x and y-axis. The gold layer with frequency-independent conductivity of $\sigma = 4.09 \times 10^7\ S/m$ is grown at the bottom of the silicon dioxide (SiO_2) substrate having a relative permittivity of ε_s=2.25 and thickness of t_s=2 μm. SSSR is placed on the top of the SiO2 layer with a relative permittivity of 11.9 and a thickness of t_{dra}=4 μm. The square split ring has a gap of g_s = 4 μm, and a length and width of $L_s = W_s$ = 50 μm. The SSSR is utilized as a resonating unit of the absorber, and the dimensions are chosen based on the procedure exhibited in [146], [188], [192]. The length and width of the silicon ring are of the order of L_s and W_s. Fig. 7.1(b) shows the proposed absorber in the top view, along with dimensions. The proposed absorber resonates at dual-band with a narrow frequency response. Fig. 1(b) shows the periodic arrangement of the proposed absorber. As illustrated in Fig. 7.1(c), the

absorber structure consists of a graphene-based circular split ring (GCSR) with a thickness of 0.34 nm, inner and outer ring radius of r_{go}= 9.5 µm and r_{gi}= 7.5 µm, respectively, with a split gap of g_c = 0.1 µm. The addition of graphene offers tunability and also enhances the frequency response of the structure by varying external electrostatic bias [193]. The electrical properties of graphene are considered based on the literature [194], [195]. Initially, the chemical potential of graphene is taken as μ_c = 0 eV at a temperature of T = 300K, with a relaxation time of τ = 0.1 ps.

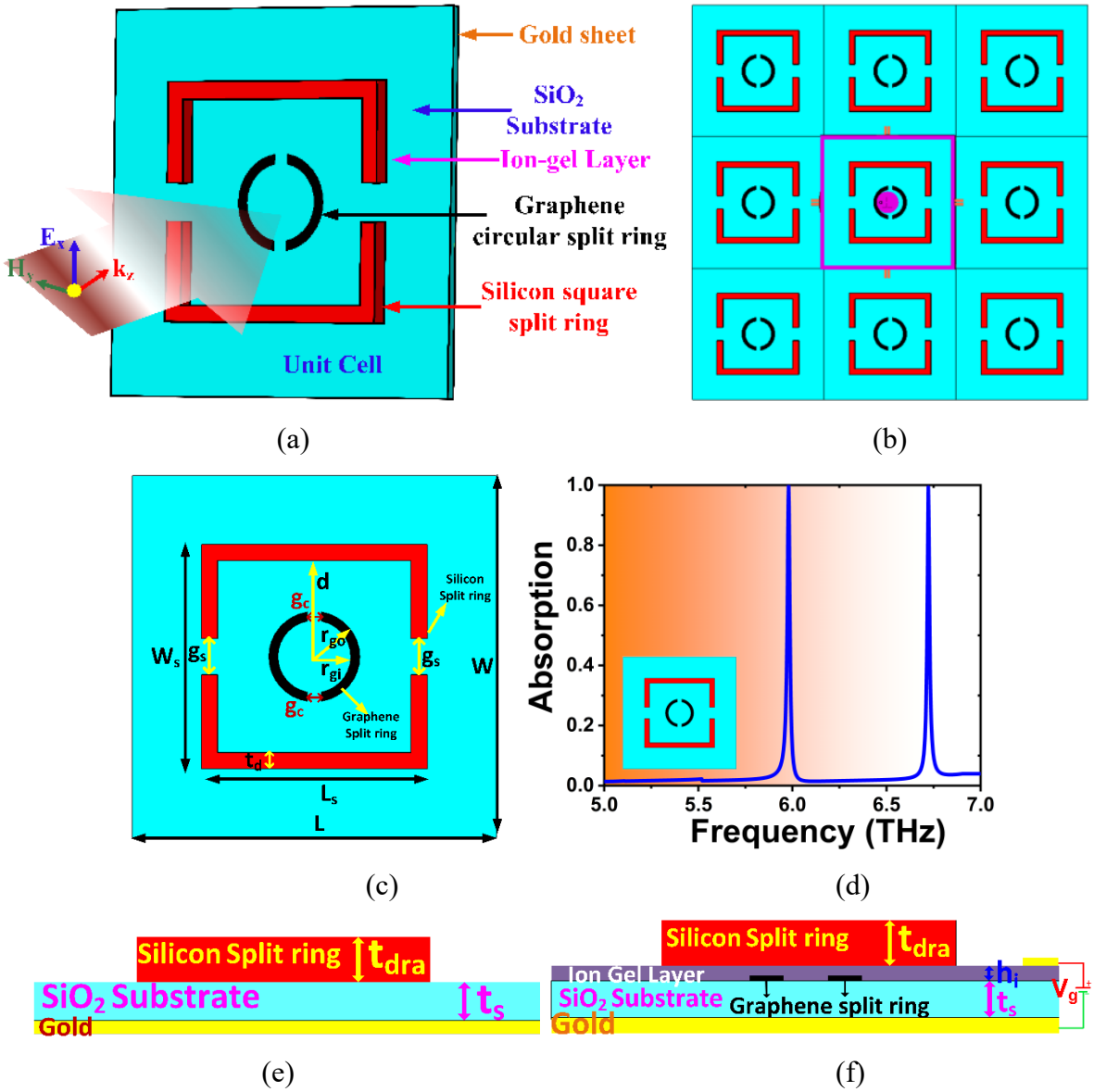

Fig. 7.1 Proposed absorber its (a) Perspective view, (b) Periodic arrangement, (c) Top view with dimensions, (d) Absorption coefficient, (e) Side view without GCSR, and (f) Side view with GCSR.

Fig. 7.1(d) depicts the proposed absorber's dual-band absorption behavior with absorption rates of 99.963 and 99.882 at a frequency of 5.98 and 6.72 THz, respectively. Fig. 7.1(e) depicts the side view of the proposed absorber structure without GCSR. The ion-gel layer of height h_i = 0.1 μm, as depicted in Fig. 7.1(f) is utilized for electrostatic biasing on the graphene ring to achieve adjustability and controllability in the absorber characteristics [146], [194]. Accordingly, the dimensions of the proposed structure are chosen so that the structure can be used as a bio-sensor in analyzing cancer, malaria, viruses, chemicals, and diseases.The use of a GCSR allows surface plasmons to form at the graphene-air contact, trapping the electric charge along its inside and outside edges [195], [196]. Because of the high concentration of produced graphene surface plasmons, the GCSR will not provide a new resonance and instead changes the absorption rate acquired by the SSSR. Hence, the GCSR is positioned in the structure's center, allowing the induced dipoles to be governed by the bias voltage fed to the GCSR. The final dimensions are optimized in CST microwave studio. A frequency-domain solver with a mesh cell size of 102 cells per wavelength and a total number of tetrahedrons of 1,73,361 is utilized for simulation. Because the graphene layer thickness is thin in relation to the absorber size, the adaptive mesh parameters keep the mesh cell size small [196].

7.2.2 Evolution of Proposed Absorber

The evolution of the absorber and corresponding absorption plots during the evolution stage of the proposed absorber are illustrated in Fig. 7.2 and Fig. 7.3. It can be observed for absorber-1 (gold sheet), which provides zero absorption and acts as a perfect reflector. Similar behavior is observed for absorber-2 (SiO_2 layer). The absorber-3 configuration consists of an SSSR resonator. The addition of SSSR provides resonance at 6.16 and 6.84 THz, respectively, with absorption percentages of 98.7 and 98.5 %. Furthermore, this structure offers a narrow absorption band spectrum. A GCSR with a thickness of 0.34 nm, with an ion gel layer (ε_r =1.89) coating, is added at the center of the structure, as illustrated in Fig. 7.2(Absorber-4). The addition of a graphene split ring enhances the absorption coefficient by shifting the resonant frequency toward a lower frequency. Because of graphene's tunability characteristics, there will be a shift in resonance frequency [146], [174], [197]. According to Kubo's formula and as described in [174], [197], tuning of resonant frequency happens because of the reconfigurability property of the surface charge conductivity of graphene [174], [185]. The shift towards lower frequency is because the oscillating

length of charge becomes larger with the addition of graphene, and with an increase in the inner or outer radius of graphene, the resonant frequency tends to shift towards the lower side [42]. As illustrated in Fig. 7.3, the absorber-4 (Proposed) configuration provides resonance at 5.98 and 6.72 THz, respectively, with a percentage of absorption of 99.963 and 99.33 %. The absorption is obtained using the equation, A=1-R-T where, A is the absorption coefficient, R is the reflection coefficient, and T is transmittance.

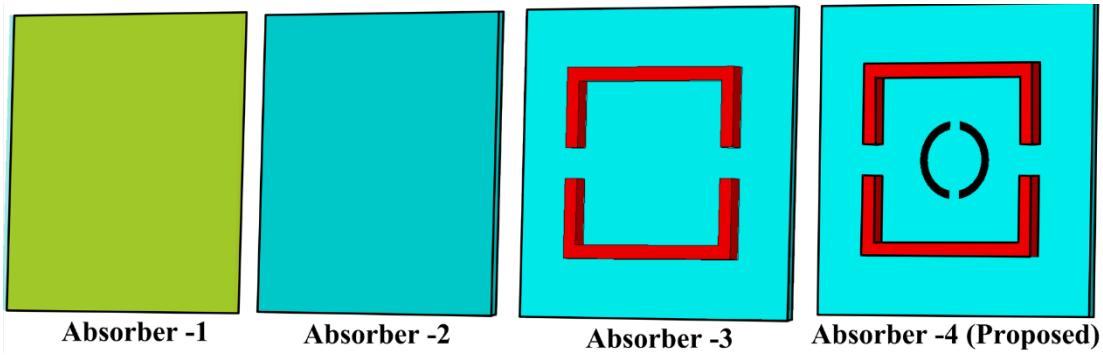

Fig. 7.2 The Proposed absorber evolution.

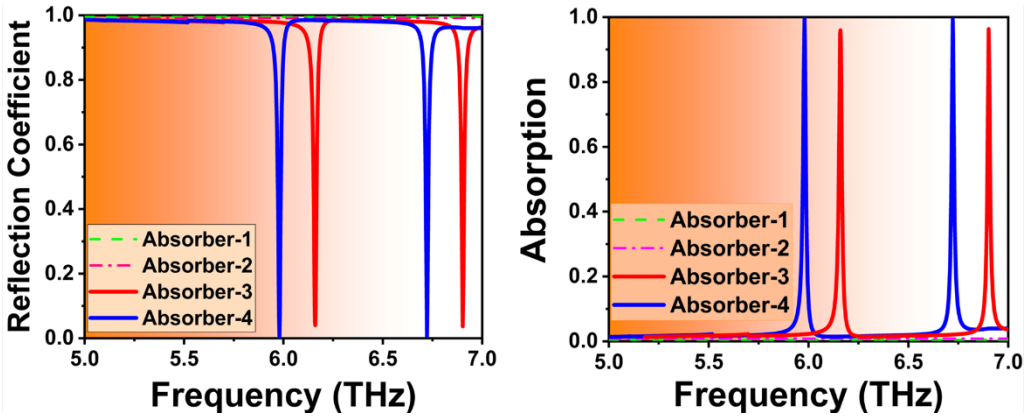

(a) (b)

Fig. 7.3 Absorption characteristics during different stages (a) Reflection coefficient, (b) Absorption coefficient.

The gold metallic layer at the bottom of the structure provides zero transmittance (T≈0). Hence the value of reflectance must be as low as possible so that A must be equal to 1. The proposed absorber configuration provides perfect absorption with a narrow absorption spectrum at both the bands with a Full-Width Half Maximum (FWHM) of 0.017 THz at LB and 0.015 THz in the UB, respectively.

Hence, the Q of the proposed absorber is also high. As a result of its high Q and small FWHM, the proposed absorber can be utilized as a bio-sensor to detect a variety of diseases and chemicals.

7.2.3 Modal Analysis

In this section, the electric field distribution (EFD) and magnetic field distribution (MFD) are studied to understand the proposed absorber's operation mechanism. Fig. 7.4 shows the EFD and MFD without a graphene split ring at two resonant frequencies. In dielectric-based resonators, it is evident that both electric dipole (ED) and magnetic dipoles (MD) will be created inside the dielectric [146], [192]. As shown in Fig. 7.4, the surface plasmons created at both resonant frequencies are high on the split ring resonator. It is inferred from Fig. 7.4(c) and Fig. 7.4(e), at the lower band (6.16 THz), the EF vectors encircle the linearly distributed MF vectors forming a magnetic dipole in the silicon split ring. As depicted in Fig. 7.4(d) and Fig. 7.4(f) at 6.84 THz, the linearly distributed EF vectors are encircled by MF vectors forming an electric dipole in the silicon split ring at the upper band. As a result, the absorber without the graphene ring functions in two modes: fundamental MD in the LB and fundamental ED in the UB.

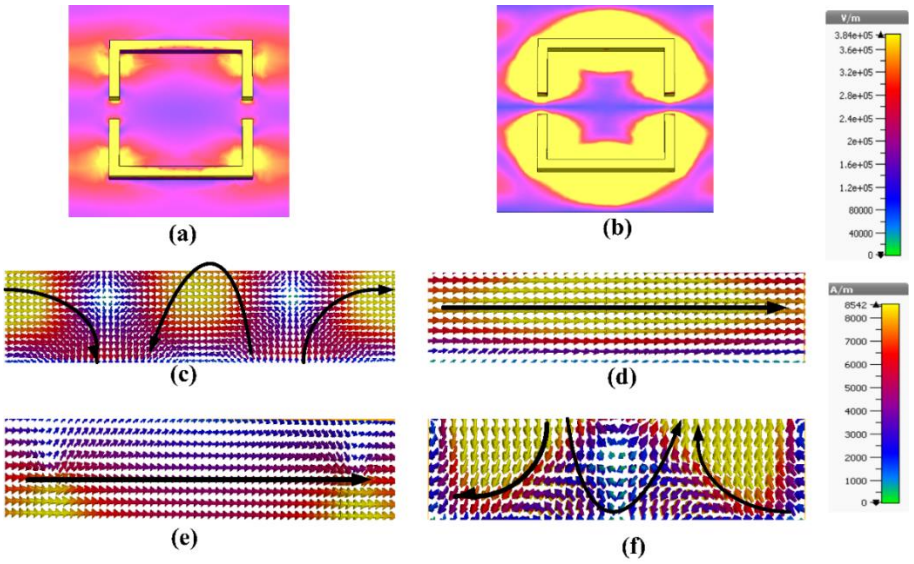

Fig. 7.4 The EFD in the absorber-3 (Without GCSR) at a frequency of (a) 6.16 and (b) 6.84 THz. The EF vector distribution at a frequency of (c) 6.16 and (d) 6.84 THz. The MF vector distribution at (e) 6.16 and (f) 6.84 THz.

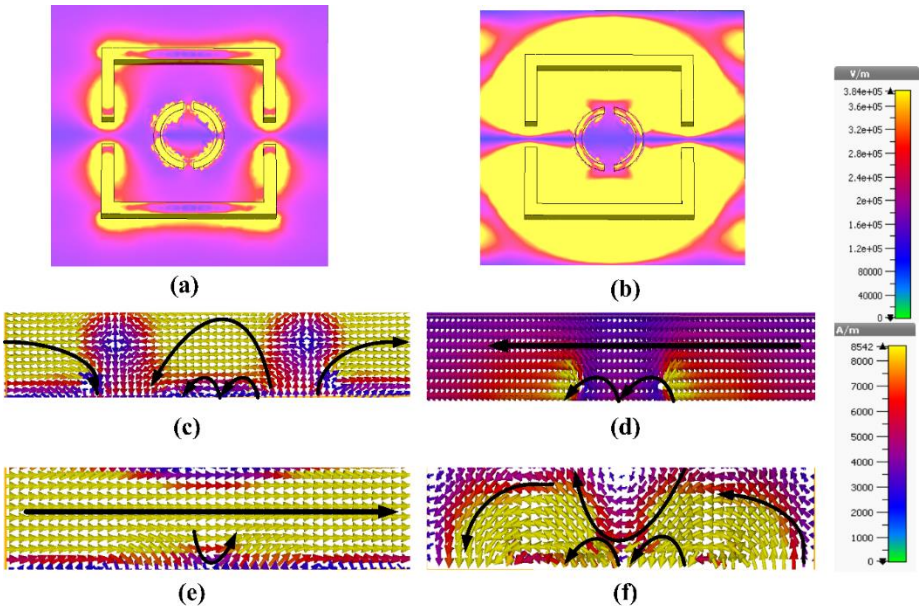

Fig. 7.5 The EFD in the proposed absorber (With GCSR) at a frequency of (a) 5.98 and (b) 6.72 THz. The EF vector distribution at a frequency of (c) 5.98 and (d) 6.72 THz. The MF vector distribution at (e) 5.98 and (f) 6.72 THz.

Fig. 7.5 illustrates the EFD and MFD in the proposed DMMA with GCSR at both resonant frequencies of 5.98 and 6.72 THz. The addition of GCSR enhances field distribution at LB and UB by creating high surface plasmon density, as shown in Fig. 7.5. From Fig. 7.5(c) and Fig. 7.5e), it is inferred that at the lower band (5.98 THz), the linearly distributed MF vector is encircled by the EF vectors forming a magnetic dipole at the lower band. From Fig. 7.5(d) and Fig. 7.5(f) at 6.72 THz, the linearly distributed electric field vectors are encircled by magnetic field vectors and result in the formation of an electric dipole at UB. The additional loops formed in the field distribution at LB and UB infers to the increase of absorptivity by the addition of GCSR. These circulating fields created by incident EM waves around the split rings built a capacitance. Thus, the absorbance or resonance can also be due to the inductive-capacitive resonance.

7.2.4 Stability Analysis

The proposed absorber is investigated for TE and TM incidence, and the behavior of absorption characteristics for variation in incidence angle (θ) is also examined. As depicted in Fig. 7.6(a), the frequency response for TE and TM incidence shows similar absorption properties. This is because of the symmetrical structure of the proposed absorber. A narrow band absorption spectrum is

observed at both bands for both TE and TM incidence. This narrow absorption bandwidth (BW) leads to strong frequency selectivity. This results in high Q, which is promising for sensor-related applications.

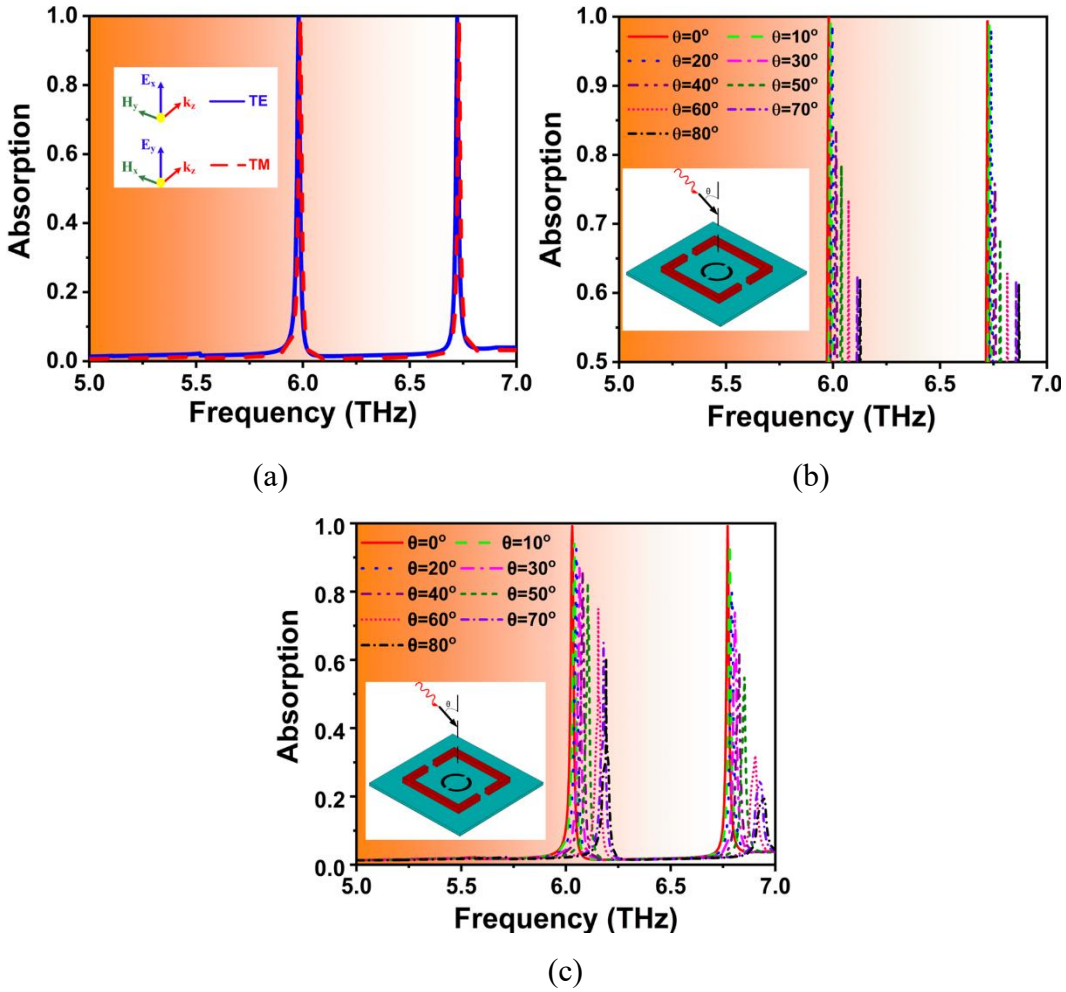

Fig. 7.6 Absorption characteristics for proposed absorber (a) TE and TM incidence and under different θ for (b) TE and (c) TM modes.

Fig. 7.6(b) shows absorption characteristics for variation in incidence angle. With an increase in θ, absorptivity decreases, as inferred from Fig. 7.6(b). The absorber shows good performance throughout the θ variation with more than 80% absorption up to $\theta<60^{o}$ and provides absorption greater than 60% for $\theta>60^{o}$. For TE incidence, as depicted in Fig. 7.6(b), the LB absorption peak is located at 5.98 THz, and the UB absorption peak is located at 6.722 THz, with absorptivity of 0.9995 and 0.9988, respectively, for $\theta=0^{o}$. However, for TM incidence, as depicted in Fig. 7.6(c), the LB is located at 6.0328 THz and UB is located at 6.781 THz, with absorptivity of 0.9985 and

0.9983, respectively, for θ=0º and also provides absorption greater than 80% up to θ=50º for the UB whereas, it provides greater than 80% up to θ=40º for the LB. It is observed for TM incidence that for higher values of θ (>50º), the UB deteriorates gradually due to impedance mismatch [10]. The above analyses thus demonstrate that the proposed absorber performs well for both TE and TM polarizations across a broad range of θ.

7.2.5 Parametric analysis of physical dimensions

The performance analysis of the proposed absorber for parametric changes in the physical dimensions is illustrated in this section. One parameter is changed at a time, while the remaining parameters are unchanged. Initially, the height of the SSSR (t_{dra}) is the primary focus of the investigation. For different values of t_{dra}, the absorption characteristics are examined for varying frequency, as depicted in Fig. 7. 7(a). Here the t_{dra} is varied from 2.5 µm to 5 µm at a step of 0.5 µm. It is observed that the proposed absorber shows good absorber performance with absorptivity greater than 95.5% for different values t_{dra} at both bands. For t_{dra} = 4 µm, the proposed absorber offers excellent perfect absorption (99.99%) performance with narrow absorption BW at LB and UB, respectively. Furthermore, with an increase in t_{dra}, there is a shift in resonance towards lower frequency, and also, for higher values of t_{dra} number of resonant peaks increases. To keep the ultrathin geometry, the smallest value of t_{dra} is chosen. Choosing a considerably smaller value of t_{dra} is also possible at the expense of almost complete absorption. This indicates how changes in t_{dra} can affect the spectra of the SSSR, which may cause the absorber response to exhibit more resonance peaks. The next investigated parameter is the width of the square split ring (t_d). Here t_{dra} is chosen as 4 µm from the above analysis. Fig. 7. 7(b) shows the absorption behavior for variation in t_d from 4 µm to 6.5 µm with a step change of 0.5 µm. The proposed absorber shows good performance with absorptivity greater than 95% for different values of t_d at both bands. There is a slight shift in the resonant frequency towards lower frequency with variation in t_d, and less absorption is exhibited for lower values of t_d. For t_d=5µm, the proposed absorber shows excellent absorption performance with narrow BW at both LB and UB, respectively. Next, Fig. 7. 7(c) shows absorption characteristics with variations in the thickness of the substrate (t_s). Here, t_{dra} and t_d were chosen as 4 µm and 5 µm, respectively, and substrate thickness (t_s) is varied from 1.6 to 2.6 µm with a step change of 0.2 µm. Good absorption performance is observed with more than 88% absorptivity for t_s varying from 1.6 to 2.6 µm. The proposed absorber shows narrow absorption

BW with perfect absorption at both lower and upper bands, respectively, for t_s=2 µm. The variation in t_s provides the shift in resonant frequency due to variation in the effective thickness of the absorber unit cell. The absorption characteristics for variation in circular graphene inner radius (r_{gi}) is examined as shown in Fig. 7. 7(d). The absorber shows good absorption performance with more than 90% absorptivity for variation of r_{gi} from 6.5 to 9 µm with a step change of 0.5 µm. For lower values of r_{gi}, the absorption is low and increases for higher values. For r_{gi}=8µm narrow absorption BW with perfect absorption is noticed. Furthermore, with an increase in r_{gi}, the resonant frequency shift towards a lower frequency. Fig. 7. 7(e) shows the absorber performance for varying outer graphene radius (r_{go}) from 8.5 µm to 11 µm at a step change of 0.5 µm. It is observed that for r_{go}=9.5 µm, perfect absorption is observed. A shift in absorption frequency is observed for variation in r_{go}. It is clear that there is a shift in absorption spectra with a change r_{gi} and r_{go}, and these values are selected at the extent of perfect absorption. Fig. 7. 7(f) and Fig. 7. 7(g) depict the absorber performance with change in the SSSR gap (g_s (µm)) and GCSR gap (g_c (µm)). For lower values of g_s, the absorber exhibits more resonance peaks with reduced absorption. Hence the choice of g_s can be chosen at the extent of perfect absorption. For SSSR split gap of g_s = 4 µm, the configuration shows excellent absorption levels at both bands, as depicted in Fig. 7. 7(f).

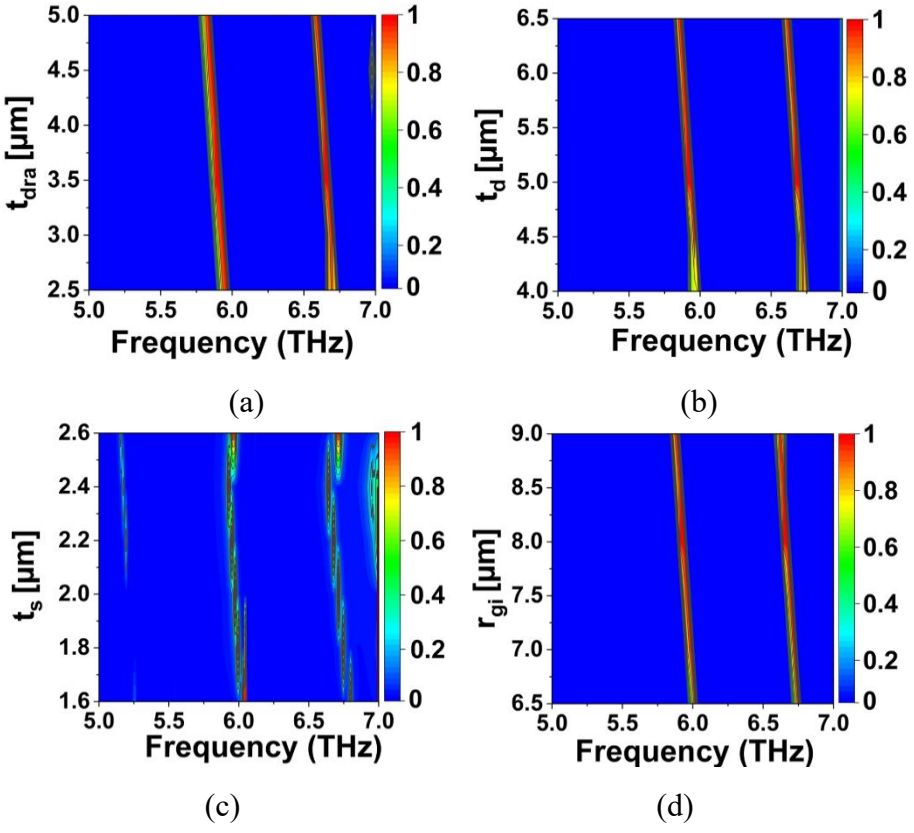

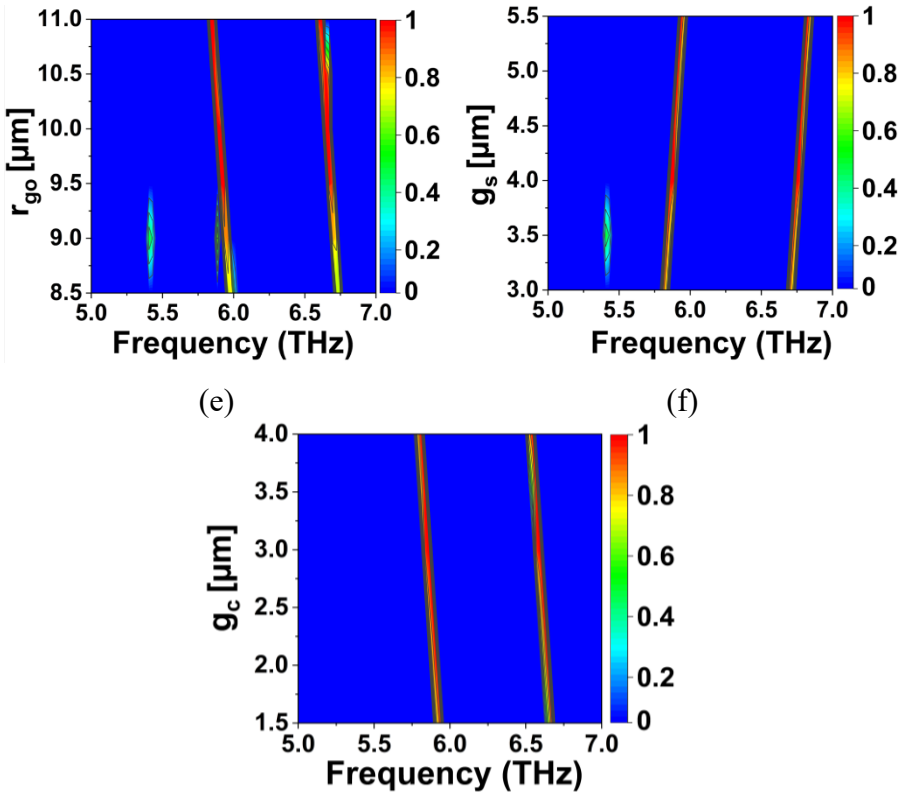

Fig. 7. 7 Absorption characteristics for proposed absorber for variation in (a) t_{dra}, (b) t_d, (c) t_s, (d) r_{gi}, (e) r_{go}, (f) g_s, and (g) g_c.

From the plot of Fig. 7. 7(g), it is observed that the configuration shows excellent absorption characteristics for the GCSR split gap of g_c = 3 µm. Thus, the parameter dimensions are selected from the above analysis, which achieves a high absorption rate at both LB and UB, respectively, with very narrow absorption BW. The narrow absorption band leads to strong frequency selectivity and increases Q, which is desired for bio-sensing applications.

7.2.6 Graphene parameters analysis

Fig. 7.8 shows absorption characteristics for the proposed absorber for variation in graphene chemical potential (μ_c) and relaxation time (τ).

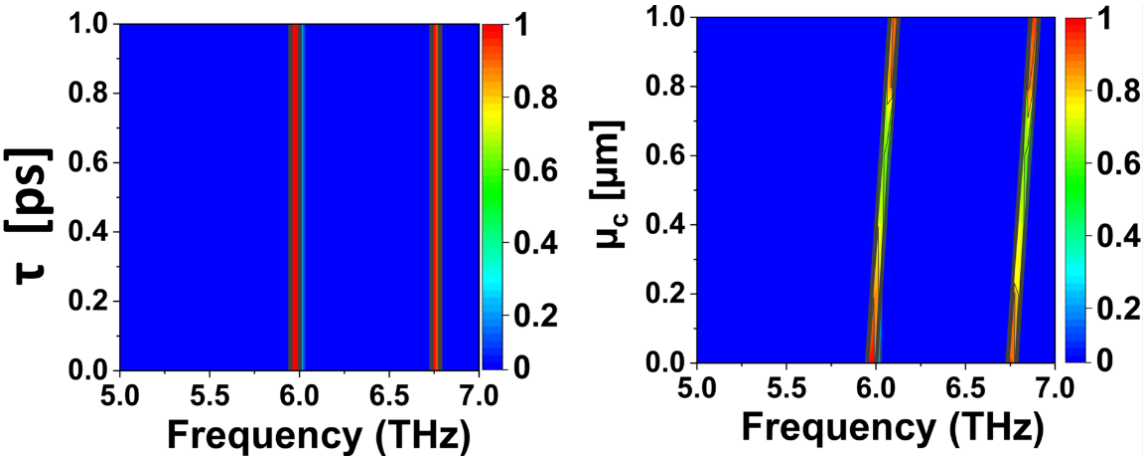

(a) (b)

Fig. 7.8 Absorption characteristics for proposed absorber for variation in (a) μ_c and (b) τ.

The parameters are selected from the above parametric analysis. Fig. 7.8(a) shows absorber performance for varying graphene chemical potential (μ_c) from 0 eV to 1 eV. For $0.1 < \mu_c < 0.4$ eV absorber shows less absorption rate of 0.75 and also for $\mu_c > 0.5$ eV absorber shows 0.8 absorption rate. The absorber shows good performance for $\mu_c = 0.4$ eV. Fig. 7.8(b) shows absorber performance for varying graphene relaxation time (τ) from 0 ps to 1 ps. As discussed previously, adding graphene enhances the absorption and does not change the number of resonant peaks. Hence, for all the values of τ, absorber performance remains unaffected with variation in τ and does not change its resonant frequency or absorption rate.

7.2.7 High-Quality Factor THz Sensor

As inferred from Fig. 7.1(f), the proposed absorber shows very narrow absorption characteristics with a Full-Width Half Maximum (FWHM) of 0.017 THz in the LB and 0.015 THz in the UB, respectively. The Q is calculated using the equation $Q = f_p / fwhm$, where f_p is peak frequency [1], [146], [189]. The calculated Q in the LB is 351.76 and 448 in the UB, respectively. The high Q and low FWHM makes the proposed absorber suitable for sensor applications for examining different analytes or test medium in the THz region. Moreover, the simple design, ultrathin structure, and high Q make the proposed absorber new in dielectric-based sensor applications.

7.2.8 Variation in t_a and its sensing

The proposed absorber's applicability for varying test medium thickness (t_a) is examined. The refractive index (n) of the analyte is chosen as 1.4. For sensor-based applications, sensitivity (S),

Q, FWHM, and FOM are the key parameters in this analysis since they show the accuracy of the absorber's sensing characteristics. The proposed sensor is depicted in Fig. 7.9(a) with a test medium with a t_a thickness on top of the DMMA. Fig. 7.9(b) illustrates the change of absorption frequency and absorptivity when t_a varies from t_a=0.1µm to t_a=2µm. Fig. 9(c) shows plots of S and shift in resonant frequency (Δf) for change in analyte thickness, Δt_a. Sensitivity for change in analyte thickness is calculated as $S = \Delta f / \Delta t_a$ (THz/TU) [1], [146], [189]. Sensitivity mainly computes the shift in the resonant frequency for a change in analyte thickness. The higher the sensitivity, the better the sensor. Change in analyte thickness (Δt_a) is computed as $\Delta t_a = t_{a1} - t_{a2}$ where t_{a1} is current, and t_{a2} is the previous thickness value of the analyte. The DMMA provides a maximum S of 0.5 (THz/TU) and 0.4625 (THz/TU) in the LB and UB, respectively, for t_a = 1.2 µm. A plot of FOM and FWHM for change in t_a is illustrated in fig. 9(d). FOM is computed using FOM=S/FWHM [1], [146], [189]. FOM is also an important parameter to evaluate the sensor's performance. The proposed absorber shows extremely low FWHM values of 0.015 THz and 0.0107 THz in the LB and UB, respectively. A very high FOM of 33.33 (TU^{-1}) in the LB and 43.242 (TU^{-1}) in the UB is obtained for t_a = 1.2 µm.

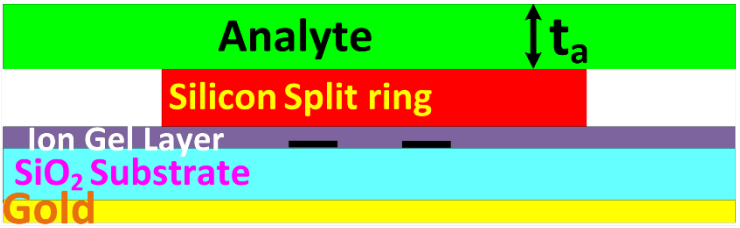

(a)

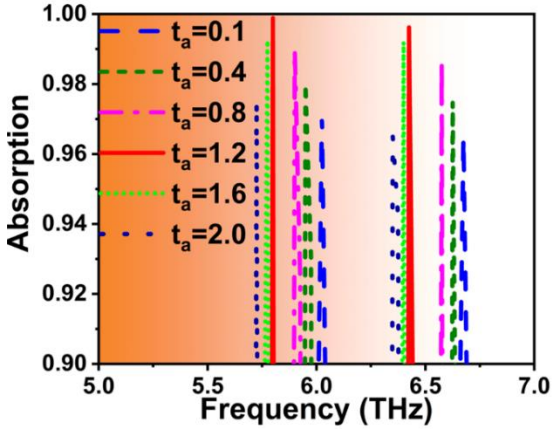

(b)

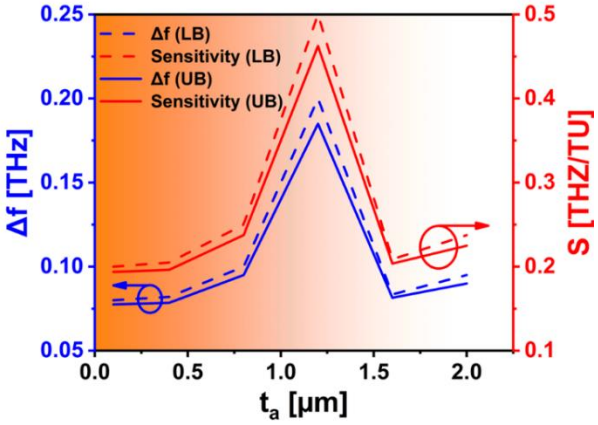

(c)

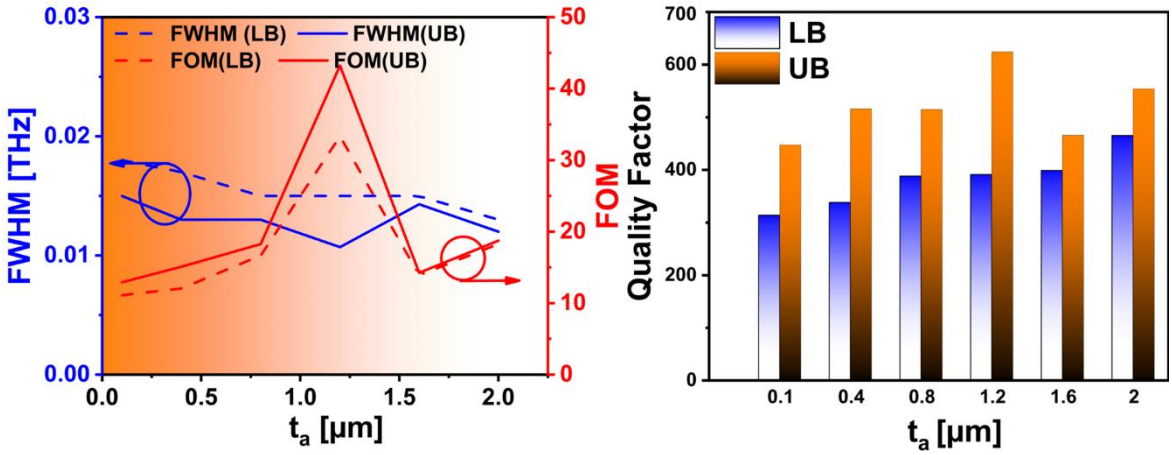

(d) (e)

Fig. 7.9 (a) Proposed absorber with analyte on top, (b) Frequency response with change in t_a, (c) Plot of Δf and Sensitivity (S) with change in t_a, (d) Plot of FWHM and FOM with change in t_a and (e) Plot of Q with change in t_a.

This ultrathin absorption peak has a high sensitivity, allowing the sensor to discover small variations in t_a. Fig. 7.9(e) shows the plot of Q with a variation of t_a. Because of very low FWHM values in both LB and UB, it is evident that the proposed absorber shows very high Q values. It is observed that a very high Q of 394.2 and 624.4 is observed for t_a=1.2 μm in the LB and UB, respectively. Moreover, for t_a=2 μm, a very high Q of 465.38 is observed in the lower band. The above analysis of sensitivity, FWHM, FOM, and Q confirms that the proposed absorber is a very good candidate for sensing applications.

7.2.9 Change in refractive index (n) and its sensing

For refractive index (RI or n) sensing, the characteristics such as sensitivity, Q, and FOM are the important parameters that represent the sensing quality. Fig. 7.10 shows the absorption plot and performance parameters for varying n with t_a=1.2 μm. Fig. 7.10(a) depicts the change in absorption characteristics with a change in n of the analyte from n=1 to n=2 with a step of 0.2. The absorber shows a very high absorption rate of > 0.96 throughout the frequency band. Fig. 7.10(b) illustrates the plot of sensitivity and Δf concerning change in n. Here, sensitivity is calculated using $S = \Delta f / \Delta n$ (THz/RIU), which measures the shift in the absorption frequency due to a shift in the refractive index from n_1 to n_2 ($\Delta n = n_2 - n_1$). Where n_1 and n_2 are past and present values of n of the analyte medium [19], [28]. A high S value of 1.9 THz/RIU and 1.45 THz/RIU is observed for n=1.4

in the LB and UB, respectively.

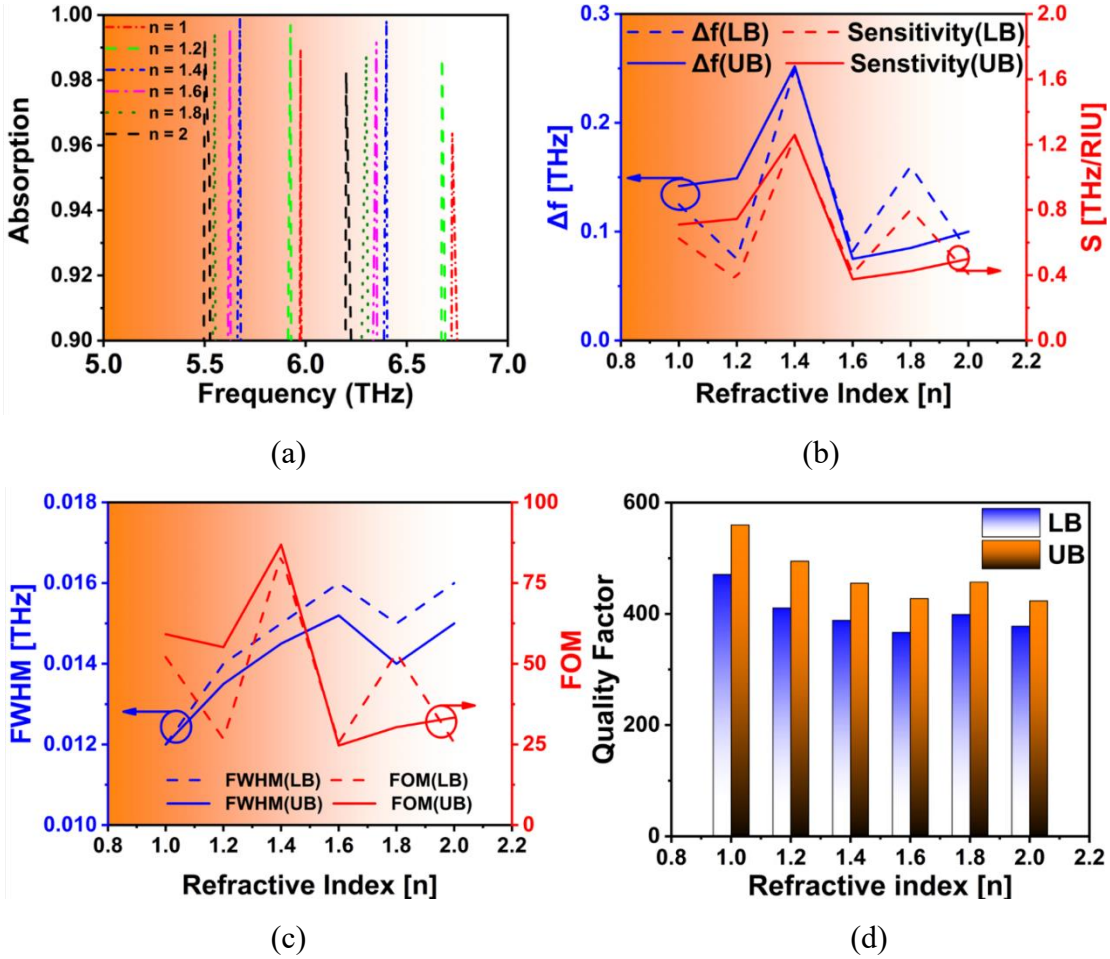

Fig. 7.10 (a) Frequency response with change in n, (b) Plot of Δf and Sensitivity (S) with change in n, (c) Plot of FWHM and FOM with change in n, and (d) Plot of Q with change in n.

Fig. 7.10(c) shows a plot of FWHM and FOM with a variation of n. A very high FOM of 126.6 (RIU^{-1}) and 100 (RIU^{-1}) is observed for n = 1.4 in the LB and UB, respectively. Fig. 7.10(d) illustrates the plot of Q for change in n. The proposed structure shows a very high Q of 470.8 in the LB and 560 in the UB, respectively. From the above analysis of sensitivity, FWHM, FOM, and Q, confirm that the proposed absorber is an excellent candidate for sensing applications.

7.2.10 Performance of proposed sensor on cancerous cells

Based on the RI profile, the proposed sensor is examined for various cancer cells, and the outcomes are reported in this section.

Table 7.1 The sensing performance for blood, skin, and breast cancerous cells.

Body Part	n	S (THz/RIU)		FWHM (THz)		FOM (RIU^{-1})		Q	
		LB	UB	LB	UB	LB	UB	LB	UB
Blood (Healthy)	1.376	2.167	2.046	0.014	0.015	152.582	136.389	411.972	441.327
Blood (Cancerous)	1.390	1.600	1.900	0.012	0.015	133.333	126.667	487.367	441.200
Breast (Healthy)	1.449	1.939	1.592	0.017	0.015	114.046	106.122	343.465	440.333
Breast (Cancerous)	1.581	0.552	0.516	0.017	0.016	32.449	32.268	342.141	410.625
Skin (Healthy)	1.844	0.188	0.189	0.017	0.015	11.078	12.615	339.576	434.400
Skin (Cancerous)	2.049	0.130	0.132	0.020	0.014	6.476	9.399	286.610	461.571

As a result, the n of cancerous and healthy cells from various areas of the human body is identified and presented in Table 7.1 with t_a=1.2 μm. As reported in [189], [198], [199], the RI of the cancerous samples lies in the range of 1.3 to 2.0. The reported sensor under investigation can sense the different types of cells in various parts of the human body, such as blood, skin, and breast are examined, and the results are reported in Table 7.1. The results show that for healthy blood cells, the proposed sensor offers a high sensitivity of 2.1667 THz/RIU and 2.0458 THz/RIU in the LB and UB. While for cancerous blood cells, the sensor shows a sensitivity of 1.6 THz/RIU and 1.9 THz/RIU in the lower and upper bands, respectively. Also, a very high FOM of 381.4553 RIU^{-1}, 283.6111 RIU^{-1} is obtained for healthy blood cells in the LB and UB, and 133.3333 RIU^{-1}, 126.6666 RIU^{-1} is found for cancerous blood in the LB and UB is exhibited by the sensor. The proposed sensor exhibits a very high Q of 487.3666 and 441.2 for cancerous blood cells. Similarly, for healthy breast cells, high S of 1.9387 THz/RIU and 1.5918 THz/RIU is observed for LB and UB, respectively, with FOM of 114.0456 RIU^{-1} and 106.1224 RIU^{-1} and very high Q of 343.4647, 440.3333 is exhibited by the sensor. For cancerous breast cells, S of 0.5516 THz/RIU and 0.5162

THz/RIU is observed for LB and UB, respectively, with FOM of 32.449 $RIU^{-1}$and 32.2680 RIU^{-1} and very high Q of 342.141, 410.625 is shown by the sensor. Similarly, the cancerous skin cells are differentiated from healthy skin cells effectively by the proposed sensor. For healthy skin cells, the proposed sensor exhibits a peak S of 0.1883 THz/RIU and 0.1892 THz/RIU in the LB and UB, respectively, with FOM of 11.0782 RIU^{-1} and 12.6154 RIU^{-1} and high Q of 339.5764 and 434.4 is exhibited by the sensor. For cancerous skin cells, a peak S of 0.1295 THz/RIU and 0.1316 THz/RIU is obtained in the LB and UB, respectively, with FOM of 6.476 and 9.3990 and high Q of 286.6095 and 461.5714 is exhibited by the sensor. From the above investigation, the proposed sensor promises to be an excellent candidate for detecting malignant cells in various parts of the human body.

7.2.11 Performance of proposed sensor for malaria detection

The past, present, and future of RI sensing for biology and disease diagnosis was published by Liu et al. in 2016 [200]. Annually, 250 million individuals worldwide are infected with malaria, according to reports. As a result, it is essential to detect malaria as soon as possible to avoid fatality as the disease progresses [200]. Infected Red Blood Cells (RBC) have refractive indexes of n_1 = 1.383 and n_2 = 1.373 in different stages of malaria infection [1], [146]. The performance of the proposed DMMA is reported in Table 7. 2 with t_a=1.2 μm.

Table 7. 2 The sensing performance for identifying malaria.

Disease	n	S (THz/RIU)		FWHM (THz)		FOM (RIU-1)		Q	
		LB	UB	LB	UB	LB	UB	LB	UB
Malaria	1.373	0.6772	0.5362	0.016	0.012	42.3275	44.6828	357.9625	543.5
	1.383	0.6666	0.5308	0.0158	0.015	42.1886	35.3873	362.322	434.58

The sensor can sense blood cells having n of 1.373 with peak S of 0.6722 THz/RIU and 0.5362 THz/RIU in the LB and UB, respectively, and with high FOM of 42.3257 RIU^{-1} and 44.6828 RIU^{-1} and also providing high Q of 357.9625 and 543.5 in the LB and UB. Similar observations are made for the proposed sensor for n=1.383. From Table 7. 2, it is evident that the proposed sensor

provides excellent sensing performance for the detection of infected red blood cells in different stages of malaria infection with good sensitivity, high FOM and very high Q.

7.2.12 Performance of the proposed sensor for Water/Glucose detection

The performance of the proposed sensor for water having n of 1.3198 and water with 25 % glucose is 1.3594, respectively [1], [146]. Table 7.3 depicts the performance of the proposed DMMA in sensing glucose with t_a=1.2 µm. The proposed sensor shows very good sensitivity, high FOM, and very high Q. The results, proves that the proposed sensor is an excellent candidate for detecting glucose in water.

Table 7.3 The sensing performance for identifying water/glucose detection.

n	**S (THz/RIU)**		**FWHM (THz)**		**FOM (RIU^{-1})**		**Q**	
	LB	**UB**	**LB**	**UB**	**LB**	**UB**	**LB**	**UB**
1.3198	0.758	0.588	0.015	0.013	50.532	45.1965	382.507	502.62
1.3594	0.6956	0.55	0.015	0.014	46.374	39.2519	382	466.04

7.2.13 Performance of proposed sensor for chemical

The performance of the proposed sensor is tested for various chemicals listed in Table 7.4. The proposed sensor is suitable for sensing various chemicals such as ethanol (n=1.36), ethylene glycol (n=1.41), glycerine (n=1.4729), benzene (n=1.5), sodium chloride (Nacl) (n=1.54), carbon disulphide (CS_2) (n=1.63), Vegetable oil (n=1.47) and acetone (n=1.35) with good sensitivity, very good FOM and very high Q.

7.2.14 Comparison with Published Research Articles

The absorber's performance is investigated in comparison with other recently published articles. The proposed structure shows ultra-narrow BW, which results in very high Q values, as depicted in table 7.5. The S of the proposed sensor is also high, which results in good absorber performance

for small changes in RI. Furthermore, the proposed sensor is compared with a cancer-detecting sensor [189].

Table 7.4 The sensing performance for identifying various chemicals.

Chemical	n	S (THz/RIU)		FWHM (THz)		FOM (RIU^{-1})		Q	
		LB	UB	LB	UB	LB	UB	LB	UB
Ethanol	1.36	0.695	0.550	0.015	0.013	46.352	42.329	381.980	501.839
Ethylene glycol	1.41	0.738	0.644	0.014	0.013	52.735	49.531	408.286	500.615
Glycerine	1.4729	0.599	0.502	0.012	0.012	49.913	41.844	474.875	540.500
Benzene	1.5	0.584	0.497	0.017	0.015	34.329	33.133	334.600	431.567
Nacl	1.54	0.561	0.489	0.017	0.013	32.974	37.607	333.959	496.769
CS_2	1.63	0.524	0.473	0.016	0.014	32.768	33.764	353.106	458.871
Oil, Vegetable 50°C	1.47	0.599	0.502	0.018	0.013	33.275	38.625	316.583	498.923
Acetone	1.35	0.485	0.402	0.012	0.014	40.417	29.778	490.833	490.370

Table 7. 5 Comparison with other research articles

Ref	No. of bands	*f* (THz)		S (THz/RIU)		FOM		Q		Thickness (µm)	Polarization Insensitivity	Tunability
		LB	UB	LB	UB	LB	UB	LB	UB			
[201]	2	1.42	2.99	0.28	1.48	1.2	24.6	7.11	59.8	10.8	Yes	No
[202]	2	1.8	2.26	0.1875	0.36	7.2	19.1	120	94	8.6	Yes	No
[181]	2	1.77	2.459	-	1.9	-	229	6.91	296	4.8	No	No
[203]	2	0.76	1.28	0.47	0.51	9.4	14..4	23	3.7	5.4	Yes	No
[148]	2	4.88	10.9	1.35	2.95	4.67	8.8	15.2	29.88	2.52	Yes	Yes
[146]	2	4.515	4.914	0.2	0.1	4.76	3.5	105.2	211.84	3.65	Yes	Yes

[189]	3	1.095, 2.865 and 4.065		0.105,0.3764 and 0.47635		0.7, 1.88 and 2.38		7.05, 12.67 and 18.06		41.5	Yes	No
This work (t_a and RI sensing)	2	5.78	6.465	0.5	0.462	33.33	43.242	394.2	624.4	4 (2.28 λ)	Yes	Yes
		5.76	6.463	1.25	1.26	83.33	86.896	470.83	494.81			
This work (Blood Cancerous cells sensing)		5.84	6.618	1.6	1.9	133.3	126.66	487.32	441.2			
This work (Breast Cancerous cell sensing)		5.81	6.618	0.551	0.516	32.44	32.268	342.14	410.62			
This work (Skin Cancerous cells sensing)		5.732	6.462	0.129	0.131	6.476	9.399	286.60	461.57			

7.3 DMMA for detecting dengue and other diseases

Our sensor provides better results in terms of S, FOM, and Q and can be used to detect cancerous cells in various parts of the human body. The features like ultra-thin structure, simple design, tunability, polarization insensitivity, ultra-narrow absorption BW, high sensitivity, high FOM, and very high Q values in a single device for detecting different diseases and chemicals make the proposed sensor new and unique. Fig. 7. 11(a) depicts the unit cell design of the proposed DMMS. It has a gold layer at the bottom with a W_g = 80 µm periodicity. This gold layer with a frequency-independent conductivity of $\sigma = 4.09X10^7$ S/m is developed at the bottom of a silicon dioxide (SiO_2)

substrate having a relative permittivity of ε_s=2.25 and a thickness of t_s=1.2 µm. A silicon-based square ring resonator (SSRR) with ε_{sr} = 11.9 having a thickness of t_{dra}=2.15 µm, with an outer radius of S_{ro} = 35 µm, and an inner radius of S_{ri} = 19.6 µm is positioned at the top of the SiO_2. At the centre of the structure, on the top of the SiO_2 substrate, a graphene-based circular-shaped ring (GCR) has a thickness of 0.34 nm with an inner radius of g_{ri} = 8 µm and an outer radius of g_{ro} = 10 µm is placed. S_{ro} and S_{ri} are set of the order $\approx \lambda_g/2$ by choosing $S_{ro} \approx \lambda_g$ and $S_{ri} \approx \lambda_g/2$, respectively. Here λ_g is the guided wavelength of Si layer operating at resonance frequency with $\lambda_g = \lambda_o/\sqrt{\varepsilon_s}$. The benefit of using SSRR along with inner GCR is it provides an ultra-thin structure with an overall thickness of the order of $\approx \lambda_g/15$, with narrow absorption bandwidth and tunability characteristics.

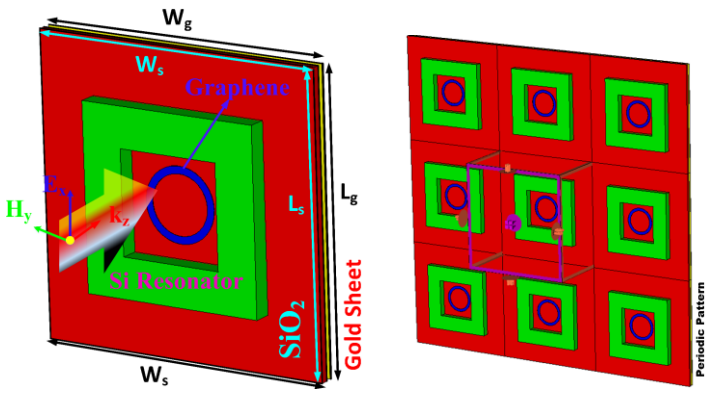

(a) (b)

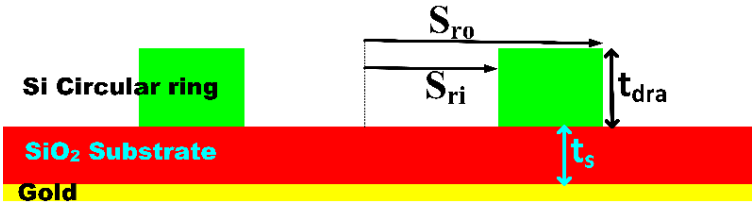

(c)

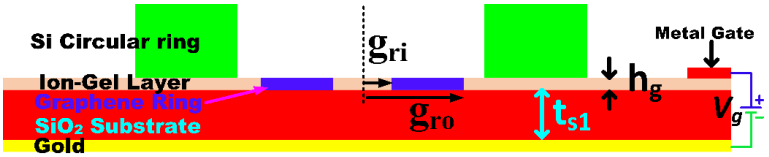

(d)

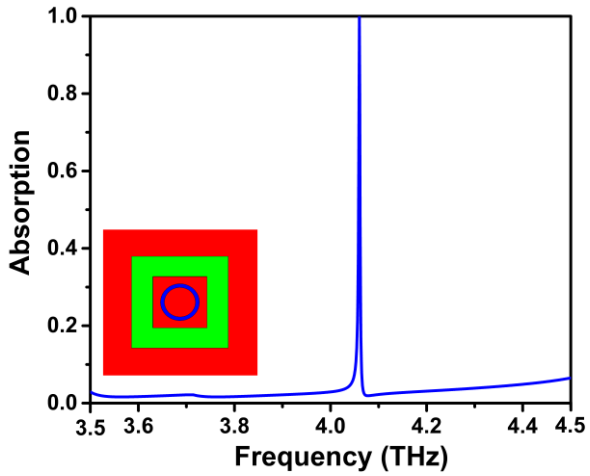

(e)

Fig. 7. 11 Proposed absorber (a) with incident wave, (b) Periodic arrangement, (c) Front view of proposed absorber without GCR, (d) Front view of Proposed absorber with GCR and biasing, and (e) Absorption spectra.

7.3.1 Equivalent Circuit Design

The suggested absorber's functioning is validated using an electrical equivalent circuit design (ECD) created utilizing the transmission line technique as illustrated in Fig. 7. 12. The ECD is separated into four parts: the first part examines the substrate (SiO_2), the second, the ion-gel, the third, the SSRR, and the fourth the functioning of the GCR. The first part is a short-circuited transmission line with a substrate of height t_s placed on the ground plane. This part provides the input impedance, as seen in eq (7.1).

$$Z_1 = jZ_{SiO_2} \tan \beta_s t_s \tag{7.1}$$

Where $\beta_s = \frac{\omega}{c}\sqrt{\varepsilon_s}$ is the propagation constant and $Z_{SiO_2} = Z_o / \sqrt{\varepsilon_s}$ is the impedance of the SiO_2 substrate, and Z_o is free space impedance. Next, the impedance of the ion-gel layer is determined using eq (7.2).

$$Z_2 = Z_{ig} \frac{\left[Z_1 + jZ_{ig} \tan \beta_i h_g \right]}{\left[Z_{ig} + jZ_1 \tan \beta_i h_g \right]} \tag{7.2}$$

Where $\beta_i = \frac{\omega}{c}\sqrt{\varepsilon_{ig}}$ is the propagation constant, and $Z_{ig} = Z_o / \sqrt{\varepsilon_{ig}}$ is the impedance exhibited by the ion-gel layer [146]. SSRR offers an impedance of Z_s and is modelled using an RLC circuit as depicted in fig. 6.

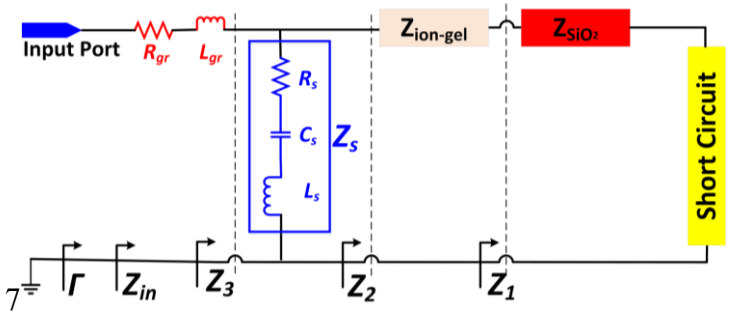

(a)

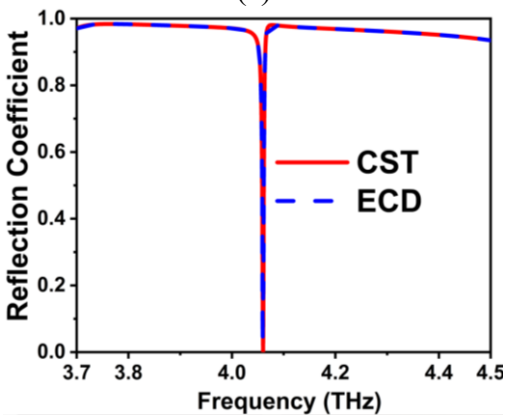

(b)

Fig. 7. 12 (a) Circuit Model, and (b) the reflection coefficient comparison.

Since GCR shifts resonant frequency, it is modelled as an RL circuit. The total input impedance of the ECD is $Z_{in} = Z_g + Z_3$. Where $Z_g = \left(R_{gr} + jwL_{gr}\right) \approx 1/\sigma_{gr}$ the impedance of GCR, and Z_3 is $Z_3 = Z_s \parallel Z_2$. The reflection coefficient is calculated based on input impedance using $\Gamma = \frac{Z_{in} - Z_o}{Z_{in} + Z_o}$.

Figure 6(b) depicts the plot of the computed reflection coefficient. The CST and ECD findings are displayed, and the high agreement between the simulation tools validates the operation's validity.

7.3.2 Sensing Performance

The proposed absorber exhibits a narrow band response (Fig. 7.9(e)), with FWHM of 0.004 THz, which results in a very high Q of 927.5. The equation Q = f_p/FWHM is used to compute the Q [1],

[200], where f_p is the peak frequency. The high Q and low FWHM of the proposed absorber make it ideal for THz biomedical virus detection applications, such as malaria, dengue, Influenza virus, etc. [204]–[209]. In this paper, the proposed sensor is utilized as a sensing device for glucose, and malaria, dengue virus detection. Refractive index sensing is evaluated using parameters such as S, FWHM, FOM, and Q. Fig. 7. 13(a) depicts the proposed sensor with a test medium or analyte on its top. Fig. 7. 13(b) shows the variation of resonant frequency (Δf) with a change in n. Here n is varied from 1 to 2 with constant t_a = 1 µm. The refractive index and t_a are chosen to analyze the proposed absorber for sensing malaria, dengue, and glucose detection [204]–[206]. From Fig. 7. 13(b) shows that the proposed sensor shows a very high absorption rate of > 0.99 and changes its resonant frequency with a change in RI. Fig. 7. 13(c) depicts the plot of S and Δf for change in n. S = Δf /Δn (THz/RIU) is used to compute sensitivity, which quantifies the shift in absorption frequency owing to a change in refractive index from n_1 to n_2 ($n = n_2-n_1$). Here n_1 and n_2 are the past and present values of n in the analyte medium, respectively. A high S value of 2.2 THz/RIU is reported for n=1.4. The plot of FWHM and FOM with change in n is shown in Fig. 7. 13(d). The sensor exhibits an ultrahigh FOM of 550 (RIU^{-1}) for n=1.4. The plot of Q for a change in n is shown in Fig. 7. 13. The proposed structure has a very high Q, with 927.5 for n=1.4. High sensitivity (S), very low FWHM values, high FOM, and high Q values for all the values of n make the proposed sensor suitable for detecting the dengue virus.

7.3.3 Glucose detection

The performance of the proposed sensor is tested for water having n of 1.3198 and water with 25 % of glucose having n of 1.3594, respectively [1], [146]. Table 7. 6 depicts the performance of the proposed DMMA in sensing glucose with t_a=1µm. The proposed sensor shows very good sensitivity, high FOM, and high Q. The results prove that the proposed sensor is an excellent candidate for detecting glucose in water.

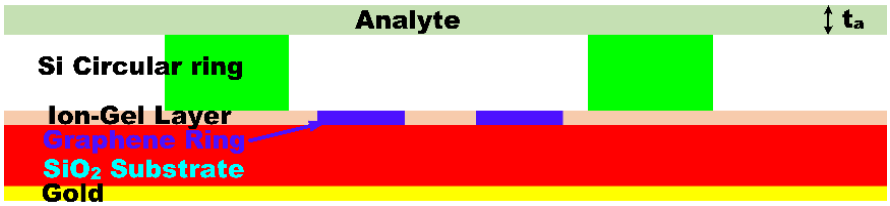

(a)

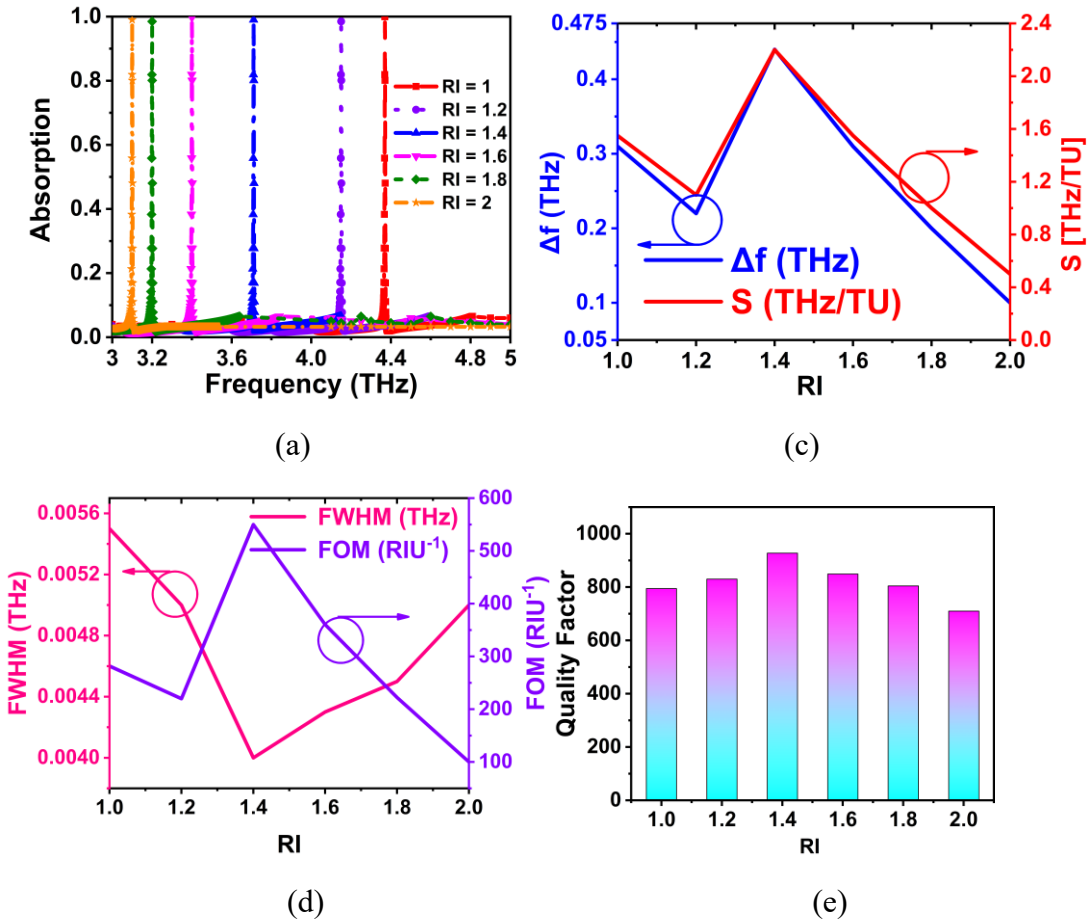

Fig. 7. 13 (a) Proposed absorber with analyte on top. With a change in RI, the plot of (b) Frequency response, (c) Δf and S, (d) FWHM and FOM, and (e) Q.

Table 7. 6 The sensing performance for identifying water/glucose

n	S	FWHM	FOM	Q
1.3198	1.452	0.0043	337.6744	937.21
1.3594	1.588	0.0055	288.7273	712.73

7.3.4 Proposed sensor for Malaria detection

According to reports, 250 million individuals worldwide are infected with malaria. As a result, it is essential to detect malaria as soon as possible to avoid fatality as the disease progresses [200]. Infected Red Blood Cells (RBC) have refractive indexes of $n_1 = 1.383$ and $n_2 = 1.373$ in different stages of malaria infection [1], [146]. The performance of the proposed DMMS is depicted in Table 7. 7 with t_a=1 µm. The proposed DMMS is an excellent candidate for the detection of malaria

disease effectively in different stages of infection with a sensitivity of 1.685 THz/RIU, very low FWHM of 0.0048, very high FOM of 351, and high Q of 806.46 for n=1.373 as depicted in Table 7. 7. For n=1.38, sensitivity of 1.87 THz/RIU, very low FWHM of 0.0042, very high FOM of 445.2, and high Q of 903.1 is exhibited.

Table 7. 7 The sensing performance of malaria

Disease	n	S	FWHM	FOM	Q
Malaria	**1.373**	1.685	0.0048	351	806.46
	1.383	1.87	0.0042	445.2	903.1

7.3.5 Proposed absorber as Dengue Sensor

Dengue fever is a quickly spreading pandemic-prone illness that affects people worldwide. Dengue fever has been 30 times more common in the last 50 years. Nearly 50-100 million cases are predicted to occur annually in over 100 endemic countries, putting 80 percent of the world's population at risk [204]–[206]. The proposed DMMS is a good candidate for the detection of dengue virus effectively with a sensitivity of 2.2 THz/RIU, very low FWHM of 0.004, very high FOM of 550 (RIU^{-1}), and high Q of 927.5 as depicted in Table 7. 8.

Table 7. 8 The sensing performance of dengue virus

Disease	n	S	FWHM	FOM	Q
Dengue	1.4	2.2	0.004	550	927.5

7.3.6 Effect of μ_c

Table 7. 9demonstrates the impact of graphene chemical potential (μ_c) on sensing parameters. It is observed that with an increase in μ_c, the sensor shows better sensing parameters with the tuning of resonant frequency and provides very low FWHM values, leading to high FOM and high Q values. But for higher values of μ_c (≥ 0.6), absorptivity gradually reduces. Better sensing performance is observed for $\mu_c = 0.4$ with S of 2.278, FOM of 949.16, and Q of 1583.3, respectively.

Table 7. 9 The effect of μc on sensing parameters

μ_c	S	FWHM	FOM	Q	A (%)
0	2.2	0.004	550	927.5	99.993
0.2	2.24	0.003	746.6667	1250	99.989
0.4	2.278	0.0024	949.1667	1583.333	99.987
0.6	2.281	0.0029	786.5517	1396.552	98.57
0.8	2.285	0.0032	714.0625	1281.25	95.26
1	2.29	0.0033	693.93	1251.51	92.05

7.3.7 Comparison with other biosensors

The absorber's performance is investigated in comparison with other recently published articles. The proposed structure shows ultra-narrow BW, which results in very high Q values, as depicted in table 7.10. The S of the proposed sensor is also high, which results in good absorber performance for small changes in RI. The proposed sensor is set to operate at 4.06 THz with high sensitivity of 2.2 (THz/TU), a very high FOM of 550, and a high Q of 927.5. The thickness of the proposed structure is also less compared to the other research articles making it feasible for nano biosensor applications. These features make the proposed sensor suitable for biosensing applications. A very high Q of 927.5 is not implemented till now and can be implemented in the near future for detection in the field of biosensing applications.

Finally, it is vital to describe the fabrication processes for the suggested absorber geometry since the realistic implementation of the DMMA, and its usage in various applications have significant potential [146], [188]. Thermal evaporation can build a metal layer on one side of the SiO_2 substrate. Using the chemical vapor deposition approach, a graphene sheet is created on copper foil and then transferred to the other side of the SiO_2 substrate. A GCR is formed by patterning the transferred graphene sheet. The geometry of the GCR placed above the substrate can then have an ion-gel layer produced on top of it using the thermal evaporation process. The SSRR is created on the ion-gel layer using photolithography and large-scale microfabrication methods. Finally, a metal

gate for connecting the bias voltage is formed on the edge of the absorber unit cell [146], [188]. Fig. 7. 14 depicts the schematic representation of the biosensor when testing a sample with THz EM wave incidence.

Table 7.10 Performance comparison with other research articles

Ref	Bands	f (THz)	S (THz/TU)	FOM (1/RIU)	Q	Thickness (µm)	Polarization Insensitivity	Tunability	Design Method	Design Complexity
[210]	1	0.6	0.007	2.3	11.6	518.2	Yes	Yes	Metamaterial	Not easy
[211]	1	0.4	0.0273	-	9.6	502	No	No	Metamaterial	Not easy
[212]	1	0.86	0.006	0.2	4.5	25	No	No	Metamaterial	Easy
[213]	1	1	0.016	-	-	25	No	No	Metamaterial	Not easy
[214]	1	0.6	0.016	-	6	500	No	No	Metamaterial	Easy
[215]	1	2.249	0.0237	0.23	20.3	10.4	No	Yes	Metamaterial	Not easy
[216]	1	3.71	1.47	36.175	92.75	8.4	Yes	No	Metamaterial	Not easy
This work	1	4.06	2.2	550	927.5	3.45	Yes	Yes	Dielectric based Metamaterial	Easy

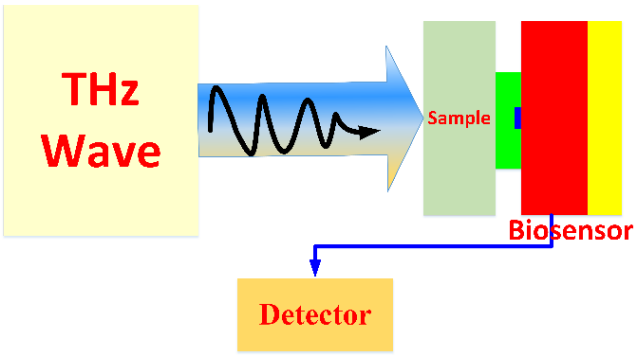

Fig. 7. 14 Schematic diagram of THz detector when the sample is examined.

It comprises a THz wave generator that emits EM waves toward the sample using an antenna. The detector is positioned at a distance to make it easier to load test samples. The incident THz wave strikes the sample, is reflected, and is subsequently transmitted and picked up by the detector. The spectrum analyser at the detector process these signals. These signals give information about transmitted (T) and reflected (R) signals. The absorption is then calculated using the equation A=1-

R-T. The shift in resonant frequency with the change in RI of the sample will be analyzed in detecting the disease.

7.4 Conclusion

Two dielectric-based MMA is being developed for biosensing applications for the detection of malaria, dengue, cancer, malaria, glucose content in water, and other chemicals. Two sensors are developed and analysed for biosensing applications. First, the absorber is designed to sense cancerous cells, malaria, glucose in water and chemicals. Results show that the absorber exhibits a high sensitivity of 1.6 THz/RIU and 1.9 THz/RIU in the LB and UB, respectively, for cancerous blood cells, 0.5516 THz/RIU and 0.5162 THz/RIU for cancerous breast cells and 0.1295 THz/RIU and 0.1316 THz/RIU for skin cancer cells detection. For analyte thickness sensing, the sensor exhibits a high sensitivity of 0.5 THz/RIU and 0.4625 THz/RIU in LB and UB, respectively. For RI sensing, the absorber provides a sensitivity of 1.25 THz/RIU and 1.26 THz/RIU in the LB and UB, respectively. Also, the proposed sensor exhibits insensitivity to incidence angles up to 80^{o} with an absorption rate greater than 0.6. Second, the absorber is designed to sense dengue, malaria, and glucose content in water. In this absorber performance is also verified by the circuit model using the transmission line method. The proposed sensor has a high S of 2.2 THz/RU for sensing the dengue virus with a FOM of 550 RIU^{-1} and a high Q of 927.5. For malaria detection, the proposed sensor offers a high S of 1.87 *THz/RIU,* a high FOM of 445.24, and a high Q of 903.1. The sensor provides a high sensitivity of 1.588 with a FOM of 288.73 and Q of 712.73 during the water detection with glucose. These features include the ultra-thin structure, simple design, tunability, polarization insensitivity, ultra-narrow absorption bandwidth, high S, high Figure of Merit (FOM), and high-quality factor (Q) values are all distinguishing features. Furthermore, the proposed sensor shows polarization-insensitive behaviour for TE and TM incident waves. The features like ultra-thin structure, simple design, tunability, polarization insensitivity, ultra-narrow absorption bandwidth, high sensitivity, high FOM, and very high Q values in a single device for detecting different diseases and chemicals make the proposed sensor new and unique.

Chapter 8

Summary, Conclusion and Future Scope

8.1 Summary

The research work reported in this thesis is carried out to find four following issues:

i. Obtaining tunable response in DRA.
ii. Obtaining tunable response in MIMO DRA.
iii. Obtaining ultra-wide band response in DRA.
iv. Obtaining multiband and ultra-wideband response in non-metallic absorber.
v. Obtaining narrow band response for biosensing applications.

8.2 Conclusion

This thesis is divided into two main parts: the design of dielectric resonator antennas (DRAs) and the design of absorbers for THz and biosensing applications.

In **Chapter 1**, we provided an introduction, background, and the motivation for this research work.

Chapter 2 focused on the design of a tunable graphene-based dielectric resonator antenna for terahertz applications. By rotating the rectangular DRA at a 45-degree angle, a quad-band circularly polarized response was achieved. The integration of graphene coating allowed for tunability, resulting in a multi-band response at different resonant frequencies. This work contributes to the field of THz dielectric resonator antennas by providing

circular polarization behaviour at multiple bands. The graphene potential of the antenna was varied to achieve CP tuning.

Chapter 3 presented the design of three circularly polarized multiple-input multiple-output (MIMO) DRAs for THz and unmanned aerial vehicle (UAV) applications. The first design involved a two-port MIMO DRA operating in the THz frequency regime, offering resonance at four bands and dual-sense circular polarization response. By varying the graphene potential, increased isolation between the two antennas was achieved. The second design introduced a 2x2 MIMO DRA, providing a dual-band dual-sense circular polarization response in the THz frequency region. Defected Ground Structures (DGS) were implemented to improve port isolation. Lastly, a CP-based wideband MIMO DRA for UAV satellite communications was introduced, featuring a new DGS technique to enhance impedance bandwidth (IBW) and axial ratio bandwidth (ARBW). This antenna exhibited a bandwidth of 8.4 GHz with tri-sense circular polarization response. The proposed designs aimed to minimize inter-channel interference and ensure high isolation between frequencies through the utilization of RHCP and LHCP responses.

Chapter 4 presented the design of an ultra-wideband CP-based cylindrical dielectric resonator antenna (CDRA) for C-band and military satellite communication applications. The design involved stacking two identical cylindrical DRAs to achieve circular polarization. Techniques such as stacking of similar DRs, a stepped conformal microstrip feed line, and a new partial ground plane with circular rings were employed to achieve an ultra-wideband impedance bandwidth and wide axial ratio bandwidth. The antenna demonstrated over 90% radiation efficiency within the operating band.

In **Chapter 5**, a graphene-based multiband absorber was designed using different geometric shapes for THz applications. Integration of circular, triangular, square, pentagon, and hexagon-shaped absorbers resulted in a unique absorber with absorption peaks at multiple resonant frequencies, averaging at 97.23% at THz frequency. The proposed absorber exhibited polarization insensitivity and wide incidence angle tolerance.

Chapter 6 presented the design of a graphene-based ultra-wideband absorber for THz applications. The absorber consisted of four graphene-based hexagonal split rings, a dielectric substrate, and a graphene layer at the bottom. By varying the graphene chemical

potential, tunability was achieved. The proposed absorber exhibited polarization-insensitive behaviour for both TE and TM modes, with absorption rates exceeding 90% for incidence angles up to 75^{o}. These characteristics make it suitable for solar and photovoltaic cells and hold promise for future nanoscale systems. The absorber's narrow absorption characteristics at higher graphene chemical potential values also make it applicable to sensor applications.

Lastly, in **Chapter 7**, two dielectric-based metamaterial absorbers (MMAs) were developed for biosensing applications, specifically for the detection of malaria, dengue, cancer, and glucose content in water. The first absorber was designed to sense cancerous cells, demonstrating high sensitivity and specific response frequencies for different types of cancer cells. The second absorber was designed for sensing dengue, malaria, and glucose content in water, exhibiting high sensitivity and excellent performance characteristics. These ultra-thin structure sensors featured simple designs, tunability, polarization insensitivity, ultra-narrow absorption bandwidths, and high sensitivity, FOM, and Q values. Additionally, they exhibited polarization-insensitive behaviour for both TE and TM incident waves.

8.3 Future Scope

The future scope of this research work encompasses several areas of interest and potential avenues for further exploration. Firstly, there is a need for optimization of antenna designs to enhance performance characteristics such as radiation efficiency and bandwidth. This can be achieved through advanced design techniques and numerical optimization algorithms. Another area of interest lies in the development of novel materials, including graphene, MXene, ceramic materials, and nanomaterials, and the exploration of fabrication techniques to improve the properties of dielectric resonator antennas. The use of these materials can lead to enhanced antenna performance and expanded operational capabilities. Investigations into the effects of environmental factors, such as temperature and humidity, on antenna performance can provide valuable insights into real-world operating conditions and aid in the development of robust antenna systems. Additionally, the utilization of circularly polarized dielectric resonator antennas in wireless power transfer systems and

their impact on the next generation of wireless communication systems, such as 6G and THz communication, can be explored to improve system efficiency and reliability.

Further research can delve into the use of circularly polarized dielectric resonator antennas in radar systems for enhanced detection and imaging capabilities. The development of circularly polarized dielectric resonator antennas for underwater communication and sensing systems holds promising applications in marine exploration and monitoring. Graphene-based dielectric resonator antennas offer the potential for operation at high frequencies, making them suitable for use in THz communication systems. Future research can focus on their integration into emerging wireless networks, such as 6G, and the development of flexible and transparent graphene-based dielectric resonator antennas for diverse applications. Moreover, graphene-based absorbers hold promise in various domains. Their application in terahertz spectroscopy for material analysis and identification can be further explored, along with the development of miniaturized and low-cost graphene-based absorbers for portable and wearable devices. Investigating the effects of substrate properties on graphene-based absorber performance can provide valuable insights for optimization.

Furthermore, the integration of graphene-based absorbers with microfluidic devices presents opportunities for rapid and high-throughput biosensing, enabling the detection of DNA, proteins, cells, viruses, and bacteria. Research focusing on enhancing the sensitivity of graphene-based biosensors through optimization of graphene thickness, surface functionalization, and hybridization with other materials can open avenues for point-of-care diagnostics and other biosensing applications. The development of graphene-based absorbers for use in stealth technology, such as in aircraft and vehicles, is another area of interest.

In future research, it is essential to explore the fabrication, characterization, and measurement of THz dielectric resonator antennas, absorbers, and biosensors. The measured data in the thesis at THz may differ from the simulation and can be explored in the future. Experimental validation and practical measurement techniques in the THz regime will provide valuable insights into their actual behaviour and performance, complementing theoretical and simulated studies. The development of low-cost and

portable devices suitable for resource-limited settings is another aspect worth exploring. Additionally, the application of graphene-based absorbers in space exploration and communication systems can be an exciting area for future research, enabling advanced communication technologies and exploration missions. To conclude, the future scope of this research encompasses optimizing antenna designs, exploring novel materials and fabrication techniques, investigating environmental effects, utilizing circularly polarized antennas in various applications, developing graphene-based absorbers for diverse purposes, integrating absorbers with biosensing platforms, and advancing THz dielectric resonator antennas and biosensors. These endeavours aim to unlock the full potential of these technologies in numerous practical applications and contribute to the advancement of the field.

References

[1] M. Nejat and N. Nozhat, "Ultrasensitive THz Refractive Index Sensor Based on a Controllable Perfect MTM Absorber," *IEEE Sens. J.*, vol. 19, no. 22, pp. 10490–10497, 2019, doi: 10.1109/JSEN.2019.2931057.

[2] P. Upender and A. Kumar, "Quad-Band Circularly Polarized Tunable Graphene Based Dielectric Resonator Antenna for Terahertz Applications," *Silicon*, 2021, doi: 10.1007/s12633-021-01336-5.

[3] P. Upender and A. Kumar, "Ultrathin, Ultra narrow band DMMA for biosensing applications," *IEEE Trans. Nanobioscience*, pp. 1–1, Nov. 2022, doi: 10.1109/TNB.2022.3217077.

[4] P. Upender and A. Kumar, "THz Dielectric metamaterial sensor with high Q for biosensing applications," *IEEE Sens. J.*, pp. 1–1, 2023, doi: 10.1109/JSEN.2023.3239669.

[5] P. Upender and A. Kumar, "HEM11δ and HEM12δ-based Quad band Quad Sense Circularly Polarized tunable Graphene-based MIMO Dielectric Resonator Antenna," *Frequenz*, Jan. 2022, doi: 10.1515/freq-2021-0145.

[6] Constantine A. Balanis, "Antenna Theory: Analysis and Design, 4th Edition | Wiley," p. 1104, 2016.

[7] M. S. Sharawi, "Printed mimo antenna engineering," *Artech House:Norwood*, p. 295, 2014.

[8] K. M. (Kwai M. Luk and K. W. (Kwok W. Leung, *Dielectric resonator antennas*. Baldock Hertfordshire England ;Philadelphia PA;Williston VT, 2003.

[9] J. D. KRAUS, *Antennas And Wave Propagation.* Tata McGraw-Hill, 2010.

[10] Y. He, Y. Chen, L. Zhang, S. W. Wong, and Z. N. Chen, "An overview of terahertz antennas," *China Commun.*, vol. 17, no. 7, pp. 124–165, Jul. 2020, doi: 10.23919/J.CC.2020.07.011.

[11] M. M. Douglas, K. B. Richard, B. H. Stephen, S. Eric, and T. M. Michael, "Introduction to Unmanned Aircraft Systems," *CRC Press*, p. 234, Apr. 2016, doi: 10.1201/B11202.

[12] S. A. Long, M. W. McAllister, and L. C. Shen, "The Resonant Cylindrical Dielectric Cavity Antenna," *IEEE Trans. Antennas Propag.*, vol. 31, no. 3, pp. 406–412, 1983, doi: 10.1109/TAP.1983.1143080.

[13] B. Mukherjee, P. Patel, and J. Mukherjee, "A review of the recent advances in dielectric resonator antennas," *https://doi.org/10.1080/09205071.2020.1744484*, vol. 34, no. 9, pp. 1095–1158, Jun. 2020, doi: 10.1080/09205071.2020.1744484.

[14] N. Ioan, I. Andrei, T. Irina, R. Ionut, B. Gabriel, and N. Liviu, *High K dielectric resonator antenna*, vol. 7, no. 5. 2008.

[15] A. Petosa and A. Ittipiboon, "Dielectric resonator antennas: A historical review and the current state of the art," *IEEE Antennas Propag. Mag.*, vol. 52, no. 5, pp. 91–116, Oct. 2010, doi: 10.1109/MAP.2010.5687510.

[16] R. K. Mongia and P. Bhartia, "Dielectric resonator antennas—a review and general design relations for resonant frequency and bandwidth," *Int. J. Microw. Millimeter-Wave Comput. Eng.*, vol. 4, no. 3, pp. 230–247, Jul. 1994, doi: 10.1002/MMCE.4570040304.

[17] S. Keyrouz and D. Caratelli, "Dielectric Resonator Antennas: Basic Concepts, Design Guidelines, and Recent Developments at Millimeter-Wave Frequencies," *Int. J. Antennas Propag.*, vol. 2016, 2016, doi: 10.1155/2016/6075680.

[18] B. Mukherjee, P. Patel, and J. Mukherjee, "A review of the recent advances in dielectric resonator antennas," *J. Electromagn. Waves Appl.*, vol. 34, no. 9, pp. 1095–1158, Jun. 2020, doi: 10.1080/09205071.2020.1744484.

[19] R. D. Richtmyer, "Dielectric Resonators," *J. Appl. Phys.*, vol. 10, no. 6, p. 391, Apr. 2004, doi: 10.1063/1.1707320.

[20] O. Sager and F. Tisi, "On Eigenmodes and Forced Resonance-Modes of Dielectric Spheres," *Proc. IEEE*, vol. 56, no. 9, pp. 1593–1594, 1968, doi: 10.1109/PROC.1968.6656.

[21] J. Van Bladel, "On the Resonances of a Dielectric Resonator of Very High Permittivity," *IEEE Trans. Microw. Theory Tech.*, vol. 23, no. 2, pp. 199–208, 1975, doi: 10.1109/TMTT.1975.1128528.

[22] M. W. McAllister, S. A. Long, and G. L. Conway, "Rectangular dielectric resonator antenna," *Electron. Lett.*, vol. 19, no. 6, pp. 218–219, Mar. 1983, doi: 10.1049/EL:19830150.

[23] M. W. McAllister and S. A. Long, "Resonant hemispherical dielectric antenna," *Electron. Lett.*, vol.

20, no. 16, pp. 657–659, Aug. 1984, doi: 10.1049/EL:19840450.
[24] A. A. Kishk, H. A. Auda, and B. C. Ahn, "Radiation Characteristics of Cylindrical Dielectric Resonator Antennas with New Applications," *IEEE Antennas Propag. Soc. Newsl.*, vol. 31, no. 1, pp. 6–16, 1989, doi: 10.1109/MAP.1989.6095674.
[25] R. K. Mongia, "Half-Split Dielectric Resonator Placed on Metallic Plane for Antenna Applications," *Electron. Lett.*, vol. 25, no. 7, pp. 462–464, Mar. 1989, doi: 10.1049/EL:19890318.
[26] Y. Kobayashi and S. Tanaka, "Resonant Modes of a Dielectric Rod Resonator Short-Circuited at Both Ends by Parallel Conducting Plates," *IEEE Trans. Microw. Theory Tech.*, vol. 28, no. 10, pp. 1077–1085, 1980, doi: 10.1109/TMTT.1980.1130228.
[27] M. Tsuji, H. Shigesawa, and K. Takiyama, "Analytical and Experimental Investigations on Several Resonant Modes in Open Dielectric Resonators," *IEEE Trans. Microw. Theory Tech.*, vol. 32, no. 6, pp. 628–633, 1984, doi: 10.1109/TMTT.1984.1132739.
[28] E. Snitzer, "Cylindrical Dielectric Waveguide Modes," *JOSA, Vol. 51, Issue 5, pp. 491-498*, vol. 51, no. 5, pp. 491–498, May 1961, doi: 10.1364/JOSA.51.000491.
[29] H. Xu, L. Hu, Y. Lu, J. Xu, and Y. Chen, "Dual-Band Metamaterial Absorbers in the Visible and Near-Infrared Regions," *J. Phys. Chem. C*, vol. 123, no. 15, pp. 10028–10033, Apr. 2019, doi: 10.1021/acs.jpcc.9b00434.
[30] M. Gastine, L. Courtois, and J. L. Dormann, "Electromagnetic Resonances of Free Dielectric Spheres," *IEEE Trans. Microw. Theory Tech.*, vol. MTT-15, no. 12, pp. 694–700, 1967, doi: 10.1109/TMTT.1967.1126568.
[31] A. Karp, H. J. Shaw, and D. K. Winslow, "Circuit Properties of Microwave Dielectric Resonators," *IEEE Trans. Microw. Theory Tech.*, vol. 16, no. 10, pp. 818–828, 1968, doi: 10.1109/TMTT.1968.1126798.
[32] E. A. J. Marcatili, "Dielectric Rectangular Waveguide and Directional Coupler for Integrated Optics," *Bell Syst. Tech. J.*, vol. 48, no. 7, pp. 2071–2102, 1969, doi: 10.1002/J.1538-7305.1969.TB01166.X.
[33] M. Verplanken and J. V. Van Bladel, "The Electric-Dipole Resonances of Ring Resonators of Very High Permittivity," *IEEE Trans. Microw. Theory Tech.*, vol. 24, no. 2, pp. 108–112, 1976, doi: 10.1109/TMTT.1976.1128782.
[34] M. Verplanken and J. van Bladel, "The Magnetic-Dipole Resonances of Ring Resonators of Very High Permittivity," *IEEE Trans. Microw. Theory Tech.*, vol. 27, no. 4, pp. 328–333, 1979, doi: 10.1109/TMTT.1979.1129624.
[35] R. A. Kranenburg and S. A. Long, "Microstrip Transmission Line Excitation of Dielectric Resonator Antennas," *Electron. Lett.*, vol. 24, no. 18, pp. 1156–1157, 1988, doi: 10.1049/EL:19880785.
[36] J. T. H. S. Martin, Y. M. M. Antar, A. A. Kishk, A. Ittipiboon, and M. Cuhaci, "Dielectric resonator antenna using aperture coupling," *Electron. Lett.*, vol. 26, no. 24, pp. 2015–2016, 1990, doi: 10.1049/EL:19901302.
[37] A. Ittipiboon, R. K. Mongia, Y. M. M. Antar, P. Bhartia, and M. Cuhaci, "Integrated rectangular dielectric resonator antenna," *AP-S Int. Symp. (IEEE Antennas Propag. Soc.*, vol. 2, pp. 604–607, 1993, doi: 10.1109/APS.1993.385273.
[38] G. Zhou, A. A. Kishk, and A. W. Glisson, "Input impedance of a hemispherical dielectric resonator antenna excited by a coaxial probe," *AP-S Int. Symp. (IEEE Antennas Propag. Soc.*, vol. 2, pp. 1038–1041, 1993, doi: 10.1109/APS.1993.385171.
[39] K. W. Leung, K. Y. A. Lai, K. M. Luk, and D. Lin, "Input impedance of aperture coupled hemispherical dielectric resonator antenna," *Electron. Lett.*, vol. 29, no. 13, pp. 1165–1167, 1993, doi: 10.1049/EL:19930779.
[40] Z. Ying, X. Zhang, Sh. Wang, F. Xie, and Y. Zhang, "Gigahertz-clocked InGaAs/InP single photon avalanche photodiode with tunable gating frequency," *Microw. Opt. Technol. Lett.*, vol. 56, no. 8, pp. 1742–1744, 2014, doi: 10.1002/mop.
[41] R. K. Mongia and P. Bhartia, "Dielectric resonator antennas—a review and general design relations for resonant frequency and bandwidth," *Int. J. Microw. Millimeter-Wave Comput. Eng.*, vol. 4, no. 3, pp. 230–247, Jul. 1994, doi: 10.1002/MMCE.4570040304.
[42] R. S. Yaduvanshi and H. Parthasarathy, "Rectangular dielectric resonator antennas: Theory and design," *Rectangular Dielectr. Reson. Antennas Theory Des.*, pp. 1–366, Sep. 2015, doi: 10.1007/978-81-322-2500-3/COVER.
[43] U. Patri and A. Kumar, "A novel ultra wideband circularly polarized stacked cylindrical dielectric resonator antenna with modified ground plane," *Int. J. RF Microw. Comput. Eng.*, vol. 32, no. 8, p.

e23221, Aug. 2022, doi: 10.1002/MMCE.23221.
[44] G. Varshney, S. Debnath, and A. K. Sharma, “Tunable circularly polarized graphene antenna for THz applications,” *Optik (Stuttg).*, vol. 223, p. 165412, Dec. 2020, doi: 10.1016/J.IJLEO.2020.165412.
[45] Vishwanath, B. C. Sahana, and G. Varshney, “Tunable terahertz dual-band circularly polarized dielectric resonator antenna,” *Optik (Stuttg).*, vol. 253, p. 168578, Mar. 2022, doi: 10.1016/J.IJLEO.2022.168578.
[46] P. Upender and A. Kumar, “Quad-Band Circularly Polarized Tunable Graphene Based Dielectric Resonator Antenna for Terahertz Applications,” *Silicon 2021*, vol. 5, no. 10, pp. 1–14, Aug. 2021, doi: 10.1007/S12633-021-01336-5.
[47] P. Upender and A. Kumar, “Circularly Polarized 2×2 MIMO Dielectric Resonator Antenna for Terahertz Applications,” *2021 IEEE Indian Conf. Antennas Propag.*, pp. 283–286, Dec. 2021, doi: 10.1109/INCAP52216.2021.9726292.
[48] G. Varshney, R. Singh, V. S. Pandey, and R. S. Yaduvanshi, “Circularly Polarized Two-Port MIMO Dielectric Resonator Antenna,” *Prog. Electromagn. Res. M*, vol. 91, pp. 19–28, 2020, doi: 10.2528/PIERM20011003.
[49] G. Varshney, S. Gotra, R. Singh, V. S. Pandey, and R. S. Yaduvanshi, “Dimensions Selection Criteria of Stair shaped Slot for Obtaining the Wideband Response of CPDRA,” *Def. Sci. J.*, vol. 69, no. 5, pp. 442–447, Sep. 2019, doi: 10.14429/DSJ.69.14948.
[50] G. Varshney, S. Gotra, V. S. Pandey, and R. S. Yaduvanshi, “Inverted-Sigmoid Shaped Multiband Dielectric Resonator Antenna with Dual-Band Circular Polarization,” *IEEE Trans. Antennas Propag.*, vol. 66, no. 4, pp. 2067–2072, Apr. 2018, doi: 10.1109/TAP.2018.2800799.
[51] Z. Zhao, J. Ren, Y. Liu, Z. Zhou, and Y. Yin, “Wideband Dual-Feed, Dual-Sense Circularly Polarized Dielectric Resonator Antenna,” *IEEE Trans. Antennas Propag.*, vol. 68, no. 12, pp. 7785–7793, Dec. 2020, doi: 10.1109/TAP.2020.2999754.
[52] R. Y. Sun, “Bandwidth enhancement of circularly polarized dielectric resonator antenna,” *ETRI J.*, vol. 37, no. 1, pp. 26–31, 2015, doi: 10.4218/etrij.15.0114.0637.
[53] G. Z. Wang and B. X. Wang, “Five-Band Terahertz Metamaterial Absorber Based on a Four-Gap Comb Resonator,” *J. Light. Technol.*, vol. 33, no. 24, pp. 5151–5156, 2015, doi: 10.1109/JLT.2015.2497740.
[54] S. Ullah *et al.*, “Microstrip system on-chip circular polarized (CP) slotted antenna for THz communication application,” *J. Electromagn. WAVES Appl.*, vol. 2020, no. 8, pp. 1029–1038, 2020, doi: 10.1080/09205071.2020.1770130.
[55] R. Chowdhury, N. Mishra, M. M. Sani, and R. K. Chaudhary, “Analysis of a Wideband Circularly Polarized Cylindrical Dielectric Resonator Antenna with Broadside Radiation Coupled with Simple Microstrip Feeding,” *IEEE Access*, vol. 5, pp. 19478–19485, Sep. 2017, doi: 10.1109/ACCESS.2017.2752210.
[56] U. Ullah, M. F. Ain, and Z. A. Ahmad, “A review of wideband circularly polarized dielectric resonator antennas,” *China Commun.*, vol. 14, no. 6, pp. 65–79, Jun. 2017, doi: 10.1109/CC.2017.7961364.
[57] G. Varshney, V. S. Pandey, and R. S. Yaduvanshi, “Dual-band fan-blade-shaped circularly polarised dielectric resonator antenna,” *IET Microwaves, Antennas Propag.*, vol. 11, no. 13, pp. 1868–1871, Oct. 2017, doi: 10.1049/IET-MAP.2017.0244.
[58] G. Varshney, V. S. Pandey, and R. S. Yaduvanshi, “Axial ratio bandwidth enhancement of a circularly polarized rectangular dielectric resonator antenna,” *Int. J. Microw. Wirel. Technol.*, vol. 10, no. 8, pp. 984–990, Oct. 2018, doi: 10.1017/S1759078718000764.
[59] M. B. Oliver, R. K. Mongia, and Y. M. M. Antar, “New broadband circularly polarized dielectric resonator antenna,” *IEEE Antennas Propag. Soc. AP-S Int. Symp.*, vol. 1, pp. 738–741, 1995, doi: 10.1109/APS.1995.530123.
[60] B. Li, C. X. Hao, and X. Q. Sheng, “A dual-mode quadrature-fed wideband circularly polarized dielectric resonator antenna,” *IEEE Antennas Wirel. Propag. Lett.*, vol. 8, pp. 1036–1038, 2009, doi: 10.1109/LAWP.2009.2030700.
[61] E. H. Lim, K. W. Leung, and X. S. Fang, “The compact circularly-polarized hollow rectangular dielectric resonator antenna with an underlaid quadrature coupler,” *IEEE Trans. Antennas Propag.*, vol. 59, no. 1, pp. 288–293, Jan. 2011, doi: 10.1109/TAP.2010.2090454.
[62] Y. Pan, K. W. Leung, and E. H. Lim, “Compact wideband circularly polarized rectangular dielectric resonator antenna with dual underlaid hybrid couplers,” *Microw. Opt. Technol. Lett.*, vol. 52, no. 12, pp. 2789–2791, Dec. 2010, doi: 10.1002/MOP.25591.

[63] S. Fakhte, H. Oraizi, R. Karimian, and R. Fakhte, "A New Wideband Circularly Polarized Stair-Shaped Dielectric Resonator Antenna," *IEEE Trans. Antennas Propag.*, vol. 63, no. 4, pp. 1828–1832, Apr. 2015, doi: 10.1109/TAP.2015.2392131.

[64] M. Khalily, M. R. Kamarudin, and M. H. Jamaluddin, "A novel square dielectric resonator antenna with two unequal inclined slits for wideband circular polarization," *IEEE Antennas Wirel. Propag. Lett.*, vol. 12, pp. 1256–1259, 2013, doi: 10.1109/LAWP.2013.2283536.

[65] G. Almpanis, C. Fumeaux, and R. Vahldieck, "Offset cross-slot-coupled dielectric resonator antenna for circular polarization," *IEEE Microw. Wirel. Components Lett.*, vol. 16, no. 8, pp. 461–463, Aug. 2006, doi: 10.1109/LMWC.2006.879484.

[66] C. Y. Huang, J. Y. Wu, and K. L. Wong, "Cross-slot-coupled microstrip antenna and dielectric resonator antenna for circular polarization," *IEEE Trans. Antennas Propag.*, vol. 47, no. 4, pp. 605–609, 1999, doi: 10.1109/8.768798.

[67] M. Zhang, B. Li, and X. Lv, "Cross-slot-coupled wide dual-band circularly polarized rectangular dielectric resonator antenna," *IEEE Antennas Wirel. Propag. Lett.*, vol. 13, pp. 532–535, 2014, doi: 10.1109/LAWP.2014.2310241.

[68] M. Zou, J. Pan, and Z. Nie, "A wideband circularly polarized rectangular dielectric resonator antenna excited by an archimedean spiral slot," *IEEE Antennas Wirel. Propag. Lett.*, vol. 14, pp. 446–449, 2015, doi: 10.1109/LAWP.2014.2364296.

[69] A. Perron, T. A. Denidni, and A. R. Sebak, "Circularly polarized microstrip/elliptical dielectric ring resonator antenna for millimeter-wave applications," *IEEE Antennas Wirel. Propag. Lett.*, vol. 9, pp. 783–786, 2010, doi: 10.1109/LAWP.2010.2064750.

[70] M. T. K. Tarn and R. D. Murch, "Circularly polarized circular sector dielectric resonator antenna," *IEEE Trans. Antennas Propag.*, vol. 48, no. 1, pp. 126–128, 2000, doi: 10.1109/8.827396.

[71] K. W. Leung, E. H. Lim, and X. S. Fang, "Dielectric resonator antennas: From the basic to the aesthetic," *Proc. IEEE*, vol. 100, no. 7, pp. 2181–2193, 2012, doi: 10.1109/JPROC.2012.2187872.

[72] K. X. Wang and H. Wong, "A Circularly Polarized Antenna by Using Rotated-Stair Dielectric Resonator," *IEEE Antennas Wirel. Propag. Lett.*, vol. 14, pp. 787–790, 2015, doi: 10.1109/LAWP.2014.2385475.

[73] G. Varshney, S. Gotra, V. S. Pandey, and R. S. Yaduvanshi, "Proximity-coupled two-port multi-input-multi-output graphene antenna with pattern diversity for THz applications," *Nano Commun. Netw.*, vol. 21, p. 100246, Sep. 2019, doi: 10.1016/J.NANCOM.2019.05.003.

[74] G. W. Hanson, "Dyadic green's functions for an anisotropic, non-local model of biased graphene," *IEEE Trans. Antennas Propag.*, vol. 56, no. 3, pp. 747–757, Mar. 2008, doi: 10.1109/TAP.2008.917005.

[75] F. Liang, Z. Z. Yang, Y. X. Xie, H. Li, D. Zhao, and B. Z. Wang, "Beam-Scanning Microstrip Quasi-Yagi-Uda Antenna Based on Hybrid Metal-Graphene Materials," *IEEE Photonics Technol. Lett.*, vol. 30, no. 12, pp. 1127–1130, Jun. 2018, doi: 10.1109/LPT.2018.2835840.

[76] L. Tai *et al.*, "Direct Growth of Graphene on Silicon by Metal-Free Chemical Vapor Deposition," *Nano-Micro Lett.*, vol. 10, no. 2, pp. 1–9, Jun. 2018, doi: 10.1007/S40820-017-0173-1/FIGURES/5.

[77] Z. Xu, X. Dong, and J. Bornemann, "Design of a reconfigurable MIMO system for THz communications based on graphene antennas," *IEEE Trans. Terahertz Sci. Technol.*, vol. 4, no. 5, pp. 609–617, 2014, doi: 10.1109/TTHZ.2014.2331496.

[78] P. H. Siegel, "Terahertz technology," *IEEE Trans. Microw. Theory Tech.*, vol. 50, no. 3, pp. 910–928, Mar. 2002, doi: 10.1109/22.989974.

[79] A. Y. Pawar, D. D. Sonawane, K. B. Erande, and D. V. Derle, "Terahertz technology and its applications," *Drug Invent. Today*, vol. 5, no. 2, pp. 157–163, Jun. 2013, doi: 10.1016/J.DIT.2013.03.009.

[80] Z. Vafapour *et al.*, "The Potential of Refractive Index Nanobiosensing Using a Multi-Band Optically Tuned Perfect Light Metamaterial Absorber," *IEEE Sens. J.*, vol. 21, no. 12, pp. 13786–13793, Jun. 2021, doi: 10.1109/JSEN.2021.3070731.

[81] Z. Xiong *et al.*, "Terahertz Sensor with Resonance Enhancement Based on Square Split-Ring Resonators," *IEEE Access*, vol. 9, pp. 59211–59221, 2021, doi: 10.1109/ACCESS.2021.3073043.

[82] C. Luo *et al.*, "Design of a tunable multiband terahertz waves absorber," *J. Alloys Compd.*, vol. 652, pp. 18–24, Dec. 2015, doi: 10.1016/J.JALLCOM.2015.08.089.

[83] H. Elayan, O. Amin, B. Shihada, R. M. Shubair, and M. S. Alouini, "Terahertz band: The last piece of rf spectrum puzzle for communication systems," *IEEE Open J. Commun. Soc.*, vol. 1, pp. 1–32, 2020, doi: 10.1109/OJCOMS.2019.2953633.

[84] H. B. Baskey, E. Johari, and M. J. Akhtar, "Metamaterial Structure Integrated with a Dielectric Absorber for Wideband Reduction of Antennas Radar Cross Section," *IEEE Trans. Electromagn. Compat.*, vol. 59, no. 4, pp. 1060–1069, Aug. 2017, doi: 10.1109/TEMC.2016.2639060.

[85] S. Tan, F. Yan, W. Wang, H. Zhou, and Y. Hou, "Ultrasensitive sensing with three-dimensional terahertz metamaterial absorber," *J. Opt.*, vol. 20, no. 5, p. 055101, Apr. 2018, doi: 10.1088/2040-8986/AAB66E.

[86] M. Q. Dinh, M. Thuy Le, S. Tung Ngo, T. Van Huynh, and N. Thanh Tung, "Terahertz cut-wire-pair metamaterial absorber," *J. Appl. Phys.*, vol. 130, no. 1, p. 013102, Jul. 2021, doi: 10.1063/5.0053648.

[87] N. I. Landy, S. Sajuyigbe, J. J. Mock, D. R. Smith, and W. J. Padilla, "Perfect metamaterial absorber," *Phys. Rev. Lett.*, vol. 100, no. 20, p. 207402, May 2008, doi: 10.1103/PHYSREVLETT.100.207402/FIGURES/5/MEDIUM.

[88] Y. Cheng and H. Yang, "Retracted: Design, simulation, and measurement of metamaterial absorber," *Microw. Opt. Technol. Lett.*, vol. 52, no. 4, pp. 877–880, Apr. 2010, doi: 10.1002/MOP.25068.

[89] J. Zhou, A. F. Kaplan, L. Chen, and L. J. Guo, "Experiment and Theory of the Broadband Absorption by a Tapered Hyperbolic Metamaterial Array," *ACS Photonics*, vol. 1, no. 7, pp. 618–624, Jul. 2014, doi: 10.1021/PH5001007/SUPPL_FILE/PH5001007_SI_001.PDF.

[90] G. Shvets and C. Wu, "Design of metamaterial surfaces with broadband absorbance," *Opt. Lett. Vol. 37, Issue 3, pp. 308-310*, vol. 37, no. 3, pp. 308–310, Feb. 2012, doi: 10.1364/OL.37.000308.

[91] H. Yang *et al.*, "Dual-band and polarization-independent metamaterial terahertz narrowband absorber," *Appl. Opt. Vol. 60, Issue 8, pp. 2235-2241*, vol. 60, no. 8, pp. 2235–2241, Mar. 2021, doi: 10.1364/AO.415461.

[92] B. X. Wang, C. Tang, Q. Niu, Y. He, and R. Chen, "A broadband terahertz metamaterial absorber enabled by the simple design of a rectangular-shaped resonator with an elongated slot," *Nanoscale Adv.*, vol. 1, no. 9, pp. 3621–3625, Sep. 2019, doi: 10.1039/C9NA00385A.

[93] L. Ye, X. Chen, F. Zeng, J. Zhuo, F. Shen, and Q. H. Liu, "Ultra-wideband terahertz absorption using dielectric circular truncated cones," *IEEE Photonics J.*, vol. 11, no. 5, Oct. 2019, doi: 10.1109/JPHOT.2019.2934653.

[94] Y. Zhou, H. Xia, L. Zhang, Y. Zhao, and W. Xie, "Temperature insensitive ultra-broadband THz metamaterial absorber based on metal square ring resonators," *Results Phys.*, vol. 22, p. 103915, Mar. 2021, doi: 10.1016/J.RINP.2021.103915.

[95] A. Mohanty, O. P. Acharya, B. Appasani, S. K. Mohapatra, and M. S. Khan, "Design of a Novel Terahertz Metamaterial Absorber for Sensing Applications," *IEEE Sens. J.*, vol. 21, no. 20, pp. 22688–22694, Oct. 2021, doi: 10.1109/JSEN.2021.3109158.

[96] chaharmahali Iman and B. Sadegh, "Ultra-broadband terahertz absorber based on graphene ribbons," *Optik (Stuttg).*, vol. 172, pp. 1026–1033, Nov. 2018, doi: 10.1016/J.IJLEO.2018.07.137.

[97] S. Barzegar-Parizi, A. Ebrahimi, and K. Ghorbani, "High-Q dual-band graphene absorbers by selective excitation of graphene plasmon polaritons: Circuit model analysis," *Opt. Laser Technol.*, vol. 132, p. 106483, Dec. 2020, doi: 10.1016/J.OPTLASTEC.2020.106483.

[98] W. M. Abdel-Wahab, A. S. Hussam, S. Safavi-Naeini, and Y. Wang, "Circularly polarized SIW-integrated DRA for low cost millimeter wave systems," *2015 Glob. Symp. Millimeter-Waves, GSMM 2015*, Aug. 2015, doi: 10.1109/GSMM.2015.7175456.

[99] S. Kong, K. M. Shum, C. Yang, L. Gao, and C. H. Chan, "Wide impedance-bandwidth and gain-bandwidth terahertz on-chip antenna with chip-integrated dielectric resonator," *IEEE Trans. Antennas Propag.*, vol. 69, no. 8, pp. 4269–4278, Aug. 2021, doi: 10.1109/TAP.2021.3060060.

[100] T. Okan, "High efficiency unslotted ultra-wideband microstrip antenna for sub-terahertz short range wireless communication systems," *Optik (Stuttg).*, vol. 242, p. 166859, Sep. 2021, doi: 10.1016/J.IJLEO.2021.166859.

[101] Z. Chen, H. Wong, and J. Kelly, "A Polarization-Reconfigurable Glass Dielectric Resonator Antenna Using Liquid Metal," *IEEE Trans. Antennas Propag.*, vol. 67, no. 5, pp. 3427–3432, May 2019, doi: 10.1109/TAP.2019.2901132.

[102] Q. Y. Guo, Q. W. Lin, and H. Wong, "A High Gain Millimeter-Wave Circularly Polarized Fabry-Pérot Antenna Using PRS-Integrated Polarizer," *IEEE Trans. Antennas Propag.*, vol. 69, no. 2, pp. 1179–1183, Feb. 2021, doi: 10.1109/TAP.2020.3011110.

[103] R. Gupta, G. Varshney, and R. S. Yaduvanshi, "Tunable terahertz circularly polarized dielectric resonator antenna," *Optik (Stuttg).*, vol. 239, p. 166800, Aug. 2021, doi: 10.1016/J.IJLEO.2021.166800.

[104] A. Nourmohammadi and M. Nikoufard, "Ultra-Wideband Photonic Hybrid Plasmonic Horn

Nanoantenna with SOI Configuration," *Silicon 2019 121*, vol. 12, no. 1, pp. 193–198, Apr. 2019, doi: 10.1007/S12633-019-00113-9.

[105] S. N. Novin, F. B. Zarrabi, M. Bazgir, S. Heydari, and S. Ebrahimi, "Field Enhancement in Metamaterial Split Ring Resonator Aperture Nano-Antenna with Spherical Nano-Particle Arrangement," *Silicon 2018 111*, vol. 11, no. 1, pp. 293–300, Apr. 2018, doi: 10.1007/S12633-018-9854-8.

[106] L. Huitema, T. Monediere, L. Huitema, and T. Monediere, "Dielectric Materials for Compact Dielectric Resonator Antenna Applications," *Dielectr. Mater.*, Oct. 2012, doi: 10.5772/50612.

[107] K. W. Luk, K. M., & Leung, *Dielectric Resonator Antennas: Research Studies*. Press Ltd., England, 2003.

[108] Y. Yang *et al.*, "Bottom-up Fabrication of Graphene on Silicon/Silica Substrate via a Facile Soft-hard Template Approach," *Sci. Reports 2015 51*, vol. 5, no. 1, pp. 1–7, Aug. 2015, doi: 10.1038/srep13480.

[109] L. Tai *et al.*, "Direct Growth of Graphene on Silicon by Metal-Free Chemical Vapor Deposition," *Nano-Micro Lett.*, vol. 10, no. 2, pp. 1–9, Jun. 2018, doi: doi.org/10.1007/s40820-017-0173-1.

[110] P. Y. Chen, C. Argyropoulos, and A. Alu, "Terahertz antenna phase shifters using integrally-gated graphene transmission-lines," *IEEE Trans. Antennas Propag.*, vol. 61, no. 4, pp. 1528–1537, 2013, doi: 10.1109/TAP.2012.2220327.

[111] K. R. Jha and G. Singh, "Terahertz planar antennas for future wireless communication: A technical review," *Infrared Phys. Technol.*, vol. 60, pp. 71–80, Sep. 2013, doi: 10.1016/J.INFRARED.2013.03.009.

[112] P. Ranjan and R. K. Gangwar, "Design and Fabrication of High Gain Multi-element Multi-segment Quarter-sector Cylindrical Dielectric Resonator Antenna," *Frequenz*, vol. 72, no. 1–2, pp. 15–25, Dec. 2017, doi: 10.1515/FREQ-2016-0353/MACHINEREADABLECITATION/RIS.

[113] Z. Xu, X. Dong, and J. Bornemann, "Spectral efficiency of carbon nanotube antenna based MIMO systems in the terahertz band," *IEEE Wirel. Commun. Lett.*, vol. 2, no. 6, pp. 631–634, 2013, doi: 10.1109/WCL.2013.090313.130366.

[114] R. H. Elabd, H. H. Abdullah, and M. Abdelazim, "Compact Highly Directive MIMO Vivaldi Antenna for 5G Millimeter-Wave Base Station," *J. Infrared, Millimeter, Terahertz Waves*, vol. 42, no. 2, pp. 173–194, Feb. 2021, doi: 10.1007/S10762-020-00765-4/TABLES/6.

[115] G. Varshney, S. Gotra, S. Chaturvedi, V. S. Pandey, and R. S. Yaduvanshi, "Compact four-port MIMO dielectric resonator antenna with pattern diversity," *IET Microwaves, Antennas Propag.*, vol. 13, no. 12, pp. 2193–2198, Oct. 2019, doi: 10.1049/IET-MAP.2018.5799/CITE/REFWORKS.

[116] G. Das, A. Sharma, and R. K. Gangwar, "Dielectric resonator based circularly polarized MIMO antenna with polarization diversity," *Microw. Opt. Technol. Lett.*, vol. 60, no. 3, pp. 685–693, Mar. 2018, doi: 10.1002/MOP.31033.

[117] P. Upender and A. Kumar, "Quad-Band Circularly Polarized Tunable Graphene Based Dielectric Resonator Antenna for Terahertz Applications," *Silicon 2021*, vol. 5, no. 10, pp. 1–14, Aug. 2021, doi: 10.1007/S12633-021-01336-5.

[118] H. Shakhatreh *et al.*, "Unmanned Aerial Vehicles (UAVs): A Survey on Civil Applications and Key Research Challenges," *IEEE Access*, vol. 7, pp. 48572–48634, 2019, doi: 10.1109/ACCESS.2019.2909530.

[119] R. W. Beard and T. W. McLain, "Small unmanned aircraft: Theory and practice," *Princet. Univ. Press*, Feb. 2012, doi: 10.2514/1.61067.

[120] H. Xu *et al.*, "Single-Fed Dual-Circularly Polarized Stacked Dielectric Resonator Antenna for K/Ka-Band UAV Satellite Communications," *IEEE Trans. Veh. Technol.*, vol. 71, no. 4, pp. 4449–4453, Apr. 2022, doi: 10.1109/TVT.2022.3144414.

[121] M. S. Sharawi, D. N. Aloi, and O. A. Rawashdeh, "Design and implementation of embedded printed antenna arrays in small UAV wing structures," *IEEE Trans. Antennas Propag.*, vol. 58, no. 8, pp. 2531–2538, Aug. 2010, doi: 10.1109/TAP.2010.2050440.

[122] J. Zhu, Y. Yang, S. Li, S. Liao, and Q. Xue, "Dual-Band Dual Circularly Polarized Antenna Array Using FSS-Integrated Polarization Rotation AMC Ground for Vehicle Satellite Communications," *IEEE Trans. Veh. Technol.*, vol. 68, no. 11, pp. 10742–10751, Nov. 2019, doi: 10.1109/TVT.2019.2938266.

[123] J. Chen *et al.*, "Long-range and broadband aerial communication using directional antennas (ACDA): Design and implementation," *IEEE Trans. Veh. Technol.*, vol. 66, no. 12, pp. 10793–10805, Dec. 2017, doi: 10.1109/TVT.2017.2723802.

[124] Z. P. Zhong *et al.*, "A Compact Dual-Band Circularly Polarized Antenna with Wide Axial-Ratio Beamwidth for Vehicle GPS Satellite Navigation Application," *IEEE Trans. Veh. Technol.*, vol. 68, no. 9, pp. 8683–8692, Sep. 2019, doi: 10.1109/TVT.2019.2920520.

[125] Y. H. Huang, Y. Wang, Y. L. Zou, and J. L. Guo, "A Miniature Circularly Polarized Air-Borne Antenna with Wide Angle Coverage," *IEEE Antennas Wirel. Propag. Lett.*, vol. 16, pp. 497–500, 2017, doi: 10.1109/LAWP.2016.2585758.

[126] R. Xu, S. S. Gao, J. Li, K. Wei, and Q. Luo, "A Reconfigurable Dual-Band Dual-Circularly Polarized Antenna for Vehicle Global Navigation Satellite System Application," *IEEE Trans. Veh. Technol.*, vol. 69, no. 10, pp. 11857–11867, Oct. 2020, doi: 10.1109/TVT.2020.3020261.

[127] P. Mallick, M. Ameen, R. Chowdhury, A. K. Ray, and R. K. Chaudhary, "Wideband Circularly Polarized Cavity-Backed Dielectric Resonator Antenna With Low RCS for Aerial Vehicle Communications," *IEEE Antennas Wirel. Propag. Lett.*, vol. 21, no. 7, pp. 1418–1422, Jul. 2022, doi: 10.1109/LAWP.2022.3170407.

[128] P. Upender and A. Kumar, "HEM11δ and HEM12δ-based Quad band Quad Sense Circularly Polarized tunable Graphene-based MIMO Dielectric Resonator Antenna," *Frequenz*, vol. 76, no. 5, pp. 273–285, Jun. 2022, doi: 10.1515/freq-2021-0145.

[129] Vishwanath, G. Varshney, and B. C. Sahana, "Implementing the single/multiport tunable terahertz circularly polarized dielectric resonator antenna," *Nano Commun. Netw.*, vol. 32–33, Jun. 2022, doi: 10.1016/J.NANCOM.2022.100408.

[130] X. Ren, S. Liao, and Q. Xue, "A Circularly Polarized Spaceborne Antenna with Shaped Beam for Earth Coverage Applications," *IEEE Trans. Antennas Propag.*, vol. 67, no. 4, pp. 2235–2242, Apr. 2019, doi: 10.1109/TAP.2018.2889188.

[131] R. Sen Chen *et al.*, "S-Band Full-Metal Circularly Polarized Cavity-Backed Slot Antenna with Wide Bandwidth and Wide Beamwidth," *IEEE Trans. Antennas Propag.*, vol. 69, no. 9, pp. 5963–5968, Sep. 2021, doi: 10.1109/TAP.2021.3061116.

[132] M. Akbari, S. Gupta, M. Farahani, A. R. Sebak, and T. A. Denidni, "Gain Enhancement of Circularly Polarized Dielectric Resonator Antenna Based on FSS Superstrate for MMW Applications," *IEEE Trans. Antennas Propag.*, vol. 64, no. 12, pp. 5542–5546, Dec. 2016, doi: 10.1109/TAP.2016.2623655.

[133] Y. D. Zhou, Y. C. Jiao, Z. Bin Weng, and T. Ni, "A Novel Single-Fed Wide Dual-Band Circularly Polarized Dielectric Resonator Antenna," *IEEE Antennas Wirel. Propag. Lett.*, vol. 15, pp. 930–933, 2016, doi: 10.1109/LAWP.2015.2481462.

[134] R. Kumar and R. K. Chaudhary, "A Wideband Circularly Polarized Cubic Dielectric Resonator Antenna Excited with Modified Microstrip Feed," *IEEE Antennas Wirel. Propag. Lett.*, vol. 15, pp. 1285–1288, 2016, doi: 10.1109/LAWP.2015.2504840.

[135] N. Yang, K. W. Leung, K. Lu, and N. Wu, "Omnidirectional Circularly Polarized Dielectric Resonator Antenna with Logarithmic Spiral Slots in the Ground," *IEEE Trans. Antennas Propag.*, vol. 65, no. 2, pp. 839–844, Feb. 2017, doi: 10.1109/TAP.2016.2634280.

[136] R. Kumar and R. K. Chaudhary, "Compact asymmetric cross-shaped rectangular dielectric resonator antenna for wideband circular polarization," *Microw. Opt. Technol. Lett.*, vol. 61, no. 7, pp. 1863–1873, Jul. 2019, doi: 10.1002/MOP.31808.

[137] U. Illahi, J. Iqbal, M. I. Sulaiman, M. Alam, M. M. Su'ud, and M. I. Khattak, "Design and development of a singly-fed circularly polarized rectangular dielectric resonator antenna for WiMAX/Satellite/5G NR band applications," *AEU - Int. J. Electron. Commun.*, vol. 126, p. 153443, Nov. 2020, doi: 10.1016/J.AEUE.2020.153443.

[138] M. Moniruzzaman, M. T. Islam, G. Muhammad, M. S. J. Singh, and M. Samsuzzaman, "Quad band metamaterial absorber based on asymmetric circular split ring resonator for multiband microwave applications," *Results Phys.*, vol. 19, p. 103467, Dec. 2020, doi: 10.1016/J.RINP.2020.103467.

[139] D. Hu, H. Y. Wang, and Q. F. Zhu, "Design of Six-Band Terahertz Perfect Absorber Using a Simple U-Shaped Closed-Ring Resonator," *IEEE Photonics J.*, vol. 8, no. 2, Apr. 2016, doi: 10.1109/JPHOT.2016.2538758.

[140] Y. Chen, X. Pan, Z. Bao, Y. Wang, Z. Da Hu, and J. Wang, "Tunable Terahertz Perfect-Absorbers with Dual Peak Based on Reverse Graphene Patch Metamaterials," *IEEE Photonics J.*, vol. 13, no. 3, Jun. 2021, doi: 10.1109/JPHOT.2021.3075466.

[141] Y. He, Q. Wu, and S. Yan, "Multi-Band Terahertz Absorber at 0.1–1 THz Frequency Based on Ultra-Thin Metamaterial," *Plasmonics*, vol. 14, no. 6, pp. 1303–1310, Dec. 2019, doi: 10.1007/S11468-019-00936-7/FIGURES/10.

[142] B. X. Wang and G. Z. Wang, "New Type Design of the Triple-Band and Five-Band Metamaterial Absorbers at Terahertz Frequency," *Plasmonics*, vol. 13, no. 1, pp. 123–130, Feb. 2018, doi: 10.1007/S11468-016-0491-Z/FIGURES/7.
[143] A. K. Soni and G. Varshney, "Multiband Generation and Absorption Enhancement in a Graphite-Based Metal-Free Absorber," *Plasmonics*, vol. 16, no. 1, pp. 241–252, Feb. 2021, doi: 10.1007/S11468-020-01286-5/FIGURES/13.
[144] G. W. Hanson, "Dyadic Green's functions and guided surface waves for a surface conductivity model of graphene," *J. Appl. Phys.*, vol. 103, no. 6, p. 064302, Mar. 2008, doi: 10.1063/1.2891452.
[145] Y. Wang, X. Hong, G. Yang, and T. Sang, "Filtering characteristics of a graphene ribbon with a rectangle ring in infrared region," *AIP Adv.*, vol. 6, no. 11, p. 115311, Dec. 2016, doi: 10.1063/1.4967822.
[146] M. S. Khan, G. Varshney, and P. Giri, "Altering the multimodal resonance in ultrathin silicon ring for tunable THz biosensing," *IEEE Trans. Nanobioscience*, vol. 20, no. 4, pp. 488–496, Oct. 2021, doi: 10.1109/TNB.2021.3105561.
[147] N. Mou *et al.*, "Hybridization-induced broadband terahertz wave absorption with graphene metasurfaces," *Opt. Express, Vol. 26, Issue 9, pp. 11728-11736*, vol. 26, no. 9, pp. 11728–11736, Apr. 2018, doi: 10.1364/OE.26.011728.
[148] G. Varshney and P. Giri, "Bipolar charge trapping for absorption enhancement in a graphene-based ultrathin dual-band terahertz biosensor," *Nanoscale Adv.*, vol. 3, no. 20, pp. 5813–5822, Oct. 2021, doi: 10.1039/D1NA00388G.
[149] Q. Y. Wen, H. W. Zhang, Y. S. Xie, Q. H. Yang, and Y. L. Liu, "Dual band terahertz metamaterial absorber: Design, fabrication, and characterization," *Appl. Phys. Lett.*, vol. 95, no. 24, p. 241111, Dec. 2009, doi: 10.1063/1.3276072.
[150] M. Janneh, A. De Marcellis, E. Palange, A. T. Tenggara, and D. Byun, "Design of a metasurface-based dual-band Terahertz perfect absorber with very high Q-factors for sensing applications," *Opt. Commun.*, vol. 416, pp. 152–159, Jun. 2018, doi: 10.1016/J.OPTCOM.2018.02.013.
[151] G. Z. Wang and B. X. Wang, "Five-Band Terahertz Metamaterial Absorber Based on a Four-Gap Comb Resonator," *J. Light. Technol.*, vol. 33, no. 24, pp. 5151–5156, Dec. 2015, doi: 10.1109/JLT.2015.2497740.
[152] J. Wu, X. Yan, X. Yuan, Y. Zhang, and X. Zhang, "A dual-tunable ultra-broadband terahertz absorber based on graphene and strontium titanate," *Results Phys.*, vol. 31, Dec. 2021, doi: 10.1016/J.RINP.2021.105039.
[153] J. Zhang, G. Wang, B. Zhang, T. He, Y. He, and J. Shen, "Photo-excited broadband tunable terahertz metamaterial absorber," *Opt. Mater. (Amst).*, vol. 54, pp. 32–36, Apr. 2016, doi: 10.1016/J.OPTMAT.2016.02.011.
[154] A. Fardoost, F. G. Vanani, A. Amirhosseini, and R. Safian, "Design of a Multilayer Graphene-Based Ultrawideband Terahertz Absorber," *IEEE Trans. Nanotechnol.*, vol. 16, no. 1, pp. 68–74, Jan. 2017, doi: 10.1109/TNANO.2016.2627939.
[155] W. Pan, X. Yu, J. Zhang, and W. Zeng, "A Novel Design of Broadband Terahertz Metamaterial Absorber Based on Nested Circle Rings," *IEEE Photonics Technol. Lett.*, vol. 28, no. 21, pp. 2335–2338, Nov. 2016, doi: 10.1109/LPT.2016.2593699.
[156] H. Feng *et al.*, "Tunable polarization-independent and angle-insensitive broadband terahertz absorber with graphene metamaterials," *Opt. Express, Vol. 29, Issue 5, pp. 7158-7167*, vol. 29, no. 5, pp. 7158–7167, Mar. 2021, doi: 10.1364/OE.418865.
[157] A. Ebrahimi, K. Ghorbani, and S. Barzegar-Parizi, "Dual-broadband and single ultrawideband absorbers from the terahertz to infrared regime," *JOSA B, Vol. 38, Issue 9, pp. 2628-2637*, vol. 38, no. 9, pp. 2628–2637, Sep. 2021, doi: 10.1364/JOSAB.432329.
[158] G. Feng, S. Lin, and X. Li, "Ultra-wideband terahertz absorber based on graphene modulation," *Appl. Opt. Vol. 60, Issue 11, pp. 3170-3175*, vol. 60, no. 11, pp. 3170–3175, Apr. 2021, doi: 10.1364/AO.420143.
[159] H. Liu, Z. H. Wang, L. Li, Y. X. Fan, and Z. Y. Tao, "Vanadium dioxide-assisted broadband tunable terahertz metamaterial absorber," *Sci. Reports 2019 91*, vol. 9, no. 1, pp. 1–10, Apr. 2019, doi: 10.1038/s41598-019-42293-9.
[160] M. Shahidul Islam, G. Kok Beng, N. Misran, N. Amin, and M. Tariqul Islam, "A Gap Coupled Hexagonal Split Ring Resonator Based Metamaterial for S-band and X-band Microwave Applications," doi: 10.1109/ACCESS.2020.2985845.
[161] R. Marqués, F. Medina, and R. Rafii-El-Idrissi, "Role of bianisotropy in negative permeability and

left-handed metamaterials," *Phys. Rev. B*, vol. 65, no. 14, p. 144440, Apr. 2002, doi: 10.1103/PhysRevB.65.144440.
[162] S. Maslovski, P. Ikonen, I. Kolmakov, S. A. Tretyakov, and M. Kaunisto, "Artificial Magnetic Materials Based on the New Magnetic Particle: Metasolenoid," *Prog. Electromagn. Res.*, vol. 54, pp. 61–81, 2005, doi: 10.2528/PIER04101101.
[163] P. Upender, A. Kumar, and A. Kumar, "Design of a multiband graphene-based absorber for terahertz applications using different geometric shapes," *JOSA B, Vol. 39, Issue 1, pp. 188-199*, vol. 39, no. 1, pp. 188–199, Jan. 2022, doi: 10.1364/JOSAB.440757.
[164] Y. Wang, X. Hong, G. Yang, and T. Sang, "Filtering characteristics of a graphene ribbon with a rectangle ring in infrared region," *AIP Adv.*, vol. 6, no. 11, p. 115311, Dec. 2016, doi: 10.1063/1.4967822.
[165] N. Mou *et al.*, "Hybridization-induced broadband terahertz wave absorption with graphene metasurfaces," *Opt. Express, Vol. 26, Issue 9, pp. 11728-11736*, vol. 26, no. 9, pp. 11728–11736, Apr. 2018, doi: 10.1364/OE.26.011728.
[166] N. Yi, R. Zong, J. Gong, and R. Qian, "Dynamically tunable broadband absorber with a single ultra-thin layer of graphene in the terahertz regime," *Mater. Sci. Semicond. Process.*, vol. 136, p. 106161, Dec. 2021, doi: 10.1016/J.MSSP.2021.106161.
[167] F. Gao *et al.*, "Broadband wave absorption in single-layered and nonstructured graphene based on far-field interaction effect," *Opt. Express, Vol. 25, Issue 9, pp. 9579-9586*, vol. 25, no. 9, pp. 9579–9586, May 2017, doi: 10.1364/OE.25.009579.
[168] Z. Song, M. Jiang, Y. Deng, and A. Chen, "Wide-angle absorber with tunable intensity and bandwidth realized by a terahertz phase change material," *Opt. Commun.*, vol. 464, p. 125494, Jun. 2020, doi: 10.1016/J.OPTCOM.2020.125494.
[169] Y. Li *et al.*, "Tunable broadband metamaterial absorber with single-layered graphene arrays of rings and discs in terahertz range," *Phys. Scr.*, vol. 94, no. 3, p. 035703, Jan. 2019, doi: 10.1088/1402-4896/AAF68B.
[170] J. Wang, T. Lang, T. Shen, C. Shen, Z. Hong, and C. Lu, "Numerical Study of an Ultra-Broadband All-Silicon Terahertz Absorber," *Appl. Sci. 2020, Vol. 10, Page 436*, vol. 10, no. 2, p. 436, Jan. 2020, doi: 10.3390/APP10020436.
[171] J. Yang *et al.*, "Broadband terahertz absorber based on multi-band continuous plasmon resonances in geometrically gradient dielectric-loaded graphene plasmon structure," *Sci. Reports 2018 81*, vol. 8, no. 1, pp. 1–8, Feb. 2018, doi: 10.1038/s41598-018-21705-2.
[172] F. G. Vanani, A. Fardoost, and R. Safian, "Design of double ring label-free terahertz sensor," *IEEE Sens. J.*, vol. 19, no. 4, pp. 1293–1298, 2019, doi: 10.1109/JSEN.2018.2881411.
[173] P. U. Jepsen, D. G. Cooke, and M. Koch, "Terahertz spectroscopy and imaging – Modern techniques and applications," *Laser Photon. Rev.*, vol. 5, no. 1, pp. 124–166, Jan. 2011, doi: 10.1002/LPOR.201000011.
[174] U. Patri and A. Kumar, "Graphene-based ultra-wideband absorber for terahertz applications using hexagonal split ring resonators," *Phys. Scr.*, Apr. 2022, doi: 10.1088/1402-4896/AC6AF1.
[175] A. Chen and Z. Song, "Tunable Isotropic Absorber with Phase Change Material VO2," *IEEE Trans. Nanotechnol.*, vol. 19, pp. 197–200, 2020, doi: 10.1109/TNANO.2020.2974801.
[176] G. Varshney, "Wideband THz Absorber: By Merging the Resonance of Dielectric Cavity and Graphite Disk Resonator," *IEEE Sens. J.*, vol. 21, no. 2, pp. 1635–1643, 2021, doi: 10.1109/JSEN.2020.3017454.
[177] X. Huang, C. Lu, C. Rong, Z. Hu, and M. Liu, "Multiband ultrathin polarization-insensitive terahertz perfect absorbers with complementary metamaterial and resonator based on high-order electric and magnetic resonances," *IEEE Photonics J.*, vol. 10, no. 6, Dec. 2018, doi: 10.1109/JPHOT.2018.2878455.
[178] A. Ebrahimi, R. T. Ako, W. S. L. Lee, M. Bhaskaran, S. Sriram, and W. Withayachumnankul, "High-Q Terahertz Absorber with Stable Angular Response," *IEEE Trans. Terahertz Sci. Technol.*, vol. 10, no. 2, pp. 204–211, 2020, doi: 10.1109/TTHZ.2020.2964812.
[179] M. F. Ali, R. Bhattacharya, and G. Varshney, "Graphene-based tunable terahertz self-diplexing/MIMO-STAR antenna with pattern diversity," *Nano Commun. Netw.*, vol. 30, p. 100378, Dec. 2021, doi: 10.1016/J.NANCOM.2021.100378.
[180] S. Asgari, N. Granpayeh, and T. Fabritius, "Controllable terahertz cross-shaped three-dimensional graphene intrinsically chiral metastructure and its biosensing application," *Opt. Commun.*, vol. 474, no. April, p. 126080, 2020, doi: 10.1016/j.optcom.2020.126080.

[181] B.-X. Wang, Y. He, P. Lou, and W. Xing, "Design of a dual-band terahertz metamaterial absorber using two identical square patches for sensing application," 2020, doi: 10.1039/c9na00770a.
[182] Z. Vafapour, "Polarization-Independent Perfect Optical Metamaterial Absorber as a Glucose Sensor in Food Industry Applications," *IEEE Trans. Nanobioscience*, vol. 18, no. 4, pp. 622–627, 2019, doi: 10.1109/TNB.2019.2929802.
[183] J. Ma, J. Wang, Z. Da Hu, Z. Zhang, L. Pan, and A. Di Falco, "High-efficiency and ultrabroadband flexible absorbers based on transversely symmetrical multi-layer structures," *AIP Adv.*, vol. 9, no. 11, p. 115007, Nov. 2019, doi: 10.1063/1.5119406.
[184] P. Xiang *et al.*, "In situ synthesis of monolayer graphene on silicon for near-infrared photodetectors," *RSC Adv.*, vol. 9, no. 64, pp. 37512–37517, Nov. 2019, doi: 10.1039/C9RA06792B.
[185] A. K. Soni and G. Varshney, "Multiband Generation and Absorption Enhancement in a Graphite-Based Metal-Free Absorber," *Plasmonics*, vol. 16, no. 1, pp. 241–252, Feb. 2021, doi: 10.1007/s11468-020-01286-5.
[186] A. K. Soni, P. Giri, and G. Varshney, "Metal-free super-wideband THz absorber for electromagnetic shielding," *Phys. Scr.*, vol. 96, no. 12, p. 125866, Dec. 2021, doi: 10.1088/1402-4896/AC3EA1.
[187] Y. L. Liao and Y. Zhao, "Ultra-narrowband dielectric metamaterial absorber with ultra-sparse nanowire grids for sensing applications," *Sci. Reports 2020 101*, vol. 10, no. 1, pp. 1–7, Jan. 2020, doi: 10.1038/s41598-020-58456-y.
[188] I. V. Shadrivov, K. Fan, W. J. Padilla, and X. Liu, "Experimental realization of a terahertz all-dielectric metasurface absorber," *Opt. Express, Vol. 25, Issue 1, pp. 191-201*, vol. 25, no. 1, pp. 191–201, Jan. 2017, doi: 10.1364/OE.25.000191.
[189] A. Veeraselvam, G. N. A. Mohammed, K. Savarimuthu, and P. D. Vijayaraman, "An Ultra-Thin Multiband Refractive Index-Based Carcinoma Sensor Using THz Radiation," *IEEE Sens. J.*, vol. 22, no. 3, pp. 2045–2052, Feb. 2022, doi: 10.1109/JSEN.2021.3134663.
[190] J. Zhou *et al.*, "Perfect ultraviolet absorption in graphene using the magnetic resonance of an all-dielectric nanostructure," *Opt. Express, Vol. 26, Issue 14, pp. 18155-18163*, vol. 26, no. 14, pp. 18155–18163, Jul. 2018, doi: 10.1364/OE.26.018155.
[191] W. Su, Z. Geng, J. Qi, and H. Wu, "Multi-fano resonances in graphene coated all-dielectric metasurface for refractive index sensing with high figure of merits," *IEEE J. Sel. Top. Quantum Electron.*, vol. 27, no. 1, Jan. 2021, doi: 10.1109/JSTQE.2020.2991884.
[192] J. Y. Suen, K. Fan, W. J. Padilla, and X. Liu, "All-dielectric metasurface absorbers for uncooled terahertz imaging," *Opt. Vol. 4, Issue 6, pp. 601-604*, vol. 4, no. 6, pp. 601–604, Jun. 2017, doi: 10.1364/OPTICA.4.000601.
[193] E. S. Torabi, A. Fallahi, and A. Yahaghi, "Evolutionary Optimization of Graphene-Metal Metasurfaces for Tunable Broadband Terahertz Absorption," *IEEE Trans. Antennas Propag.*, vol. 65, no. 3, pp. 1464–1467, Mar. 2017, doi: 10.1109/TAP.2016.2647580.
[194] X. Wang and S. A. Tretyakov, "Toward Ultimate Control of Terahertz Wave Absorption in Graphene," *IEEE Trans. Antennas Propag.*, vol. 67, no. 4, pp. 2452–2461, Apr. 2019, doi: 10.1109/TAP.2018.2889144.
[195] M. B. Heydari and M. H. V. Samiei, "Analytical Study of Chiral Multi-Layer Structures Containing Graphene Sheets for THz Applications," *IEEE Trans. Nanotechnol.*, vol. 19, pp. 653–660, 2020, doi: 10.1109/TNANO.2020.3018015.
[196] A. Lakhtakia, P. Kumar, and P. K. Jain, "Graphene pixel-based polarization-insensitive metasurface for almost perfect and wideband terahertz absorption," *JOSA B, Vol. 36, Issue 8, pp. F84-F88*, vol. 36, no. 8, pp. F84–F88, Aug. 2019, doi: 10.1364/JOSAB.36.000F84.
[197] M. Nejat and N. Nozhat, "Design, Theory, and Circuit Model of Wideband, Tunable and Polarization-Insensitive Terahertz Absorber Based on Graphene," *IEEE Trans. Nanotechnol.*, vol. 18, pp. 684–690, 2019, doi: 10.1109/TNANO.2019.2925964.
[198] M. A. Mollah, R. J. Usha, S. Tasnim, and K. Ahmed, "Detection of cancer affected cell using Sagnac interferometer based photonic crystal fiber refractive index sensor," *Opt. Quantum Electron.*, vol. 52, no. 9, pp. 1–12, Sep. 2020, doi: 10.1007/S11082-020-02542-Y/TABLES/2.
[199] Z. Vafapour, A. Keshavarz, and H. Ghahraloud, "The potential of terahertz sensing for cancer diagnosis," *Heliyon*, vol. 6, no. 12, p. e05623, Dec. 2020, doi: 10.1016/J.HELIYON.2020.E05623.
[200] P. Y. Liu *et al.*, "Cell refractive index for cell biology and disease diagnosis: past, present and future," *Lab Chip*, vol. 16, no. 4, pp. 634–644, Feb. 2016, doi: 10.1039/C5LC01445J.
[201] B. X. Wang, X. Zhai, G. Z. Wang, W. Q. Huang, and L. L. Wang, "A novel dual-band terahertz metamaterial absorber for a sensor application," *J. Appl. Phys.*, vol. 117, no. 1, p. 014504, Jan. 2015,

doi: 10.1063/1.4905261.
[202] B. X. Wang, Q. Xie, G. Dong, and W. Q. Huang, “Simplified Design for Broadband and Polarization-Insensitive Terahertz Metamaterial Absorber,” *IEEE Photonics Technol. Lett.*, vol. 30, no. 12, pp. 1115–1118, Jun. 2018, doi: 10.1109/LPT.2018.2834902.
[203] J. Yang, H. Deng, Z. Xiong, Z. Xiong, and L. Shang, “Terahertz sensor based on a three-dimensional double I-type metamaterial integrated microfluidic channel,” *Appl. Opt. Vol. 60, Issue 13, pp. 3816-3822*, vol. 60, no. 13, pp. 3816–3822, May 2021, doi: 10.1364/AO.421910.
[204] A. Panda and P. D. Pukhrambam, “Design and modelling of reconfigurable surface plasmon resonance refractive index sensor employing graphene and Sb2S3 for detection of dengue virus,” *Phys. B Condens. Matter*, vol. 638, Aug. 2022, doi: 10.1016/J.PHYSB.2022.413965.
[205] O. Parkash, R. H. Shueb, and A. Ploss, “Diagnosis of Dengue Infection Using Conventional and Biosensor Based Techniques,” 2015, doi: 10.3390/v7102877.
[206] N. Alia Sheh omar *et al.*, “Sensitive Detection of Dengue Virus Type 2 E-Proteins Signals Using Self-Assembled Monolayers/ Reduced Graphene Oxide-PAMAM Dendrimer Thin Film-SPR Optical Sensor,” 2020, doi: 10.1038/s41598-020-59388-3.
[207] B. X. Wang, X. Zhai, G. Z. Wang, W. Q. Huang, and L. L. Wang, “A novel dual-band terahertz metamaterial absorber for a sensor application,” *J. Appl. Phys.*, vol. 117, no. 1, p. 014504, Jan. 2015, doi: 10.1063/1.4905261.
[208] B. Zhang, J. Duan, Y. Xu, and Y. Liu, “Flexible ultrawideband microwave metamaterial absorber with multiple perfect absorption peaks based on the split square ring,” *Appl. Opt. Vol. 57, Issue 35, pp. 10257-10263*, vol. 57, no. 35, pp. 10257–10263, Dec. 2018, doi: 10.1364/AO.57.010257.
[209] A. R. Khan *et al.*, “Dual-band refractometric terahertz biosensing with intense wave-matter-overlap microfluidic channel,” *Biomed. Opt. Express, Vol. 10, Issue 8, pp. 3789-3799*, vol. 10, no. 8, pp. 3789–3799, Aug. 2019, doi: 10.1364/BOE.10.003789.
[210] L. Cong, S. Tan, R. Yahiaoui, F. Yan, W. Zhang, and R. Singh, “Experimental demonstration of ultrasensitive sensing with terahertz metamaterial absorbers: A comparison with the metasurfaces,” *Appl. Phys. Lett.*, vol. 106, no. 3, p. 031107, Jan. 2015, doi: 10.1063/1.4906109.
[211] M. Gupta, Y. K. Srivastava, M. Manjappa, and R. Singh, “Sensing with toroidal metamaterial,” *Appl. Phys. Lett.*, vol. 110, no. 12, p. 121108, Mar. 2017, doi: 10.1063/1.4978672.
[212] Y. K. Srivastava, L. Cong, and R. Singh, “Dual-surface flexible THz Fano metasensor,” *Appl. Phys. Lett.*, vol. 111, no. 20, p. 201101, Nov. 2017, doi: 10.1063/1.5000428.
[213] Y. K. Srivastava, R. T. Ako, M. Gupta, M. Bhaskaran, S. Sriram, and R. Singh, “Terahertz sensing of 7 nm dielectric film with bound states in the continuum metasurfaces,” *Appl. Phys. Lett.*, vol. 115, no. 15, p. 151105, Oct. 2019, doi: 10.1063/1.5110383.
[214] M. Gupta and R. Singh, “Terahertz Sensing with Optimized Q/Veff Metasurface Cavities,” *Adv. Opt. Mater.*, vol. 8, no. 16, p. 1902025, Aug. 2020, doi: 10.1002/ADOM.201902025.
[215] A. S. Saadeldin, M. F. O. Hameed, E. M. A. Elkaramany, and S. S. A. Obayya, “Highly Sensitive Terahertz Metamaterial Sensor,” *IEEE Sens. J.*, vol. 19, no. 18, pp. 7993–7999, Sep. 2019, doi: 10.1109/JSEN.2019.2918214.
[216] S. Banerjee, P. Dutta, A. V. Jha, B. Appasani, and M. S. Khan, “A Biomedical Sensor for Detection of Cancer Cells Based on Terahertz Metamaterial Absorber,” *IEEE Sensors Lett.*, vol. 6, no. 6, Jun. 2022, doi: 10.1109/LSENS.2022.3178918.

Contributions

Journals:

1. P. Upender and A. Kumar, "THz Dielectric Metamaterial Sensor With High Q for Biosensing Applications," in IEEE Sensors Journal, vol. 23, no. 6, pp. 5737-5744, 15 March15, 2023, doi: 10.1109/JSEN.2023.3239669. **[SCI]**

2. P. Upender and A. Kumar, "Ultrathin, Ultra narrow band DMMA for biosensing applications," IEEE Transactions on NanoBioscience, 2022, doi: 10.1109/TNB.2022.3217077. **[SCI]**
3. P. Upender and A. Kumar, “Graphene-based ultra-wideband absorber for terahertz applications using hexagonal split ring resonators,” Phys. Scr., vol. 97, no. 6, p. 065503, May 2022, doi: 10.1088/1402-4896/AC6AF1. **[SCI]**
4. U. Patri and A. Kumar, “A novel ultra wideband circularly polarized stacked cylindrical dielectric resonator antenna with modified ground plane,” Int. J. RF Microw. Comput. Eng., vol. 32, no. 8, p. e23221, Aug. 2022, doi: 10.1002/MMCE.23221. **[SCI]**
5. P. Upender and A. Kumar, “$HEM_{11\delta}$ and $HEM_{12\delta}$-based Quad band Quad Sense circularly polarized tunable Graphene-based MIMO Dielectric Resonator Antenna,” Frequenz, vol. 76, no. 5, pp. 273–285, Jun. 2022, doi: https://doi.org/10.1515/freq-2021-0145. **[SCI]**
6. P. Upender, A. Kumar, and A. Kumar, “Design of a multiband graphene-based absorber for terahertz applications using different geometric shapes,” JOSA B, Vol. 39, Issue 1, pp. 188- 199, vol. 39, no. 1, pp. 188–199, Jan. 2022, doi: 10.1364/JOSAB.440757. **[SCI]**
7. P. Upender and A. Kumar, “Quad-Band Circularly Polarized Tunable Graphene Based Dielectric Resonator Antenna for Terahertz Applications,” Silicon 2021, vol. 5, no. 10, pp. 1– 14, Aug. 2021, doi: 10.1007/S12633-021-01336-5. **[SCI]**
8. Upender, P., Kumar, A. Implementing reconfigurable circularly polarized two port MIMO DRA for THz applications. Opt Quant Electron 55, 900 (2023). https://doi.org/10.1007/s11082-023-05188-8. **[SCI]**

Conferences:

1. P. Upender and A. Kumar, “Circularly Polarized 2×2 MIMO Dielectric Resonator Antenna for Terahertz Applications,” 2021 IEEE Indian Conf. Antennas Propagation, InCAP 2021, pp. 283–286, 2021, doi: 10.1109/INCAP52216.2021.9726292.
2. P. Upender and A. Kumar, "A new technique for Hexa Band Quad Sense Cylindrical Dielectric Resonator antenna for THz Applications," 2023 IEEE IAS Global

Conference on Emerging Technologies (GlobConET), London, United Kingdom, 2023, pp. 1-5, doi: 10.1109/GlobConET56651.2023.10149946.